Development of Microscopy Hardware & Imaging Techniques for Macrophage Host Defence Research





THE UNIVERSITY *of* EDINBURGH

A thesis submitted in partial fulfillment of the requirements for the degree of Doctor of Philosophy with Integrated Study

Gemma Sharon Cairns

NanoBioPhotonics, Department of Physics, University of Strathclyde
Centre for Inflammation Research, The University of Edinburgh
OPTIMA: The EPSRC and MRC CDT in Optical Medical Imaging

2022

This thesis is the result of the author's original research. It has been composed by the author and has not been previously submitted for examination which has led to the award of a degree.

The copyright of this thesis belongs to the author under the terms of the United Kingdom Copyright Acts as qualified by University of Strathclyde Regulation 3.50. Due acknowledgement must always be made of the use of any material contained in, or derived from, this thesis.

Signed: 

Date: 15/07/2022

Abstract

Mitochondrial reactive oxygen species (mROS) have recently emerged as critical microbicidal factors employed by macrophages in the clearance of internalised *Streptococcus pneumoniae* [1]. *S. pneumoniae* is a type of bacteria found in the upper respiratory tract, which when colonised can spread and lead to life threatening invasive pneumococcal diseases (IPD) [2]. Infants, the elderly and immunocompromised individuals are more susceptible to IPD [3]. A study has shown alveolar macrophages from patients with chronic obstructive pulmonary disease were unable to increase mROS production after bacterial challenge with *S. pneumoniae*, which correlated with impaired bacterial clearance [1]. They also observed colocalization between mROS, phagolysosomes and *S. pneumoniae* in human monocyte derived macrophages from healthy donors.

There is a growing need to develop alternatives to conventional antimicrobials, for example pharmacologically enhancing the responses of macrophages, due to the growing worldwide problem of antimicrobial resistance, which has already been identified in *S. pneumoniae* to penicillin [4]. Furthermore, the number of *S. pneumoniae* serotypes included in currently available vaccinations is limited [5, 6]. Advances in microscopy and image analysis offer new opportunities to quantify interactions between mROS and *S. pneumoniae*.

This thesis presents early studies which showed aberrations were present in confocal images of mitochondria labelled within human monocyte derived macrophages and the types and magnitudes of aberrations present varied across the sample, which could be problematic for colocalization imaging studies. Also, as prevalence of IPD is higher in some developing countries in Africa and Asia [7, 8] where resources are lower, we devel-

oped M4All: MultiModal Modular Microscopy for All [9], a 3D printable microscopy system, to increase accessibility to advanced microscopy techniques for macrophage host defence research. We also carried out initial studies implementing open-source computational microscopy techniques such as super-resolution radial fluctuations [10] and the transport of intensity equation [11].

Acknowledgements

Firstly, I thank the OPTIMA CDT for giving me the opportunity to pursue a PhD, especially Dr Jean O'Donoghue who always went out of her way to support us and visited me at Heriot-Watt to tell me all about the programme when I was still an undergraduate student. I have had some fantastic experiences with OPTIMA along the way, from our business course modules to summer schools and Christmas parties, all of which have enhanced my PhD experience. I'm also thankful to my cohort who I wouldn't have got through this PhD without.

Secondly, I thank my two PhD supervisors, Dr Brian Patton and Prof. David Dockrell, who have been continuously supportive throughout my PhD, always there for constructive discussions and pushing me to develop as a researcher. I thank Brian for working with me through all the curve balls that we faced during my PhD and for helping to modify my research project when we had to adapt. I thank David for being patient with me as a physicist delving into the world of immunology and for the opportunity to learn and develop key biological lab skills within his group.

Thank you to all the members of both my research groups at the University of Strathclyde and the University of Edinburgh, past and present. In particular, thank you to Dr Graeme Johnstone who, aside from Brian, was the only other member of NanoBioPhotonics when I joined - I won't forget that first day in the lab when you told me we had to move every element on the optical table back by an inch! Also thanks to Dr Stephen Grant who helped me to get up and running with everything 3D printer related. Thank you to Jennifer and Katharin who helped me out massively in the biology lab, teaching me lab techniques and helping to prepare samples. Big thanks

to Ryan and Petros who became good friends when I moved to Glasgow after the first lockdown and helped me settle into the city. Especially Ryan - I'm so thankful that we had each other to help get through the past couple of years since COVID, finishing up in the lab, writing our theses and finding jobs. We made it!

I want to thank Hannah, Crystel and Réka for being amazing flatmates when I moved to Glasgow after the first lockdown and making the move a lot less daunting. I also thank Hollie who I met when I moved, I've been thankful to have you as a friend and cycling buddy. Also thanks to my DnD friends, Charlotte, Grant, Alex, Will and Emma, for giving me something fun to do every week to take my mind off the PhD. Especially Charlotte who has become one of my closest friends since we met in first year of OPTIMA - looking forward to going to more rugby matches and our holiday!

A big thanks also goes to my friends who have been in my life for a very long time. Robyn you've been there for me through thick and thin since we were kids - can't believe it's been 20 years! I wouldn't have got this far without you and I'm truly lucky to have such a long standing best friend. Emma, I'm so thankful you came into my life during undergrad, your sense of humour and infectious laughter always brings me joy. The past 10 years wouldn't have been the same without you and again I'm truly lucky to have found such a close friend. Sorcha, you've also been one of my closest friends since we were kids, and despite geographical distances you were still there sending support when I was going through a tough time during lockdown. Eilidh, I'm thankful we have stayed close friends since school and I'll never forget you and Robyn serenading me with giant balloons and a microphone in my car park on my birthday this year.

Last but certainly not least, a huge thank you to my family who are always there for me. To my Mum ("Seriously") and Dad ("Runs with Beer") who supported me through tough times during lockdown and kept me going with the PhD, I can't thank you both enough for everything you do for me and I couldn't ask for better parents. To my brother, Ross ("Cheerio"), thank you for being the calm and positive one and for always keeping me laughing, again I couldn't ask for a better brother. Also to my Grandma and Granny who always send messages of support and to both my Grandads who I know have been watching over me.

Research Outputs

1. Johnstone, G. E., **Cairns, G. S.** & Patton, B. R. Nanodiamonds enable adaptive-optics enhanced, super-resolution, two-photon excitation microscopy. *Royal Society Open Science* **6**, 190589 (2019).

2. Grant, S. D., **Cairns, G. S.**, Wistuba, J. & Patton, B. R. Adapting the 3D-printed Openflexure microscope enables computational super-resolution imaging. *F1000Research* **8** (2019).

3. **Cairns, G. S.** NanoBioPhotonics-Strathclyde/M4All version 1.0.0. (2021) https://doi.org/10.5281/zenodo.5569711.

Conference Presentations

1. **Cairns, G. S.**, Dockrell, D. H. & Patton, B. R., "M4All: MultiModal Modular Microscopy for All", Oral Presentation, PHASE - Photonics for Healthcare, Atmosphere, Safety and Education hybrid workshop (2022).

2. **Cairns, G. S.**, Dockrell, D. H. & Patton, B. R., "M4: MultiModal Modular Microscopy", Oral Presentation, Microscience Microscopy Congress (mmc) (2021).

3. **Cairns, G. S.**, Dockrell, D. H. & Patton, B. R., "M4: MultiModal Modular Microscopy", Oral Presentation, European Light Microscopy Initiative (elmi) (2021).

4. **Cairns, G. S.**, Dockrell, D. H. & Patton, B. R., "M4: MultiModal Modular Microscopy", Oral Presentation, Scottish Microscopy Society's Virtual Symposium (2020).

5. **Cairns, G. S.**, Dockrell, D. H. & Patton, B. R., "Multimodal Microscopy for Macrophages", Oral Presentation, SHIELD Consortium meeting (2019).

6. **Cairns, G. S.**, Grant, S. D., & Patton, B. R., "Low-Cost Quantitative Phase Microscopy", Oral Presentation, Glasgow Imaging Network Symposium (2019).

7. **Cairns, G. S.**, Johnstone, G. E., Dockrell, D. H. & Patton, B. R., "Adaptive Optics Enhanced Microscopy for Respiratory Infection Clinical Research", Oral Presentation, Photon (2018).

8. **Cairns, G. S.**, Johnstone, G. E., Dockrell, D. H. & Patton, B. R., "Imaging mitochondrial interactions with bacteria in macrophages after bacterial challenge", Poster Presentation, European Light Microscopy Initiative (elmi) (2018).

Contents

Declaration **i**

Abstract **ii**

Acknowledgements **iv**

Research Outputs **vi**

Conference Presentations **vii**

List of Figures **xii**

List of Tables **xxxiv**

1 Introduction **1**

1.1 *Streptococcus pneumoniae* 1

1.2 The Innate and Adaptive Immune Responses 4

1.3 Macrophages 5

1.3.1 Origin 5

1.3.2 Function 5

1.4 Macrophage Pathogen Interaction with *Streptococcus pneumoniae* 6

1.4.1 Macrophage Antimicrobials 6

1.4.2 Apoptosis 7

1.4.3 The Role of Mitochondria and Mitochondrial Reactive Oxygen Species (mROS) 7

1.5 Methods for Mitochondria and mROS Detection 10
1.6 Aims 15
1.7 COVID-19 Impact Statement 17

2 Methods **19**
2.1 Isolation of Human Peripheral Blood Mononuclear Cells (PBMCs) from Whole Blood Sample Using Percoll Density Gradient 19
2.2 Culturing Monocyte Derived Macrophages (MDMs) from PBMCs 20
2.3 Macrophage Bacterial Internalisation with *Streptococcus pneumoniae* . . 20
2.4 Macrophage Bacterial Internalisation with *Staphylococcus aureus* 21
2.5 Macrophage Fluorescent Labelling for Microscopy 21

3 Early Adaptive Optics, Computational Super-Resolution and Phase Imaging Studies **23**
3.1 Introduction 23
3.1.1 Review of Super-Resolution Techniques 23
3.1.2 Adaptive Optics (AO) 31
3.1.3 Transport of Intensity Equation (TIE) 41
3.2 Initial Study of Aberration Correction of Confocal Macrophage Images . 43
3.3 Super-Resolution Radial Fluctuations (SRRF) Reconstructions of Mitochondria 51
3.4 Effect of Image Aberrations on SRRF Reconstructions 54
3.5 TIE Microscopy of Macrophages 63
3.6 Conclusions 69

4 M4All Hardware Design **71**
4.1 Introduction 71
4.1.1 3D Printing 72
4.1.2 Open-Source Microscopy Systems 73
4.2 Initial Test Microscope Design Parameters 78
4.3 Initial Testing of Available Open-Source Systems 81

4.3.1 UC2 . . . 81
4.3.2 UC2-OpenFlexure . . . 84
4.3.3 Assembly and Alignment . . . 87
4.3.4 Discussion . . . 90
4.4 M4All Modular Cube Design . . . 91
4.5 M4All Practical Considerations . . . 94
4.5.1 Optical Component Insert Designs . . . 94
4.5.2 Microscope Stage . . . 97
4.5.3 Test Parts for Printing . . . 98
4.5.4 3D Printing Material Choice . . . 99
4.6 M4All Initial Tests . . . 100
4.7 Conclusions . . . 101

5 M4All Practical Applications 103
5.1 Introduction . . . 103
5.1.1 Optical Design Theory . . . 103
5.1.2 Ray Transfer Matrix Analysis (RTMA) . . . 108
5.2 M4All TIE and Fluorescence Microscope . . . 113
5.2.1 Camera and Lens Selection . . . 113
5.2.2 Imaging Challenges . . . 116
5.2.3 Final Microscope . . . 127
5.2.4 RTMA Magnification Analysis and Calibration . . . 128
5.2.5 Stepper Motor Calibration . . . 140
5.2.6 Stability Tests . . . 144
5.2.7 TIE Microscopy . . . 146
5.2.8 Fluorescence Microscopy . . . 151
5.3 M4All Dual Channel Fluorescence Microscope . . . 152
5.3.1 Design Parameters . . . 152
5.3.2 RTMA Magnification Analysis and Calibration . . . 157
5.3.3 Single and Dual Channel Fluorescence Microscopy . . . 159

5.3.4 SRRF Reconstruction 163
5.4 M4All Incubator Microscope 164
5.4.1 Design Parameters 164
5.4.2 Initial Incubator Microscope Drift Measurements 165
5.5 Conclusions 167

6 M4All Microscope Control **169**
6.1 Introduction 169
6.2 Control Hardware 169
6.3 Control Software 172
6.3.1 M4All TIE and Fluorescence, and Dual Channel Fluorescence Microscopes 172
6.3.2 Stepper Motor GUI 176
6.3.3 M4All Incubator Microscope GUI 178
6.4 Note on Raspberry Pi Camera Settings 180
6.5 Conclusions 180

7 Conclusions **181**

Bibliography **186**

List of Figures

1.1 Schematic (Jablonski) diagram illustrating the process of fluorescence. The blue arrow indicates absorption of a photon, exciting an electron from the ground state S_0 to a higher energy state e.g. S_2. Following a non-radiative relaxation to the lowest excited state, S_1, either spontaneous emission (green arrow) or stimulated emission (red arrow) occurs. 10

1.2 **(a)** Schematic of widefield microscopy where both the in focus and out of focus light are imaged on the detector. **(b)** Schematic of confocal microscopy where pinhole 2 rejects the out of focus light from the detector. 11

2.1 **(a)** Mock infected MDM where mitochondria are labelled with Alexa Fluor 488. **(b)** MDM nuclei and *S. pneumoniae* bacteria, 16 hours after challenge, labelled with DRAQ5. White arrows indicate clusters of *S. pneumoniae* and the red arrow indicates an apoptotic nucleus. Images acquired using a Leica SP5 confocal microscope. 22

3.1 **(a)** Model of a plane wave. **(b)** Model of a non-aberrated spherical wave. **(c)** Model of an aberrated spherical wave, where the only change was to modify the phase and not the amplitude. These figures were made by Dr Brian Patton. 32

3.2 **(a)** Flowchart of the indirect (sensorless) adaptive optics aberration correction routine. **(b)** Example quality metric fitting for coma aberration. Three images were acquired (red dots) with varying amplitudes of coma applied using the adaptive correction element. The quality metric was calculated for each image and the plot shows the metric values vs coma amplitude applied. Using a Gaussian fit, the metric curve peak is found, which gives the optimal aberration amplitude to apply to the adaptive correction element (green dot). **(b)** is reprinted with permission from [92] © The Optical Society. 34

3.3 Schematic of our custom adaptive optics enhanced confocal microscope. Adapted from an original schematic made by Dr Graeme Johnstone. . . 36

3.4 Schematic of the deformable mirror incorporated into one arm of a Michelson interferometer. 39

3.5 **(a)** Reference image for DM calibration. **(b)** Image of the back focal plane of the objective. **(c)** Trefoil aberration applied using the required control voltages determined by $\mathbf{B}^{\dagger}$. 40

3.6 Confocal image, from a z-stack acquired using an Andor Revolution XDi spinning disk confocal microscope, of a mock infected human MDM sample with labelled mitochondria (Alexa Fluor 488) and nuclei (DRAQ5). The orthogonal planes from the z-stack are also shown where the magenta arrow highlights mitochondria deeper in the sample with greater blurring and elongation, due to spherical aberration, compared to those closer to the coverslip (yellow arrow). 44

3.7 Image of a mock infected human MDM, where mitochondria have been labelled with Alexa Fluor 488. Image acquired using our custom confocal microscope detailed in section 3.1.2. AO corrections were carried out on the full image plane (orange) and four quadrants: quadrant 1 - green, quadrant 2 - purple, quadrant 3 - yellow and quadrant 4 - blue. 46

3.8 Amplitude of the correction modes 5 - 10 (Zernike Noll index) calculated using the full image plane, quadrant 1, quadrant 2, quadrant 3 and quadrant 4 as defined in figure 3.7. 47

3.9 Schematic illustrating the position of the three image planes (orange) in figure 3.10 with reference to the cell (green) and slide and coverslip (blue). 47

3.10 Each row shows three image planes at different axial positions of a mock infected human MDM sample with labelled mitochondria (Alexa Fluor 488), acquired using our custom confocal microscope detailed in section 3.1.2. **(a)**, **(b)** and **(c)** shows non AO corrected data. **(d)**, **(e)** and **(f)** was AO corrected for plane **(d)**. **(g)**, **(h)** and **(i)** was AO corrected for plane **(h)**. **(j)**, **(k)** and **(l)** was AO corrected for plane **(l)**. The AO metric used was I^2 (the intensity of each pixel squared and summed) and is shown for each image. Zernike modes 5 - 11 (using the Noll index) were corrected for. **(m)**, **(n)** and **(o)** is the colour bar scale for each column with units counts per 1.5 ms. 49

3.11 Correction amplitudes for Zernike modes 5 - 11 (Noll index) for AO correction of image planes 1, 2 and 3 as shown in figures 3.9 and 3.10. . 51

3.12 **(a)** Andor Revolution XDi spinning disk confocal image of a mock infected human MDM with labelled mitochondria (single frame extracted from 100 raw frames acquired for SRRF reconstruction). Colour bar scale units are counts per 1.5 ms. The following images are SRRF reconstructions using different temporal correlation methods: **(b)** temporal radiality average, **(c)** temporal radiality pairwise product mean, **(d)** temporal radiality auto-cumulant second order, **(e)** temporal radiality auto-cumulant third order and **(f)** temporal radiality auto-cumulant fourth order. Colour bars for the SRRF reconstructions are pixel gray values. 53

3.13 **(a)** Andor Revolution XDi spinning disk confocal image of a human MDM challenged with *S. pneumoniae* (4 hour time point) with labelled mitochondria (single frame extracted from 100 raw frames acquired for SRRF reconstruction). Colour bar scale units are counts per 1.5 ms. The following images are SRRF reconstructions using different temporal correlation methods: **(b)** temporal radiality average, **(c)** temporal radiality pairwise product mean, **(d)** temporal radiality auto-cumulant second order, **(e)** temporal radiality auto-cumulant third order and **(f)** temporal radiality auto-cumulant fourth order. Colour bars for the SRRF reconstructions are pixel gray values. 54

3.14 Raw image frame acquired on our custom AO confocal microscope in section 3.1.2 of a mock infected human MDM, where mitochondria were labelled with Alexa Fluor 488, from **(a)** a non AO corrected data set and **(d)** an AO corrected data set (corrected for modes 5 - 10 (Zernike Noll index using the metric filtered peak intensity). **(b)** and **(e)** are SRRF reconstructions of the data sets in **(a)** and **(d)** respectively. **(c)** and **(f)** are SQUIRREL error maps for the SRRF reconstructions in **(b)** and **(e)** respectively. 55

3.15 **(a)** Raw image frame acquired on our custom AO confocal microscope in section 3.1.2 of a mock infected human MDM where mitochondria were labelled with Alexa Fluor 488. The yellow box highlights the ROI shown in **(b)** which was used for SRRF and SQUIRREL analysis. **(c)** Non AO corrected data set and **(f)** an AO corrected data set (corrected for modes 5 - 10 (Zernike Noll index using the metric filtered peak intensity) of the ROI. **(d)** and **(g)** are SRRF reconstructions of the data sets in **(c)** and **(f)** respectively. **(e)** and **(h)** are SQUIRREL error maps for the SRRF reconstructions in **(d)** and **(g)** respectively. 57

3.16 **(a)**, **(b)** and **(c)** are single frames from two-photon emission (TPE) microscopy data sets containing 100 raw frames, of samples containing a mix of 40 nm and 100 nm nanodiamonds prepared according to Johnstone *et al.* [85], in the case of no, low and high aberration respectively. Images were acquired by Dr Graeme Johnstone and Dr Brian Patton on our custom confocal microscope, detailed in section 3.1.2, which was adapted for TPE microscopy as in Johnstone *et al.* [85]. I carried out SRRF reconstructions on the data as shown in **(d)**, **(e)** and **(f)** using the following settings: Ring Radius 0.5, Radiality Magnification - 10, Axes in Ring - 8, Temporal Analysis - Temporal Radiality Pairwise Product Mean (TRPPM). 58

3.17 FRC curves for the SRRF reconstructions in figure 3.16 for the no aberration (orange), low aberration (blue) and high aberration (green) cases. The threshold curve (black) is shown where the threshold used is a half-bit of information per pixel, where the pixel real-space size is 7 nm. . . . 59

3.18 SQUIRREL error analysis of the SRRF reconstructions in figure 3.16. Column one is the diffraction limited reference image used, where in this case **(a)** is a single frame from the no aberration data set, **(d)** is a single frame from the low aberration data set and **(g)** is a single frame from the high aberration data set. Column two is the SRRF reconstructions for the **(b)** no, **(e)** low and **(h)** high aberration cases. Column three is the SQUIRREL error maps including the global RSP and RSE values for the **(c)** no, **(f)** low and **(i)** high aberration cases. The images in each row have been cropped and registered to one another in the NanoJ-SQUIRREL plugin. 60

3.19 SQUIRREL error analysis of the SRRF reconstructions in figure 3.16. Column one is the diffraction limited reference image used, where in this case **(a)**, **(d)** and **(g)** are all from the no aberration data set. Column two is the SRRF reconstructions for the **(b)** no, **(e)** low and **(h)** high aberration cases. Column three is the SQUIRREL error maps including the global RSP and RSE values for the **(c)** no, **(f)** low and **(i)** high aberration cases. The images in each row have been cropped and registered to one another in the NanoJ-SQUIRREL plugin. 61

3.20 **(a)** Raw image frame acquired on our custom AO confocal microscope, detailed in section 3.1.2, of a mock infected human MDM with labelled mitochondria (ATTO647N). Sample prepared by Katharin Balbirnie-Cumming at the University of Edinburgh. **(b)** Higher resolution image of the highlighted ROI in **(a)**. **(c)** SRRF reconstruction using settings: Ring Radius 0.5, Radiality Magnification - 10, Axes in Ring - 8, and TRPPM temporal analysis. 63

3.21 TIE microscopy data set of a human MDM where **(a)** is the brightfield image above the focal plane, **(b)** is the brightfield image at the focal plane, and **(c)** is the brightfield image below the focal plane. The axial spacing between the images is 0.53 μm and they were acquired on the wide area detection path of our custom AO confocal microscope (figure 3.3). **(d)** is the resulting TIE image. 65

3.22 TIE microscopy data set of a human MDM where **(a)** is the brightfield image above the focal plane, **(b)** is the brightfield image at the focal plane, and **(c)** is the brightfield image below the focal plane. The axial spacing between the images is 2.5 μm and they were acquired on the wide area detection path of our custom AO confocal microscope (figure 3.3). **(d)** is the resulting TIE image. 66

3.23 TIE microscopy data set of a human MDM. Data analysis was carried out using the Open Source PhaseGUI [117]. **(a)** GP regression TIE - equally spaced z stack. **(b)** GP regression TIE - exponentially spaced z stack. 67

3.24 TIE results using the image data set of the cheek cell sample from Jingshan *et al.* [116]. The first three images are the raw brightfield images **(a)** above the focal plane ($+4\,\mu$m), **(b)** at the focal plane, and **(c)** below the focal plane ($-4\,\mu$m). **(d)** TIE result using the finite difference method of estimating the derivative as described in section 3.1.3. **(e)** TIE result using the GP regression method and the full equally spaced z stack from $-256\,\mu$m to $+256\,\mu$m in $4\,\mu$m steps. 68

4.1 UC2 v0 system highlighting the key components of the cube, lid and base plate, where screws connecting the lid and cube magnetically connect to the base plate via ball magnets. Figure was created using STL files originally obtained from the UC2 GitHub repository [133] which were published under the licence CERN Open Hardware Licence v1.2. 75

4.2 Initial test microscope optical design schematic. Infinite-conjugate system including a single far red fluorescence imaging channel (magenta), separated by a 650 nm shortpass dichroic mirror (Thorlabs DMSP650), and one brightfield channel (green). Illumination provided by a 532 nm diode laser (Thorlabs CPS532). Detection provided by a USB CMOS camera (IDS UI-3060CP-M-GL Rev.2) and Raspberry Pi v2 camera module for the fluorescence and brightfield detection channels respectively. The 30:70 beamsplitter (Thorlabs BSS10R) is to allow for future multifocal plane imaging. 80

4.3 Concept of building the microscope illustrated in figure 4.2 with the UC2 v0 system. Figure was created using STL files originally obtained from the UC2 GitHub repository [133] which were published under the licence CERN Open Hardware Licence v1.2. 82

4.4 **(a)** UC2 v0 dichroic/beamsplitter insert. **(b)** Different view showing the slot to slide the optic into the insert. **(c)** My insert design for the Thorlabs DMSP650 1 inch dichroic mirror. Includes M3 self tapping screw holes, originally designed by Dr Richard Bowman from the Bath Open INstrumentation Group [146], to allow locking plates to be attached. **(d)** My insert design for the Thorlabs BSS10R 25 x 36 mm beamsplitter. Includes a groove at the bottom to hold the optic in and M3 holes at the top for the retaining plate. **(a)** and **(b)** were made using an STL file originally obtained from the UC2 GitHub repository [133] which was published under the licence CERN Open Hardware Licence v1.2. 83

4.5 **(a)** UC2 v0 turning mirror insert which uses the slot mechanism on the UC2 v0 cubes. This insert is not the correct orientation for use with a sample stage above the cubes. **(b)** My 1 inch turning mirror design for use with the cage system. **(a)** was made using an STL file originally obtained from the UC2 GitHub repository [133] which was published under the licence CERN Open Hardware Licence v1.2. 84

4.6 UC2 modified OpenFlexure stage with M3 screw holes in the side for combination with the UC2 base plate ball magnet system. Figure made using an STL file originally obtained from the UC2 GitHub repository [133] which was published under the licence CERN Open Hardware Licence v1.2. 84

4.7 **(a)** The UC2 modified OpenFlexure stage in practice where two vertical base plates were attached to connect the stage to the system. **(b)** Exploded schematic, including just one cube, to illustrate where the screw and ball magnet connections were. **(c)** Schematic of the back of the three base plates, highlighting that they were not joined together and that the vertical plates didn't sit flush against the table. **(b)** and **(c)** were made using STL files originally obtained from the UC2 GitHub repository [133] which was published under the licence CERN Open Hardware Licence v1.2 85

4.8 **(a)** The UC2-OpenFlexure stage adapter in practice. **(b)** Illustration of the bottom face of our modified adapter, highlighting the ball magnet divots and screw holes, along with the bars to replace the OpenFlexure feet. The adapter is a modified version of the STL file originally posted by Benedict Diederich on the OpenFlexure GitLab repository [147]. **(c)** Our modified adapter attached to the stage showing two of the elastic bands looped around the bars. 86

4.9 Alignment of the laser and turning mirror cube. **(a)** Laser was mounted on a XY translation stage and a tip/tilt kinematic mount. The green path highlights the desired laser path where it is reflected by 45° by the turning mirror cube. **(b)** Shows cage rods attached to the cube and the laser was adjusted so the beam was centred along the optical axis using an alignment target. **(c)** A second empty cube was added to extend the cage rods further to check the beam was still aligned further along the optical path. 87

4.10 **(a)** Reflected beam from the dichroic mirror. **(b)** Angular error in the reflected beam alignment. **(c)** Transmitted beam through the dichroic mirror. **(d)** Shows the same angular error as **(b)** but in the transmitted beam. 88

4.11 Illustration of dichroic mirror tilt where the incident beam is on axis but the reflected and transmitted beam paths have an angular error (α) to the optical axis. The black dashed line shows the expected paths if the dichroic mirror was at the correct position of 45° to the optical axis. . . 89

4.12 Shows the reflected beam path from the dichroic mirror after adjustment of the UC2 cube-lid screws. **(a)** Shows the double reflection from the dichroic mirror on the alignment target, where I centred one of the reflections. **(b)** Shows that the reflected beam was still centred on the optical axis when the test target was placed further along the optical path. **(c)** Shows the resulting position of the dichroic mirror cube did not sit flat after adjustment. 89

4.13 M4All CAD design suite. CAD files were designed using FreeCAD [148]. Designs are grouped into design categories, each of which is described in this thesis. 92

4.14 **(a)** 3D model of the M4All base cube where the jigsaw system, 30 mm cage system and M6 mounting holes are highlighted. **(b)** M4All cube lid where the corresponding jigsaw system to the cube can be seen. **(c)** 3D model illustrating the cube and lid together. The notches to help remove the lid are highlighted. 92

4.15 **(a)** Array of M4All base cube designs. **(b)** M4All open ended cubes. **(c)** Illustration of a combination of different cubes to create an internally closed system. 93

4.16 M4All Inserts **(a)** 1 inch turning mirror insert. **(b)** Turning mirror insert second orientation. **(c)** 1 inch dichroic mirror insert and locking plate. The red dashed lines show where the locking plate connects to the insert with M3 screws. **(d)** 1 inch lens holder and retaining ring. There are grub screw holes on the top to lock in place on the cage rods. **(e)** Drop in 1 inch filter holder. The retaining ring in **(d)** is compatible with this design. **(f)** Raspberry Pi Camera v2 module insert. 95

4.17 M4All beamsplitter cube options. **(a)** Option 1 with slot mechanism to take insert in and out of the cube. The top view and blue arrows indicate where the insert slots in. **(b)** Option 2 where the insert is printed monolithically inside the cube. The red lines highlight the mounting points for the locking plates. **(c)** Option 3 is also printed monolithically, however the locking plate holes have been moved to the top of the insert (red lines) and there is two slots for the bottom of the locking plate (blue arrows). 96

4.18 M4All OpenFlexure stage attachment utilising the jigsaw system. **(a)** Top view. **(b)** Bottom view. **(c)** The attachment connected to an OpenFlexure stage. The version in **(c)** has the corner removed for partial access to the cube underneath. 97

4.19 M4All cage rod test pieces. **(a)** Vertical test piece with three walls to simulate rod travelling through multiple cubes, and six different hole radii ranging from 3.0 mm to 3.25 mm. **(b)** Two horizontal test pieces, each with six different hole radii. The first ranges from 3.0 mm to 3.25 mm and the second ranges from 3.3 mm to 3.55 mm. 99

4.20 M4All jigsaw test piece including both male (left) and female (right) sections. 99

4.21 M4All initial test microscope. The OpenFlexure stage and objective lens were not included so the beam alignment within the cubes could be checked. **(a)** Laser aligned on centre of alignment target on channel one. **(b)** Alignment target moved further along the optical axis of channel one to show the beam was still centred. **(c)** Laser aligned on centre of alignment target on channel two. **(d)** Alignment target moved further along the optical axis of channel two to show the beam was still centred. 100

5.1 Optical schematics of **(a)** a finite-conjugate optical system where the sample is positioned between f_o and $2f_o$ and the objective lens focuses and forms an image at a finite distance, and **(b)** an infinite-conjugate optical system where the sample is positioned at f_o and objective lens does not directly form a real image of the object, therefore a tube lens with focal length f_t must be used to focus the collimated beam. The collimated path is referred to as the infinity space. 104

5.2 Illustration of the definition of the working distance of an objective lens with reference to the sample coverslip. 104

5.3 **(a)** Schematic indicating the variables needed to analyse the divergence of an objective lens, including the horizontal field of view ($HFOV$), the angular field of view ($AFOV$) and the effective focal length of the objective lens (f_o). The divergence x at a distance along the optical axis y is calculated using equation 5.8. **(b)** Schematic showing that to calculate the total beam width at a distance y then the diameter of the objective lens aperture D also needs to be added. 107

5.4 **(a)** Schematic for the propagation of a ray in free space where two reference planes, z_1 and z_2, and the corresponding height, y, and angle, θ, with respect to the optical axis z at each plane are indicated. **(b)** Schematic for the propagation of a ray through a thin lens where z_1 and z_2 correspond to the front and back surfaces of the lens. 109

5.5 Simplified schematic of a single infinity-corrected imaging channel to define variables for ray transfer matrix analysis. 111

5.6 TIE and fluorescence microscope optical design schematic. This is an extension of the design in figure 4.2, including two more brightfield channels, separated by a 50:50 beamsplitter, to allow for multifocal plane microscopy. The turning mirror on the third brightfield channel is included to make the system more compact. Tube lens focal lengths determined by equations 5.1 and 5.3. 113

5.7 First iteration of a TIE and fluorescence microscope built using the M4All system in combination with the OpenFlexure microscope stage. . 115

5.8 Initial brightfield images of a 10 μm graticule slide from the M4All TIE and fluorescence microscope: **(a)** first brightfield channel, **(b)** second brightfield channel, **(c)** third brightfield channel. 116

5.9 Cross drawn on microscope slide with permanent marker pen. A drop of immersion oil was placed on the cross before fixing two 0.17 mm thick coverslips on top and securing with nail varnish. 117

5.10 Schematic of the fluorescence and TIE microscope noting the size of the optics and the distances between them which are used for divergence calculations and analysis. 118

5.11 Schematic of a simple microscope rig which is sufficient to test the level of lens distortion for different focal length tube lenses, camera and objective lens combinations. Laser - Thorlabs CPS635. Mirrors - Thorlabs PF10-03-P01. Lens - Thorlabs 35 mm bi-convex lens LB1811-A. Sample - 10 μm grid sample. Objective lens - either Newport LI-40X or LI-60X. Tube lens - Thorlabs 50 mm (LB1471-A), 75 mm (LB1901-A), 100 mm (LB1676-A) and 125 mm (LB1904-A) bi-convex lenses. Camera - either Raspberry Pi v2 camera module, Raspberry Pi HQ camera module, IDS CMOS UI-3060CP-M-GL Rev. 2 or Thorlabs CMOS CS235MU. 122

5.12 Images of a 10 μm calibration grid from the test rig in figure 5.11 showing the level of lens distortion for different combinations of objective and tube lenses for the Raspberry Pi v2 camera module. **(a)** Newport LI-40X and Thorlabs 50 mm bi-convex tube lens. **(b)** Newport LI-40X and Thorlabs 75 mm bi-convex tube lens. **(c)** Newport LI-40X and Thorlabs 100 mm bi-convex tube lens. **(d)** Newport LI-60X and Thorlabs 50 mm bi-convex tube lens. **(e)** Newport LI-60X and Thorlabs 75 mm bi-convex tube lens. **(f)** Newport LI-60X and Thorlabs 100 mm bi-convex tube lens. 123

5.13 Images of a 10 μm grid from the test rig showing the level of lens distortion for different combinations of objective and tube lenses for the Raspberry Pi HQ camera module. **(a)** Newport LI-40X and Thorlabs 75 mm bi-convex tube lens. **(b)** Newport LI-40X and Thorlabs 100 mm bi-convex tube lens. **(c)** Newport LI-40X and Thorlabs 125 mm bi-convex tube lens. **(d)** Newport LI-60X and Thorlabs 75 mm bi-convex tube lens. **(e)** Newport LI-60X and Thorlabs 100 mm bi-convex tube lens. **(f)** Newport LI-60X and Thorlabs 125 mm bi-convex tube lens. 124

5.14 Images of a 10 μm grid from the test rig showing the level of lens distortion for different combinations of objective and tube lenses for the IDS CMOS camera. **(a)** Newport LI-40X and Thorlabs 100 mm bi-convex tube lens. **(b)** Newport LI-40X and Thorlabs 125 mm bi-convex tube lens. **(c)** Newport LI-60X and Thorlabs 100 mm bi-convex tube lens. **(d)** Newport LI-60X and Thorlabs 125 mm bi-convex tube lens. 124

5.15 Images of a 10 μm calibration grid taken on the test rig in figure 5.11 showing the level of lens distortion for different combinations of objective and tube lenses for the Thorlabs CMOS camera. **(a)** Newport LI-60X and Thorlabs 100 mm bi-convex tube lens. **(b)** Newport LI-60X and Thorlabs 125 mm bi-convex tube lens. 125

5.16 Images of a 10 μm calibration grid from the test rig in figure 5.11 showing the difference in chromatic aberration between a **(a)** Thorlabs bi-convex lens and a **(b)** Thorlabs achromatic doublet lens. There is noticeably less chromatic distortion for the latter. 126

5.17 Final version of the M4All TIE and fluorescence microscope. **(a)** Close up image of the optical component inserts within the cubes. **(b)** Overall view of the microscope with the lids on, also showing the illumination rig and the Raspberry Pi Zeros within 3D printed holders. 127

5.18 **(a)** Plot of lateral magnification (calculated by ray transfer matrix analysis) vs *d_sample* for the three brightfield channels in the TIE and fluorescence microscope. **(b)** The lateral magnification values in **(a)** have been normalised to the first brightfield channel. 128

5.19 Flow chart to highlight the steps in the magnification calibration of an infinity corrected system using RTMA data. A line profile on each channel image of the calibration grid is drawn and then plotted. From the plots the distance (number of pixels) corresponding to a number of grid squares on each channel is obtained. The distances are normalised to the first channel (measured normalised magnifications) and compared to the theoretical plot of normalised lateral magnification to determine the theoretical *d_sample* value. The position of the objective lens is then corrected and the process repeated until $d_sample = f_o$ within the axial resolution of the system. 130

5.20 Magnification calibration repeatability data for the situation where the objective lens was deliberately positioned too far away from the sample. **(a)** Three repetitions showing the measured normalised magnification values for two iterations of the calibration routine for repetitions 1 and 2, and three iterations for repetition 3. **(b)** The resulting working distance error for the calibration iterations for each repetition based on the data in **(a)**. The red dashed lines in **(b)** indicate the positive and negative axial resolution values of $\pm 2.518\,\mu$m. 132

5.21 Magnification calibration repeatability data for the situation where the objective lens was deliberately positioned too close to the sample. **(a)** Three repetitions showing the measured normalised magnification values for three iterations of the calibration routine for each repetition. **(b)** The resulting working distance error for the three calibration iterations for each repetition based on the data in **(a)**. The red dashed lines in **(b)** indicate the positive and negative axial resolution values of $\pm 2.518\,\mu$m. . 133

5.22 Illustration of the process of increasing *d_total* by raising the sample up with coverslips as the axial sample position on the OpenFlexure microscope stage is fixed. 133

5.23 Measured real lateral magnifications of brightfield channels 1 and 3 as *d_total* was increased by raising the height of the sample with coverslips. The magnifications of the two channels did not remain equal and at their starting values which was not the expected result. 134

5.24 Test rig to check that the magnifications of two brightfield channels remained equal after calibration when *d_total* was increased. **(a)** Test rig schematic. **(b)** Test rig in practice. Laser - Thorlabs CPS635. Mirrors - Thorlabs PF10-03-P01. Lens - Thorlabs 35 mm bi-convex lens LB1811-A. Sample - 10 m grid sample. Objective lens - Newport LI-60X. Tube lenses - Thorlabs achromatic doublets. Camera - IDS CMOS UI-3060CP-M-GL Rev. 2. 135

5.25 The measured real lateral magnification of the two brightfield channels on the test rig in figure 5.24 as *d_interlens* was increased. **(a)** Both channels had $f_t = 125\,\text{mm}$ thus the expected lateral magnification of both channels was 41.6x. **(b)** The result of swapping the tube lens on one of the channels for one with $f_t = 125\,\text{mm}$, changing the expected lateral magnification of the channel to 25x. 136

5.26 Images of a $10\,\mu\text{m}$ calibration grid at different focal planes acquired on one of the channels on the test rig in figure 5.24, highlighting that there is a plane above **(a)** and below **(e)** the correct focal plane **(c)** which could be mistaken for being in focus. **(b)** and **(d)** show clearly out of focus planes above and below the correct focal plane. 137

5.27 Repeated data set of measured lateral magnification of brightfield channels 1 and 3 as *d_total* was increased by raising the height of the sample with coverslips. It was made sure the objective lens was focused on the correct focal plane of the calibration grid each time the sample was raised. The magnifications of the two channels remained within 0.7 % of the expected magnification of 10x. 138

5.28 Theoretical data from RTMA to determine the refocus distance of the objective lens between channels 1/3 and 2 on the TIE and fluorescence microscope when the channel 2 tube lens is offset **(a)** 1 mm, **(b)** 2 mm and **(c)** 3 mm towards the objective lens. The theoretical refocus distance was determined for a range of *d_total* values. 139

5.29 **(a)** Starting position of the 10 μm calibration grid for lateral stepper motor calibration where y_1 highlights the starting position in y of the central thick line of the calibration grid. **(b)** Position of the calibration grid after moving the y lateral stepper motor by 10 steps, highlighting the y_2 position of the thick grid line. **(c)** Position of the calibration grid after moving the y lateral stepper motor another 10 steps, highlighting the y_3 position of the thick grid line. 141

5.30 **(a)** Plot of x pixel coordinate of the thick vertical line on the calibration grid shown in figure 5.29 vs increment of movement of the x lateral stepper motor on the OpenFlexure stage. **(b)** Plot of real distance the grid moved in x per x motor increment. **(c)** Plot of y pixel coordinate of the thick horizontal line on the calibration grid shown in figure 5.29 vs increment of movement of the y lateral stepper motor. **(d)** Plot of real distance the grid moved in y per y motor increment. Each motor increment for both the x and y motors was 10 motor steps. 141

5.31 **(a)** Custom axial stepper motor calibration sample where four 1.5H coverslips are mounted one on top of the other with a permanent marker line drawn on each. **(b)** Second custom axial stepper motor calibration sample with two 1.5H coverslips. 143

5.32 Distance in pixels measured across four grid lines of a 10 μm grid sample on the three brightfield channels of the M4All TIE and fluorescence microscope before looping the stepper motors (iteration 0) and after looping the stepper motors for two hours at a time (iterations 1, 2 and 3) to test short term stability of the microscope. 145

5.33 In focus images from brightfield **(a)** channel 1, **(b)** channel 2 and **(c)** channel 3 after offsetting the tube lenses of channels 2 and 3 for TIE microscopy. 147

5.34 TIE pre-processing steps. Step 1: Import images to ImageJ/Fiji and scale magnifications, normalising to camera 1. Step 2: Convert images to 32-bit and crop each image to an area of the same width and height containing the feature of interest. Step 3: Image registration using NanoJ-Core Drift Correction plugin, then crop images to same FOV. Step 4: Scale intensities using the yellow ROIs shown in step 3, normalising to the background of camera 1. 148

5.35 Row 1 is a TIE data set of a Diatom sample where **(a)** is the brightfield image above the focal plane, **(b)** is the brightfield image at the focal plane, **(c)** is the brightfield image below the focal plane, and **(d)** is the TIE image. Row 2 is a TIE data set of a second Diatom sample where **(a)** is the brightfield image above the focal plane, **(b)** is the brightfield image at the focal plane, **(c)** is the brightfield image below the focal plane, and **(d)** is the TIE image. Row 3 is a TIE data set of a nanodiamond sample where **(a)** is the brightfield image above the focal plane, **(b)** is the brightfield image at the focal plane, **(c)** is the brightfield image below the focal plane, and **(d)** is the TIE image. Row 4 is a TIE data set of a human MDM sample where **(a)** is the brightfield image above the focal plane, **(b)** is the brightfield image at the focal plane, **(c)** is the brightfield image below the focal plane, and **(d)** is the TIE image. Brightfield images acquired on the M4All TIE and Fluorescence microscope and pre-processed with the steps in figure 5.34. 149

5.36 **(a)** One image frame from the set of 100 images of a 90 nm nanodiamond sample captured on the fluorescence channel of the M4All TIE and fluorescence microscope. **(b)** SRRF processed image of the data set in **(a)**. **(c)** and **(d)** are zoomed in images of the highlighted region of interest shown in **(a)** and **(b)** respectively. 152

5.37 Optical schematic of the M4All dual channel fluorescence microscope design. The microscope is an infinity-corrected design including a far red ($> 650\,\text{nm}$) fluorescence imaging channel (magenta) separated by a 650 nm shortpass dichroic mirror (Thorlabs DMSP650). The second fluorescence channel detects between $490 - 650\,\text{nm}$ (green) and is separated by a 490 nm shortpass dichroic mirror (Thorlabs DMSP490). The RGB laser provides illumination at 450 nm, 520 nm and 635 nm. Raspberry Pi HQ camera modules are used to capture the fluorescence signal. 153

5.38 WORLD STAR TECH compact-multiwave laser spectrum. Data was acquired on an Ocean Optics QE65000 Scientific-grade Spectrometer. . . 154

5.39 Final version of the M4All dual channel fluorescence microscope. **(a)** Close up image of the optical component inserts within the cubes, the OpenFlexure stage with stepper motors connected to a Raspberry Pi Zero and PiStep2, and Raspberry Pi HQ cameras connected to two Raspberry Pi 4 8GB boards. **(b)** Overall view of the microscope also showing the illumination rig. 155

5.40 Illustration of the illumination rig. The WORLD STAR TECH compact-multiwave RGB laser is coupled into the system via a Thorlabs M42L02 patch cable containing a FG050LGA multimode fiber ($50\,\mu\text{m}$ core diameter). The fibre mount consists of a Thorlabs SM1FC fibre adapter attached to a Thorlabs KC1-T/M SM1 threaded kinematic mount. . . . 155

5.41 Power at the sample vs current for the **(a)** 450 nm, **(b)** 520 nm, and **(c)** 635 nm laser lines (WORLD STAR TECH compact-multiwave laser). Beam profile at the sample for the **(c)** 450 nm, **(d)** 520 nm, and **(e)** 635 nm laser lines. The area of the focal spot is highlighted on each image which can be used to calculate the power density. 157

5.42 Plot of normalised lateral magnification (calculated by ray transfer matrix analysis and normalised to the first brightfield channel) vs *d_sample* for the two fluorescence channels in the dual fluorescence channel microscope. 158

5.43 **(a)** Mock infected human MDM sample with labelled mitochondria (Alexa Fluor 488). Image acquired on the M4All dual channel fluorescence microscope. **(b)** Cropped and enlarged view of the central cell in **(a).** Brightness/contrast adjusted in ImageJ/Fiji for representation. 159

5.44 Images of a human MDM sample challenged with *S. aureus* (4 hour time point). Mitochondria labelled with Alexa Fluor 488. Nuclei and *S. aureus* labelled with DRAQ5. **(a)-(e)** are images of different areas of the same sample. Images were processed using the process outlined in figure 5.45. The 450 nm RGB laser emission line was set to 50 mA and the 635 nm emission line was set to 85 mA for image acquisition. 160

5.45 Image processing steps (ImageJ/Fiji) used to produce the representative images in figure 3.13. Step 1: Rolling ball background subtraction. Step 2: Manual image registration using Fijiyama [168]. Step 3: Create composite image. 161

5.46 Raw image from detection channel two of the M4All dual channel fluorescence microscope of a commercial sample with labelled actin filament. 162

5.47 **(a)** First raw image frame from the 100 image frames acquired on the second channel of the M4All dual channel fluorescence microscope. Mock infected human MDM sample with labelled mitochondria. **(b)** SRRF reconstruction using settings Ring Radius - 0.5, Radiality Magnification - 10, Axes in Ring - 8, Temporal Analysis - Temporal Radiality Pairwise Product Mean (TRPPM). 163

5.48 **(a)** M4All incubator microscope optical design schematic. The microscope is a finite conjugate optical design where the camera is placed at the primary image plane of the finite conjugate objective lens (Newport M-60X). **(b)** Practical M4All incubator microscope set up within an incubator. 165

5.49 **(a)** Single time point image from time lapse of a 0.01 mm graticule acquired on the M4All incubator microscope. **(b)** Cropped region of interest highlighted by the yellow region of interest in **(a)**. Cropped image was converted to an 8-bit image from an RGB image. 166

5.50 **(a)** X-drift plot of three 6 hour time lapse data sets of a 0.01 mm graticule sample acquired on the M4All incubator microscope. **(b)** Y-drift plot of three 6 hour time lapse data sets of a 0.01 mm graticule sample acquired on the M4All incubator microscope. Drift plots obtained using the NanoJ-Core Drift Correction ImageJ/Fiji plugin. 167

6.1 M4All TIE and fluorescence microscope control hardware. Each 28BYJ-48 stepper motor on the OpenFlexure microscope stage was connected to a PiStep2 Quad Stepper Motor Control Board, which was connected to the GPIO pins on a Raspberry Pi 4 8Gb board. Each Raspberry Pi v2 camera module was connected to a separate Raspberry Pi Zero W board. 170

6.2 M4All incubator microscope control hardware. Each 28BYJ-48 stepper motor on the OpenFlexure microscope stage was connected to a PiStep2 Quad Stepper Motor Control Board, which was connected to the GPIO pins on a Raspberry Pi 4 8Gb board. An LED was also connected to the PiStep2 board, connecting the cathode to the ground pin on the spare motor controller connector, and the anode to the pin next to it via a resistor. A Raspberry Pi v2 camera module was connected to the camera port on the Raspberry Pi 4 8Gb board. 171

6.3 Running Compound Pi from a client Raspberry Pi terminal where camera settings can be set and images can be captured from servers and then downloaded onto the client. 174

6.4 Client Raspberry Pi desktop showing one of the server remote desktops with a live stream from the Raspberry Pi camera. The stepper motor Python GUI for controlling the motors on the OpenFlexure stage is also shown. 175
6.5 Stepper motor Python GUI interface including buttons for controlling the x,y and z stepper motors and a box to change how many steps the motors rotate per button click. 177
6.6 Stepper motor Python GUI process diagram. 177
6.7 M4All incubator microscope Python GUI interface. 178
6.8 M4All incubator microscope Python GUI process diagram. 179

List of Tables

5.1 Divergence analysis results for the M4All TIE and fluorescence microscope. The optical elements are listed in order of their position in the optical path. The y distances are the distance between the back face of the objective lens and the centre of the optical element. Equation 5.8 was used to calculate x. The beam width cross section is the width of the beam at the optical element for the desired FOV, calculated using equation 5.10 (if the element was at 45° then equation 5.18 was also used). The highlighted values in red indicate that clipping occurred on turning mirror 2. 119

5.2 Number of axial motor steps recorded for focusing between the two coverslips on the calibration sample in figure 5.31(b). Five iterations were recorded for moving between the top and bottom coverslip and repeated for the opposite direction. The average of each was calculated. 143

Chapter 1

Introduction

1.1 *Streptococcus pneumoniae*

Streptococcus pneumoniae is a type of bacteria, also known as the pneumococcus, which resides in the normal flora of the upper respiratory tract in many individuals, particularly children. *S. pneumoniae* colonises in the nasopharynx where in healthy individuals its presence does not usually cause symptomatic infection, as the immune system is able to clear the bacteria when they translocate to the lower airway before becoming pathogenic. However, in a minority of those where the bacteria colonises, *S. pneumoniae* can lead to a number of potentially life threatening invasive pneumococcal diseases (IPD). IPD occurs when the immune responses become overwhelmed, allowing pneumococci to spread to a sterile site, for example the blood or cerebrospinal fluid (CSF) [2], where it becomes pathogenic. *S. pneumoniae* remains the commonest cause of community-acquired pneumonia (CAP) [12] and can also cause bacterial meningitis and sepsis [13].

Prevalence of disease is much greater in early childhood, the elderly and those who are immunocompromised [3]. The adaptive immune system of a child is much less developed than that of an adult (more detail on the innate and adaptive immune systems is provided in section 1.2) thus they have a greater susceptibility to infection. The immune system of elderly adults also deteriorates as they get older thus also increasing their susceptibility. Furthermore, patients with, for example, Chronic Obstructive Pul-

monary Disease (COPD) or Human Immunodeficiency Virus (HIV), have been shown to have increased susceptibility to pneumococcal infections compared to healthy individuals. A population based study by Braeken *et al.* [14] comparing two cohorts (cohort one had a confirmed diagnosis of COPD and the second was a control group) found that those with COPD had a fourfold increased risk of developing CAP. Similarly, a study by Sadlier *et al.* [15] in Ireland between 2006-2015 showed that although there was a decrease in IPD incidence in HIV-positive patients over the course of the study, the rate was still higher in HIV-positive patients compared to the general population. It has also been shown that this remains the case even in HIV-positive patients who undergo antiretroviral therapy [16].

Sadlier *et al.* [15] associated the reduction in the incidence of IPD over the course of their study with a reduction of IPD in the general population since the introduction of a childhood vaccination programme to *S. pneumoniae*. However, although there are *S. pneumoniae* vaccinations available, there are still currently limitations with them. There are greater than 90 serotypes of *S. pneumoniae*, including both encapsulated and unencapsulated pneumococci. Encapsulated pneumococci serotypes have chemically distinct polysaccarhide capsules [17] which forms the outer layer of the bacteria and plays a key role in pneumococcal virulence [18]. Currently available vaccines protect only against encapsulated serotypes but only a limited number. The 23-valent polysaccharide vaccine (PPV23) was licensed in 1983 and targets 23 encapsulated serotypes [5]. The PPV23 vaccine contains antigens in the form of purified polysaccharide capsules [6] of the 23 serotypes. It has been identified, however, that the PPV23 vaccine is unable to generate immunological memory [5] due to the fact the vaccine elicits a T-cell independent immune response [19]. The vaccine also does not elicit an immune response in children under the age of two years old [6]. These limitations led to the development of pneumococcal conjugate vaccines (PCVs) in 2000 [5]. PCVs conjugate the polysaccharide capsules to diptheria toxin [6] as a protein carrier which allows the polysaccharide to become a T-cell dependent antigen [19], thus allowing the ability to generate immunological memory and increase effectiveness in children under two. The most current pneumococcal conjugate vaccine is PCV13, which targets 13 serotypes

[6].

Although the PPV23 and PCV13 vaccines have had a positive impact on reducing the incidence of IPD caused by the included serotypes (which were identified to cause the majority of pneumococcal infections), the vaccines do not, as mentioned, include all serotypes. In fact, it has been shown that the introduction of pneumococci vaccinations has led to serotype replacement, where non-vaccine serotypes have become more likely to colonise and cause disease [5], filling an ecological niche. Furthermore, there has been an increase in resistance to antibiotics of the non-vaccine serotypes [6].

Antimicrobial resistance (AMR) in *S. pneumoniae* against penicillin was first reported in the 1960's [4] and the problem has increased worldwide since, coinciding with a global overuse of antibiotics [20]. Although AMR in *S. pneumoniae* is not as significant a problem as it is for some other pathogens, it is particularly problematic for the demographics outlined above, and particularly some regions of the world, who are at a higher risk of developing life threatening IPDs. To tackle the continuing issue of AMR and serotype replacement in *S. pneumoniae*, and also other problematic bacteria, along with extending the number of serotypes included in the vaccines, alternative treatments to standard antimicrobials must also be developed. One possible avenue is by pharmacologically enhancing the microbicidal responses of phagocytes, such as alveolar macrophages.

The development of alternative treatments firstly requires an in depth understanding of the complex immune system and specific responses of phagocytes, which have not yet been fully characterised. The aim of this research project was to develop microscopy hardware and imaging techniques to overcome imaging challenges when investigating macrophage host defence responses against the pneumococcus. This chapter will give a general overview of the immune system (section 1.2) and the origin and function of macrophages (section 1.3), before reviewing what is already known in the literature about macrophage pathogen interaction with *S. pneumoniae* (section 1.4). Methods for imaging macrophage microbicidal responses and imaging challenges will also be covered (section 1.5), before the aims of this research project and an overview of the structure of the thesis will be given (section 1.6).

1.2 The Innate and Adaptive Immune Responses

The human immune system is broadly divided into two types of response, namely the innate and adaptive immune responses. The innate immune system is a set of responses that a human is born with [21] and is not specific to any one pathogen. Innate immune responses are the first line of defence [22] and act rapidly to either ideally clear, or if not contain, the bacteria or other pathogen until an adaptive immune response can be established [23]. Innate immunity has traditionally been viewed as not requiring immunological memory and not improving with repeated exposure to the same foreign agents, although this view is being challenged with recent evidence of epigenetic modulation of innate responses by prior exposure [24]. The adaptive immune response, on the other hand, takes days to develop and is acquired and improved throughout the human's lifetime on repeated exposures [21]. It is also highly specific such that variation in a specific pathogen can allow immune escape [25].

Innate immune responses can be characterised into sub-groups: anatomical and physiological barriers, humoral factors such as complement and other factors in blood or tissue fluid, and cellular responses which kill pathogens either extracellularly or after phagocytosis in the intracellular environment using a variety of microbicidal responses [23]. Anatomical barriers include the skin and mucous membranes and prevent microorganisms entering the body [22]. Temperature, pH and other chemical mediators make up the physiological barriers [26]. When both the anatomical and physiological barriers are breached, the complement system is the next response which is triggered [27]. Complement activation enables opsonisation to facilitate phagocytosis by macrophages, neutrophils and dendritic cells, but can also directly kill bacteria and can aid recruitment of inflammatory cells to sites of infection by acting as chemotaxis factors [23]. Phagocytosis allows uptake of larger structures as opposed to pinocytosis which allows uptake of molecules or fluid. Endocytosis, like phagocytosis is receptor mediated but involves smaller structures. In phagocytosis the cell membrane expands and surrounds the bacteria, encapsulating it in a vesicle called a phagosome [28]. The phagosome subsequently fuses with a series of endosomes and ultimately matures by fusion with

lysosomes, forming a phagolysosome [29]. The bacteria within the phagolysosome is broken down by enzymes from the lysosomes, other proteases and reactive oxygen species (ROS) [30]. Phagocytes can also produce mediators to orchestrate other key inflammatory responses [28].

1.3 Macrophages

Our research focuses on the responses that macrophages employ in the clearance of *S. pneumoniae*. Therefore the remainder of this chapter will focus on what has already been discovered in that area and the challenges when it comes to imaging studies of macrophage host defence responses.

1.3.1 Origin

Macrophages are derived from either circulating monocytes in the blood when they migrate into different tissues and differentiate, or from resident tissue macrophages [31]. In many tissues, such as the lung, the macrophage is derived from the resident macrophage pool and has a distinct origin from foetal yolk sac-derived cells. This steady state population is complemented by the recruited monocyte-derived cells during inflammation [32].

1.3.2 Function

Macrophages are the resident phagocytes in tissue and specialist macrophages reside in different areas of the body [31]. In most cases resident tissue macrophages are the first phagocyte to mount a response against pathogens [27]. Macrophages express what are called pattern recognition receptors (PRRs) which recognise pathogen-associated molecular patterns (PAMPs), molecular structural patterns which discriminate between self and non-self, such as microorganisms [28]. Different receptors induce different responses, for example scavenger receptors trigger phagocytosis through binding to non-self ligands [23] and Toll-like receptors (TLRs) determine the activation state of the macrophages [33] and are key in cytokine production [34].

The resident macrophage in the air space of the lung is the alveolar macrophage (AM), protecting the lung from respiratory pathogens. AMs are particularly good at keeping lung damage to a minimum whilst activating and regulating inflammatory responses, thus preserving lung function [35]. AMs can eliminate small numbers of bacteria but when they become overwhelmed they orchestrate other key inflammatory responses, such as the recruitment of neutrophils [35], through production of cytokines and chemokines [28].

1.4 Macrophage Pathogen Interaction with *Streptococcus pneumoniae*

1.4.1 Macrophage Antimicrobials

Exact microbicidal mechanisms of macrophages are, in general, not well defined. Although macrophages do phagocytose extracellular pathogens like *S. pneumoniae*, the ability to clear the bacteria after ingestion is less effective than other types of phagocytes like neutrophils [36]. Reasons for this can include the polysaccharide capsule of encapsulated serotypes of *S. pneumoniae* aiding in pneumococcal virulence by inhibiting being recognised and phagocytosed by macrophages and other innate immune cells [3]. Also, it is known that macrophages generate ROS via the nicotinamide adenine dinucleotide phosphate (NADPH) oxidase system, but don't generate more potent halogenated ROS which are used by neutrophils, such as hypochlorous (HOCl), as they usually lack myeloperoxidase [35, 36]. *S. pneumoniae* has also adapted to resist oxidative stress, however, macrophages can produce nitric oxide (NO) through the inducible nitric oxide synthase (NOS2) system. This allows NO to react with ROS to generate reactive nitrogen species, which are more potent antimicrobials than ROS [35], although the production of NO is found to be lower in human macrophages than in murine macrophages [35]. It has also been proposed that macrophage-derived proteases, such as MMP12, contribute as microbicidal factors to kill bacteria [37]. However, macrophages lack the granule-associated serine proteases of neutrophils, e.g. cathepsin G and neutrophil elastase [35]. Therefore, macrophages need to use a combination of

factors including reactive oxygen species, peptides and proteases, as well as a low pH environment in the phagolysosome to overcome pathogen resistance.

1.4.2 Apoptosis

The role of apoptosis, a form of programmed cell death, has also been confirmed in the clearance of *S. pneumoniae* by AMs [35]. Macrophages must resist apoptosis until they have performed key antimicrobial functions, including those outlined above, and only then can host-mediated apoptosis be induced to aid in the clearance of bacteria. This transition is a delayed response to clear residual bacteria that have not been killed by intraphagosomal mechanisms and is regulated by the anti-apoptotic Bcl-2 family protein Mcl-1 [38]. Mcl-1 has a short half-life and is subject to dynamic regulation. It is also a critical regulator of macrophage life-span [39]. Downregulation of Mcl-1 allows pro-apoptotic Bcl-2 family members to activate a mitochondrial pathway of apoptosis and this is exactly what happens following pneumococcal challenge [38]. Down-regulation of Mcl-1 occurs upstream of loss of inner mitochondrial membrane potential, mitochondrial outer membrane permeabilization and caspase-3 activation [40].

1.4.3 The Role of Mitochondria and Mitochondrial Reactive Oxygen Species (mROS)

Mitochondria are double-membrane organelles which are found in all eukaryotic cells. Mitochondria are known as "the powerhouse" of the cell, producing adenosine triphosphate (ATP) which provides energy for most cellular functions [41]. They also play an integral role in mediating the microbicidal responses of macrophages [41, 42], offering a new target for alternative antimicrobial strategies. Recently, the microbicidal role of mitochondrial reactive oxygen species (mROS) has emerged as a critical factor in macrophage bacterial clearance [1, 43]. Mitochondrial fission is also a factor associated with mitochondrial ROS production and a shift to glycolytic metabolism [44, 45]. Glycolytic metabolism is critical in classical activation of macrophages in response to lipopolysaccharide (LPS) [46].

Mitochondrial Reactive Oxygen Species (mROS)

Mitochondria are one of the largest generators of reactive oxygen species in the form of mitochondrial ROS (mROS). Production takes place during oxidative phosphorylation at the electron transport chain located on the inner membrane of the mitochondria. By using oxygen and simple sugars it is oxidative phosphorylation which produces ATP. Involved in this process are five protein complexes. Superoxide ($O_2^{\cdot -}$) is generated by electron leakage at complex I and complex III [47]. Hydrogen peroxide (H_2O_2) is also then quickly produced by the dismutase of superoxide [47, 48].

Historically, mROS were not appreciated as having a microbicidal role. It was thought that mROS were only produced as a by-product of metabolism [43], causing cellular damage as opposed to having a physiological function [49]. Since then mROS have been recognised as signalling molecules [50–52] and in determining cell viability or cell death [53]. The main microbicidal source of ROS was originally understood to be generated by the NADPH oxidase system to kill intraphagosomal microorganisms [29]. More recently the role of mROS in host defence against intracellular bacteria has been acknowledged by West *et al.* [43]. They studied the effects of TLRs on bactericidal activity and found that macrophages with depleted amounts of cells-surface TLRs have decreased production of mROS induced by TLRs. This correlated with decreased microbicidal activity against intracellular *Salmonella typhimurium*. To confirm the role of mROS the study also reduced the amount of mROS produced by expressing catalase in the mitochondria as a control and again found that the macrophages had an impaired ability to clear engulfed bacteria.

The role of mROS against extracellular bacteria, like *S. pneumoniae*, had not been defined until a more recent study by Bewley *et al.* [1] showed that those diagnosed with COPD have AMs with impaired mitochondrial microbicidal responses involving the production of mROS. The early microbicidal response to bacteria in COPD AMs following phagocytosis does not appear to be altered, however the delayed apoptotic phase of bacterial killing is. The levels of Mcl-1 in COPD AMs are elevated and the AMs fail to downregulate Mcl-1 at the point where healthy AMs would induce apoptosis mediated killing. COPD AMs were shown to have an increased basal production of

mROS, however after bacterial challenge with *S. pneumoniae* they failed to increase mROS production, linked with the failure to downregulate Mcl-1. Failure to increase mROS production was connected with the COPD AMs reduced ability to clear *S. pneumoniae*.

Mitochondrial ROS are essential to the microbicidal function of macrophages, however their role is not yet fully understood. Initial imaging of mROS with confocal and structured illumination microscopy has suggested colocalization between mROS and bacteria [1]. However, imaging studies require improvement to better characterise kinetics and localization of mROS with respect to bacteria and the phagolysosome.

Morphology Changes and Fission

A recent study by Mohasin *et al.* [44] has also shown that the mitochondrial network within macrophages becomes significantly fragmented, through a process called fission, 12 hours after bacterial challenge with *S. pneumoniae*. Mitochondria are very dynamic organelles with a complex network - they continually fuse together and break apart depending on cell requirements. Fission allows dividing or growing cells to repopulate mitochondrial numbers [54] and fusion allows healthy mitochondria to fuse with mutant mitochondria to increase respiratory function [55].

Mohasin *et al.* [44] found that there's an interplay between mitochondrial fission and production of mROS. Fission was associated with a reduction in oxidative phosphorylation and an increase in mROS production following bacterial challenge. Inhibiting mROS production using mitoTEMPO resulted in reduced mitochondrial fission. As did inhibition of cathepsin B (which also stimulates mROS production). Inhibition of cathepsin B also reduced clearance of ingested bacteria. As discussed in section 1.4.2, apoptosis is a key response utilised by macrophages to clear residual bacteria and is regulated by Mcl-1. Mohasin *et al.* [44] have suggested fission is activated to enhance mROS as an additional microbicidal response which may lead to apoptosis, however mROS itself does not drive apoptosis. Further imaging studies must be carried out to further investigate the interplay between mROS production and mitochondrial fission and their role in clearance of internalised *S. pneumoniae* within macrophages.

1.5 Methods for Mitochondria and mROS Detection

To investigate and understand the roles of mitochondria and mROS in the clearance of *S. pneumoniae* and other bacteria, it is imperative to carry out imaging studies to view and localize any interactions with the pathogens. Currently the imaging sections of the studies discussed in section 1.4.3 by Mohasin *et al.* [44], West *et al.* [43] and Bewley *et al.* [1] focused mainly on confocal microscopy of fixed cells.

Confocal microscopy is a fluorescence based microscopy technique which removes out of focus signal from the imaging plane to increase contrast and signal to noise ratio (SNR) compared to widefield fluorescence microscopy. As with widefield fluorescence microscopy, samples are labelled with fluorophores to specifically view only the structures of interest. Generally, fluorophores are dye molecules or fluorescent proteins that absorb excitation light, from a spectrum associated with that fluorophore, and then spontaneously relax to emit light of a longer wavelength (figure 1.1). Fluorophores can also be forced to carry out stimulated emission, as is the case in stimulated emission depletion (STED) microscopy which is discussed further in section 3.1.1.

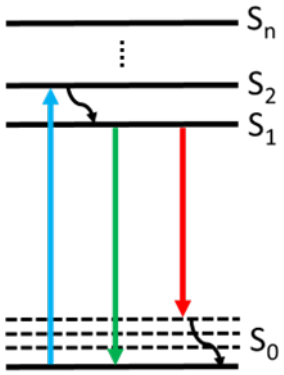

Figure 1.1: Schematic (Jablonski) diagram illustrating the process of fluorescence. The blue arrow indicates absorption of a photon, exciting an electron from the ground state S_0 to a higher energy state e.g. S_2. Following a non-radiative relaxation to the lowest excited state, S_1, either spontaneous emission (green arrow) or stimulated emission (red arrow) occurs.

Fluorescence labelling methods include fluorescent dyes, fluorescent proteins and immunolabelling. Fluorescent dyes have chemical modifications which allow them to specifically bind to certain sites within the cell, for example those which bind to nucleic

acids and allow labelling of cell nuclei. Whereas immunolabelling is based on antibodies which bind to specific antigens within the cell. A primary and a secondary antibody can be used. The primary antibody binds to the specific target within the cell, the secondary antibody has the fluorophore bound to it and binds to the primary antibody. A primary antibody on its own can also be used if it is conjugated to a fluorophore itself.

The fluorescence emission signal is spectrally separated from the excitation light, using optics such as filters and dichroic mirrors, so as to only image the fluorescence emission and thus the structures of interest. In widefield microscopy both the in focus light originating from the sample image plane and the out of focus light originating from other planes in the sample are imaged onto the detector (figure 1.2(a)). Whereas in confocal microscopy, a pinhole placed before the detector provides optical sectioning by only allowing the in focus light to pass through (figure 1.2(b)).

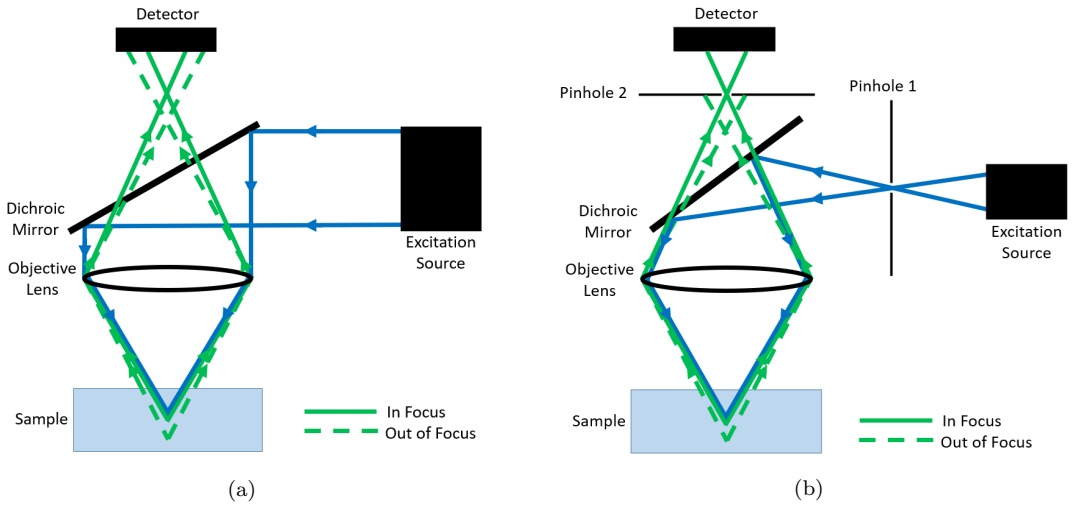

Figure 1.2: **(a)** Schematic of widefield microscopy where both the in focus and out of focus light are imaged on the detector. **(b)** Schematic of confocal microscopy where pinhole 2 rejects the out of focus light from the detector.

Mitochondria within macrophages can be fluorescently labelled very specifically using either immunolabelling with a Tomm20 primary antibody (protocol is outlined in section 2.5) or fluorescent dye such as MitoTracker which has different forms that either rely on the mitochondrial membrane potential [56] or work independently from it. Using confocal microscopy, Mohasin *et al.* [44] were able to study changes in

mitochondrial morphology between healthy and challenged macrophages. There are however some limitations with confocal microscopy that pose challenges for studying the specific locations of mitochondria, mROS and bacteria with reference to one another and to image any interactions between them. Although confocal microscopy provides greater contrast images and a slight lateral resolution increase compared to widefield fluorescence microscopy, the greatest improvement is in the axial resolution from the optical sectioning capability and the resolution of confocal microscopy is still inherently limited by diffraction theory. Diffraction theory says that an objective lens will image a point source in the sample as a diffraction pattern, known as the Airy disk. The Airy disk is the smallest feature in a microscope image that can be resolved and depends upon the wavelength of excitation light (λ) and the numerical aperture (NA) of the objective lens according to Abbe's lateral diffraction limit equation:

$$d_{xy} = \frac{\lambda}{2NA} \tag{1.1}$$

In confocal microscopy the equation becomes:

$$d_{xy} = \frac{0.8\lambda}{2NA} \tag{1.2}$$

Abbe's axial resolution equation is:

$$d_z = \frac{2\lambda}{NA^2} \tag{1.3}$$

In confocal microscopy, the optical sectioning capability improves this to:

$$d_z = \frac{1.4\eta\lambda}{NA^2} \tag{1.4}$$

where η is the immersion medium refractive index.

This highlights in confocal microscopy there is still a limited resolution based on optical theory. Therefore with confocal microscopy there is a limit to which colocalization studies within macrophages can be accurately carried out. Individual mitochondria are

approximately 0.5-1 μm in size [57] and so can be resolved by standard optical microscopy techniques. The pneumococcus is also a similar size and can therefore also be resolved. The problem arises when localizing them with respect to one another. If the distance between them is less than the diffraction limit, it cannot be determined whether they are interacting with one another, or whether there is a gap between them that cannot be resolved.

In the past couple of decades there has been the development of super-resolution microscopy techniques which break the diffraction resolution limit (further information in section 3.1.1). One of which is structured illumination microscopy (SIM) and as mentioned in section 1.4.3 initial studies using this technique has suggested colocalization between mROS and *S. pneumoniae* 16 hours after macrophage bacterial challenge. Therefore, further imaging studies using super-resolution microscopy techniques need to be carried out.

As mentioned at the beginning of this section, the studies by Mohasin *et al.* [44], West *et al.* [43] and Bewley *et al.* [1] all imaged fixed cells. However, the mitochondrial network dynamically changes and not only do mROS have a very short half-life, ranging from 10^{-9} s to a few seconds [58], but as mentioned before, they can react with NO to form reactive nitrogen species [59]. Therefore it would be advantageous to use live cell microscopy to image interactions between mitochondria and mROS with pneumococci within macrophages. Live cell microscopy can be challenging with confocal microscopy and some super-resolution microscopy methods. Confocal microscopy is a laser scanning based technique. The laser is focused down to a small spot size and raster scanned across the sample plane to build up an image. A single photon detector detects the signal at each scanning point, building up the image pixel by pixel. Depending on the desired image size, scans can take a sufficiently long enough time that some dynamic processes will have taken place before the scan is complete, especially if imaging full z-stacks. Spinning disk confocal microscopy can alleviate this problem to a certain extent with faster scanning times - typically hundreds of frames per second compared to tens of frames per second for laser scanning confocal microscopy [60].

The short half-life of mROS also causes limitations for the development of fluo-

rescent probes to image them. Probes must be very specific to a certain mROS, be resistant to photobleaching and also be non-toxic [61]. MitoSOX is one of few commercially available probes which was developed to be specific to imaging mitochondrial superoxide. Originally it was found that the reaction of dihydroethidium (DHE) with superoxide formed a superoxide-specific product [62]. MitoSOX is a modification of DHE by the addition of a lipophilic triphenylphosphonium cation (TPP^+) allowing it to be targeted to mitochondria [63]. Mitochondria have two membranes, an outer membrane and an inner membrane. The latter has a large potential across it, in living cells this is between 120-170 mV [64]. The positive charge of lipophilic cations means they are driven into the mitochondrial matrix by the potential gradient across the inner membrane [65]. TPP^+ accumulation within the mitochondrial matrix is therefore dependent upon the magnitude of the inner membrane potential and can be described by the Nernst equation:

$$membranepotential(mV) = 61.5log_{10}(C_i/C_o) \tag{1.5}$$

where C_i is the concentration of TPP^+ inside the mitochondrion and C_o is the concentration of TPP^+ outside [64]. When mitochondria depolarize, selective accumulation of MitoSOX within the mitochondrial matrix as opposed to in the cytoplasm will not occur [59], which could cause problems around the time point at which apoptosis in macrophages is triggered as this process involves a loss of mitochondrial inner membrane potential.

The reaction of MitoSOX with superoxide also in fact produces two fluorescent products, one being superoxide specific and the other formed in response to general oxidative stress [47]. Therefore if using this dye, fluorescence microscopy may not be sufficient on its own to quantify measurements of superoxide and it has been suggested that the use of high performance liquid chromatography or mass spectrometry may need to be employed [61]. Controls could also be used to inhibit mROS and other reactive species to show that the signal comes from mROS.

There is another commercially available fluorescent probe which is boronate-based,

namely MitoPY1, for detection of hydrogen peroxide within the mitochondria [66]. MitoPY1 can also be used with confocal microscopy and flow cytometry [63]. However, like MitoSOX, it is not completely specific and also reacts with peroxynitrate [47]. Because of the limitations with commercially available dyes there is ongoing research into fluorescent probes that are specific to mROS [63].

1.6 Aims

The broad aim of this research project was to improve detection and quantification of mitochondrial microbicidal responses (specifically mROS and related pathways) in response to internalised *S. pneumoniae* in alveolar macrophages. Highlighted in the previous sections is the rationale behind the need to improve imaging studies in macrophages and the challenges to overcome.

The first aim was to address challenges with spatial resolution when carrying out colocalization studies between mitochondria, mROS and pneumococci. As mentioned in section 1.5 individual mitochondria and the pneumococcus are of a size which is resolvable by diffraction limited optical microscopy techniques. Diffraction limited spatial resolution becomes a problem when localizing a network of mitochondria and bacteria with respect to each other and quantifying interactions. The smaller the achievable resolution of the microscope is, the more accurately the mitochondrial network and bacteria can be mapped. Some super-resolution microscopy techniques can achieve resolutions down to $\approx$10 nm, however they can be particularly sensitive to image aberrations which can cause errors in colocalization measurements. Therefore, we endeavoured to investigate the effect of image aberrations on confocal fluorescence images of macrophages using a custom adaptive optics enhanced confocal microscope, hypothesising that image aberrations may result in inaccuracies of colocalization measurements, with a future aim of extending this research to super-resolution microscopy. Chapter 3 includes an introduction to super-resolution microscopy and adaptive optics (section 3.1) before presenting early studies we carried out to assess the extent to which aberrations were present in confocal images of mitochondria labelled within human monocyte

derived macrophages (MDMs) (section 3.2). We also wanted to assess the suitability and effectiveness of using computational super-resolution microscopy methods, namely Super-Resolution Radial Fluctuations (SRRF) [10], to improve spatial resolution (section 3.3), and to what extent aberrations affected SRRF reconstructions (section 3.4).

The second aim was to address challenges with temporal resolution. There are two challenges relating to this. The first relates to short time scales where we want to image fast dynamic processes, such as changes in mitochondrial morphology and the production of mROS and any interactions with bacteria. The second relates to long time scales as the responses of macrophages to pneumococci occurs over a period of 16+ hours when apoptosis is induced. Not only are there problems with imaging live cells continuously over this time frame (which will be explained further in chapter 3), but narrowing down important fast dynamic events over such a long period poses a challenge. Chapter 3 also introduces the Transport of Intensity Equation (TIE) as a label-free computational phase microscopy technique. Label-free microscopy techniques mitigate problems with photobleaching and phototoxicity when imaging over long time periods. Section 3.5 includes early imaging studies to determine the applicability of TIE microscopy to imaging macrophages.

The third aim was to address challenges with accessibility to advanced microscopy techniques which allow high spatial and high temporal resolution imaging studies. Not only is access to advanced microscopy techniques in more developed countries often limited to specialist facilities due to equipment costs, or specialist research groups developing custom imaging equipment, access is limited even more so in developing countries in Africa and Asia where occurrence of IPD is more prevalent [7, 8]. Therefore we aimed to develop a low-cost and open-source 3D printable microscopy system that would not only increase accessibility to advanced microscopy techniques but could also aid in some of the challenges with spatial and temporal resolution mentioned in this chapter. There is a trade-off when developing low-cost 3D printable microscopes between resolution and the cost of equipment. As mentioned in this section, improving resolution beyond the diffraction limit will improve colocalization studies. However, super-resolution microscopy techniques can be costly, therefore to begin with

we aimed to develop low-cost diffraction limited microscopes and test computational super-resolution microscopy techniques as an alternative to keep costs down whilst improving resolution. The same is true for temporal resolution. For this project we chose to test low-cost cameras with a range of frame rates from 30 fps to 166 fps, to investigate the quantitative information achievable from cameras in this price range (£30 - £1000).

Chapter 4 introduces the concept of 3D printing and includes a review of available open-source microscopy systems within the open-hardware community (section 4.1), before covering initial tests we carried out using 3D printed hardware from the UC2 [67] and OpenFlexure [68] projects (section 4.3). Chapter 4 then includes the development of the hardware for our new open-source 3D printable microscopy system, M4All: MultiModal Modular Microscopy for All, to address specific design parameters we required for imaging macrophages (sections 4.4-4.6).

Chapter 5 includes information on optical design theory and ray transfer matrix analysis for optical modelling (section 5.1), before presenting the design, implementation, and applicability to imaging macrophage host-pathogen interactions, of three microscopes using the M4All system: a TIE and fluorescence microscope (section 5.2), a dual channel fluorescence microscope (section 5.3), and an incubator microscope (section 5.4). We also present a novel method of calibrating and aligning infinite-conjugate microscopes based on ray transfer matrix analysis (section 5.2.4). Finally, chapter 6 provides a review of the hardware and software used to control the M4All microscopes in this research project.

1.7 COVID-19 Impact Statement

This chapter introduces the role of alveolar macrophages in response to *S. pneumoniae* infection, describes challenges to overcome when imaging macrophage host-pathogen interactions and gives an overview of the structure of the thesis and the outputs from this body of research. At the beginning of my PhD we had a focus on using adaptive optics enhanced confocal and super-resolution microscopy to address challenges with colocalization studies between mROS, mitochondria and bacteria. Chapter 3 details

initial work and outputs in this area, as well as work using computational microscopy techniques, which was mostly carried out prior to the COVID-19 pandemic. Due to a fault which incurred before the pandemic with the deformable mirror required for carrying out adaptive optics on our microscope, I began investigating the use of low-cost 3D printable microscopes in imaging macrophage host-pathogen interactions as they had the potential to provide impact in widening accessibility to imaging research tools in developing countries with high IPD burden. Due to the pandemic, access to the lab became limited and therefore, although a new deformable mirror had been implemented on our custom adaptive optics microscope, it was not possible to keep reconfiguring the microscope between my project and another PhD student's project. Therefore, I was unable to return to my work on adaptive optics and focused my research on developing M4All (chapters 4-6).

During the first lockdown, I did not have access to the lab from March-August 2020 and therefore adapted my project to work on developing control software for the M4All system, detailed in chapter 6, as I could not work on the physical 3D printing, design and implementation of M4All. A second lockdown in Glasgow from January-April 2020 resulted in my access to the lab being cut to 50%, which impacted data collection further at a key phase of my research. My collaboration with Prof. David Dockrell's group at the University of Edinburgh was also impacted by the pandemic, as travel between Glasgow and Edinburgh was limited and I did not have access to the lab in Edinburgh. Therefore, I mainly focused on developing alignment methods for the M4All system, refining the design, carrying out stability tests and implementing the computational microscopy techniques from chapter 3 on the M4All system. Chapter 5 includes initial images of fixed macrophage samples which were acquired once I was able to obtain samples from Edinburgh, however I was not able to carry out any live cell work.

Chapter 2

Methods

2.1 Isolation of Human Peripheral Blood Mononuclear Cells (PBMCs) from Whole Blood Sample Using Percoll Density Gradient

To obtain human monocyte derived macrophages, peripheral blood mononuclear cells (PBMCs) were first isolated from healthy human blood samples. Whole blood samples were obtained after informed consent from healthy donors on the Centre for Inflammation Research Blood Resource (approved by AMREC, Reference number 15-HV-013). 3.8% tri-sodium citrate was added to the sample and subsequently spun down in a centrifuge (350xg for 20 minutes) to form an upper phase platelet rich plasma (PRP) layer and a lower cell phase. The PRP layer was removed and warm 6% dextran was added to the lower layer and topped up to 50 ml with saline. The sample was then placed in an incubator for 20-30 minutes until the red blood cells sedimented into a bottom layer and there was a clear top layer. The top layer was removed and placed into a clean tube, topped up to 50 ml with saline and subsequently spun in the centrifuge (350xg for 6 minutes) to form a pellet.

A Percoll density gradient was then prepared. The stock Percoll solution was 27 ml Percoll + 3 ml phosphate buffered saline (PBS). The Percoll gradient had three layers; the bottom layer was 8.1 ml stock + 1.9 ml PBS and the next layer was 6.8 ml stock +

3.2 ml PBS. The sample pellet was then resuspended in 3 ml of a 5.5 ml stock + 4.5 ml PBS (without Ca and Mg) solution which then formed the third layer of the gradient. The gradient was then spun in the centrifuge (720xg for 20 minutes) which formed three layers; the bottom layer was red blood cells, the second layer was polymorphonuclear neutrophils (PMNs), and the third layer was the desired layer of PBMCs. The PBMCs were carefully transferred to a clean 50 ml falcon tube and topped up to 40 ml with PBS, spun in the centrifuge (230xg for 6 minutes) and resuspended in PBS. A cell count was then carried out using a hemocytometer before plating cells.

2.2 Culturing Monocyte Derived Macrophages (MDMs) from PBMCs

The PBMCs were plated onto coverslips in 24 well plates. They were plated out at a concentration of 2.5x10^6 cells/coverslip and cultured in complete media (RPMI containing 10% low lipopolysaccharide (LPS) fetal calf serum (FCS)) in an incubator at 37°C with 5% carbon dioxide (CO_2). They were cultured for 14 days to differentiate into monocyte derived macrophages (MDMs) with media changed twice per week to provide adherent cells with increased cytoplasmic to nuclear ratio versus PBMC.

2.3 Macrophage Bacterial Internalisation with *Streptococcus pneumoniae*

After 14 days of culturing the cells bacterial challenge was carried out. *S. pneumoniae* were first opsonised with pooled immune sera from healthy volunteers vaccinated with the 13-valent protein conjugate pneumococcal vaccine (PCV13) - 450 μl RPMI + 50 μl immune sera, shaking for 30 minutes at 37°C. Opsonisation is where the bacteria are coated with antibodies that enhance phagocytosis of this bacterium and to oppose the inhibitory effect of the polysaccharide capsule [69]. The bacteria were then washed three times with PBS. The MDMs were also washed two times with PBS and replaced with 1 ml of complete media. The bacteria were then added to the wells at a multiplicity

of infection (MOI) of 10 (i.e. 2x10^5 MDMs/well receive 2x10^6 bacteria/well).

The macrophages were put on ice for 1 hour to promote adherence and then transferred to the incubator at 37°C and 5% CO_2 for 3 hours. Depending what time point after bacterial challenge was to be observed, the macrophages were then either washed with PBS and returned to the incubator for the required amount of time or washed and labelled straight away for imaging. Mock infected cells were not challenged with bacteria but the same procedure of putting them on ice for 1 hour, transferring to the incubator for 3 hours, then washing with PBS and either returning to the incubator or labelling straight away was followed as a control.

2.4 Macrophage Bacterial Internalisation with *Staphylococcus aureus*

Separate MDM samples were also challenged with *S. aureus*. The bacteria were washed twice with PBS. MDMs were also washed twice with PBS and replaced with 1 ml of complete media. The bacteria were added to the wells at an MOI of 10. The MDMs were then placed within an incubator at 37°C and 5% CO_2 for 4 hours. They were then subsequently washed with PBS and labelled for microscopy.

2.5 Macrophage Fluorescent Labelling for Microscopy

The outer membranes of MDM mitochondria were labelled for fluorescence microscopy using immunolabelling after fixing the MDMs with 2% paraformaldehyde (PFA). After fixing, the cells were permeabilised using 50 mM ammonium chloride (NH4Cl) with 0.1% triton-x-100, to allow antibodies to pass into them, and then blocked with a blocking solution (0.2% gelatin, 0.02% sodium azide and 0.01% triton-x-100 in PBS) to reduce non-specific antibody binding. The blocking solution was replaced with the primary antibody, rabbit anti-TOMM20 (1:500 dilution in the above blocking solution) for 1 hour at room temperature. The primary antibody can also be incubated overnight at 4°C with good results. The primary antibody solution was then replaced with

the secondary antibody, either goat anti-rabbit Alexa Fluor 488 or goat anti-rabbit ATTO647N (both 1:1000 dilution in the above blocking solution), also for 1 hour at room temperature. The coverslips were then washed three times with the blocking solution and, only if ending the labelling protocol at this stage, twice with PBS before washing quickly in distilled water and mounting onto microscope slides using ProLong Diamond. Figure 2.1(a) shows a mock infected MDM sample where mitochondria are labelled with Alexa Fluor 488.

If also labelling internalised *S. pneumoniae*, or *S. aureus*, and MDM nuclei, after fixing the MDMs with 2% PFA and labelling the mitochondria as above if required, the DNA probe DRAQ5 was used. As it is a membrane permeable dye, permeabilisation of the MDMs before use is not required, and so if using alone without the mitochondrial labelling stage above, the permeabilisation step can be skipped. DRAQ5 was used at a dilution of 1:1000 in PBS for 12 minutes at room temperature, then washed three times with PBS and quickly washed in distilled water before mounting the coverslips onto microscope slides with ProLong Diamond. Figure 2.1(b) shows *S. pneumoniae* and nuclear staining 16 hours after bacterial internalisation of MDMs.

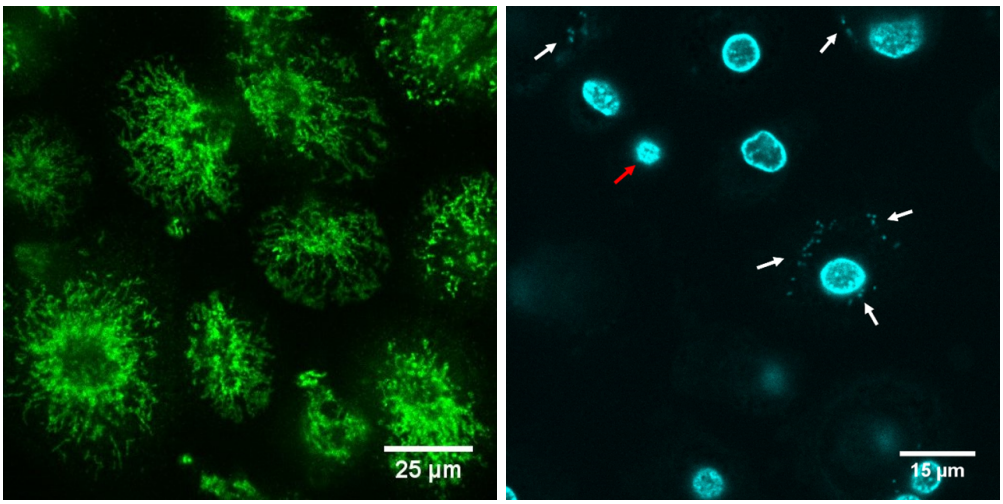

(a) (b)

Figure 2.1: **(a)** Mock infected MDM where mitochondria are labelled with Alexa Fluor 488. **(b)** MDM nuclei and *S. pneumoniae* bacteria, 16 hours after challenge, labelled with DRAQ5. White arrows indicate clusters of *S. pneumoniae* and the red arrow indicates an apoptotic nucleus. Images acquired using a Leica SP5 confocal microscope.

Chapter 3

Early Adaptive Optics, Computational Super-Resolution and Phase Imaging Studies

3.1 Introduction

In the previous chapter I discussed the challenges posed with spatial and temporal resolution when imaging mROS in macrophages, particularly when correlating mROS dynamics and location with specific macrophage host responses. This chapter will include initial imaging studies using a range of different microscopy techniques, including computational super-resolution microscopy using the Super-Resolution Radial Fluctuations (SRRF) algorithm, adaptive optics (AO) enhanced confocal microscopy, and quantitative phase imaging (QPI) based on the Transport of Intensity Equation (TIE) to begin addressing the challenges.

3.1.1 Review of Super-Resolution Techniques

Introduction to Super-Resolution Microscopy

For accurate localization of subcellular features in macrophages, imaging studies require high spatial resolution. The resolution of standard microscopy techniques like widefield

and confocal fluorescence is limited by diffraction theory, where the resolution is typically around half of the excitation wavelength. For visible light, the diffraction limit means that features either smaller, or closer together, than $\approx 200\,\text{nm}$ cannot be unambiguously discriminated. Therefore conventional/traditional microscopy techniques may not be able to distinguish and localize individual pneumococci from mitochondria within macrophages, or be able to accurately represent the complex mitochondrial network.

Methods like deconvolution can help to increase image contrast and resolution in diffraction limited systems. Objective lenses collect only a fraction of the light from an object over a certain range of angles, defined by the numerical aperture (NA) of the objective lens:

$$NA = nsin\theta \tag{3.1}$$

where n is the refractive index of the medium between the sample and the front element of the objective lens, and θ is the maximum half-angle of the cone of light which can be collected by the objective lens. An objective lens is unable to focus light collected from a point object down to an infinitely small point. Instead, interference occurs at the focal point, producing a three dimensional diffraction pattern of the point object, known as the point spread function (PSF). The width of the PSF determines the resolution of the microscope and it is this width which is limited by diffraction theory. An image produced by a microscope of an extended sample is therefore a convolution of the real object with the PSF. Deconvolution is a method of reversing the convolution process to retrieve the object information. It typically relies on either assumptions about the PSF based on optical theory for the specific microscope or acquiring a calibration image of the PSF. Deconvolution is used in both widefield and confocal microscopy to improve the contrast and fine detail observable in images [70].

Further improvements in imaging resolution have been obtained in the past couple of decades with the advent of "super-resolution" microscopy imaging techniques. Super-resolution techniques overcome the diffraction limit to achieve resolutions capa-

ble of imaging the $10-100\,\text{nm}$ length scale. Super-resolution techniques include Stimulated Emission Depletion (STED) microscopy [71], Structured Illumination Microscopy (SIM) [72], and Single-Molecule Localization Microscopy (SMLM) methods such as Photoactivated Localization Microscopy (PALM) [73] and Stochastic Optical Reconstruction Microscopy (STORM) [74], among others. I concentrate here on STED and PALM/STORM as they are most relevant to this research project.

STED microscopy achieves resolutions down to $\approx 50\,\text{nm}$ [75] using a modified scanning confocal configuration. The main principle of STED microscopy is to use the process of stimulated emission to reduce the spatial extent of the emission PSF. STED microscopy is achieved through the combination of the standard confocal excitation laser beam with a second laser beam, known as the depletion beam. The depletion beam is co-aligned to the excitation beam and uses a structured focal volume that places a zero of intensity at the same position as the maximum intensity of the excitation beam. This structured focus is generated by placing an optical phase modulating element in the depletion beam path - self interference of the depletion beam means that destructive interference results in the required intensity minima. The depletion beam forces fluorophores to emit via stimulated emission. Fluorophores at the depletion beam minima will still emit via spontaneous emission from the confocal excitation laser. As the stimulated emission photons will have a different wavelength to the spontaneous emission photons, the stimulated emission can be filtered out. This effectively "turns off" those fluorophores as observed by the detector, successfully reducing the emission PSF to a volume near the zero intensity region at the centre of the depletion laser beam profile. The increase in resolution obtained is proportional to the square of the depletion beam intensity [76].

As mentioned, the increase in resolution obtained by STED comes from spectrally separating the spontaneous emission from the stimulated emission. STED can be implemented with either continuous wave (CW) lasers or pulsed lasers. In pulsed STED, the excitation and depletion pulses are tightly controlled so that the depletion pulse occurs immediately after the excitation pulse [77]. Time-gated STED can also be used to improve detection using time-correlated single photon counting (TCSPC) electronics.

The depletion beam will not perfectly cause stimulated emission in all fluorophores, especially close to the minimum intensity region at the centre of the beam. The fluorescence lifetime of the fluorophores will however differ to those unaffected by the depletion beam at the centre. Therefore by tuning the photon detector to only detect photons after a certain time, based on the lifetime, improves resolution further.

The basis behind SMLM techniques like PALM and STORM is to employ the use of photoactivatable, photoconvertible or photoswitchable fluorophores [78] to map the fluorophore density. The PSF of each individual fluorophore is diffraction limited, however as long as the PSF of one fluorophore does not overlap with another, the centre of mass of the PSF can be used to accurately localize the fluorophore. Using photoactivatable, photoconvertible or photoswitchable fluorophores allows subsets of fluorophores in the sample to be stochastically activated, thus reducing their density in the image frame, balancing the desire to have multiple fluorophores present in each image frame with the requirement that there is a low probability that any bright spot in the image is due to >1 emitter. Capturing a series of image frames of different subsets of fluorophores allows a full super-resolution image of the sample to be built up. The number of frames required can be >10k, thus there is a high data storage and processing time overhead. The main difference between PALM and STORM is the types of fluorophores used. PALM uses genetically expressed fluorophores, whereas STORM uses fluorescent dyes and immunolabelling of photoswitchable fluorophores [78].

Further information on the super-resolution techniques mentioned above can be found in the review by Leung and Chou [79]. I have highlighted these super-resolution methods as a basis to discuss their limitations when it comes to live cell imaging of macrophages in particular and where they could be problematic for our macrophage studies. Culley *et al.* [75] also discusses some of the following challenges when it comes to live cell microscopy in general. Although STED microscopy can achieve resolutions down to tens of nanometers, the technique requires very high depletion beam intensities (on the order of GW/cm^2 [75]). Laser intensities of this magnitude can cause phototoxic effects on live biological samples. Therefore STED microscopy could lead to detrimental

effects on the specific immunological responses that we want to study in macrophages, such as the generation of mROS and mitochondrial dynamics. As STED microscopy is also based on confocal laser scanning microscopy, the speed of scanning equipment will determine the temporal resolution available for imaging fast dynamic processes within the cells.

Like STED, PALM and STORM can achieve resolutions on the order of tens of nanometers, and although SMLM techniques use lower excitation intensities (1-20kW/cm^2 [10]), illumination can still be phototoxic. STORM in particular can include the use of toxic buffers which are used to induce fluorophore photoswitching [78]. Again, toxic effects could have detrimental consequences when the aim is to image specific cellular processes within the macrophages.

Super-Resolution Radial Fluctuations (SRRF)

Since the development of the super-resolution techniques mentioned above, there have been developments made in addressing some of the concerns when it comes to applying them to live cell imaging. One notable image processing technique which has emerged is the Super-Resolution Radial Fluctuations (SRRF) algorithm originally published by Gustafsson *et al.* [10] which is provided as an easy to use ImageJ/Fiji plugin [80, 81]. The algorithm was developed as an alternative to conventional SMLM reconstruction techniques to allow lower excitation intensities to be used when acquiring image data. As discussed, traditional PALM and STORM reconstruction techniques require non overlapping PSFs in order to localize the fluorophores, which relies on high phototoxic laser intensities. Lower laser intensities will result in higher density images [75]. To distinguish the overlapping PSFs from one another in the low excitation intensity case, instead of localizing fluorophores using centre of mass, SRRF measures "radiality", which the authors define as the degree of local gradient convergence [10].

The SRRF algorithm comprises of two analysis steps: spatial analysis followed by temporal analysis. SRRF requires at least 100 raw image frames to be acquired of the desired sample plane [10]. During spatial analysis a radiality map of each image frame is produced. The concept of radiality emerges from the fact that the microscope

PSF has a radial symmetry [75] that comes from using circular lenses. To generate the radiality map for each frame, the local intensity gradient vectors are measured on a subpixel basis along with the degree of convergence of each vector [75]. The radiality map of each image frame maps the degree of convergence. This allows fluorophores to be localized as their local convergence will be significantly higher than the background [10]. The second step to the algorithm, temporal analysis, utilises all radiality maps generated to reconstruct the computational super-resolution image. Radiality peaks can also occur from noise in the data, however these will not be correlated in time, and so temporal correlation of the radiality maps is used to remove them from the final image [10]. The supplemental information in Gustafsson *et al.* [10] provides detailed information about the spatial analysis algorithm along with various types of temporal analysis methods available in the software plugin.

Gustafsson *et al.* [10] used SRRF for imaging actin cortex dynamics in Jurkat T cells during immunological synapse formation. Actin density is inhomogeneous across the synapse, where denser regions present challenges for localizing individual fluorophores by conventional SMLM methods. They showed that SRRF is able to resolve the actin structure below the diffraction limit. The mitochondrial network in macrophages presents a similar imaging challenge. From figure 2.1(a) it can be seen that the mitochondrial network can be much denser in the vicinity of the nucleus. When setting up imaging parameters such as illumination intensity, it is difficult to get the right balance between being able to detect the less dense mitochondrial network and not saturating the denser regions on the camera/detector. The resulting SRRF reconstruction is independent of variations in fluorophore brightness and the use of higher-order temporal statistics notably improves reconstructions of dense fluorophores and overlapping PSFs [10]. Therefore, we carried out initial imaging studies of applying the SRRF algorithm to image data of mitochondria in fixed macrophages from spinning disk confocal microscopy (section 3.3), laser scanning confocal microscopy (section 3.4) and widefield fluorescence microscopy (section 5.3.4) to determine if the algorithm could resolve the mitochondrial network.

Super-Resolution Quantitative Image Rating and Reporting of Error Locations (SQUIRREL)

Because SRRF is a computational technique there is the chance that image artifacts could be present in the reconstructed image. Artifacts could occur from the algorithm itself, or from errors in the raw data which carry on into the algorithm. We wanted to know whether there were any artifacts created in our reconstructions for the data sets noted above for parts of the images that we are particularly interested in. Culley *et al.* [82] have developed an algorithm called super-resolution quantitative image rating and reporting of error locations (SQUIRREL) which compares a super-resolution image with a diffraction limited image to analytically and quantitatively highlight potential locations of errors in the super-resolution image. Like SRRF, the algorithm is again provided as an easy to use ImageJ/Fiji plugin [80, 81]. I concentrate here on the application of SQUIRREL to SRRF reconstructions, however Culley *et al.* [82] provide a discussion of its application to not only SRRF but also other super-resolution techniques including STED, SIM and SMLM methods.

There are three steps to the SQUIRREL process: The first step is correction of spatial offsets between the the super-resolution image (in this case the SRRF image) and the diffraction limited reference image (we use the first raw data frame acquired from the SRRF data set). For comparison of the diffraction limited reference image with the SRRF image, the second step is to scale the SRRF image to its diffraction limited equivalent. This is carried out by convolution of the SRRF image with a resolution scaling function (RSF) image. The RSF can be estimated using the plugin. Finally, the SQUIRREL error map is the pixel wise absolute difference between the diffraction limited reference image and the resolution scaled SRRF image. The error map highlights local scale errors. SQUIRREL also calculates two quality metrics between the diffraction limited reference image and the resolution scaled SRRF image on a global scale, namely the resolution-scaled error (RSE), which is a root-mean-squared error, and the resolution-scaled Pearson (RSP) coefficient, which is a Pearson correlation coefficient. Full details of the SQUIRREL algorithm is presented in the supplemental information of Culley *et al.* [82].

Culley *et al.* [75] demonstrated SQUIRREL applied to SRRF reconstructions of actin and mitochondria labelled within Bovine Pulmonary Artery Endothelial (BPAE) cells. They demonstrate that the image acquisition parameters used for acquiring the raw data for SRRF can affect the quality of the SRRF reconstruction, determined by comparing the SQUIRREL error maps and the RSP values, and therefore SQUIRREL can be used to optimise acquisition parameters. We have used SQUIRREL for initial studies into the effects of image aberrations on SRRF reconstructions using adaptive optics enhanced confocal microscopy (section 3.4). Information on aberrations and adaptive optics is presented in section 3.1.2.

Fourier Ring Correlation (FRC)

The resolution measurement of super-resolution microscopy requires a different approach to conventional diffraction limited microscopy methods. The theoretical resolution obtainable by diffraction limited microscopy is usually defined by the imaging optics, more specifically the wavelength of light, λ, and the numerical aperture of the objective lens, NA. The Abbe, Rayleigh and Sparrow resolution criterion all define the ability of the microscope to distinguish two Airy diffraction patterns produced by point sources on the order of λ/NA.

As super-resolution microscopy methods break the diffraction resolution limit using techniques that extend further than the microscope optics (photo-physical and computational methods), calculation of the resolution must include more parameters than the microscope optics alone. Factors such as labelling density, localization precision and reconstruction algorithm used, amongst others, must also be taken into account. As an alternative, Fourier Ring Correlation (FRC) is a method of calculating image resolution based on the image data alone, using no prior information about the microscope itself or acquisition parameters [83]. FRC is a global resolution measurement, based on cross-correlation of two similar super-resolution images (only differing by the noise floor) in the Fourier domain.

For application of FRC to SRRF reconstructions, the raw image time series is first corrected for lateral drift using the NanoJ-Core [84] ImageJ/Fiji plugin [80, 81] and

then split in half (we deinterleave odd and even frames [85]). A SRRF reconstruction is then generated from each set. The two SRRF images are then Fourier transformed for FRC analysis. The analysis provides an FRC curve, which is a plot of FRC vs spatial frequency. Noise dominates the data at high spatial frequencies, whereas the sample structure dominates at low spatial frequencies, therefore the FRC curve is ≈ 1 at low spatial frequencies and tends to 0 at high spatial frequencies. The resolution is typically determined as the spatial frequency where the FRC curve meets a threshold of 1/7 [83]. We however use a half-bit threshold (where each pixel contains 1/2 bit of information) which takes into account the difference in the number of pixels contained in the Fourier-domain rings, from which the FRC curve is derived from, in the low and high spatial frequency cases [85]. Moreover, as FRC is related to information theory and not the specifications of the microscope, using a half-bit threshold is more logical.

Culley *et al.* [82] have shown that high FRC resolution values for super-resolution images does not always result in low errors in the super-resolution image as quantified by SQUIRREL. Therefore we use both SQUIRREL, as mentioned before, and FRC to assess the effect of aberrations on SRRF images. It is worth noting here that FRC has a dependence on the signal to noise ratio of the images - cross-correlating an image to itself will give a perfect correlation which would imply infinite resolution. Therefore, FRC has limitations when applied to images of samples which can achieve arbitrarily high signal to noise ratios, such as nanodiamond which does not photobleach. The best method of measuring spatial resolution in super-resolution images is still a current and ongoing discussion within the microscopy community.

3.1.2 Adaptive Optics (AO)

One of the main imaging aims to address for our macrophage research was colocalization studies between mitochondria, mROS and bacteria. A concern that we wanted to investigate further was the detrimental effects that image aberrations could cause on being able to accurately localize structures and molecules with respect to each other.

AO Background

In this work we consider phase aberrations - distortions to the optical wavefront, where there is no energy taken from the beams under consideration, but the phase errors lead to effects on how the beam propagates and forms foci. There are a number of potential sources of aberrations in microscopy [86]. Planar (figure 3.1(a)) and spherical (figure 3.1(b)) wavefronts are good approximations for the best case wavefronts in collimated and focusing beams respectively [87]. An objective lens will create a spherical wavefront when a collimated beam is focused through it down to a diffraction limited spot (figure 3.1(b)). This finite size can only be achieved if the wavefront does not become distorted. However, when imaging thick biological samples, aberrations to the ideal wavefront can occur due to refractive index variations (figure 3.1(c)). Even if these variations are small, they can add up over the propagation length. Aside from the sample, optical components can have imperfections causing aberrations and using a microscope outside of its design specifications can also be detrimental [88]. Aberrations can cause broadening of the focal spot and reduced intensity and image contrast, which would therefore cause large errors in localization measurements.

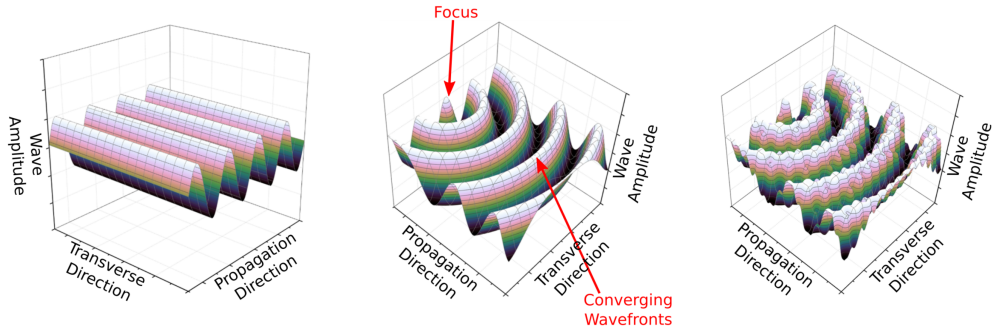

Figure 3.1: **(a)** Model of a plane wave. **(b)** Model of a non-aberrated spherical wave. **(c)** Model of an aberrated spherical wave, where the only change was to modify the phase and not the amplitude. These figures were made by Dr Brian Patton.

Adaptive optics (AO) is an active way to correct for aberrations in an optical system to improve image quality. AO has been used extensively in the field of astronomy for decades, for example to correct for the phenomenon of twinkling stars, a distortion caused by the atmosphere [87], and has since then been applied to the field of microscopy

[88].

Aberrations can be described by a set of mathematical functions (modes). It is useful for the functions to closely resemble the most common aberrations, such as spherical, coma and astigmatism [89]. It is also desirable for the functions to be orthogonal to one another, meaning there will be no crosstalk between them, allowing an aberration mode to be corrected for without affecting previous corrections of other aberration modes. A suitable set of functions that match both these properties are the Zernike polynomials [89]. Assuming that the total aberration in the system is a linear superposition of the individual aberration modes, which is generally the case, the total aberration in the system can be corrected for by purposely introducing an aberration, identical to the total aberration but with an opposite phase [86].

To perform an aberration correction three elements are generally required:

- The description of the aberrations as a set of orthogonal modes.
- A method of quantifying the amount of any given aberration mode in the system.
- A control system, which includes an adaptive correction element and computing hardware, to apply the phase conjugated aberration.

To quantify the amount of an aberration mode in the system, techniques are available which work in either a direct or indirect modality. Direct measurement techniques measure the phase of the wave and give feedback to the adaptive element. The adaptive element then alters itself to correct the aberration. Suitable methods include interferometric sensing or the use of a Shack-Hartmann wavefront sensor [90, 91]. It can be difficult to incorporate the hardware required for direct sensing into a microscope optical system. Direct wavefront sensors are only able to measure well defined wavefronts originating from point sources. In microscopy, fluorescent labelling of biological structures results in a more complex sample which simultaneously produces different wavefronts from different parts of the sample, which the wavefront sensor will not be able to distinguish between [88]. Therefore, indirect wavefront sensing is more often employed for AO correction. Instead of using a wavefront sensor, the correction routine

is as follows (figure 3.2(a)): a sequence of images is acquired each with an intentional and known applied aberration. For each image, a quality metric is calculated, such as image sharpness or image intensity. From this set of images, we can estimate the amount of any given correction that will maximise the metric by plotting the quality metric values measured vs applied aberration amplitude and creating a Gaussian fit (an example is given in figure 3.2(b)) [92]. The process is repeated for each type of aberration to be corrected for. Typically, a couple of iterations of the correction routine are required to minimise any crosstalk between the aberration modes as in practice they will not be perfectly orthogonal to one another. When imaging deep into tissue where aberrations are stronger five to six iterations may be required - crosstalk will not be as apparent with smaller aberrations. The total phase correction is then applied to the adaptive correction element before acquiring corrected imaging data.

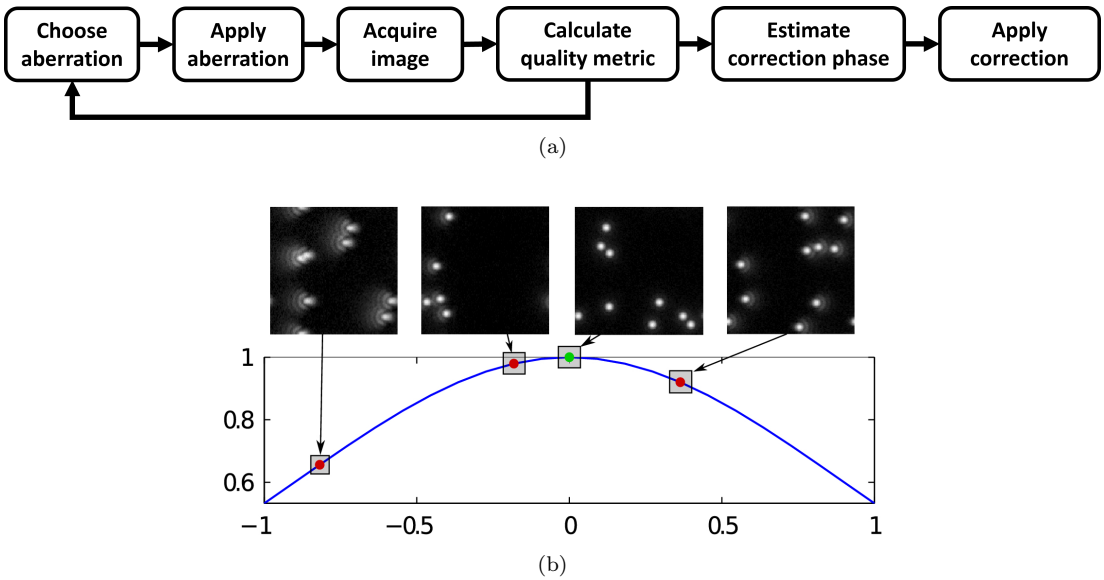

Figure 3.2: **(a)** Flowchart of the indirect (sensorless) adaptive optics aberration correction routine. **(b)** Example quality metric fitting for coma aberration. Three images were acquired (red dots) with varying amplitudes of coma applied using the adaptive correction element. The quality metric was calculated for each image and the plot shows the metric values vs coma amplitude applied. Using a Gaussian fit, the metric curve peak is found, which gives the optimal aberration amplitude to apply to the adaptive correction element (green dot). **(b)** is reprinted with permission from [92] © The Optical Society.

Options for the adaptive correction element for microscopy based work include both spatial light modulators (SLMs) and deformable mirrors (DMs). Each pixel of an SLM

is a liquid crystal element and when a voltage is applied the direction of the liquid crystal changes, altering the optical path length within each element. This change imparts a phase shift on the light which passes through the elements [93]. A DM has an array of actuators behind its surface to control the shape of the mirror. There are numerous types of DMs that employ different actuator technologies. However, like SLMs they all operate on the principle that altering the surface of the DM modifies the optical path length of the reflected wavefront, varying its phase. The adaptive element chosen depends on the specific application and various factors. Differences include speed of reconfiguration; DMs can operate at a rate of a few kilohertz whereas this is only a few tens of hertz for SLMs. On the other hand, SLMs are capable of producing more complex phase patterns due to the larger number of pixels compared to the number of actuators on a DM [86]. SLM phase patterns are also designed for specific wavelengths, meaning they are not suitable for multicolour fluorescence microscopy, and are also designed for specific polarisation states, meaning in fluorescence microscopy the signal would be halved. However, the latter is not a problem for STED microscopy as the lasers are modified to have a well defined polarisation which can be matched to the SLM.

AO Enhanced Confocal Microscopy

Our research group have developed a custom AO enhanced confocal microscope, designed primarily for exploiting the properties of nanodiamond (ND) for magnetic field sensing [94], particularly when imaging ND embedded in living tissue to minimise aberrations due to thick samples [95]. Dr Graeme Johnstone and Dr Brian Patton primarily designed and constructed the original version of the microscope. I contributed to the construction and alignment of the microscope and also used it for initial studies into the effects of aberrations when imaging mitochondria in macrophages, which is discussed in section 3.2. A schematic of the microscope design is shown in figure 3.3. Note that the schematic does not include every optical element and has been simplified for illustration as this thesis will not fully cover the microscope development.

The microscope design includes three excitation lasers (488 nm continuous wave,

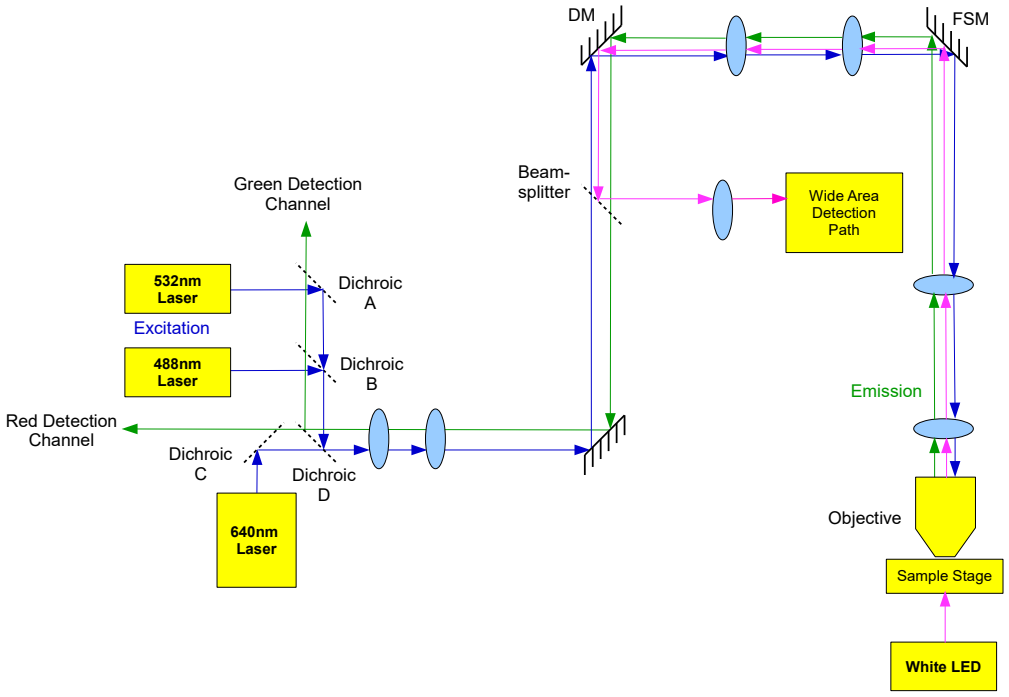

Figure 3.3: Schematic of our custom adaptive optics enhanced confocal microscope. Adapted from an original schematic made by Dr Graeme Johnstone.

532 nm picosecond pulsed and 640 nm picosecond pulsed) and two single-photon avalanche diode (SPAD) detectors for fluorescence detection. The excitation laser wavelengths were chosen to enable optical measurements on NDs and on other, conventional, fluorophores. Further information about ND fluorescence is discussed in section 4.2. The lasers are coupled into the system through dichroic mirrors as shown in figure 3.3, where the optical properties of the dichroic mirrors were chosen to allow the returning fluorescence emission from the sample to travel to the appropriate detector.

Dichroic mirror D separates the emission fluorescence from the sample into two detection paths by reflecting wavelengths below 560 nm (green detection channel) and transmitting wavelengths above this value (red detection channel). The 488 nm excitation laser is coupled into the green detection channel and allows the use of green fluorescent protein (GFP) or Alexa Fluor 488 labelling of samples. As we couple all light below 560 nm into this path, it is also where the 532 nm laser for exciting the nitrogen-vacancy (NV) centres in nanodiamond must be placed. The red detection

channel allows fluorescence emission to be collected from samples labelled with, for example, Atto647N, by excitation with the 640 nm laser.

The microscope operates in an upright configuration and has the option of two different objective lenses, a 60x oil immersion lens with a numerical aperture (NA) of 1.35 or a 60x water immersion lens with a NA of 1. The microscope has a manual sample stage and fine control of the axial imaging position is achieved through controlling the height of the objective lens compared to the sample using a PIFOC nanopositioner. The PIFOC is a piezo-actuated z-scanner that attaches to the objective lens to control its position and has a total movement range of 400 μm. In closed loop operation the PIFOC has an accuracy of approximately 5 nm. A DM was chosen as the adaptive correction element as there are multiple excitation wavelengths in the system. Confocal laser beam scanning is provided by a fast steering mirror (FSM), giving x and y axis beam steering on a single mirror. The beamsplitter between dichroic mirror E and the DM provides a widefield/brightfield detection channel to be used with the white LED which is positioned below the sample and I used this channel for TIE microscopy which will be discussed in sections 3.1.3 and 3.5.

Interferometric Calibration of the DM

The DM must be calibrated to allow for optimal aberration correction. Generating Zernike polynomial modes is achieved using control signals that correlate the desired mirror surface deformation with the necessary combination of actuator displacements. However, the relationship between the voltages applied to the actuators and the deformation of the mirror surface must first be determined as there is typically crosstalk between adjacent actuators due to their coupling via the mirror surface. We use a control matrix [96], which tabulates the required combination of actuator positions for each Zernike mode which that mirror is capable of producing accurately. Note too that, for a modal scheme, the total number of distinct modes will be less than or equal to the degrees of freedom in the system, which is typically the number of actuators driving the mirror.

Applying a unit signal to a single actuator gives the influence function of that

actuator, ψ_i, (the shape of the DM). The total aberration produced by the DM can then be described by:

$$\phi(r,\theta) = \sum_{i=1}^{N} c_i \psi_i(r,\theta) \tag{3.2}$$

where N is the number of actuators and c_i is the control signal for the ith actuator [97]. As the DM will be controlled using a set of Zernike polynomial modes the aberration can instead be expressed as:

$$\phi(r,\theta) = \sum_{i=1}^{\infty} a_i Z_i(r,\theta) \tag{3.3}$$

where a_i is the coefficient of the ith Zernike mode $Z_i(r,\theta)$ [96]. The vector of Zernike mode coefficients, $\mathbf{a}$, are related to the control signal vector, $\mathbf{c}$, through the linear transformation [96]:

$$\mathbf{a} = \mathbf{B}\mathbf{c} \tag{3.4}$$

The inverse of this equation gives the control matrix, $\mathbf{B}^{\dagger}$, allowing the coefficients of the Zernike modes to be specified and the required control signals to be calculated [96]:

$$\mathbf{c} = \mathbf{B}^{\dagger}\mathbf{a}' \tag{3.5}$$

We used an interferometric method to determine the control matrix. The DM was incorporated into one arm of a Michelson interferometer as illustrated in figure 3.4. The other arm of the interferometer, called the reference path, was altered to control the number and orientation of the fringes in the interferogram viewed on the camera. The phase introduced to the beam by the DM is encoded in the fringe pattern seen on the camera. The number of fringes in the interferogram determines the spatial sampling of the phase - you want to measure the phase at a higher spatial frequency than the actuators. Orientating the fringes so they don't run parallel to the rows or columns of actuators increases the change in the interference pattern as voltages are applied to

the actuators which improves phase recovery. Using fringe pattern analysis and phase unwrapping techniques, the full unwrapped phase information can be uncovered which relates directly to the shape of the DM [96]. Dr Graeme Johnstone and Dr Brian Patton built the Michelson interferometer into our custom confocal microscope in figure 3.3 so that the DM could be calibrated whilst positioned within the microscope.

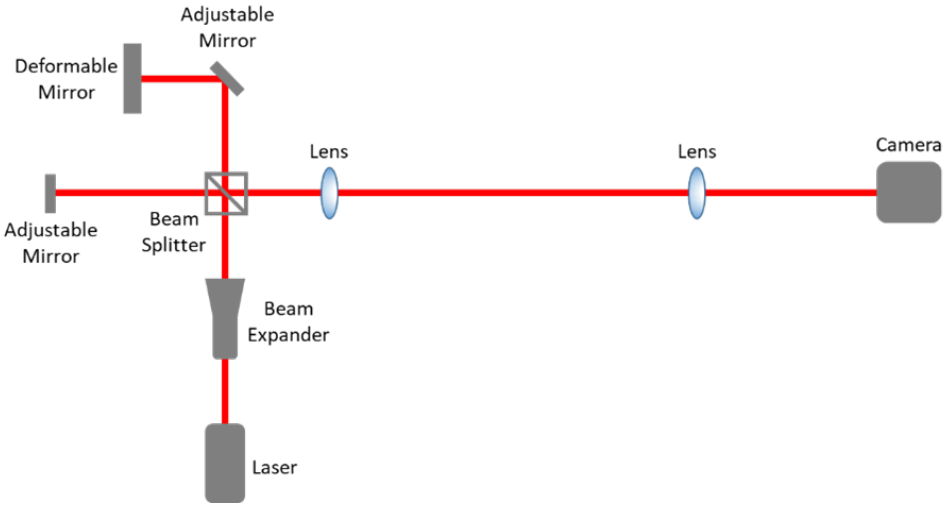

Figure 3.4: Schematic of the deformable mirror incorporated into one arm of a Michelson interferometer.

The mirror in the reference path was adjusted until there were at least 4 fringes per actuator and the fringes were tilted across the surface. A reference image of the DM was taken, as in figure 3.5(a), which was used to determine which region of the DM corresponded to the image of the back focal plane of the objective, figure 3.5(b). The yellow circle in each image in figure 3.5 indicates this region. The original DM used in this work was from Boston Micromachines Corporation and had 140 actuators. Five different control signals were applied to each of the 140 actuators in turn and the influence function was measured for each actuator. Fringe analysis and phase unwrapping allowed the matrix $\mathbf{B}$ to be determined from the calibration data set. Singular-value decomposition (SVD) was used to invert the matrix to obtain $\mathbf{B}^{\dagger}$. Various different Zernike modes could then be applied, where the required control voltages were determined using $\mathbf{B}^{\dagger}$. Figure 3.5(c) shows the change in interference pattern when a trefoil aberration was applied.

I carried out this initial calibration, and the MATLAB code I used for fringe analysis

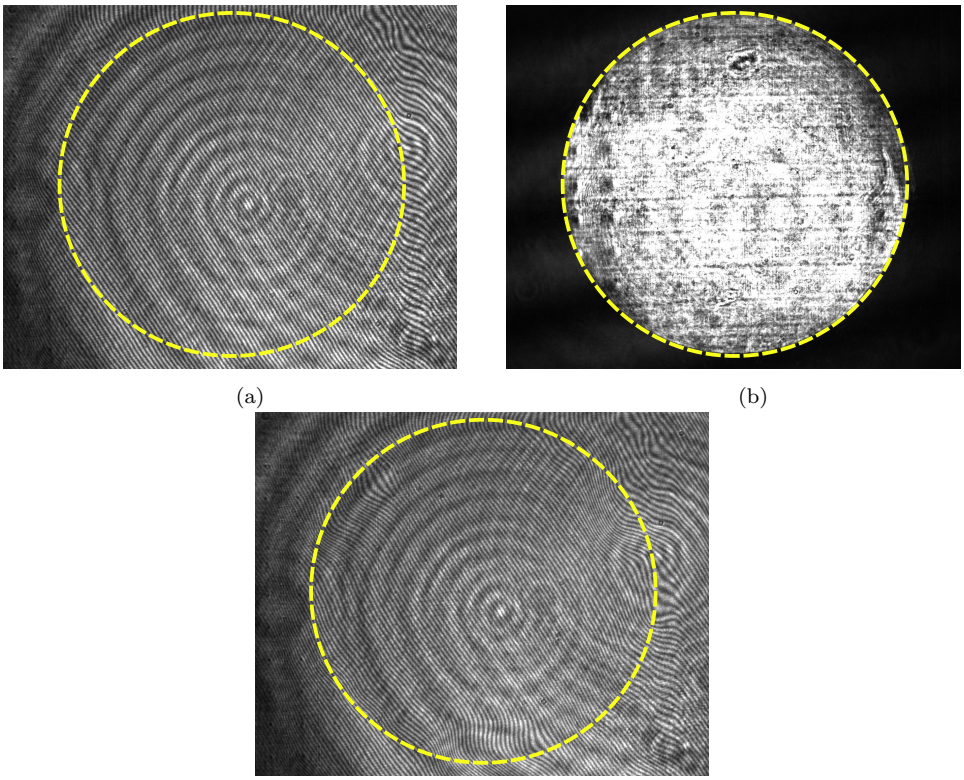

(a) (b)

(c)

Figure 3.5: **(a)** Reference image for DM calibration. **(b)** Image of the back focal plane of the objective. **(c)** Trefoil aberration applied using the required control voltages determined by $\mathbf{B}^{\dagger}$.

and phase unwrapping was developed by Dr Jacopo Antonello, who at the time was part of the Dynamic Optics and Photonics group at the University of Oxford. Since then there have been multiple iterations of the DM calibration. There have also been upgrades and changes to the microscope design. First of all, due to the original Boston Micromachines DM incurring faults with a number of the mirror actuators, the DM needed to be replaced and the new one calibrated. The new and current DM is a Mirao 52-e DM with 52 actuators and was implemented and calibrated by both Ryan Corbyn and Dr Brian Patton. Secondly, Ryan Corbyn and Dr Brian Patton also replaced the Michelson interferometer in the microscope with a compact, slot-in interferometer outlined in Antonello *et al.* [98] so that the interferometer can be easily inserted into the microscope only when required.

3.1.3 Transport of Intensity Equation (TIE)

As discussed in section 1.5 mROS have a very short half-life and are quickly neutralised. Therefore it is important to be able to image mROS live with high temporal resolution, especially when trying to localize mROS in relation to mitochondria and bacteria within the macrophages. A second challenge arises when combining imaging mROS over short time scales with the fact that the response of macrophages to pneumococcal bacteria is over a period of 16+ hours. Therefore not only is live cell imaging required for imaging fast dynamic processes within the cells but it must also be carried out over long periods of time to determine at what time points mitochondrial dynamics and mROS play a key role in bacterial clearance.

Fluorescence microscopy has become the industry standard for imaging cellular functions, as fluorescently labelling structures of interest allows them to be imaged in an isolated way with high signal to noise ratio. However, if imaging studies are to be carried out over long periods of time, effects such as photobleaching and phototoxicity can become significant problems [99]. There are also concerns over whether labelling affects cellular physiology [100]. Label-free microscopy techniques offer an alternative to fluorescence microscopy in some situations. Not only do label-free techniques mitigate the aforementioned problems of photobleaching and phototoxicity, allowing for imaging studies over a long time frame, but some can also provide quantitative information not achievable from fluorescence microscopy.

Brightfield microscopy is the oldest label-free microscopy technique and simply involves illuminating a sample with an excitation source and imaging the transmitted light either onto a camera sensor or relaying the image plane to the human eye via an eyepiece for direct viewing. Biological samples however, can often have very low absorption and as a consequence appear almost transparent when in focus in brightfield if no contrast agents are added. The samples will however induce phase changes to the light passing through the sample and therefore there have been many imaging techniques developed to enhance the contrast of label-free images based on phase changes. Zuo *et al.* [101] provides a review of the different techniques available, explaining that the techniques are broadly split up into two different categories: phase contrast microscopy

and quantitative phase imaging (QPI). The former includes techniques such as Zernike Phase Contrast (ZPC) microscopy and Differential Interference Contrast (DIC) microscopy. These methods however do not provide quantitative phase information. On the other hand, QPI techniques not only increase image contrast but they do provide quantitative phase information and allow refractive index differences across the sample to be determined. Zuo *et al.* [101] follows on to explain that QPI techniques can be either interferometric or non-interferometric based methods.

We concentrate here on a non-interferometric QPI method based on the Transport of Intensity Equation (TIE). In section 3.5 I discuss early imaging studies we carried out to determine how applicable TIE microscopy is to macrophage research and whether there are quantitative refractive index differences between, for example, mitochondria and bacteria which could provide an alternative to long term fluorescence imaging. Also in section 5.2 I show how this technique was implemented on a low-cost 3D printable microscopy system. The remainder of the current section will discuss the background of the TIE and explain how it can be used for QPI.

Teague first published the TIE in 1983 [102]. The TIE describes the relationship between the change in intensity with respect to the axial position as light passes through a sample, $\partial I/\partial z$, and the corresponding phase value ϕ_0:

$$-k_0\frac{\partial I}{\partial z} = \nabla \cdot (I_0 \nabla \phi_0) \tag{3.6}$$

where $k_0 = (2\pi/\lambda)$ is the wavenumber (λ is the wavelength), I_0 is the intensity of the in focus image plane, and ∇ is the vector differential operator. Phase retrieval using the TIE is an inverse problem and the imaging system that is required to achieve QPI only requires brightfield illumination of the sample, a method of accurately taking images at different z positions and a suitable camera. The wavelength of illumination and therefore k_0 is known, as is I_0 from the experimental in focus image of the sample. The partial differential, $\partial I/\partial z$, can be experimentally estimated using a minimum of two out of focus images spaced equally, Δz, on either side of the focal plane:

$$\frac{\partial I}{\partial z} \approx \frac{(I_{\Delta z} - I_{-\Delta z})}{2\Delta z} \tag{3.7}$$

Therefore ϕ_0 is the only unknown and consequently the TIE can be solved for the phase. To solve the equation, first an auxiliary function, ψ, is introduced to simplify equation 3.6 into a Poisson equation. Teague [102] defined ψ as:

$$\nabla\psi = I_0\nabla\phi_0 \tag{3.8}$$

and therefore equation 3.6 becomes:

$$-k_0\frac{(I_{\Delta z} - I_{-\Delta z})}{2\Delta z} = \nabla^2\psi \tag{3.9}$$

This simplification allows the TIE to be quickly solved by Fast Fourier Transform (FFT) to determine ψ which is then subsequently integrated to determine the phase ϕ_0. TIE microscopy has been used in the past to image isolated microtubules [11], the morphology of macrophages during apoptosis and phagocytosis [103], and for determining optical path length (OPL) information in living algal cells [104]. Therefore TIE posed as an interesting technique for our subcellular imaging studies in macrophages.

3.2 Initial Study of Aberration Correction of Confocal Macrophage Images

As discussed in section 3.1.2, we wanted to investigate the effects of image aberrations on macrophage colocalization studies. Aberrations can occur from the microscope optics or from refractive index variations within the sample, which is a greater problem for thick samples. In future, imaging studies of alveolar macrophages from bronchoalveolar lavage (BAL) or tissue samples would be beneficial. Therefore, we first wanted to assess the effects of aberrations in imaging human MDM samples.

Whilst acquiring confocal microscopy images, from a commercial microscope, of a mock infected MDM sample with labelled mitochondria and nuclei, we observed the effects of spherical aberration when viewing the orthogonal planes of a z-stack data set

(figure 3.6). Spherical aberration is where rays transmitting through a lens at different distances from the optical axis do not all focus at the same focal point [105] due to the range of angles being refracted at the spherical interface. Image degradation due to spherical aberration is greater in the orthogonal planes versus the lateral image planes due to the distortion of the PSF [106]. The resulting images have reduced intensity and signal to noise ratio and elongation of features along the optical axis which gets worse with focus depth [105].

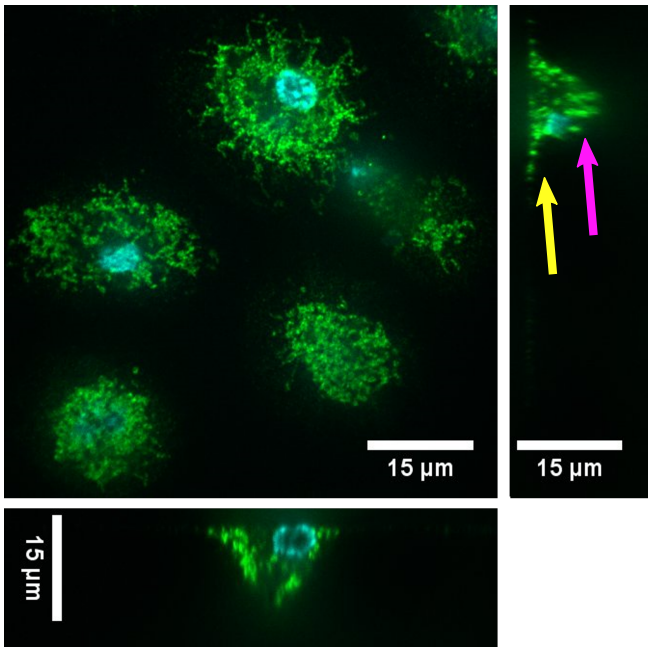

Figure 3.6: Confocal image, from a z-stack acquired using an Andor Revolution XDi spinning disk confocal microscope, of a mock infected human MDM sample with labelled mitochondria (Alexa Fluor 488) and nuclei (DRAQ5). The orthogonal planes from the z-stack are also shown where the magenta arrow highlights mitochondria deeper in the sample with greater blurring and elongation, due to spherical aberration, compared to those closer to the coverslip (yellow arrow).

This is exactly what we see in the orthogonal planes in figure 3.6. The yellow arrow points towards mitochondria closest to the coverslip where the mitochondria are more likely to be orientated flat along the bottom of the cell, appearing smaller in the orthogonal plane compared to mitochondria further away from the coverslip (magenta arrow), which have a greater chance of being orientated along the orthogonal plane, thus appearing longer in the orthogonal image in any case without spherical aberration. However looking at the distribution of blur around the mitochondria in the orthogonal

plane, as opposed to structure length, it can be seen that there is greater blurring and elongation of structures further away from the coverslip due to spherical aberration. We know that it is spherical aberration causing this effect as it is seen in the axial planes, whereas astigmatism, coma or trefoil causes distortions observable in the lateral planes. As shown in equation 1.4, the axial PSF of a confocal microscope depends on the wavelength, NA and immersion medium. Patton *et al.* [107] show experimental data for how the FWHM of the confocal axial PSF increases as you focus deeper into the sample in the presence of spherical aberration. They observed an increase of $\approx 360\,\text{nm}$ in the axial PSF over a depth of $20\,\mu\text{m}$.

Spherical aberration can occur from light passing through different regions of refractive index within the sample [105] or from mismatches between the refractive index of immersion media and the glass coverslip [106]. Using too thick a layer of mounting medium for the sample can also worsen spherical aberration [105]. The average refractive index of bone marrow derived macrophages (BMDMs) has been reported as 1.378±0.003 [108] and 1.384±0.015 [109]. The sample in figure 3.6 was mounted in Prolong Diamond which has a refractive index of 1.470 when cured, the coverslip was glass with a refractive index of 1.515 and the objective lens immersion medium was Olympus IMMOIL-F30CC which has a refractive index of 1.518. The sample was set up as a gradient of small changes in refractive index from the objective lens immersion medium to the cells themselves to minimise aberrations. Therefore as we are seeing spherical aberration in this sample it highlights the need to consider aberration correction when carrying out colocalization studies in MDMs.

Macrophage samples are not homogeneous on the way through the sample at different angles. Therefore we wanted to carry out a study into whether a single cell would induce quantifiable/important aberrations. Figure 3.7 shows an x-y image of a human MDM with labelled mitochondria acquired using our custom confocal AO microscope detailed in section 3.1.2. Once the image was acquired, an AO correction was carried out on the full image plane (orange), correcting for Zernike modes 5 - 10 (Noll index where modes 5 and 6 are oblique and vertical astigmatism, modes 7 and 8 are vertical and horizontal coma, and modes 9 and 10 are vertical and oblique trefoil) and using

the metric filtered peak intensity, which maximises the brightest 10% of pixels. The correction procedure was repeated for each quadrant shown in figure 3.7 so that we had five independent corrections (whole cell and one each per quadrant) to compare. Dr Brian Patton acquired this data set and I analysed the data.

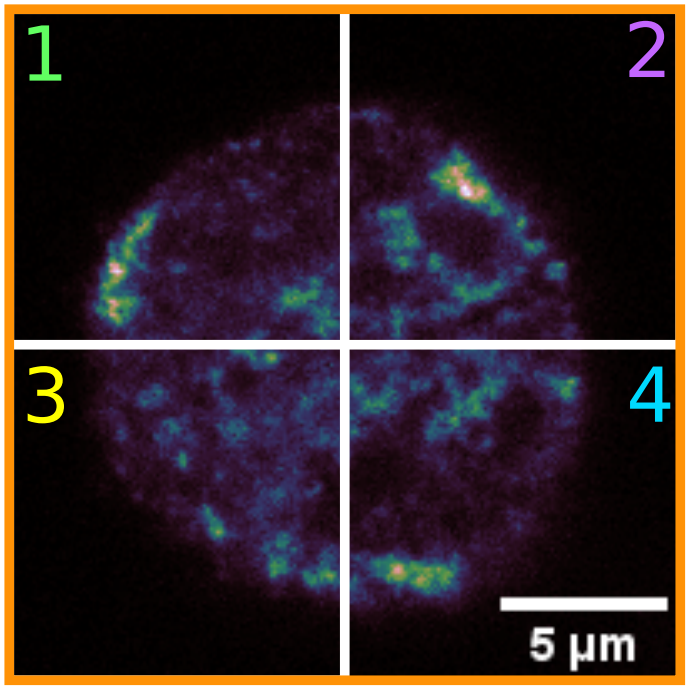

Figure 3.7: Image of a mock infected human MDM, where mitochondria have been labelled with Alexa Fluor 488. Image acquired using our custom confocal microscope detailed in section 3.1.2. AO corrections were carried out on the full image plane (orange) and four quadrants: quadrant 1 - green, quadrant 2 - purple, quadrant 3 - yellow and quadrant 4 - blue.

The resulting AO correction values for the full image plane and each quadrant can be seen in figure 3.8. The data shows that the two types of astigmatism (modes 5 and 6) are the aberrations which required the greatest correction for the full image plane and each quadrant. The data also shows that the correction amplitude of each mode differed for the full image plane versus each quadrant. For example, for mode 5 there is a 43% difference between the correction amplitude for the full image plane versus quadrant 4. The difference highlights the need to think carefully about applying AO aberration corrections to single cells: The data suggests that applying AO corrections to smaller regions of the image plane (potentially areas of particular interest, for example an area where localization of mitochondria with respect to bacteria or mROS is required) is

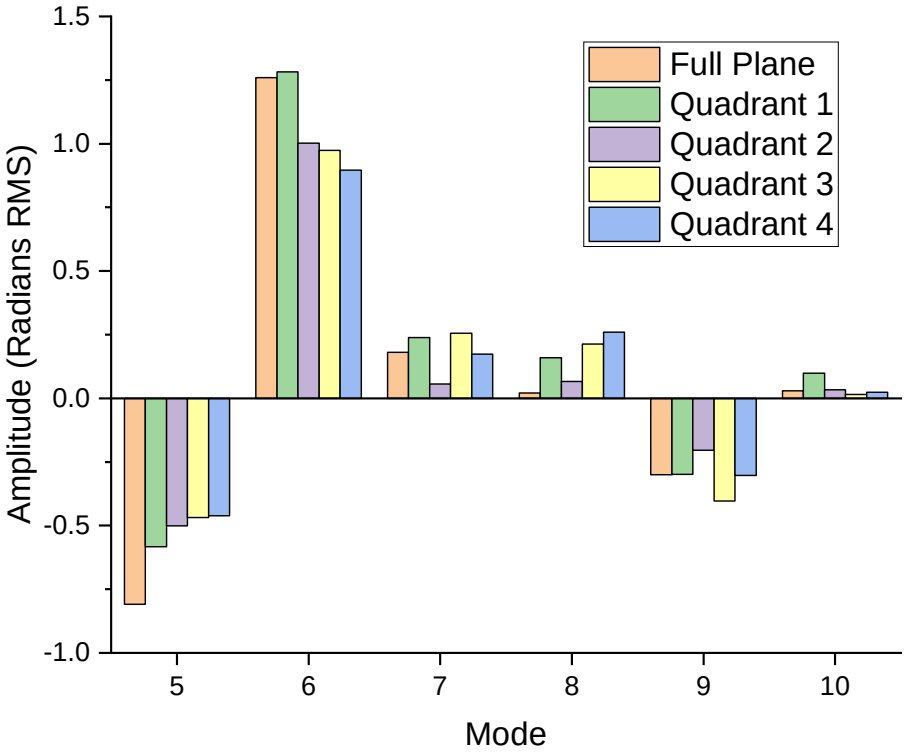

Figure 3.8: Amplitude of the correction modes 5 - 10 (Zernike Noll index) calculated using the full image plane, quadrant 1, quadrant 2, quadrant 3 and quadrant 4 as defined in figure 3.7.

more suitable and would be more accurate than correcting based on the full plane.

Secondly, I acquired data to investigate the difference in AO correction values obtained from corrections using x-y images from different points along the optical axis of a human MDM sample, again using our custom confocal AO microscope. I used three image planes for the analysis, as illustrated in figure 3.9, where plane 1 resided close to the coverslip where the MDM is at its widest diameter, plane 2 resided in the middle of the cell and plane 3 was at the top of the cell furthest away from the coverslip where the MDM is at its smallest diameter.

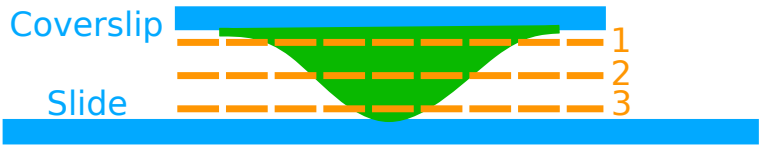

Figure 3.9: Schematic illustrating the position of the three image planes (orange) in figure 3.10 with reference to the cell (green) and slide and coverslip (blue).

Figure 3.10 shows the data acquired. Row one shows the original non corrected image planes. An AO correction routine was then carried out for image plane 1, where modes 5 - 11 (Zernike Noll index) were corrected for using the intensity squared metric (I^2), which is the the intensity of each pixel squared and then summed. Row 2 shows the three image planes with this AO correction applied. Then, the same AO correction routine was carried out for plane 2 and row 3 shows the three image planes with this AO correction applied. Lastly, the process was repeated for plane three, and row 4 shows the resulting three image planes. The I^2 value and the maximum intensity value (I_{max}) is shown for each image. The values highlighted in magenta is the image plane used for the AO correction. Each column in the figure has been plotted on the same intensity scale, for which figures 3.10(m), 3.10(n) and 3.10(o) show the colour bars.

Note that the I^2 and I_{max} values are provided for transparency. I had expected the I^2 values for each column to be maximum for the image plane which the AO correction routine was performed for (magenta). This was however only the case for column one. Potential reasons for this not being the case include that the final images shown in the figure were acquired after all three of the correction routines had been carried out, therefore the imaged planes may not be exactly the same plane used for the correction calculation. Also, our system did not have defocus free spherical aberration correction. Therefore, we can't necessarily compare the I^2 values, however a qualitative difference can be seen in the images.

Note here also that system aberrations need to be taken into account. Deformable mirrors usually will not be completely flat when no voltages are applied, therefore a correction needs to be applied to compensate for this and also compensate for any other aberrations originating from the optics in the microscope. Correcting for the flatness of the DM can be done using the interferometric DM calibration method outlined in section 3.1.2. We then used a nanodiamond calibration sample on the microscope to correct for system aberrations, using the sensorless correction routine, as nanodiamond is a point like emitter and so shouldn't induce sample aberrations. This was carried out prior to the AO corrections calculated in this section.

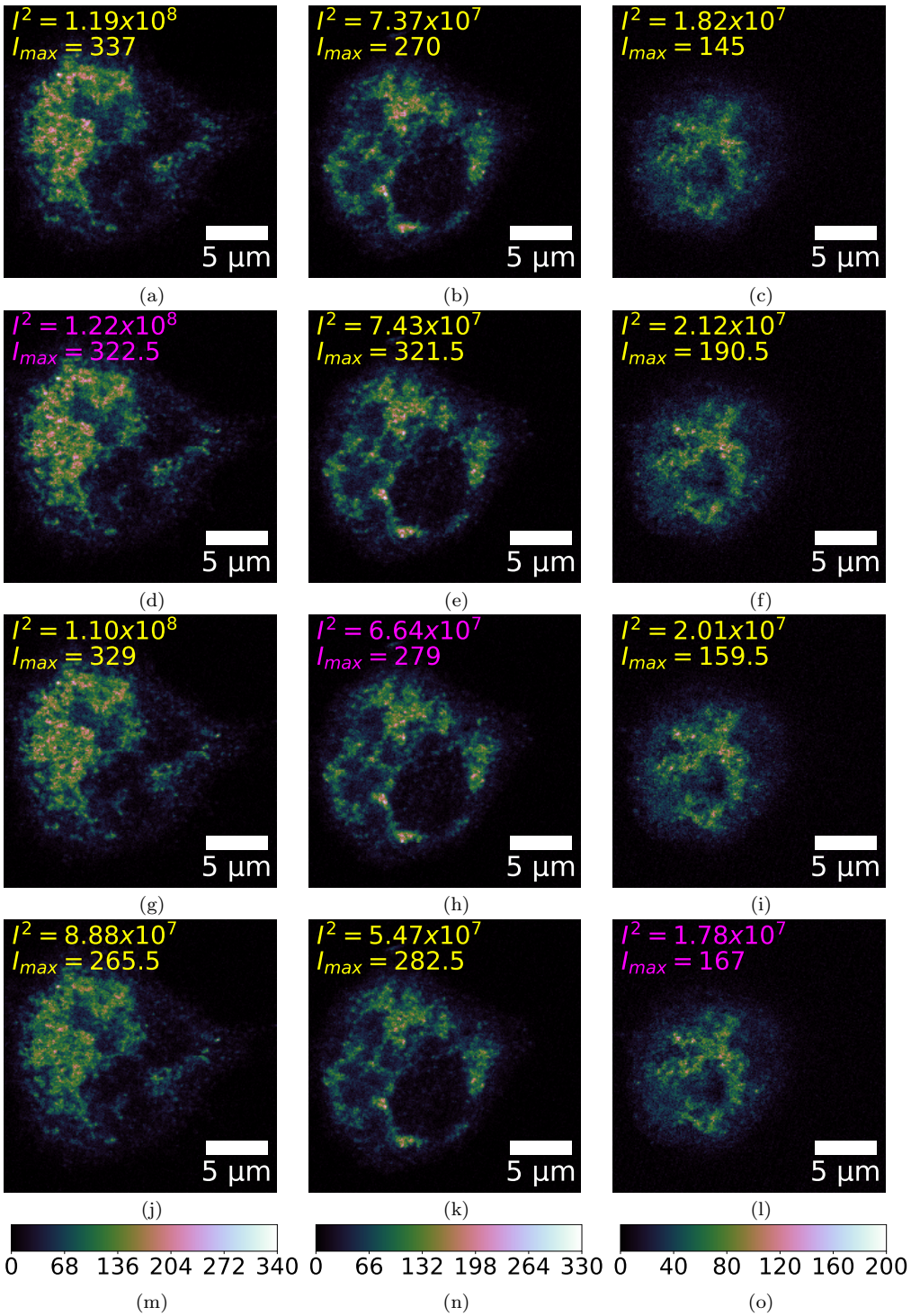

Figure 3.10: Each row shows three image planes at different axial positions of a mock infected human MDM sample with labelled mitochondria (Alexa Fluor 488), acquired using our custom confocal microscope detailed in section 3.1.2. **(a)**, **(b)** and **(c)** shows non AO corrected data. **(d)**, **(e)** and **(f)** was AO corrected for plane **(d)**. **(g)**, **(h)** and **(i)** was AO corrected for plane **(h)**. **(j)**, **(k)** and **(l)** was AO corrected for plane **(l)**. The AO metric used was I^2 (the intensity of each pixel squared and summed) and is shown for each image. Zernike modes 5 - 11 (using the Noll index) were corrected for. **(m)**, **(n)** and **(o)** is the colour bar scale for each column with units counts per 1.5 ms.

The correction amplitudes for modes 5 - 11 for each image plane are shown in figure 3.11. The data shows that the dominant aberration modes are strongly sample dependent as compared to figure 3.8, as in this case astigmatism is no longer the greatest aberration in the image, the two types of coma (modes 7 and 8) and also spherical (mode 11) show greater correction amplitudes for the three planes. It is worth noting here that for high NA objective lenses, first order spherical (mode 11) is not sufficient to correct for real spherical aberration. A combination of higher order spherical Zernike modes would be required [110]. Figure 3.11 also highlights the variation in correction amplitudes for each mode across each image plane, much like the variation when correcting for full image planes versus sub sections. In this case, not only do the amplitude magnitudes vary for each plane, but also the sign. For example for mode 5, the correction amplitude for plane 1 was 0.109, whereas the correction amplitude for plane 2 was -0.102. Meaning for plane 1, astigmatism needed to be added to the phase of the wavefront, whereas for plane 2, astigmatism needed to be subtracted from the phase of the wavefront.

We have shown from the data sets in this section that further consideration is needed when applying AO aberration corrections to images of macrophages. As our initial data has shown that correction amplitudes vary between sub sections of the image plane and also between different image planes separated along the optical axis, we have verified it is therefore not optimal to simply correct for the full image plane and to also then apply this correction to imaging full z-stacks, or using the correction to image different cells. As mentioned, it may be more appropriate to firstly locate smaller regions of interest and produce more localized corrections. For live cells the inhomogeneity of aberrations would also be across time, therefore how quickly the correction changes in time and space would need to be determined.

Unfortunately we were unable to continue this work and investigate further due to our deformable mirror malfunctioning and delays with implementing a new one. There has however been a study recently published by Rodrigues de Mercado *et al.* [111] on the analysis of astigmatism induced by different structures within HeLa cell samples. They found structures like the nucleus induce greater amounts of astigmatism when

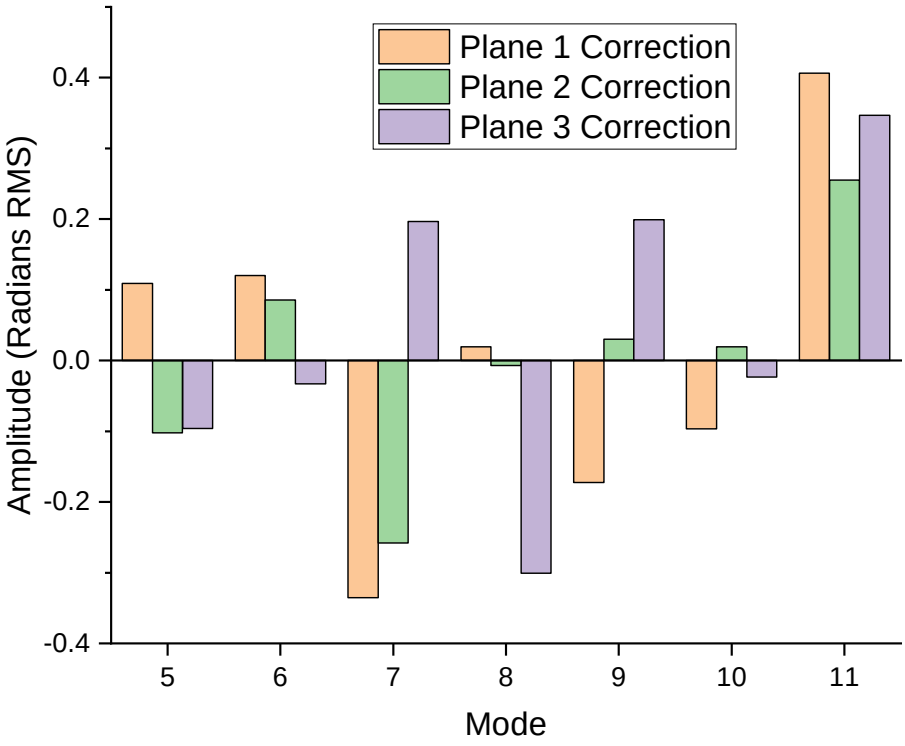

Figure 3.11: Correction amplitudes for Zernike modes 5 - 11 (Noll index) for AO correction of image planes 1, 2 and 3 as shown in figures 3.9 and 3.10.

imaging through the cell than smaller structures. In future, it would be useful to extend their analysis to macrophages and also other types of aberrations, such as spherical and coma as we have shown significant correction amplitudes for these modes were required in figure 3.11. We would also want to assess the effect of aberrations specifically on colocalization studies.

3.3 Super-Resolution Radial Fluctuations (SRRF) Reconstructions of Mitochondria

As discussed in section 3.1.1, SRRF is a computational super-resolution reconstruction method using spatial analysis based on radiality followed by a temporal correlation analysis. We wanted to apply SRRF to image data sets of human MDM samples with fluorescently labelled mitochondria to assess the suitability of SRRF for resolving the mitochondrial network as an alternative to conventional super-resolution methods.

The reason being is SRRF is open-source and can generate super-resolution reconstructions from diffraction limited microscopy techniques such as widefield and confocal microscopy. Meaning SRRF has greater accessibility than the complex hardware required for techniques such as PALM and STED.

The SRRF algorithm offers different temporal analysis methods, namely temporal radiality maximum (TRM), temporal radiality average (TRA), temporal radiality pairwise product mean (TRPPM) and temporal radiality auto-cumulant (TRAC) [10]. TRM and TRA are pixel by pixel projections of the radiality maps, where TRM is a maximum projection which has the advantage of constant emitters not dominating, and TRA is an average projection which is less affected by noise [10]. TRPPM and TRAC use higher-order statistics for temporal analysis of radiality fluctuations, which Gustafsson *et al.* [10] have demonstrated improves SRRF's ability to resolve fluorophores in high density data sets. Therefore, I have carried out an analysis comparing the TRA, TRPPM and TRAC methods on human MDM data sets.

I prepared two different human MDM samples with labelled mitochondria (Alexa Fluor 488), one mock infected and one challenged with *S. pneumoniae*, both fixed after 4 hours. Using an Andor Revolution XDi spinning disk confocal microscope, I then acquired 100 raw frames of an interesting image plane within a cell in each sample and subsequently performed SRRF reconstructions on the data sets. The SRRF settings used in each case were: Ring Radius 0.5, Radiality Magnification - 10 and Axes in Ring - 8. Figures 3.12 and 3.13 show a comparison of the different temporal analysis methods for the mock infected and challenged samples respectively.

It can be seen from the figures that in both cases, using the TRA (figures 3.12(b) and 3.13(b)) and TRPPM (figures 3.12(c) and 3.13(c)) methods both qualitatively appear to provide good reconstructions of the raw data in figures 3.12(a) and 3.13(a). However in the case of the TRAC method, especially in the cases of third-order (figures 3.12(e) and 3.13(e)) and fourth-order (figures 3.12(f) and 3.13(f)), the reconstruction appears to break down visualisation of the mitochondrial network.

SRRF was designed to reconstruct data sets which statistically fluctuate in radiality between image frames, although unlike Super-Resolution Optical Fluctuation Imaging

(SOFI) [112] SRRF doesn't require fluorophores to switch between strictly fluorescing and non-fluorescing states. The data sets in figures 3.12 and 3.13 however, have minimal temporal fluctuations as the image frames were acquired with a constant illumination power and the fluorophore Alexa Fluor 488 does not have emission fluctuation properties. Therefore, because of the lack of statistically correlated temporal fluctuations, SRRF may act more like deconvolution and the use of higher-order temporal analysis is inappropriate. In future, labelling the mitochondria with a photo-switchable fluorophore such as Alexa Fluor 647 would provide the statistical fluctuations necessary.

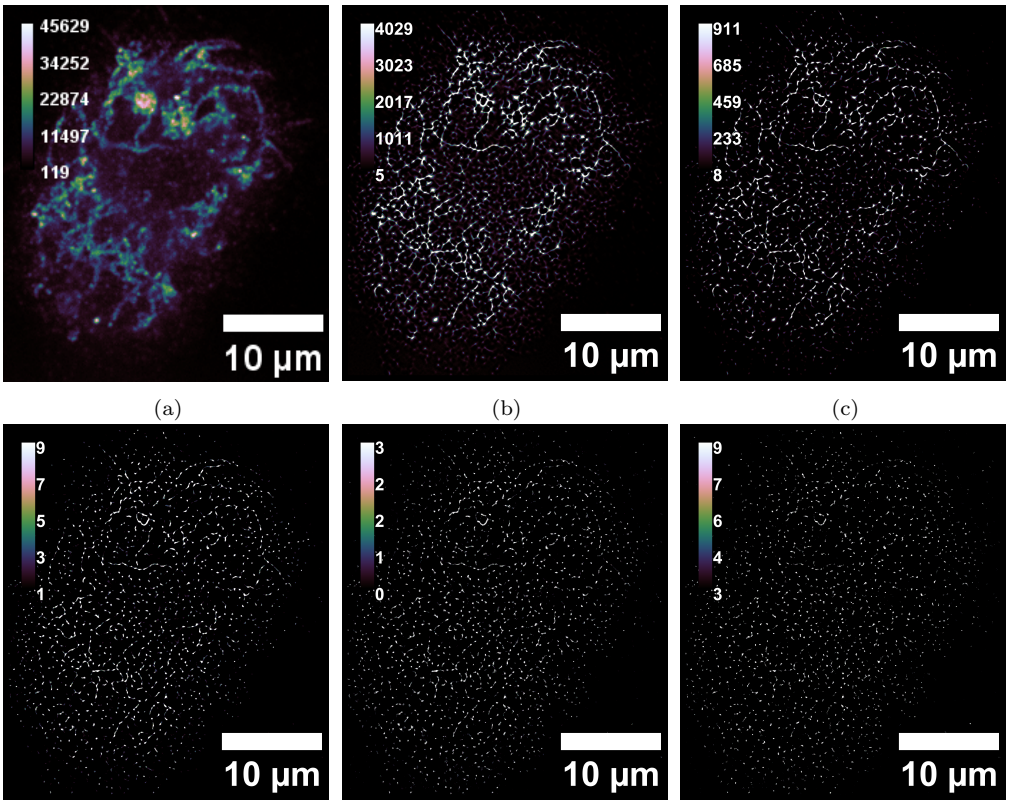

Figure 3.12: **(a)** Andor Revolution XDi spinning disk confocal image of a mock infected human MDM with labelled mitochondria (single frame extracted from 100 raw frames acquired for SRRF reconstruction). Colour bar scale units are counts per 1.5 ms. The following images are SRRF reconstructions using different temporal correlation methods: **(b)** temporal radiality average, **(c)** temporal radiality pairwise product mean, **(d)** temporal radiality auto-cumulant second order, **(e)** temporal radiality auto-cumulant third order and **(f)** temporal radiality auto-cumulant fourth order. Colour bars for the SRRF reconstructions are pixel gray values.

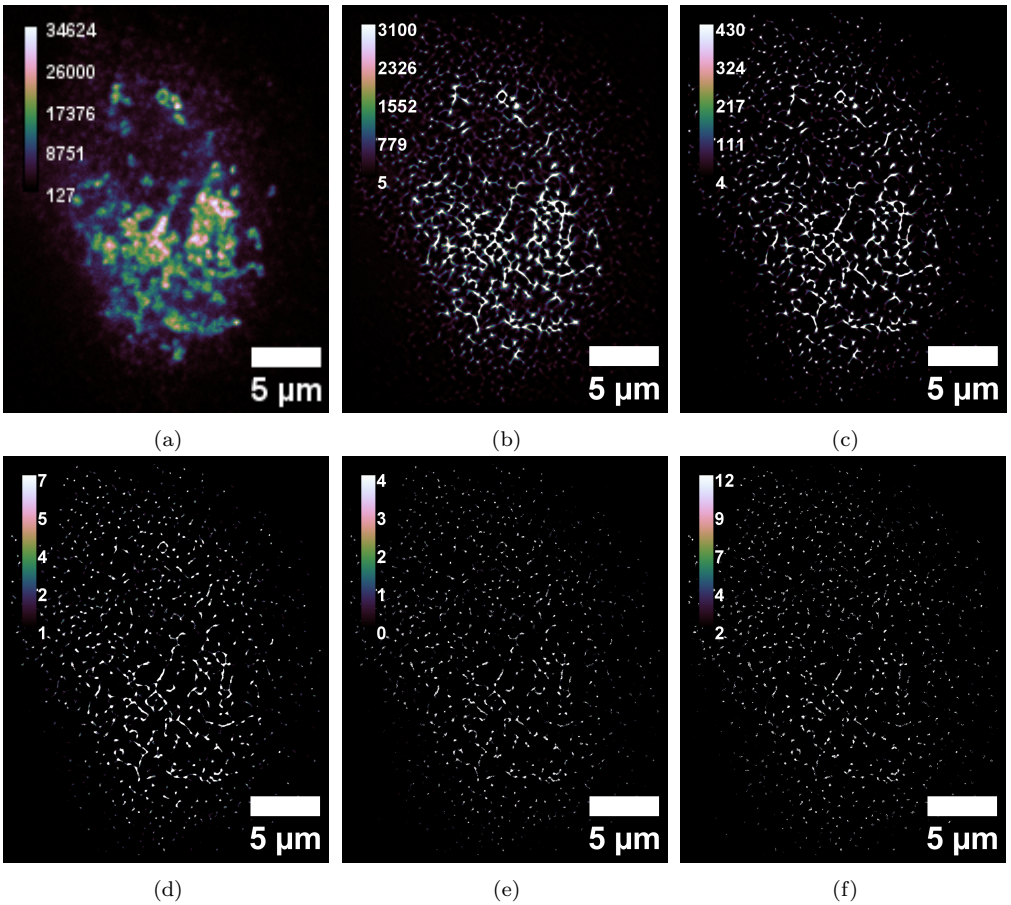

Figure 3.13: **(a)** Andor Revolution XDi spinning disk confocal image of a human MDM challenged with *S. pneumoniae* (4 hour time point) with labelled mitochondria (single frame extracted from 100 raw frames acquired for SRRF reconstruction). Colour bar scale units are counts per 1.5 ms. The following images are SRRF reconstructions using different temporal correlation methods: **(b)** temporal radiality average, **(c)** temporal radiality pairwise product mean, **(d)** temporal radiality auto-cumulant second order, **(e)** temporal radiality auto-cumulant third order and **(f)** temporal radiality auto-cumulant fourth order. Colour bars for the SRRF reconstructions are pixel gray values.

3.4 Effect of Image Aberrations on SRRF Reconstructions

We wanted to assess the effect of image aberrations on SRRF reconstructions of human MDM samples with labelled mitochondria. We hypothesised that carrying out an aberration correction on an image plane would decrease reconstruction errors shown in a SQUIRREL error map, increase the SQUIRREL RSP value and decrease the SQUIRREL RSE value. To investigate this, I acquired 100 raw frames of an image

plane of a human MDM sample with labelled mitochondria (Alexa Fluor 488) on our custom AO confocal microscope detailed in section 3.1.2. I then performed an AO aberration correction, correcting for modes 5 - 10 (Zernike Noll index) using the filtered peak intensity metric. Then subsequently acquired another 100 raw image frames with the AO correction applied. Figures 3.14(a) and 3.14(d) shows a single raw frame from the non AO corrected and AO corrected data respectively. Figures 3.14(b) and 3.14(e) show the corresponding SRRF reconstructions using settings: Ring Radius 0.5, Radiality Magnification - 10, Axes in Ring - 8, and the TRPPM temporal analysis method. The raw data sets were laterally drift corrected using the NanoJ-Core Drift Correction [84] ImageJ/Fiji plugin before SRRF reconstruction. SQUIRREL error maps were then generated using the NanoJ-SQUIRREL ImageJ/Fiji plugin with the first frame of the raw image data set being used as the diffraction limited reference image (figures 3.14(c) and 3.14(f)).

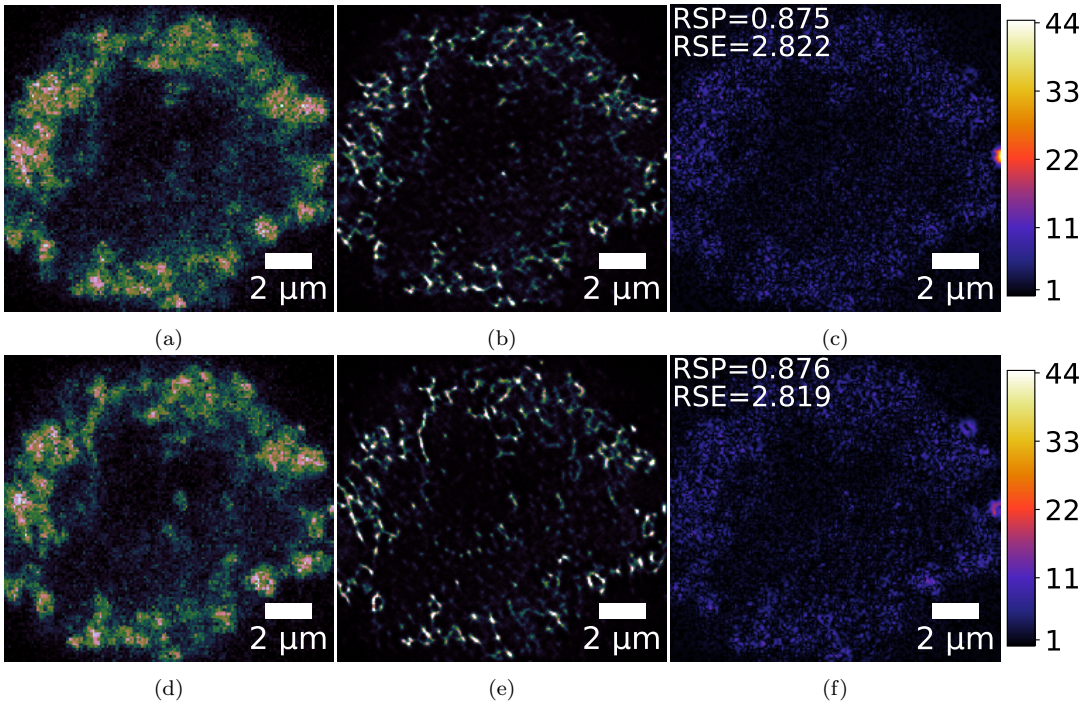

Figure 3.14: Raw image frame acquired on our custom AO confocal microscope in section 3.1.2 of a mock infected human MDM, where mitochondria were labelled with Alexa Fluor 488, from **(a)** a non AO corrected data set and **(d)** an AO corrected data set (corrected for modes 5 - 10 (Zernike Noll index using the metric filtered peak intensity). **(b)** and **(e)** are SRRF reconstructions of the data sets in **(a)** and **(d)** respectively. **(c)** and **(f)** are SQUIRREL error maps for the SRRF reconstructions in **(b)** and **(e)** respectively.

It can be seen from the error maps that across the map the errors remained of similar magnitude, apart from the hot spot towards the right hand side of the image, which was reduced in the AO corrected reconstruction. There was also minimal change in the RSP and RSE values. The RSP value for the AO corrected reconstruction only increased by 0.1%, and the RSE value only decreased by 0.1%.

I repeated this experiment on a different sample on a different day to see if the results were similar or different. The full image plane of the human MDM in the second sample is shown in figure 3.15(a). The yellow box highlights the region of the cell used to acquire images for SRRF and SQUIRREL. The smaller region was used to reduce drift whilst performing the image acquisition and AO correction by reducing scanning time. **(b)** shows a higher resolution image of the smaller ROI. As before, 100 raw image frames of the ROI were acquired (figure 3.15(c)) before performing the same AO aberration correction routine as the previous data set and acquiring another 100 raw frames with the AO correction applied (figure 3.15(f)). Figures 3.15(d) and 3.15(g) show the SRRF reconstructions, using the same settings as for the first data set, for the non AO corrected and AO corrected data respectively. Finally, figures 3.15(e) and 3.15(h) show the corresponding SQUIRREL error maps, including the RSP and RSE values, for the SRRF reconstructions, again using the first frame in the raw data sets as the diffraction limited reference images. The raw data sets were drift corrected as before, before producing SRRF reconstructions.

Again the magnitude of the errors in the SQUIRREL maps appeared relatively similar for both the non AO corrected and AO corrected reconstructions. The improvement in the RSP value for the AO corrected reconstruction was only 0.7% and the reduction in the RSE value was however larger at 4.4%. Due to the DM malfunctioning and delays with implementing a new one, I was unable to acquire any more data sets to investigate further. These two data sets would suggest, given our hypothesis, that the level of aberrations present in the non AO corrected images are not of a significant enough magnitude that when corrected, would significantly improve SRRF reconstructions according to the SQUIRREL algorithm analysis. Due to the limited data, I am however unable to draw a definitive conclusion from these results.

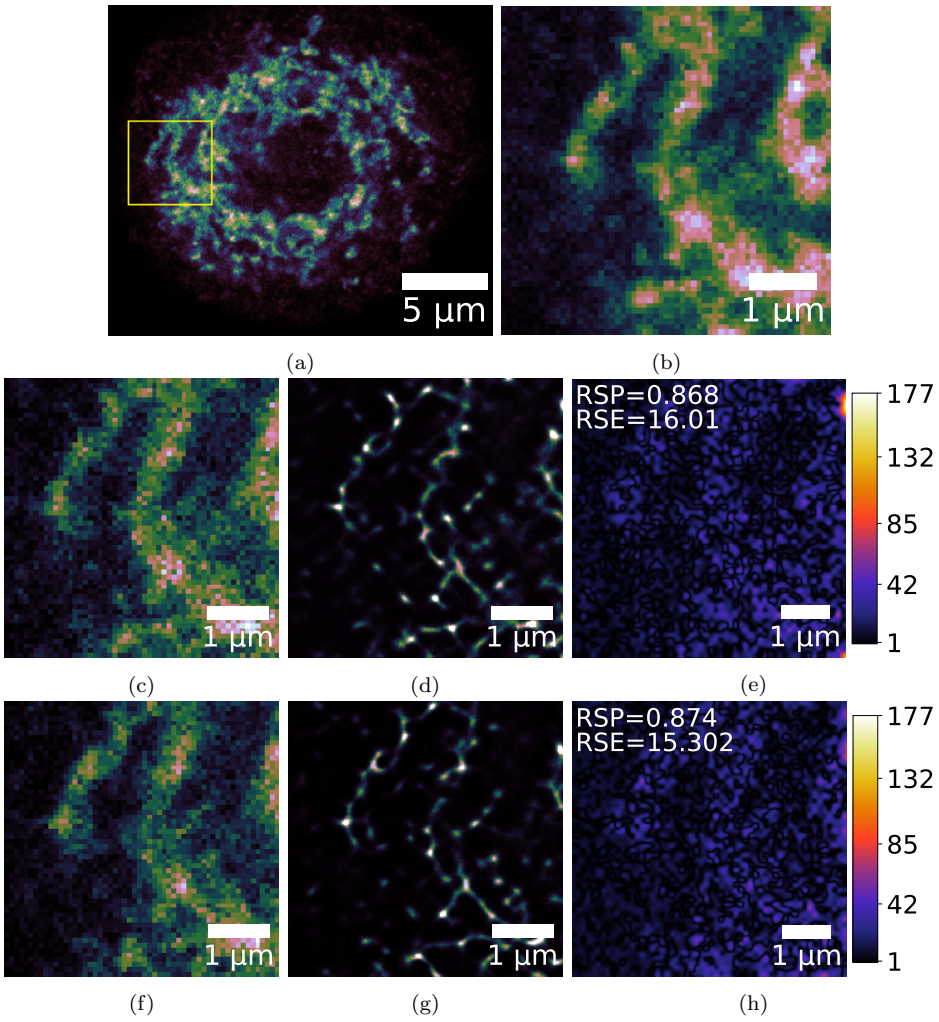

Figure 3.15: **(a)** Raw image frame acquired on our custom AO confocal microscope in section 3.1.2 of a mock infected human MDM where mitochondria were labelled with Alexa Fluor 488. The yellow box highlights the ROI shown in **(b)** which was used for SRRF and SQUIRREL analysis. **(c)** Non AO corrected data set and **(f)** an AO corrected data set (corrected for modes 5 - 10 (Zernike Noll index using the metric filtered peak intensity) of the ROI. **(d)** and **(g)** are SRRF reconstructions of the data sets in **(c)** and **(f)** respectively. **(e)** and **(h)** are SQUIRREL error maps for the SRRF reconstructions in **(d)** and **(g)** respectively.

Looking at the problem in reverse, we wanted to see how intentionally adding aberrations to the system affected the SRRF reconstructions and SQUIRREL error maps. As I was unable to acquire imaging data of MDMs, I utilised a data set previously acquired by Dr Graeme Johnstone and Dr Brian Patton of a nanodiamond sample containing a mix of 40 nm and 100 nm particles. The data was acquired on our custom AO confocal microscope which at the time had been adapted for two-photon excitation

(TPE) microscopy. The details of the sample preparation and microscope adaptation can be found in Johnstone *et al.* [85]. Briefly, a 1070 nm pulsed fibre laser was coupled into the microscope via a 746 nm shortpass dichroic mirror positioned between the beamsplitter and dichroic mirror D in figure 3.3 to provide two-photon excitation. The 746 nm dichroic mirror was already in place in the microscope for coupling in the depletion laser for STED microscopy in the future. The red detection channel in figure 3.3 was used to detect the emitted nanodiamond fluorescence. The microscope optics were not optimised for two-photon microscopy, however coupling the 1070 nm laser into the depletion laser channel on the microscope still allowed two-photon excitation to be achieved.

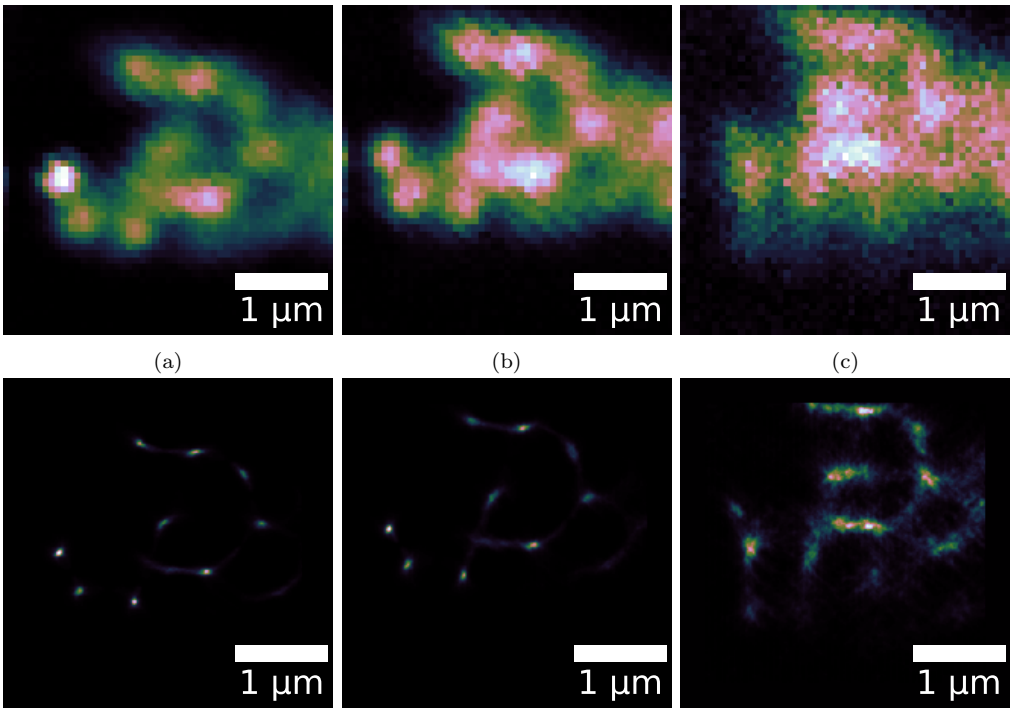

Figure 3.16: **(a)**, **(b)** and **(c)** are single frames from two-photon emission (TPE) microscopy data sets containing 100 raw frames, of samples containing a mix of 40 nm and 100 nm nanodiamonds prepared according to Johnstone *et al.* [85], in the case of no, low and high aberration respectively. Images were acquired by Dr Graeme Johnstone and Dr Brian Patton on our custom confocal microscope, detailed in section 3.1.2, which was adapted for TPE microscopy as in Johnstone *et al.* [85]. I carried out SRRF reconstructions on the data as shown in **(d)**, **(e)** and **(f)** using the following settings: Ring Radius 0.5, Radiality Magnification - 10, Axes in Ring - 8, Temporal Analysis - Temporal Radiality Pairwise Product Mean (TRPPM).

Figures 3.16(a), 3.16(b) and 3.16(c) show single frames from the SRRF data sets acquired for the no aberration, low aberration (1 unit each of modes 6 and 7 (Zernike Noll index)) and high aberration (3 units each of modes 6 and 7 (Zernike Noll index)) cases respectively. Figures 3.16(d), 3.16(e) and 3.16(f) show my corresponding SRRF reconstructions using settings: Ring Radius 0.5, Radiality Magnification - 10, Axes in Ring - 8, and TRPPM temporal analysis.

I also performed an FRC resolution analysis on the SRRF reconstructions. The raw data sets were split into two by deinterleaving the odd and even frames, drift correcting each half using the NanoJ-Core Drift correction [84] ImageJ/Fiji plugin before producing a SRRF image from each half. The two SRRF images from each data set were used to produce the FRC curves shown in figure 3.17 where a half-bit threshold was used to determine the resolutions. Using the SRRF image real-space pixel size of 7 nm, the calculated resolutions from the intersection of the FRC curves with the threshold curve were 33 nm, 41 nm and 175 nm for the no, low and high aberration cases respectively.

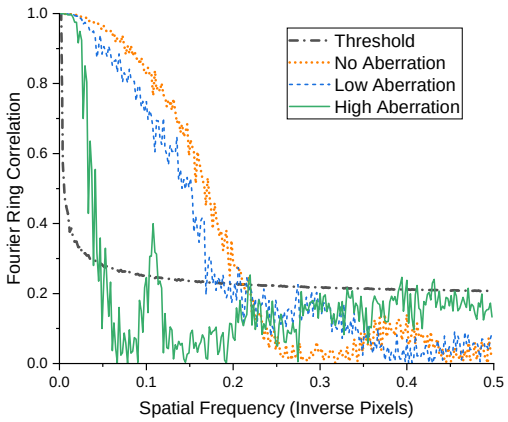

Figure 3.17: FRC curves for the SRRF reconstructions in figure 3.16 for the no aberration (orange), low aberration (blue) and high aberration (green) cases. The threshold curve (black) is shown where the threshold used is a half-bit of information per pixel, where the pixel real-space size is 7 nm.

I then carried out a SQUIRREL error map analysis on the SRRF reconstructions to see how the intentionally applied aberrations affected the errors. Figure 3.18 shows the diffraction limited reference image, the SRRF reconstruction and the SQUIRREL error maps for each aberration case using the first frame of each raw data set for the

diffraction limited reference image. From our hypothesis, we expected that SQUIRREL would show larger errors for the data sets with higher aberrations. However, figure 3.18 in fact shows the opposite.

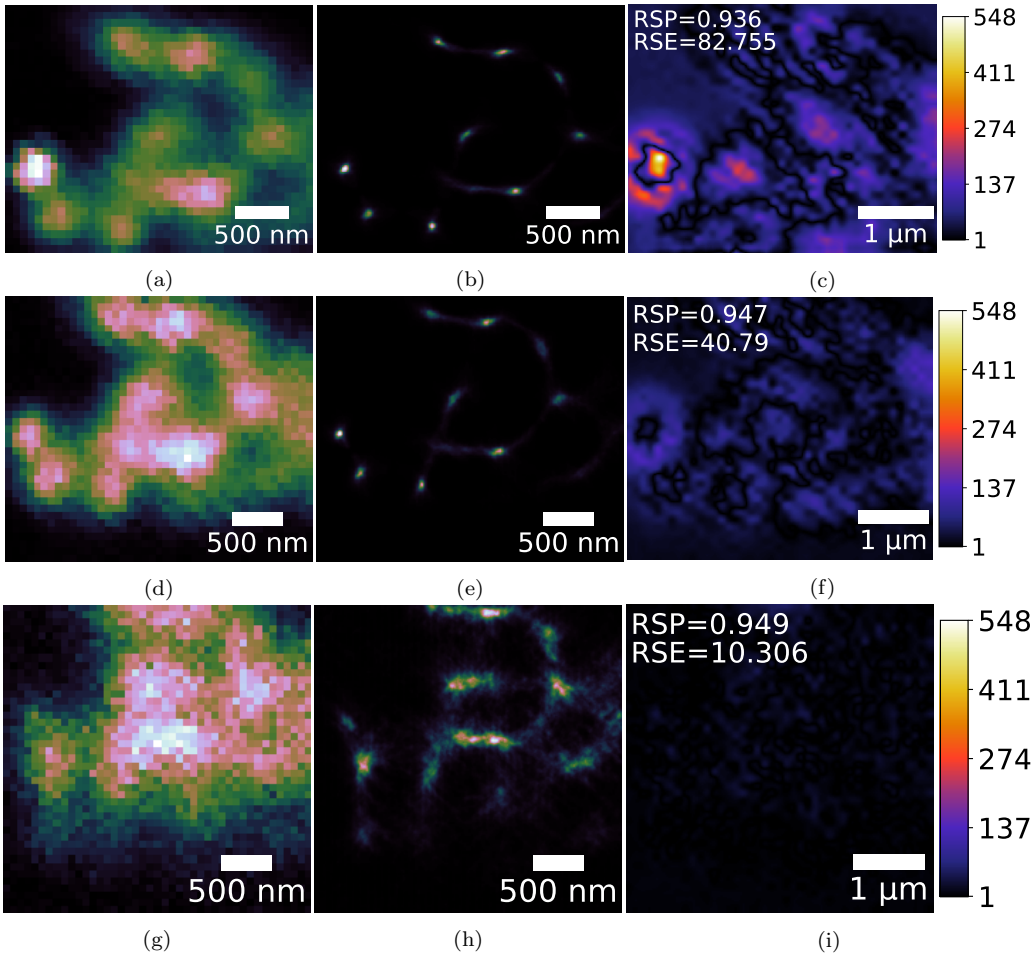

Figure 3.18: SQUIRREL error analysis of the SRRF reconstructions in figure 3.16. Column one is the diffraction limited reference image used, where in this case **(a)** is a single frame from the no aberration data set, **(d)** is a single frame from the low aberration data set and **(g)** is a single frame from the high aberration data set. Column two is the SRRF reconstructions for the **(b)** no, **(e)** low and **(h)** high aberration cases. Column three is the SQUIRREL error maps including the global RSP and RSE values for the **(c)** no, **(f)** low and **(i)** high aberration cases. The images in each row have been cropped and registered to one another in the NanoJ-SQUIRREL plugin.

The error map for the high aberration case (figure 3.18(i)) shows the lowest magnitude of errors, the highest RSP value and the lowest RSE value. From these results it became apparent that, in the case of the analysis in figure 3.18, if using an aberrated raw image from the data set which the SRRF image was reconstructed from as the

diffraction limited reference image for SQUIRREL, then SQUIRREL is comparing an aberrated image with an aberrated image and will not be able to tell you about any errors due to aberrations. I suggest that the reduction in errors produced by SQUIRREL in figure 3.18 in the case of high aberration, could be down to reconstructing a lower resolution data set, whereas higher resolution reconstructions would be more sensitive to errors, as in figure 3.18(c).

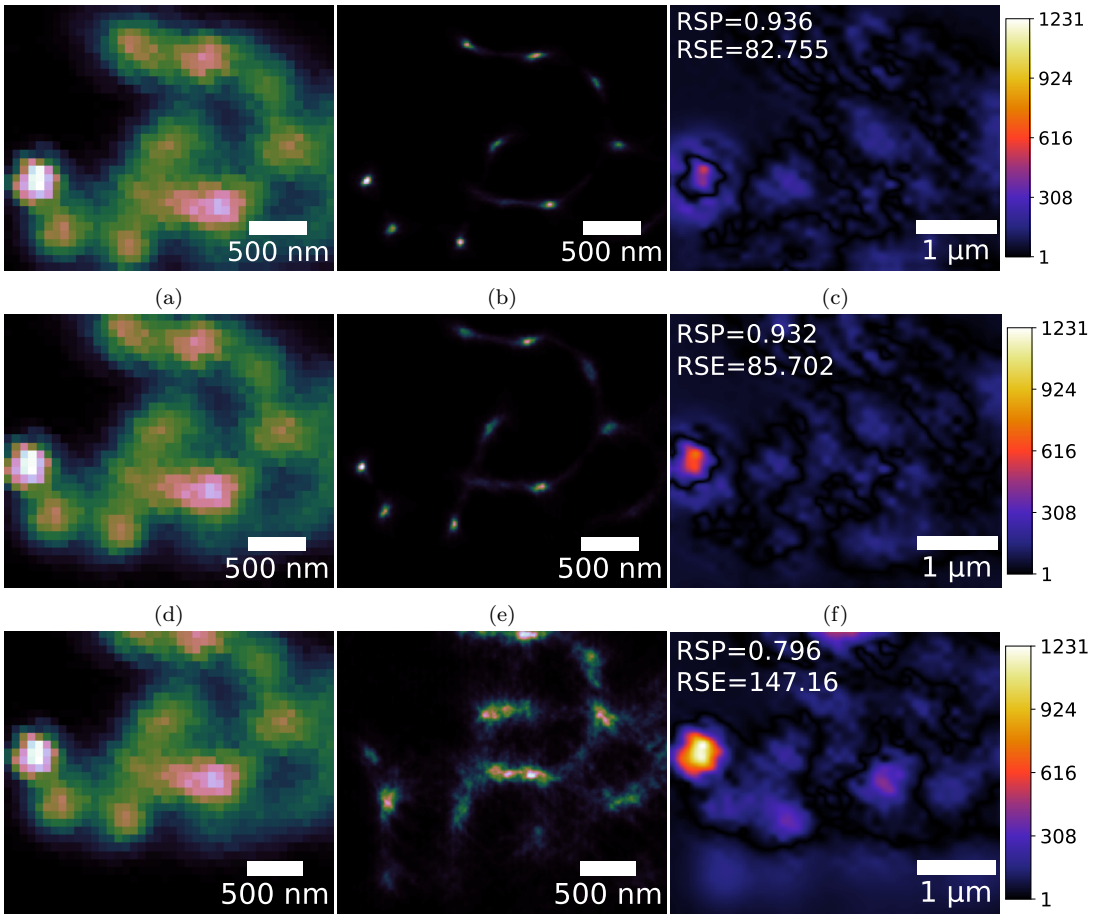

Figure 3.19: SQUIRREL error analysis of the SRRF reconstructions in figure 3.16. Column one is the diffraction limited reference image used, where in this case **(a)**, **(d)** and **(g)** are all from the no aberration data set. Column two is the SRRF reconstructions for the **(b)** no, **(e)** low and **(h)** high aberration cases. Column three is the SQUIRREL error maps including the global RSP and RSE values for the **(c)** no, **(f)** low and **(i)** high aberration cases. The images in each row have been cropped and registered to one another in the NanoJ-SQUIRREL plugin.

I then carried out a second SQUIRREL analysis on the data sets and SRRF reconstructions, but this time using a single frame from the no aberration raw data set

as the diffraction limited reference image in each case. As expected, from figure 3.19, the magnitude of the errors in the SQUIRREL error map were greater for the high aberration case, including a greater RSE value and lower RSP value, compared to the no and low aberration cases. Comparing a highly aberrated SRRF reconstruction with a non aberrated diffraction limited reference confirms that aberrations negatively affect SRRF reconstructions of samples.

The analysis in figures 3.18 and 3.19 tells us that SQUIRREL cannot be used as a tool to assess the quality of SRRF reconstructions specifically after aberration correction compared to non corrected data, however does show that aberrations have a detrimental effect. The slight improvement seen in the SQUIRREL error maps and RSP and RSE values in figures 3.14 and 3.15 were not significant, however further data sets could be acquired to fully confirm our findings.

Since the data in this section was acquired, a new deformable mirror has been implemented into the microscope, and through a combination of improved alignment of the imaging optics of the microscope and improved sample preparation, I was able to acquire the image in figure 3.20 of a mock infected human MDM where mitochondria were labelled with ATTO647N, where the quality of imaging appears to be improved. The sample was prepared by Katharin Balbirnie-Cumming at the University of Edinburgh. I have produced a SRRF reconstruction of the data set, however there was a misalignment with the DM and so I was unable to carry out an AO correction. Due to time constraints I was not able to continue this work however sections 3.2, 3.3 and 3.4 provide a basis for future investigation and considerations when applying AO aberration corrections and the SRRF algorithm to human MDM image data sets.

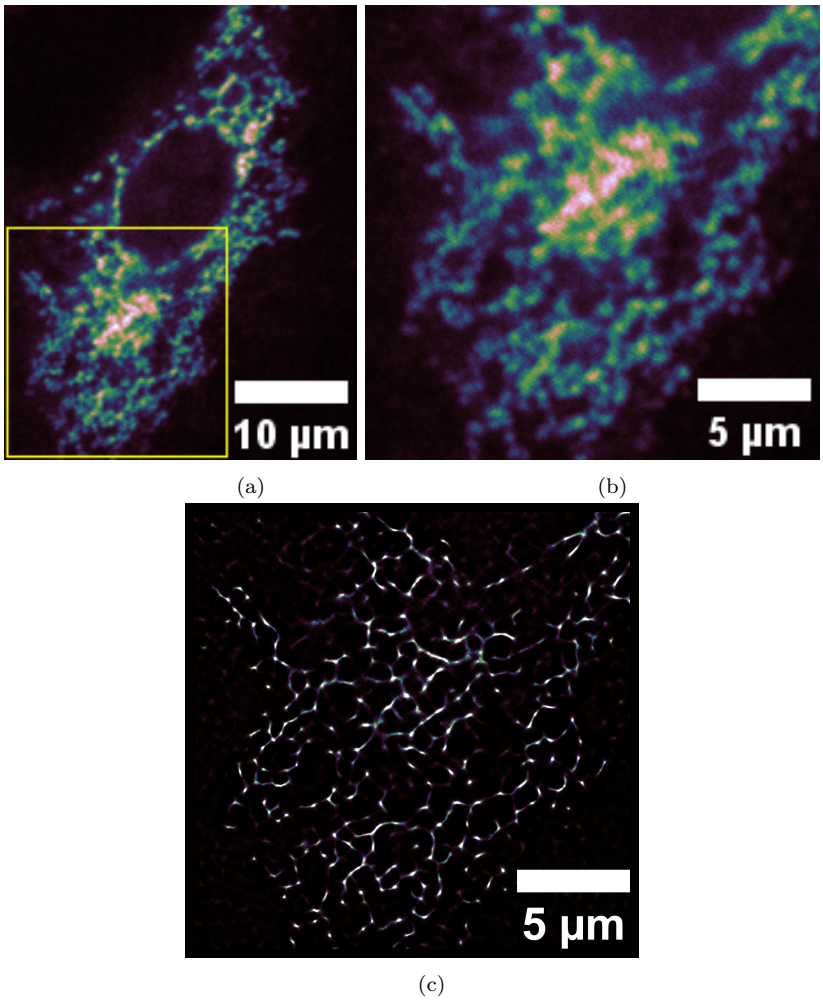

Figure 3.20: **(a)** Raw image frame acquired on our custom AO confocal microscope, detailed in section 3.1.2, of a mock infected human MDM with labelled mitochondria (ATTO647N). Sample prepared by Katharin Balbirnie-Cumming at the University of Edinburgh. **(b)** Higher resolution image of the highlighted ROI in **(a)**. **(c)** SRRF reconstruction using settings: Ring Radius 0.5, Radiality Magnification - 10, Axes in Ring - 8, and TRPPM temporal analysis.

3.5 TIE Microscopy of Macrophages

As our research group has previously shown the ability of the TIE to distinguish between different types of algae based on quantitative differences in refractive index [104], we wanted to apply this computational QPI method to imaging human MDMs. Advantages, as detailed in section 3.1.3, are that TIE microscopy is a label free technique which does not require extensive or complex hardware, only a method of acquiring

brightfield images at different axial positions within the sample. As it is also an open-source method, if the technique was able to determine quantitative information about macrophage samples, it would enable greater accessibility to quantitative imaging studies.

Using the wide area detection path on our custom AO confocal microscope (figure 3.3), I carried out initial imaging studies to determine the applicability of the TIE to imaging human MDM samples. Figure 3.21 shows one of the acquired data sets, where the raw brightfield images above the focal plane, at the focal plane and below the focal plane are included. The axial spacing between each plane was 0.53 μm. The resulting TIE image is figure 3.21(d), where the increase in contrast can be seen. Another advantage of TIE is the inherent removal of background artifacts such as dust, as can clearly be seen between the brightfield and TIE images in figure 3.21.

Paganin *et al.* [113] discusses that there is a trade off to consider when choosing the axial spacing between the brightfield images. A smaller spacing will provide greater spatial resolution in the TIE image and must be small enough for the intensity difference between the above and below images to be proportional to $\partial I/\partial z$. However smaller spacings will also be more sensitive to noise and so the spacing must also be large enough to overcome noise. Figure 3.22 shows a TIE data set of the same cell in figure 3.21, but with an axial spacing between the brightfield images of 2.5 μm. The decrease in spatial resolution can be seen in the resulting TIE image compared to figure 3.21(d) from using a larger spacing. Paganin *et al.* [113] have proposed a method for determining the optimal axial image spacing, however we did not explore the method in this research project.

Figures 3.21 and 3.22 used the Python code from Davis [11] and Grant *et al.* [104] to produce the TIE images, which, as described in section 3.1.3, used three brightfield images to estimate $\partial I/\partial z$. This method assumes a linear change in intensity between the image frames. Soto *et al.* [114] have shown that using a greater number of axially separated image planes provides a more accurate estimation of $\partial I/\partial z$. However, Waller *et al.* [115] explains if the range of planes used in z exceeds the linear range of defocus, then errors will occur. To address the problem, Jingshan *et al.* [116] have proposed a

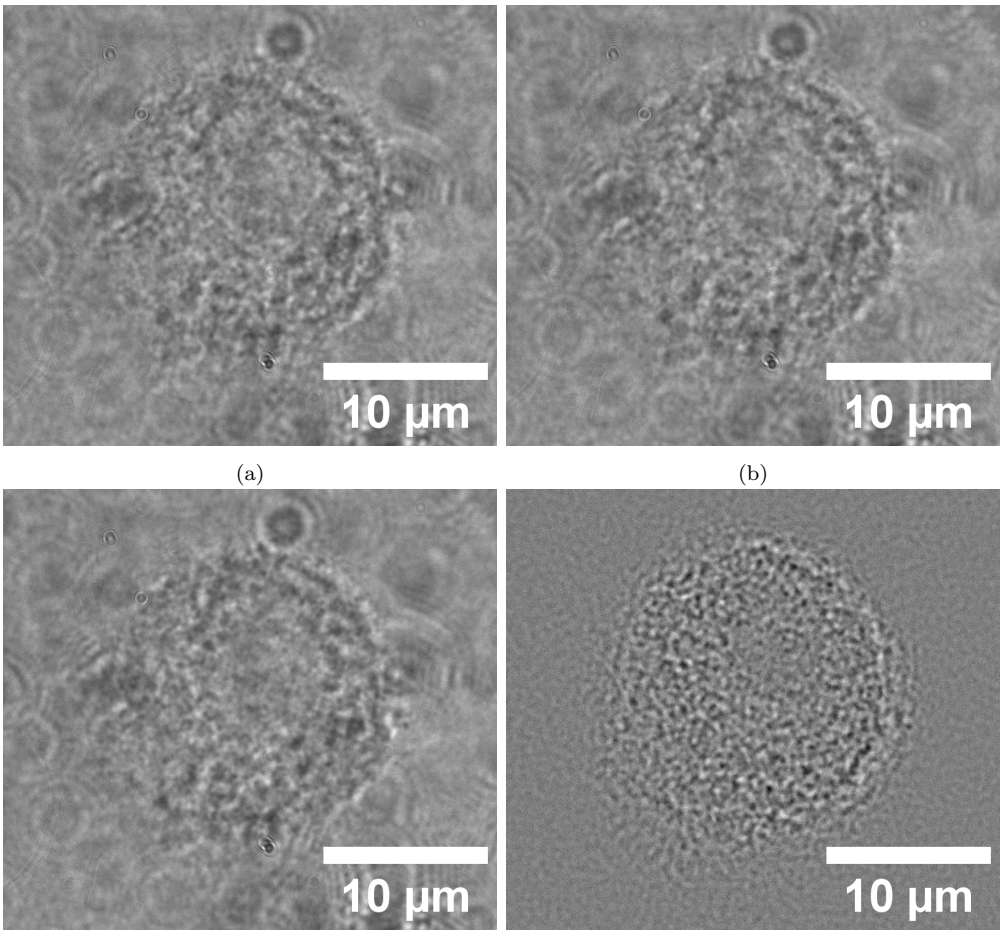

Figure 3.21: TIE microscopy data set of a human MDM where **(a)** is the brightfield image above the focal plane, **(b)** is the brightfield image at the focal plane, and **(c)** is the brightfield image below the focal plane. The axial spacing between the images is 0.53 μm and they were acquired on the wide area detection path of our custom AO confocal microscope (figure 3.3). **(d)** is the resulting TIE image.

phase recovery method from an axial image stack which is based on fitting the nonlinear intensity of each pixel vs z in Fourier space. The advantage of fitting to plots in Fourier space is the curves have a sinusoidal behaviour, whereas the plots in real space do not fit well to any particular function. Thus a good derivative estimate is provided which reduces problems of nonlinearity and noise. Fitting is carried out using Gaussian process (GP) regression which also doesn't require image planes to be spaced equally along the optical axis. In fact, Jingshan *et al.* [116] showed that exponentially spaced z stacks provided sufficient data for fitting and greatly reduced the number of images required. The GP regression TIE code is provided in a Matlab GUI [117].

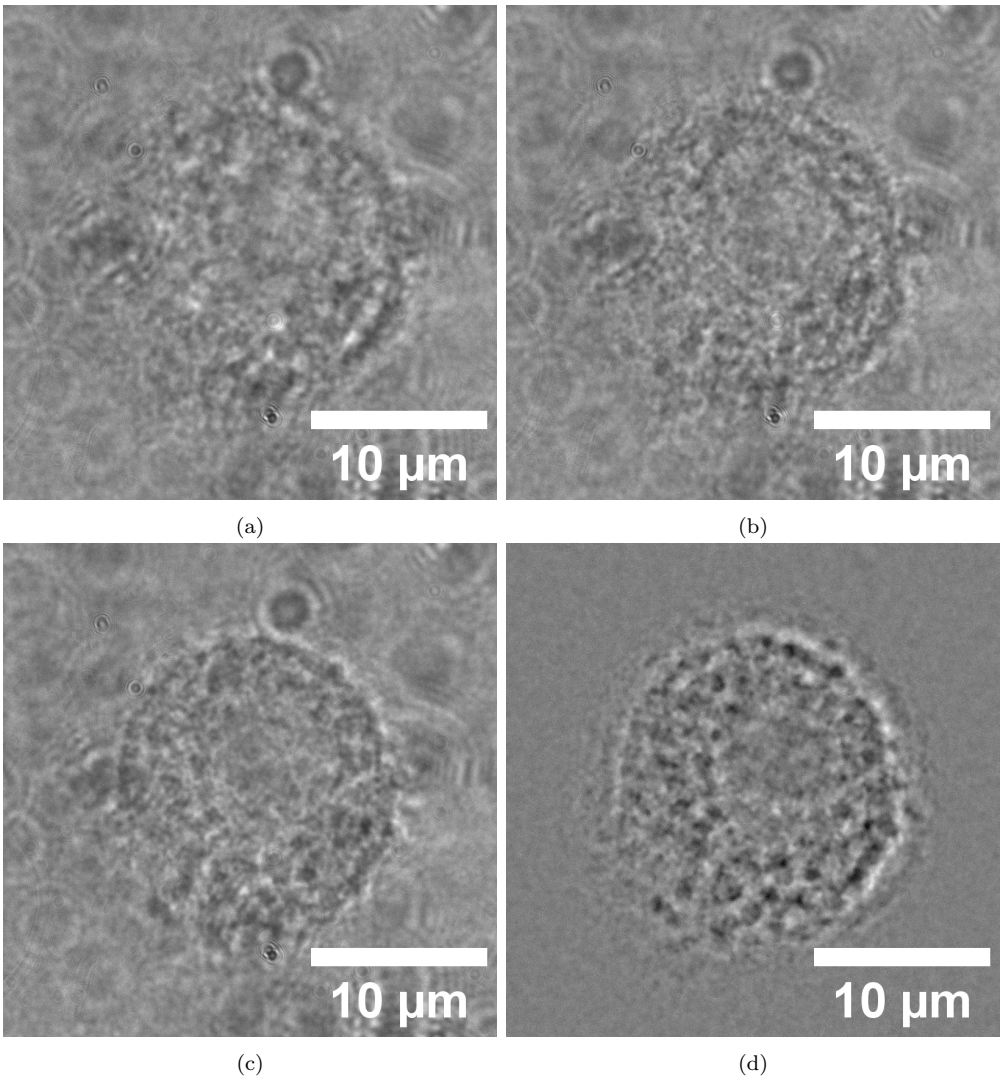

Figure 3.22: TIE microscopy data set of a human MDM where **(a)** is the brightfield image above the focal plane, **(b)** is the brightfield image at the focal plane, and **(c)** is the brightfield image below the focal plane. The axial spacing between the images is 2.5 μm and they were acquired on the wide area detection path of our custom AO confocal microscope (figure 3.3). **(d)** is the resulting TIE image.

To try the GP regression method, I acquired two image stacks of the same cell in figures 3.21 and 3.22. The first ranged in z from $-6.36\,\mu$m to $+6.36\,\mu$m in equal steps of $0.53\,\mu$m. The second ranged in z from $-3.12\,\mu$m to $+3.12\,\mu$m in exponentially spaced steps on either side of the focal plane (z = $\pm 0.16\,\mu$m, $\pm 0.29\,\mu$m, $\pm 0.53\,\mu$m, $\pm 0.96\,\mu$m, $\pm 1.73\,\mu$m and $\pm 3.12\,\mu$m), calculated using the method in Jingshan *et al.* [116]. Figure 3.23 shows the TIE result for the two stacks using the GP regression method. It can be seen that using a smaller z range and exponentially spaced planes provides a very

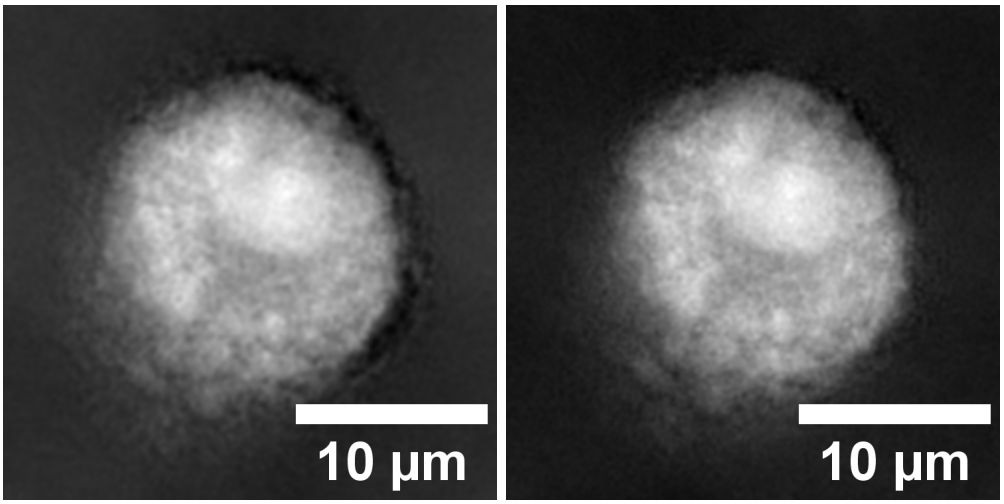

(a) (b)

Figure 3.23: TIE microscopy data set of a human MDM. Data analysis was carried out using the Open Source PhaseGUI [117]. **(a)** GP regression TIE - equally spaced z stack. **(b)** GP regression TIE - exponentially spaced z stack.

similar result to using a greater z range and equally spaced planes. The result is very different to that in figures 3.21 and 3.22. In figure 3.23 the nucleus can be clearly seen in both cases. However, like figures 3.21 and 3.22, other specific structures in the cell are not immediately apparent. A similar result for TIE applied to differential interference contrast (DIC) images of a human macrophage sample is shown in Kou *et al.* [118]. Macrophages may not be a sufficiently thin enough phase object to distinguish, for example, mitochondria in the phase image. I obtained the cheek cell raw image data set in Jingshan *et al.* [116] from Prof. Laura Waller at the University of California, Berkeley, to provide a comparison to the macrophage results.

The cheek cell image set is a brightfield z-stack with a range from $-256\,\mu$m to $+256\,\mu$m in equally spaced $4\,\mu$m steps. Figures 3.24(a), 3.24(b) and 3.24(c) show three of the raw brightfield images at $+4\,\mu$m, $0\,\mu$m and $-4\,\mu$m respectively, where already in the brightfield images distinguishable structures within the cells can be seen. Figure 3.24(d) shows the TIE image using the finite difference method of estimating the derivative (section 3.1.3) and the three brightfield images shown. Figure 3.24(e) shows the TIE image using the GP regression method described in Jingshan *et al.* [116] and the Open Source PhaseGUI [117].

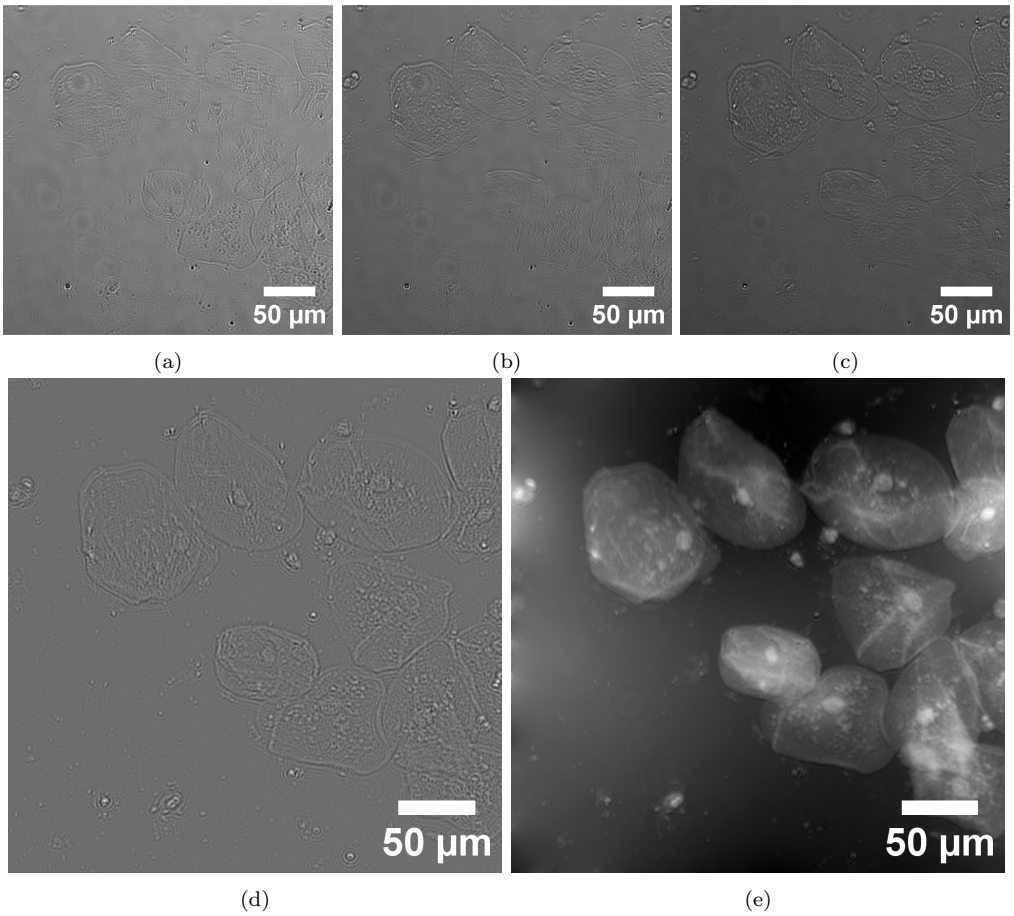

Figure 3.24: TIE results using the image data set of the cheek cell sample from Jingshan *et al.* [116]. The first three images are the raw brightfield images **(a)** above the focal plane ($+4\,\mu$m), **(b)** at the focal plane, and **(c)** below the focal plane ($-4\,\mu$m). **(d)** TIE result using the finite difference method of estimating the derivative as described in section 3.1.3. **(e)** TIE result using the GP regression method and the full equally spaced z stack from $-256\,\mu$m to $+256\,\mu$m in $4\,\mu$m steps.

Comparing the results to the macrophage TIE images, in both figures 3.24(d) and 3.24(e) the nuclei and other specific structures within the cheek cells can be seen which could potentially include mitochondria, whereas, as mentioned, in the macrophage images only the nucleus is specifically identifiable. We suggest that macrophages are optically dense cells from our initial TIE imaging studies. Optically dense samples require a model of multiple scattering to adequately reconstruct the phase [119], which developing and implementing was outwith the scope of this research project. However, the development of multiple scattering models to retrieve the phase of thick samples is one of the key research areas of Prof. Laura Waller's research group at the University of

California, Berkeley. In future, a multiple scattering model could increase the amount of quantitative information achievable from TIE images of macrophages. In its current state, the TIE does however enable greater contrast images of macrophages without added labelling.

3.6 Conclusions

This chapter has included initial imaging studies of human MDMs using AO enhanced confocal microscopy for aberration correction, computational super-resolution imaging using SRRF, and computational phase imaging using the TIE. Early work has suggested optimal correction of aberrations when imaging MDMs requires a targeted approach, where regions of interest are determined and an AO correction is calculated for the specific region, as opposed to a global correction for the full image plane across a cell and also across multiple planes spaced in z. Further work needs to be carried out to fully determine best practice and to further investigate which are the dominant types of aberrations which occur when imaging MDMs and whether they arise mainly from the sample itself or from the imaging system. Then, the effect of AO on colocalization studies between MDMs, *S. pneumoniae* and mROS can be investigated.

Initial imaging studies applying SRRF to confocal data sets has been investigated as a potential alternative to conventional super-resolution techniques which require complex and expensive hardware. The use of an open-source computational tool like SRRF has the potential to increase accessibility to super-resolution imaging studies of the host responses of MDMs to *S. pneumoniae* in areas which are resource limited. I have shown SRRF reconstructions of mock infected and challenged MDMs with labelled mitochondria. In future, SRRF could be applied to multicolour fluorescence images to look at the localization of bacteria in relation to mitochondria. I also showed the data we acquired did not contain sufficient temporal radiality fluctuations to allow the use of higher order temporal analysis methods in SRRF. Therefore, as discussed, further work is required to either label the sample with a photoswitchable fluorophore, or to vary the intensity of illumination across frames.

I have also shown the effect of aberrations on SRRF reconstructions of both human MDM and nanodiamond samples. It is clear that aberrations have a detrimental effect, but I have shown that SQUIRREL error mapping is likely unable to quantify the improvement and reduction in errors of the SRRF reconstruction after aberration correction due to the need to use an unaberrated diffraction limited reference image. Further data needs to be acquired to fully confirm. Fourier ring correlation was used to show that the resolution of aberrated images is larger than that of non-aberrated images. FRC gives a reliable global resolution measurement which has been shown to agree with FWHM measurements [85], however the value may not be true across the full image, as discussed in Johnstone *et al.* [85]. The NanoJ-SQUIRREL ImageJ/Fiji plugin has implemented FRC on a more local basis, splitting the image into blocks to produce an FRC map to try and address this problem [82]. As discussed in section 3.1.1, resolution measurement and definition in super-resolution microscopy is still an ongoing problem.

Finally, I have shown initial TIE phase imaging of human MDMs, another computational and open-source technique which could have the potential to increase accessibility to quantitative imaging studies including phase and refractive index measurements, supplementing information obtained from fluorescence microscopy. I have highlighted the trade offs between smaller and larger spacings between raw image frames used in the TIE calculation and investigated methods of using greater numbers of frames, including equally and exponentially spaced z-stacks. We believe that macrophages are optically dense samples and further modelling and analysis, including multiple scattering, must be included to obtain quantitative measurements from the TIE images.

Chapter 4

M4All Hardware Design

4.1 Introduction

The third aim of this research project was to develop a low-cost and open-source 3D printable microscopy system to increase accessibility to advanced microscopy techniques. More specifically our focus was on frugal innovation to increase availability of imaging hardware at sites of high *S. pneumoniae* infection burden in developing countries.

In targeted host based therapy if the host response is to be modified as an alternative to conventional antimicrobials, there must first be a method of calibrating the host responses to bacteria and learning what is optimal for bacterial clearance in order for immunomodulation to effectively improve responses. Therefore low-cost microscopes could aid in learning more about macrophage host responses to the pneumococcus and determining optimal responses in a research setting. Not only does low-cost mean reduced financial barriers but an open-source 3D printable microscopy system would also allow for rapid prototyping and development of different microscopy techniques to test within the lab to generate quantitative imaging data of macrophages. We also envision a 3D printable incubator microscope for low-cost live cell imaging to address challenges with temporal resolution when imaging macrophage host responses. Low-cost microscopes could also in future be included in a strategy of personalised medicine within a hospital/clinic, where the idea is an individual's response needs to

be accurately measured and then modified. Low-cost microscopes have the potential to enable this at sites of high infection in developing countries by increasing accessibility to advanced microscopy techniques for testing patient samples. For use as a medical device however, the microscopes would be required to be certified after rigorous testing and be produced according to ISO (International Organization for Standardization) standards by a manufacturer.

This chapter will give a review of currently available open-source microscopy hardware in the community and discuss the development of the hardware for our system which we have named M4All: MultiModal Modular Microscopy for All.

4.1.1 3D Printing

With the advent of readily available, high quality 3D printing technology there has been a growth in open-source hardware development over the past few years, particularly in the field of microscopy. 3D printing is an additive manufacturing technique and allows for rapid prototyping of custom designs from computer aided design (CAD) software. There are different types of 3D printers available but they all work on the principle of building up a 3D model layer by layer. The most commonly known and used 3D printers in microscopy hardware development are fused deposition modelling (FDM) and stereolithography (SLA) printers.

FDM printers use a bottom-up configuration where layers of heated plastic filament, such as polylactic acid (PLA), are extruded onto a heated print bed to build up the model. If support is needed for certain sections of the model, for example for overhangs and bridges, a second removable material is used, such as polyvinyl alcohol (PVA). SLA printers on the other hand are still most commonly configured as a bottom-up approach, however the build plate faces down into a bath of photosensitive resin. A UV laser below the resin bath, cures the resin onto the build plate layer by layer as the build plate is moved up. Supports are printed as a thin resin scaffold which are clipped off post print. SLA printers have the greatest printing precision [120], with capability to print small detailed features as the print resolution is defined by the focal spot of the curing laser. SLA printing is however more costly than FDM printing and has a

smaller selection of available printing materials.

4.1.2 Open-Source Microscopy Systems

A non-comprehensive but extensive and useful list of open-source microscopy hardware projects can be found at the OpenMicroscopy GitHub repository [121]. There are numerous projects that are not focused on 3D printable hardware, such as easySTORM [122], Foldscope [123], Incu-Stream [124] and mesoSPIM [125]. However, I focus here on the most notable 3D printing based projects that have emerged in the community in recent years.

Modular Systems

Modular 3D printable systems offer advantages with flexibility and the capability to design and build microscopes for the users specific application. The most notable modular systems are miCube [126], LifeHack [127], μCube [128] and UC2 [67].

Both miCube and LifeHack are on the more expensive scale of open-source microscopy systems as they are only partially 3D printable systems and include commercial parts, with miCube starting at €20k [129] and LifeHack at £150k [127]. The miCube microscope has a main CNC milled cube which contains the sample stage, objective lens and filters required for fluorescence microscopy. There is then an excitation path and an emission path, both of which connect to the main cube and consist of mainly 3D printed components and commercial optics and optomechanics. The miCube microscope has been used for in vivo visualisation of dCas9 [126]. Advantages of miCube include easy optical alignment, light tight design and ability to image in multiple microscopy modes, namely epifluorescence, highly inclined illumination (HiLo) and total internal reflection (TIR) [126]. Limitations depending on the user could include the need for commercial and CNC milled parts and cost.

The LifeHack microscope has three main modules [127]. The first is the excitation module which consists of four lasers all coupled into a shutter on an optical breadboard via free space optics in commercial optomechanics [130]. The second module is the beam expansion module to couple the excitation light into the main body, which is the

third main module. The beam expansion module again consists of commercial optics and optomechanics fixed to a commercial optical rail [131]. The main body includes the sample stage and imaging optics and consists of both commercial and 3D printed parts [132]. The LifeHack microscope is an advanced system requiring experience of optical alignment, limiting usability to those with the required knowledge.

On the lower end of the price scale is μCube [128] and UC2 [67]. Both are fully 3D printable microscope bodies which hold commercial optics in a modular cube system. Both projects also endeavour to increase accessibility to custom microscopy hardware and create a standard for the design of low-cost 3D printed optical systems. The μCube system consists of a hollow cube and different faces which are screwed into the walls of the cube [128]. The faces have different designs to hold different optical elements within the cubes and cubes are attached to one another using screws to build up an optical system. Alignment is made simple as the geometrical design of the system means the cubes define the optical paths. However, this could also be a limitation for some users who may require greater flexibility in the position of the optical elements and greater degrees of freedom for alignment.

The UC2 microscope system is similar and has had a number of different version updates to the core design since it was first released to the community. Each version is based on hollow cubes with cube inserts to hold optical elements. A note on UC2 version history can be found on the project's GitHub repository [133]. The first version, v0, consisted of a square base plate with which a ball magnet was pressed into on each corner. The lid of the hollow cube was screwed into the cube and the screws magnetically connected to the ball magnets on the base plate. Larger base plates could be printed to build up a system of cubes. The cube itself had 6 mm holes for a 30 mm cage system to hold the optical element inserts. A second system for holding optical inserts was also included where each corner of the cube had slots to slide inserts into. Figure 4.1 illustrates the v0 version. Note that version v0 is now deprecated and no longer available on the UC2 GitHub repository.

The second version of the UC2 system, v2, is similar to v0 in that it still uses the screw and ball magnet system, however the cage system was removed and the

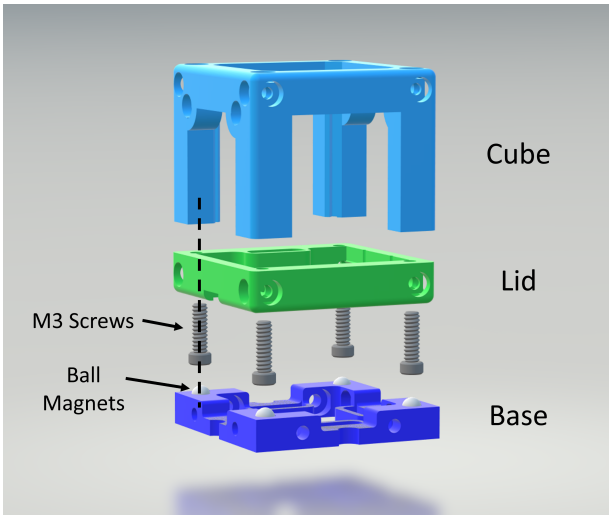

Figure 4.1: UC2 v0 system highlighting the key components of the cube, lid and base plate, where screws connecting the lid and cube magnetically connect to the base plate via ball magnets. Figure was created using STL files originally obtained from the UC2 GitHub repository [133] which were published under the licence CERN Open Hardware Licence v1.2.

method of adding inserts was updated [134]. The v2 files are currently still available to download from the UC2 GitHub repository. Version v2 has been used for a number of applications including in vitro brightfield imaging of the differentiation of human primary monocytes to macrophages [67].

The most up to date version of the UC2 system is v3 [133]. There are two different v3 cubes. The first is a 3D printed cube which is very similar to the v2 cube but has had M5 screws added to the lid to aid with alignment of the ball magnet system on the base. The base plate has been updated to include holes for the M5 screws. The second v3 cube has been designed for injection moulding as opposed to 3D printing. Injection moulding is the process of melting for example, polymers and thermoplastics, and setting the melted liquid into a metal molding cast. Injection molding is more costly than 3D printing, however the technique can produce highly accurate models. Using injection molding has allowed UC2 to create a cube which can be assembled much quicker than the 3D printed version as the system is assembled without screws. The high accuracy of injection molding allows parts to clip together with ease using a jigsaw system. The base plate is compatible with both the 3D printed and injection molded cubes and therefore the two types of cube can be used together in the same

system.

Microscope Stages

The microscope stages used in both miCube and LifeHack were commercial parts. The μCube and UC2 projects are also mainly focused on 3D printed hardware to build up an optical system, although UC2 have also produced a 3D printed microscope stage [135, 136]. The most notable 3D printed microscope stage in the open-source community is the OpenFlexure project [68]. The OpenFlexure project now has three different microscope stages; the OpenFlexure microscope, the OpenFlexure delta stage and the OpenFlexure block stage. I will concentrate here on the original OpenFlexure microscope [137].

The OpenFlexure microscope enables lateral translation of the sample and axial translation of the objective lens through the use of 3D printed flexures. Flexure hinges operate under elastic deformation, which is enabled by creating a thin and flexible region between two rigid sections [138]. The deformation is reversible, unless the flexure deformation is greater than its elastic limit where the flexure will incur permanent damage [137]. The OpenFlexure microscope uses flexure hinges to form a lever system to control the three axes of the stage, which are actuated with M3 screws and nuts controlled either manually or with stepper motors [137]. The use of stepper motors enables $\approx 50\,\text{nm}$ movement steps and stage drift has been shown to be less than $20\,\mu\text{m}$ over one week [137].

The microscope has options to use either standard RMS threaded objective lenses for high quality image acquisition, or can also use an inverted webcam lens for low-cost educational microscopes [139]. Images are also generally acquired using a Raspberry Pi v2 camera module [139], but the microscope can be adapted to use higher quality cameras such as USB CMOS cameras [140]. The OpenFlexure project have also developed software for the microscope [141], including image acquisition, motor/flexure control, autofocus [142], and Raspberry Pi v2 camera flat-field and colour correction (discussed further in chapter 5 section 5.2.2) [143].

The main application of the OpenFlexure microscope has been to image thin blood

smears for low-cost malaria diagnosis in resource limited areas [139]. Our research group have also utilised the microscope for TIE imaging to asses refractive index differences between different species of algae [104] and also adapted the microscope for SRRF microscopy of nanodiamond and nanodiamond embedded within human MDMs [140].

Incubator Microscopes

Live cell microscopy requires incubator chambers to ensure correct environmental conditions for the samples, such as temperature, CO_2 and humidity control. Options include chambers which surround a large portion of the microscope body, including the sample stage and objective lens, or sample stage top incubators. It is advantageous to include as much of the microscope within the incubator chamber as possible to minimise any temperature gradient effects. A third option is to place the entire microscope within a cell culture incubator which minimises thermal drift further [144] as the temperature of the microscope and incubator can stabilise. Although care must be taken to ensure that any microscope electronics do not cause heating within the incubator.

As mentioned above, the UC2 project developed a microscope which was used inside a cell culture incubator for imaging macrophage differentiation [67]. The incubot [144] is also an interesting project. The microscope itself is not 3D printed, but instead utilises a 3D printer body (Tronxy X1) as a 3 axis motorised microscope stage. The incubot project has used this microscope for live cell incubator imaging of HeLa cells in both oblique illumination and fluorescence microscopy. The tissue culture plate is held stationary whilst the motorised 3D printer body moves an optics unit, mounted to where the 3D printer extruder component would normally reside, for lateral movement and axial focusing. The optics unit contains an infinite-conjugate objective lens and Raspberry Pi v2 camera module along with LED illumination and any optical filters required for fluorescence microscopy. The incubot microscope costs ≈€1k compared to the commercial incubator microscope Etaluma LS720 which can cost between £45k and £63k [144].

A low-cost 3D printed microscope which operates within a cell culture incubator has the potential to enable greater accessibility to live cell imaging studies of macrophage

host-pathogen interactions. Along with the challenges faced with live cell imaging discussed in chapters 1 and 3, access to live cell microscopy equipment can be limited. The cost of commercial advanced microscopy systems can be $\geq$ £100k, therefore often in academic biological institutions there is a core microscope facility where equipment can be booked and is charged on an hourly basis. Access to and available time on microscopes is therefore split between many different research groups which can be challenging for long term live cell image acquisition. Furthermore, from my personal experience during this research project, hourly costs can be around £50 per hour. Therefore, due to costs, it is advantageous to know before carrying out image acquisition that cell preparation protocols and imaging time points are optimised. Low-cost incubator microscopes could therefore not only widen access to live cell microscopy in areas where resources are low, but could also offer the opportunity to carry out initial imaging studies to optimise protocols and determine interesting time points before utilising advanced microscopy equipment. At academic core microscope facilities, trained members of staff are also employed to maintain the microscope equipment, including calibration and cleaning. Technical assistance may not be available if microscopes were to be deployed for use in remote settings for testing patient samples by non-specialists, therefore a low-cost incubator microscope would need to require minimal calibration and be relatively simple to set up for those not trained in optical engineering.

4.2 Initial Test Microscope Design Parameters

A key requirement in developing low-cost microscopes for our research was the ability to perform fluorescence colocalization studies in macrophages. We also wanted to combine computational microscopy techniques, including TIE and SRRF, with low-cost microscopes to enhance and extend functionality. This resulted in the following key parameters for designing and constructing a low-cost system:

- Multichannel microscopy (for example, multichannel fluorescence for colocalization studies and multichannel brightfield for TIE microscopy).
- Ability to include multiple modes of imaging in one microscope.

- Long term stability to enable time-lapse imaging of live cells.
- Minimal calibration requirements and simple setup and optical alignment.

From the above requirements, we wanted to develop an initial test microscope with one fluorescence and one brightfield channel, before extending this microscope to include multiple fluorescence and brightfield channels. The following optical design decisions therefore needed to be made:

- Infinite- or finite-conjugate objective lenses and corresponding imaging optics.
- Choice of excitation and detection wavelengths for the fluorescence channel.
- Choice of cameras for fluorescence and brightfield imaging.
- Required field of view for each channel.
- Trade offs between the cost and quality of the optics.

An optical schematic of our first desired test setup can be seen in figure 4.2. We chose an infinite-conjugate imaging system, the reason for which is discussed in section 5.1.1. The next decision was choice of excitation and detection wavelengths. The cost of certain consumables, such as fluorescent beads and immunolabelling antibodies, is comparatively high ($\geq$ £200) compared to the cost of the optics and sensors often used in low-cost 3D printed microscopes, such as Raspberry Pi camera modules and optical elements, for example objective lenses and dichroic mirrors, costing $\leq$ £200. For this reason it is economically advantageous to have relatively low-cost and stable test samples to develop and characterise low-cost microscopes.

Therefore, we designed the initial fluorescence channel to allow imaging of fluorescence generated by the negatively charged nitrogen-vacancy (NV^-) centers in nanodiamond. We have used fluorescent nanodiamond (FND) extensively in our research group for different applications. FND is an excellent microscopy test sample due to the high photostability of the NV^- centers, and the ability to create FND particles smaller than the diffraction limit to allow characterisation of the PSF of the system. FND is also non-toxic and because the particles surfaces can be functionalised they also offer promise as fluorophores for future macrophage research.

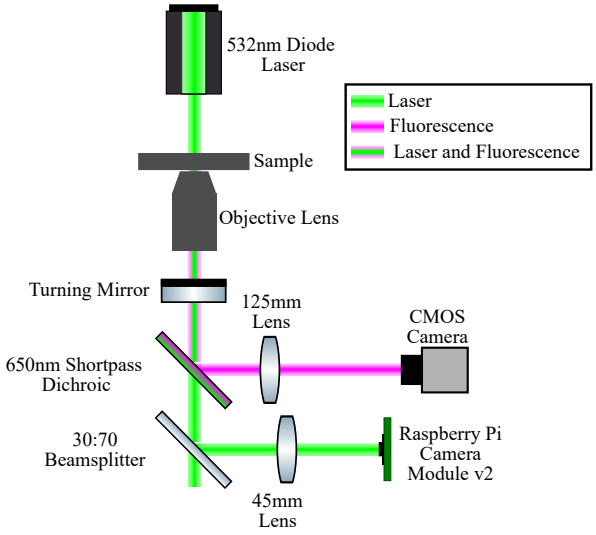

Figure 4.2: Initial test microscope optical design schematic. Infinite-conjugate system including a single far red fluorescence imaging channel (magenta), separated by a 650 nm shortpass dichroic mirror (Thorlabs DMSP650), and one brightfield channel (green). Illumination provided by a 532 nm diode laser (Thorlabs CPS532). Detection provided by a USB CMOS camera (IDS UI-3060CP-M-GL Rev.2) and Raspberry Pi v2 camera module for the fluorescence and brightfield detection channels respectively. The 30:70 beamsplitter (Thorlabs BSS10R) is to allow for future multifocal plane imaging.

This figure partly includes illustrations of optical components from the gwoptics ComponentLibrary designed by Alexander Franzen with reuse permitted under a CC BY-NC 3.0 licence

The NV^- center emits fluorescence over a band from 637 nm to ~800 nm when excited by 532 nm light. Therefore we chose a 532 nm compact diode laser (Thorlabs CPS532) with 4.5 mW of power for excitation on our first test microscope. This laser has a circular beam profile with a TEM001 mode, meaning additional beam conditioning was not required and the beam only needed to be expanded to the correct spot size to fill the required field of view. The fluorescence signal was spectrally separated using a 650 nm shortpass dichroic mirror (Thorlabs DMSP650).

The dichroic mirror allowed the remaining transmitted laser light to be utilised for brightfield imaging. In the future we wanted to extend this microscope to include three brightfield channels for multifocal plane imaging for TIE microscopy. Therefore the 30:70 beamsplitter (Thorlabs BSS10R) was included to initially allow the 30% reflected light to form the single brightfield channel, leaving the 70% transmitted light to be split into two more brightfield channels later on with roughly equal intensities.

As our group had used the very low-cost (£20−30) Raspberry Pi v2 camera modules before for brightfield imaging and TIE microscopy with good results [104], we chose to

continue using the same camera for the brightfield channel on this microscope. For the fluorescence channel, however, we required a camera with higher quantum efficiency to maximise photon capture as fluorescence signal is typically weaker than brightfield. We have used a relatively low-cost (≈£600 compared to an ≈£10k EMCCD or high end sCMOS) USB CMOS camera before (IDS UI-3060CP-M-GL Rev.2) for imaging FND and SRRF microscopy [140] and so we chose to continue using this camera for the fluorescence channel.

As our imaging application was macrophage research, we chose an imaging field of view of 250 μm x 250 μm. Human MDMs are on average approximately 21 μm in size [145] and so this field of view allowed multiple cells to be imaged at once, increasing statistical sampling compared to imaging a single cell. As the brightfield and fluorescence cameras had different sensor sizes, different focal length tube lenses were required to create equal field of views in the two channels, as shown in figure 4.2. Further information and discussion on the choice of cameras and lenses is included in chapter 5.

4.3 Initial Testing of Available Open-Source Systems

4.3.1 UC2

As outlined in section 4.1, there are a number of 3D printable microscopy systems available in the open-source hardware community. We identified the modular nature of the UC2 system offered the potential and flexibility to set up many different microscopy techniques, including an infinite-conjugate multichannel microscope. Therefore testing the UC2 system for our application was our natural starting point for constructing low-cost microscopes for our macrophage research, including the initial test microscope design in figure 4.2.

The concept of realising the design in figure 4.2 using the UC2 system can be seen in figure 4.3. We were working with version v0 of the UC2 cubes at the time. UC2 had designs for v0 cube inserts for dichroic mirrors/beamsplitters, turning mirrors and one for the Raspberry Pi v2 camera which used the slot mechanism on the corners of

the v0 cube. The UC2 v0 lens insert used the cage system. There were also other designs for inserts not required for our microscope design. On the fluorescence channel, we intended on using the cage system to mount the USB CMOS camera attached to a Thorlabs cage plate since there was no UC2 C-mount adapter.

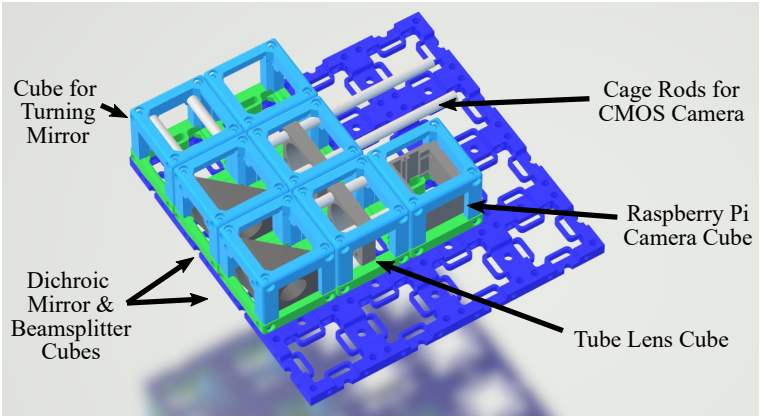

Figure 4.3: Concept of building the microscope illustrated in figure 4.2 with the UC2 v0 system. Figure was created using STL files originally obtained from the UC2 GitHub repository [133] which were published under the licence CERN Open Hardware Licence v1.2.

The UC2 v0 inserts were however not the correct dimensions for mounting standard 1 inch and 25 x 36 mm rectangular optics, which we wanted to use. Therefore I designed new, compatible inserts. The UC2 v0 dichroic mirror/beamsplitter insert can be seen in figure 4.4(a). Figure 4.4(b) is a rotated and zoomed in view of (a) to show the slot on the insert for mounting the optic. Figure 4.4(c) shows my 1 inch dichroic mirror insert design which utilises the cage rod system. This includes self tapping M3 screw holes (designed by Dr Richard Bowman from the Bath Open INstrumentation Group) [146]) for locking plates to hold the optic in place, as opposed to the optics slot feature on the UC2 insert, to minimise the chance of optics becoming scratched/damaged.

I designed a similar insert for 25 x 36 mm beamsplitters (figure 4.4(d)). However, because 25 x 36 mm was too large to fit between the rods in the 30 mm cage system, this insert instead uses the insert slot mechanism on the v0 cubes. I designed a permanent groove on the bottom of the insert for the optic to sit in as the M3 screws for a locking plate interfered with the lid of the cube. This is highlighted in figure 4.4(d).

The UC2 v0 turning mirror insert design was also the incorrect orientation for our

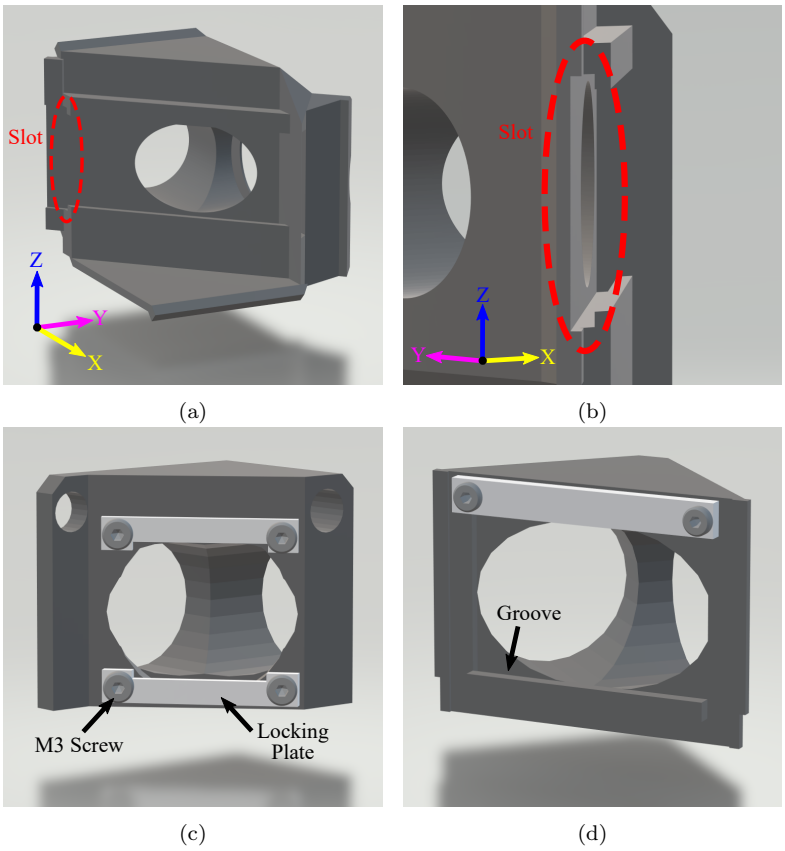

Figure 4.4: **(a)** UC2 v0 dichroic/beamsplitter insert. **(b)** Different view showing the slot to slide the optic into the insert. **(c)** My insert design for the Thorlabs DMSP650 1 inch dichroic mirror. Includes M3 self tapping screw holes, originally designed by Dr Richard Bowman from the Bath Open INstrumentation Group [146], to allow locking plates to be attached. **(d)** My insert design for the Thorlabs BSS10R 25 x 36 mm beamsplitter. Includes a groove at the bottom to hold the optic in and M3 holes at the top for the retaining plate. **(a)** and **(b)** were made using an STL file originally obtained from the UC2 GitHub repository [133] which was published under the licence CERN Open Hardware Licence v1.2.

microscope (figure 4.5(a)). The UC2 v0 system was limited to manipulating beams in an XY plane within the setup, while we also needed to stack components, introducing an additional Z axis. For example to allow a sample stage to be mounted above the cube system and the beam to be reflected 90° to the first dichroic mirror. We required the sample stage to be mounted here for the microscope to be compatible with any live cell imaging in future. Therefore I designed a turning mirror insert with the required orientation and which was compatible with the cage rod system (figure 4.5(b)). The insert holds a 1 inch mirror (Thorlabs PF10-03-P01) at 45° to the vertical optical axis.

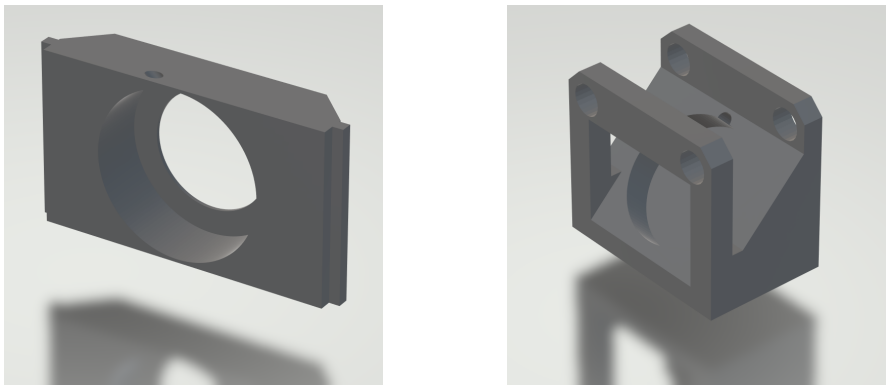

(a) (b)

Figure 4.5: **(a)** UC2 v0 turning mirror insert which uses the slot mechanism on the UC2 v0 cubes. This insert is not the correct orientation for use with a sample stage above the cubes. **(b)** My 1 inch turning mirror design for use with the cage system. **(a)** was made using an STL file originally obtained from the UC2 GitHub repository [133] which was published under the licence CERN Open Hardware Licence v1.2.

4.3.2 UC2-OpenFlexure

We wanted to use the OpenFlexure microscope stage, as we had used it previously within our group for both TIE imaging of algae [104] and computational super-resolution imaging of nanodiamond [140], as described in section 4.1. For compatibility between the UC2 v0 cubes and the OpenFlexure stage, UC2 had a modified version of the stage which included sections on the sides of the stage with holes for M3 screws to attach to the ball magnet system on vertically orientated UC2 base plates (figure 4.6).

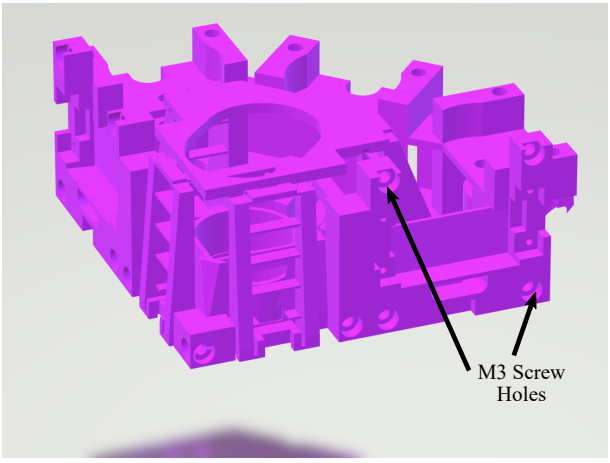

Figure 4.6: UC2 modified OpenFlexure stage with M3 screw holes in the side for combination with the UC2 base plate ball magnet system. Figure made using an STL file originally obtained from the UC2 GitHub repository [133] which was published under the licence CERN Open Hardware Licence v1.2.

Our microscope design in figure 4.3, however, had the base plate horizontal so that it would sit flat against the table for longer term imaging stability for future live cell time-lapse imaging of macrophages, compared to a vertically stacked cube system. To enable the modified stage to be compatible with our design, we needed to also include vertical base plates in the setup. This was done by inserting M3 screws into the sides of the cubes to magnetically attach to the plates. The stage then sat on top of the cubes and also magnetically attached to the vertical plates. Figure 4.7(a) shows the resulting setup in practice. Figure 4.7(b) is an exploded schematic of the setup (with just one cube for illustration) showing more clearly where the ball magnets and screws were.

This setup was however very unstable as we weren't using the base plates as intended by UC2. Figure 4.7(c) illustrates the back of the three base plates, highlighting that they were not joined together. The two vertical plates also didn't sit against the table and were only supported using the ball magnet system. If we had printed the three plates monolithically they would have been much more stable. This influenced our decision when designing our own 3D printed microscope system to monolithically print modular cubes, which will be described in section 4.4, as we noted the improvements printing parts joined together would have on stability for our research.

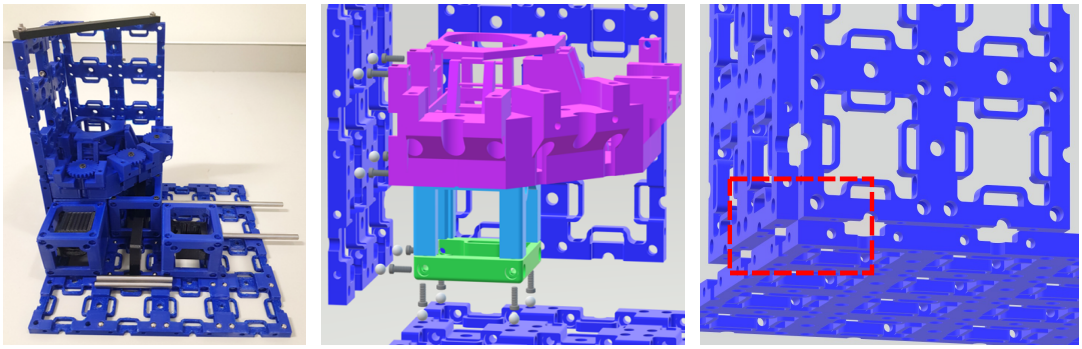

(a) (b) (c)

Figure 4.7: **(a)** The UC2 modified OpenFlexure stage in practice where two vertical base plates were attached to connect the stage to the system. **(b)** Exploded schematic, including just one cube, to illustrate where the screw and ball magnet connections were. **(c)** Schematic of the back of the three base plates, highlighting that they were not joined together and that the vertical plates didn't sit flush against the table. **(b)** and **(c)** were made using STL files originally obtained from the UC2 GitHub repository [133] which was published under the licence CERN Open Hardware Licence v1.2

Along with the modified UC2-OpenFlexure stage, UC2 also designed an attachment

piece to combine the OpenFlexure stage with the cubes. The attachment connected onto the OpenFlexure stage with two sets of M3 nuts and bolts. The underneath of the attachment had divots for ball magnets to magnetically fix to M3 screws in the top of the UC2 cubes. Initial versions, including that in figure 4.8(a), did not include space for the feet of the OpenFlexure stage, which are required to connect elastic bands between the feet and the flexures for increased flexure tension. As the attachment approach was much more stable than the modified stage above due to the stage being fixed to the cubes themselves, I designed a modified version which replaced the OpenFlexure feet with bars on the attachment for the elastic bands to loop around. Figure 4.8(b) illustrates the bottom of my modified attachment, where the M3 screw holes and ball magnet divots can be seen along with the elastic band bars. The top of the elastic band bars were flat, whereas the bottom of the bars had a rounded finish to reduce the likelihood of the elastic bands snapping. Figure 4.8(c) shows the modified attachment connected to the stage with two of the elastic bands looped around the attachment. The approach here was taken forward into our designs for our own 3D printed microscope system, which is discussed later in section 4.4.

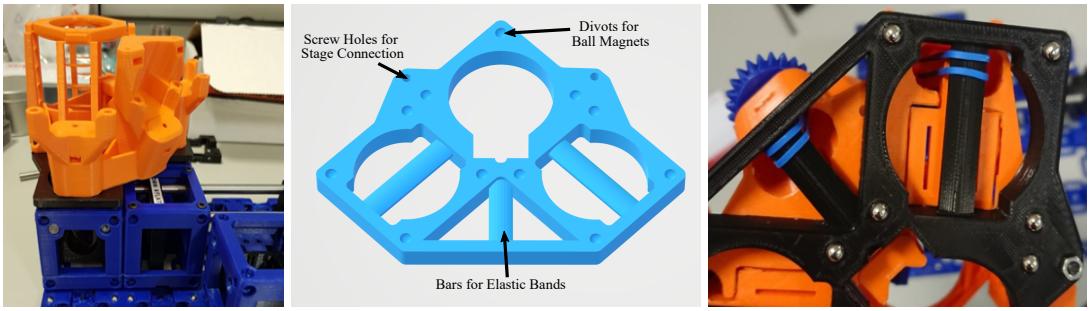

(a) (b) (c)

Figure 4.8: **(a)** The UC2-OpenFlexure stage adapter in practice. **(b)** Illustration of the bottom face of our modified adapter, highlighting the ball magnet divots and screw holes, along with the bars to replace the OpenFlexure feet. The adapter is a modified version of the STL file originally posted by Benedict Diederich on the OpenFlexure GitLab repository [147]. **(c)** Our modified adapter attached to the stage showing two of the elastic bands looped around the bars.

4.3.3 Assembly and Alignment

The next step was to assemble the UC2 set up and align it. I firstly constructed an illumination rig from standard Thorlabs parts for the 532 nm laser. This included an XY translation stage and a tip/tilt kinematic mount to allow the position of the laser to be adjusted (figure 4.9(a)). Figure 4.9 shows the first step of setting up the turning mirror so that it was reflecting the laser 45° into the cube system. This was checked with a Thorlabs cage alignment plate (figures 4.9(b) and 4.9(c)).

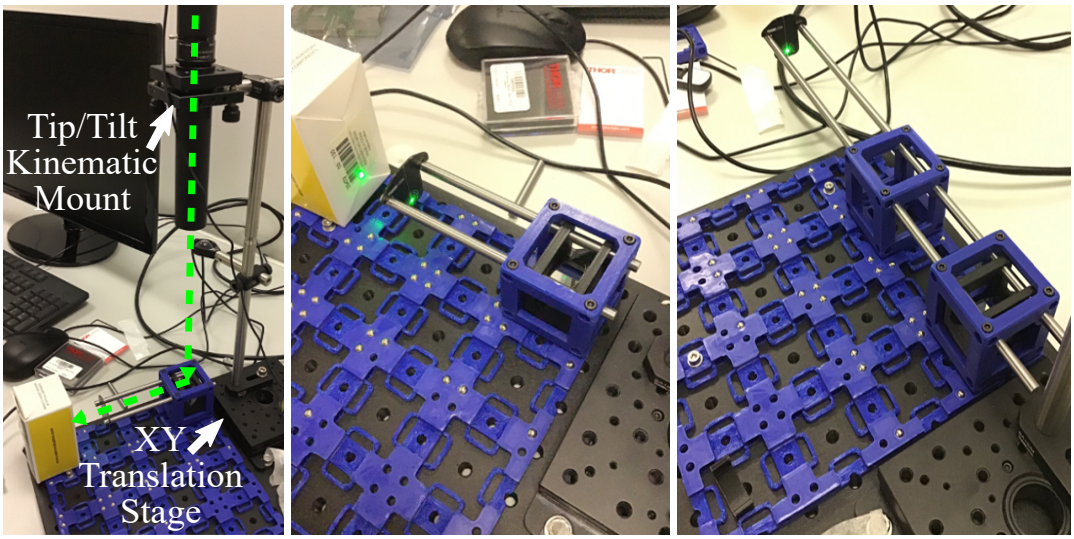

(a) (b) (c)

Figure 4.9: Alignment of the laser and turning mirror cube. **(a)** Laser was mounted on a XY translation stage and a tip/tilt kinematic mount. The green path highlights the desired laser path where it is reflected by 45° by the turning mirror cube. **(b)** Shows cage rods attached to the cube and the laser was adjusted so the beam was centred along the optical axis using an alignment target. **(c)** A second empty cube was added to extend the cage rods further to check the beam was still aligned further along the optical path.

The second step was to add in the dichroic mirror cube and check the transmitted and reflected beams were aligned. A double reflection from the dichroic mirror can be seen in figure 4.10(a) where the left hand reflection was centred on the alignment target. Figure 4.10(b) shows the beam walked off to the right of the optical axis when the alignment target was moved further along the cage rods. The same can be seen for the transmitted laser beam, where the beam is centred in figure 4.10(c) and then again walks off to the right of the optical axis in figure 4.10(d). The walk off was an

angular error and not the expected lateral displacement of the beam when transmitting through the dichroic mirror. The angular error is illustrated further in figure 4.11. The error was caused by the dichroic mirror being tilted, but it was unknown whether the tilt originated within the insert or whether there was a tilt on the cube.

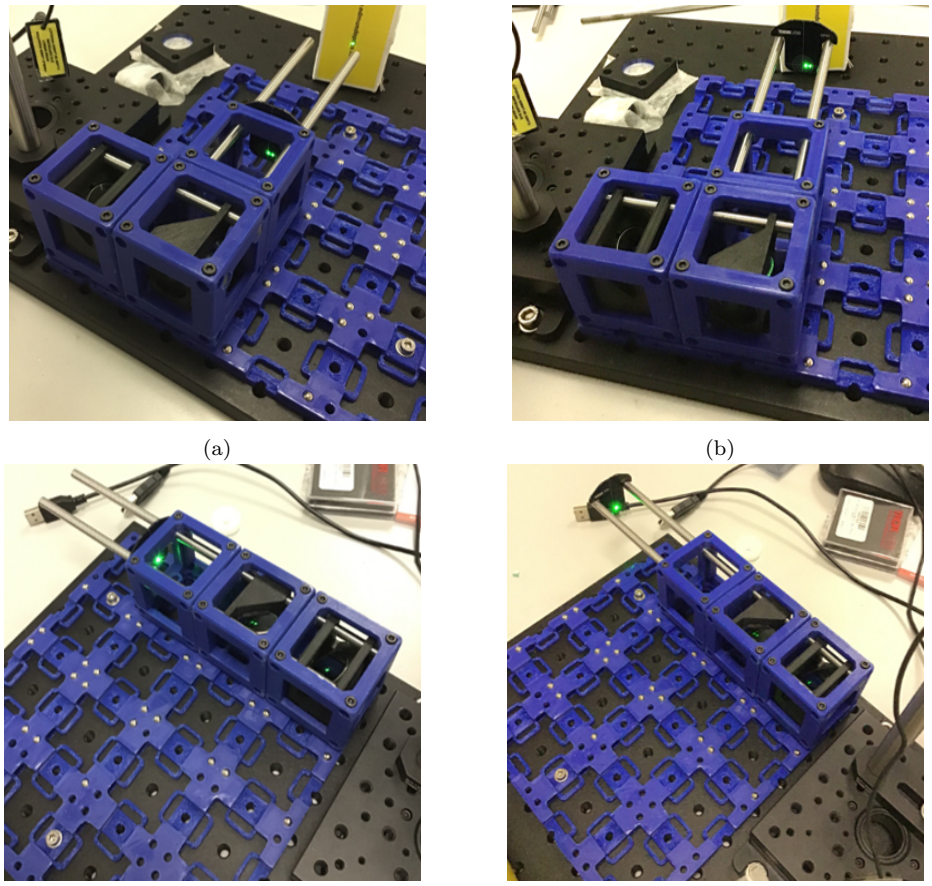

(a) (b)

(c) (d)

Figure 4.10: **(a)** Reflected beam from the dichroic mirror. **(b)** Angular error in the reflected beam alignment. **(c)** Transmitted beam through the dichroic mirror. **(d)** Shows the same angular error as **(b)** but in the transmitted beam.

The two options to fix the tilt were:

- Taking the dichroic mirror out of its insert and replacing it again to ensure it was positioned flat in its holder.
- Adjusting the height of the screws on the dichroic mirror cube lid to correct/compensate for any tilt.

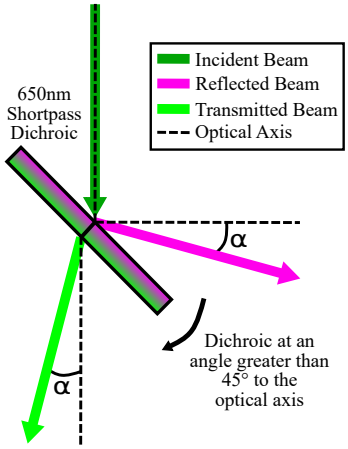

Figure 4.11: Illustration of dichroic mirror tilt where the incident beam is on axis but the reflected and transmitted beam paths have an angular error (α) to the optical axis. The black dashed line shows the expected paths if the dichroic mirror was at the correct position of 45° to the optical axis.
This figure partly includes illustrations of optical components from the gwoptics ComponentLibrary designed by Alexander Franzen with reuse permitted under a CC BY-NC 3.0 licence

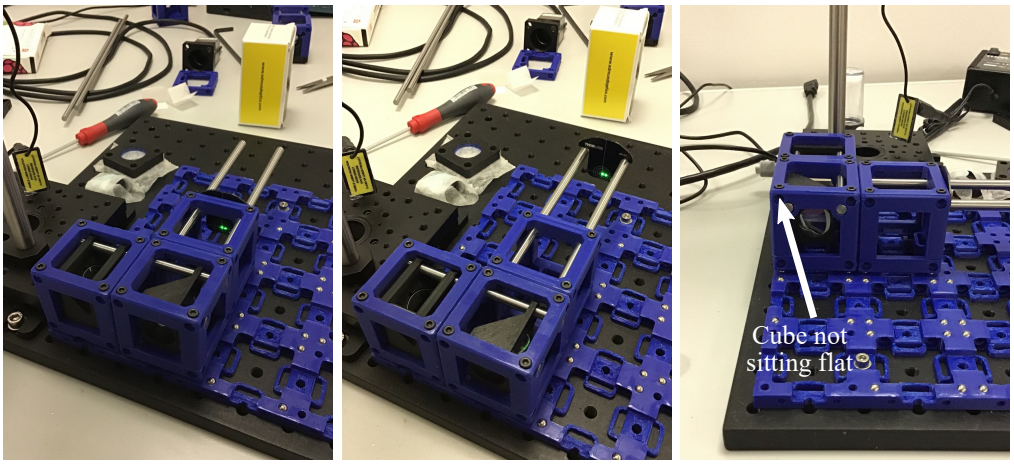

(a) (b) (c)

Figure 4.12: Shows the reflected beam path from the dichroic mirror after adjustment of the UC2 cube-lid screws. **(a)** Shows the double reflection from the dichroic mirror on the alignment target, where I centred one of the reflections. **(b)** Shows that the reflected beam was still centred on the optical axis when the test target was placed further along the optical path. **(c)** Shows the resulting position of the dichroic mirror cube did not sit flat after adjustment.

The former did not solve the problem and I encountered further problems with the latter. Firstly, as the cube needed removed from the base plate to adjust the screws, they couldn't be adjusted whilst viewing the beam on the alignment target and so it was a very iterative process. The second problem encountered was the cube itself actually being more tilted after adjustment (figure 4.12(c)) to align the reflected beam

along the optical axis (figures 4.12(a) and 4.12(b)). The tilt on the cube meant the OpenFlexure stage would also mount at an angle, resulting in sample and objective lens tilt.

4.3.4 Discussion

From my initial tests we noted several advantages and limitations of using the UC2-OpenFlexure system for our macrophage research. The UC2 cubes offer a great deal of flexibility for building optical systems, where a single base cube design can house many different types of optics and cubes can be easily swapped to change the optical design. The combination of 3D printed parts and low-cost screws and ball magnets means the system is more economical and more accessible than commercial optomechanics and microscope systems. The open-source nature of the project adds to the accessibility and allows for collaborations with other such projects like OpenFlexure.

The flexibility does though come with its limitations. Uncertainties in ball magnet and screw height meant the number of degrees of freedom within the system made it difficult to identify which problems were, for example, the dominant cause of the dichroic mirror tilt. 3D printing cubes individually can also result in problems due to common printer errors and printing tolerances across different printers. Common errors such as over extrusion, warping and cracks in prints, can become multiplicative across parts and result in, for example, cubes not sitting flush together. The last limitation we noted was the UC2 cubes are not light tight, as the cubes have open walls to allow their flexibility when adding many of them to the base plate. For fluorescence microscopy however, it is advantageous for the microscope to be light tight for good signal to noise ratio. These highlighted limitations were problems for our particular application and did not allow the level of accuracy, in combination with long term stability, that we needed. Therefore we made the decision to design a new 3D printed microscope system to address the problems which were key requirements for our macrophage research (in particular fluorescence colocalization studies).

4.4 M4All Modular Cube Design

From our initial tests of available open-source systems in section 4.3, we established certain design features we required in a 3D printable microscopy system for our imaging application. These were:

- A modular system for flexibility and the ability to easily create setups for different imaging modalities in future.
- Fully open-source with easily modifiable CAD files.
- A method to secure the parts onto a standard optical bench/breadboard.
- 30 mm cage system to allow compatibility with commercial optomechanics from, for example, Thorlabs and Edmund Optics.
- Light tight for improved imaging data quality.
- Compatible with the OpenFlexure microscope stage.

As none of the already available systems addressed all of these features together, we therefore developed "M4All" which stands for MultiModal Modular Microscopy for All. Like UC2, M4All is an open-source 3D printable modular microscopy system which is based on a cubic design, however the modularity mainly comes from modular cube CAD files which are printed monolithically. The reasoning for this is to address the issue of multiplicative 3D printing errors, as discussed in section 4.3.4, and to provide longer term stability compared to individually printed parts. I chose to design this system using FreeCAD [148], a fully open-source CAD package, which has allowed us to openly share a suite of CAD designs, released as a GitHub repository [9], which can be easily modified to create parts for desired optical systems. The suite can be seen in figure 4.13 and each design category will be described in further detail in subsequent sections.

The base cube is shown in figure 4.14 and is 50 mm in length in x and y, which is large enough to diagonally accommodate rectangular 25 x 36 mm optics. The cube dimensions also allow the cubes to align with the mounting holes on standard metric optical breadboards which are spaced 25 mm apart, therefore a cross hole on the bottom of each cube is included for M6 mounting screws. For compatibility with com-

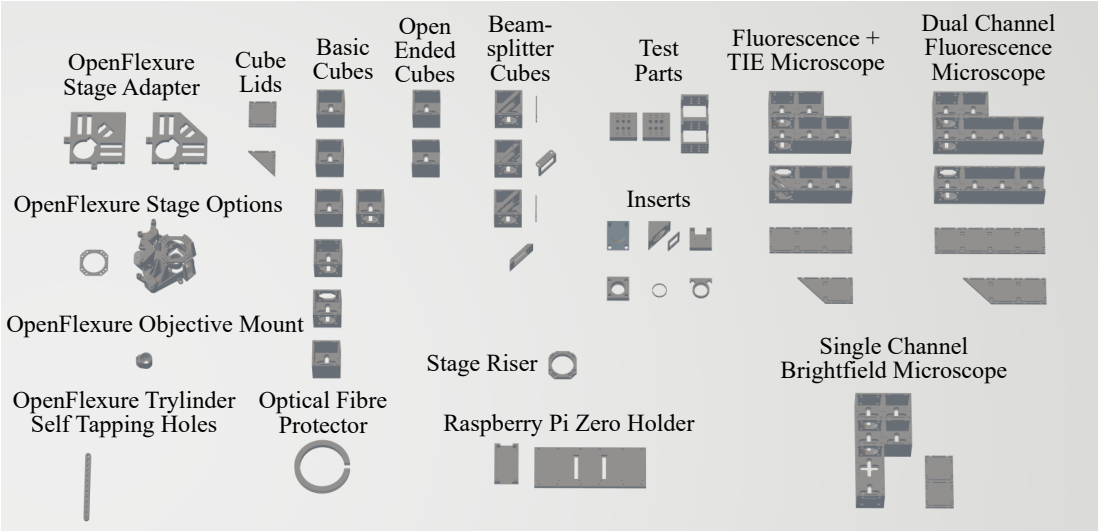

Figure 4.13: M4All CAD design suite. CAD files were designed using FreeCAD [148]. Designs are grouped into design categories, each of which is described in this thesis.

mercial optomechanics, we chose to create the whole system as a 30 mm cage system by including 6 mm cage rod holes (figure 4.14(a)).

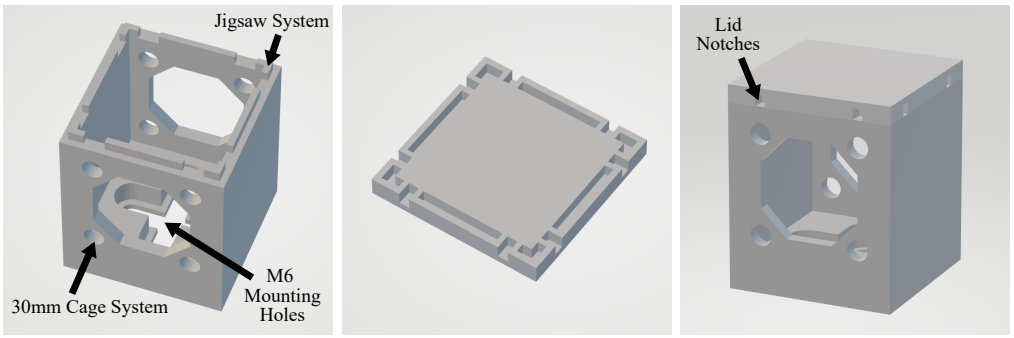

(a) (b) (c)

Figure 4.14: **(a)** 3D model of the M4All base cube where the jigsaw system, 30 mm cage system and M6 mounting holes are highlighted. **(b)** M4All cube lid where the corresponding jigsaw system to the cube can be seen. **(c)** 3D model illustrating the cube and lid together. The notches to help remove the lid are highlighted.

Included on the top of the base cube is a jigsaw system (figure 4.14(a)) for a light tight lid (figure 4.14(b)). The combination of the cube and lid is illustrated in figure 4.14(c). We also use the jigsaw system for attaching the OpenFlexure stage to the cubes (this is described further in section 4.5.2).

Along with cube lids to produce a light tight setup, I designed an array of different

base cubes which can be joined together in the CAD software to create an enclosed optical system. Figure 4.15(a) shows the different base cubes with different numbers of walls closed off. In the case that an optical element needs to be positioned where there is a wall, I also designed two open ended cubes (figure 4.15(b)) that can be used to create longer sections. An illustration of joining various cubes together to create a larger part for printing can be seen in figure 4.15(c). Ideally all the cubes for a microscope would be printed monolithically. However if the desired optical system is too large to be printed as one piece then the mounting holes on the bottom of the cubes allow larger parts to be held together, along with running cage system rods through separate parts to align them.

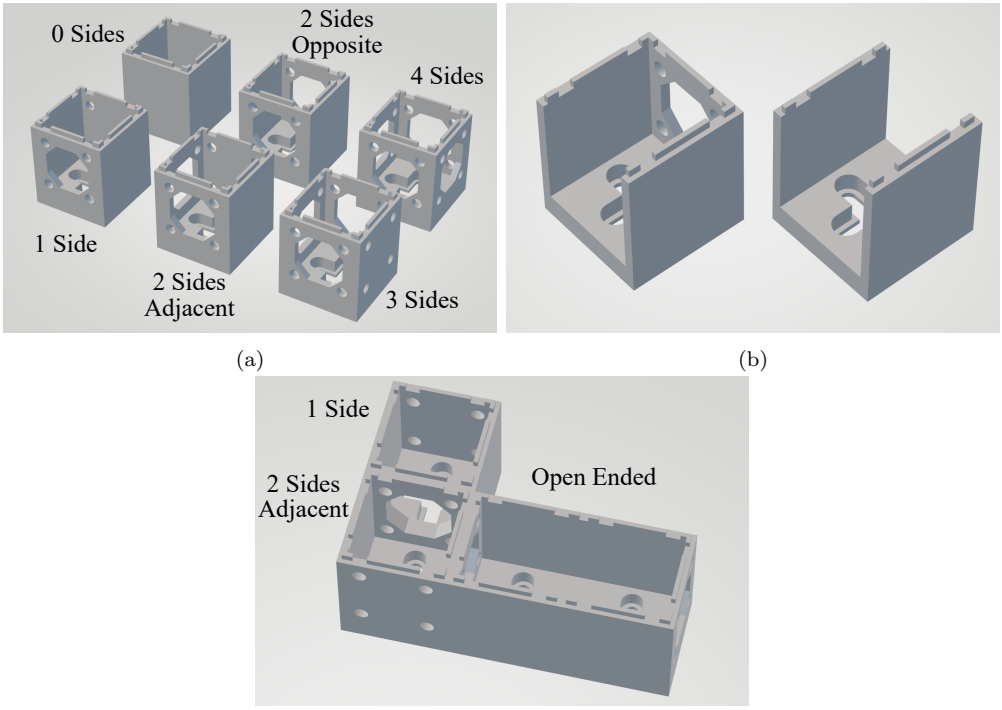

Figure 4.15: **(a)** Array of M4All base cube designs. **(b)** M4All open ended cubes. **(c)** Illustration of a combination of different cubes to create an internally closed system.

4.5 M4All Practical Considerations

4.5.1 Optical Component Insert Designs

As discussed in section 4.2, we wanted to build a single channel fluorescence and brightfield microscope as an initial test setup. Later this would be extended to include three brightfield channels for TIE microscopy, section 5.2, and a second microscope would be developed for dual channel fluorescence imaging, section 5.3. The required optical elements for these two systems included:

- 1 inch optics (lenses, filters, turning mirrors and dichroic mirrors).
- 25 x 36 mm rectangular optics (beamsplitters and turning mirrors).
- Cameras (Raspberry Pi models and CMOS cameras).

In section 4.3 I discussed my designs for optical component inserts suitable for many of the above optics, which were compatible with the UC2 system. This section will describe the further adjustments I made to these designs to improve their compatibility with our M4All system and new designs for other elements, such as lenses and drop in filters.

Firstly I altered the turning mirror design in figure 4.5(b). The design required support material on the front section to support the cage system holes when 3D printing, thus increasing printing and print cleanup time. The design also only allowed for one orientation of the insert inside the cubes to turn the beam in Z from the microscope stage 90° into the XY plane of the cubes. For flexibility I redesigned the insert to have two possible orientations so that it could also be used for turning the beam within the cube system. The two orientations can be seen in figures 4.16(a) and 4.16(b), and the design now requires minimal support material.

The next step was to increase the stability of the dichroic mirror insert design in figure 4.4(c) to fix the tilt on the element discussed in section 4.3.3. Therefore I added cage rod holes to the bottom of the insert as well as the top to minimise any tilt of the insert itself. I also created a single locking plate which covers the sides of the dichroic mirror as well as the top and bottom to minimise tilt of the optic within the insert.

The final design is shown in figure 4.16(c).

As our microscope optical designs were all infinite-conjugate systems, we required 1 inch tube lens inserts. My lens insert design can be seen in figure 4.16(d) which includes grub screw holes on the top for locking in place on the cage rods and a 3D printable retaining ring. The thickness of the insert allows for lens thicknesses up to 7.7 mm but this can also be altered in FreeCAD. For fluorescence microscopy, we required edgepass filters in front of the cameras to cleanup the signal. It is often helpful to be able to easily insert and remove these filters and so I also designed a drop in insert for 1 inch filters (figure 4.16(e)) which uses the same retaining ring as the lens insert.

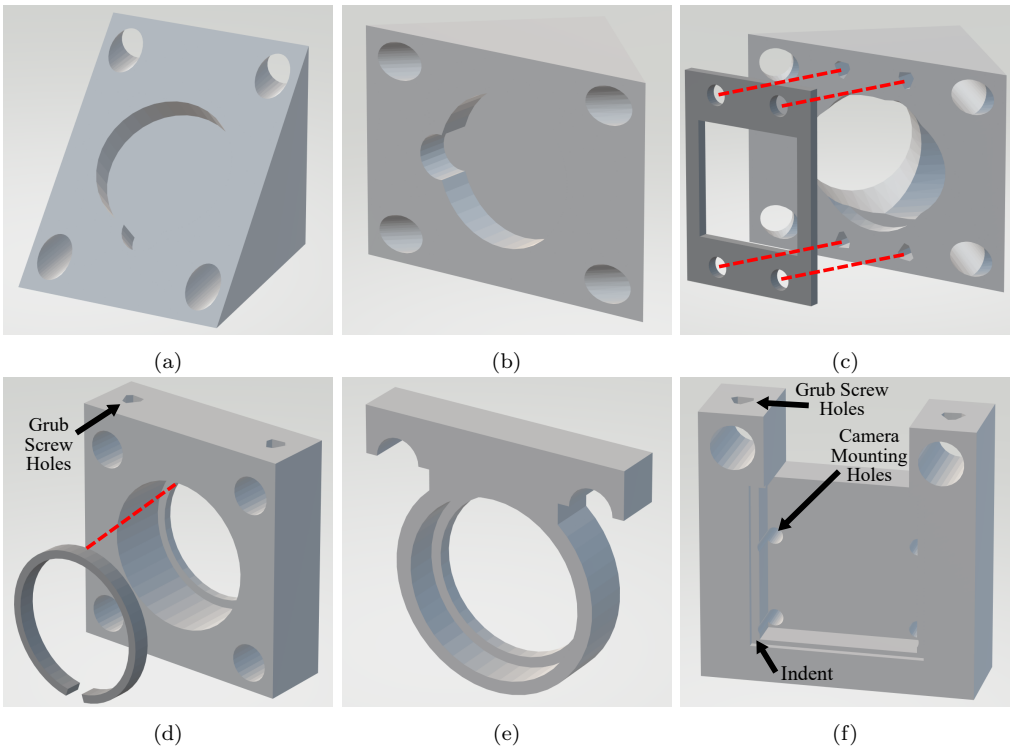

Figure 4.16: M4All Inserts **(a)** 1 inch turning mirror insert. **(b)** Turning mirror insert second orientation. **(c)** 1 inch dichroic mirror insert and locking plate. The red dashed lines show where the locking plate connects to the insert with M3 screws. **(d)** 1 inch lens holder and retaining ring. There are grub screw holes on the top to lock in place on the cage rods. **(e)** Drop in 1 inch filter holder. The retaining ring in **(d)** is compatible with this design. **(f)** Raspberry Pi Camera v2 module insert.

Figure 4.16(f) shows my design for an insert for the Raspberry Pi v2 camera module. The camera itself has four M2 compatible screw holes and so the insert includes four corresponding mounting holes for M2 nuts and bolts. To centre the camera sensor on the optical axis and mitigate any offset due to potential slack on the mounting holes,

an indented area for the camera to sit in is also included, leaving a gap at the back for air circulation to the PCB (printed circuit board) of the camera. Grub screw holes are again included on the top of the insert for locking onto the cage rods.

The last insert we required was for 25 x 36 mm rectangular beamsplitters. The design in figure 4.4(d) used the specific insert slot mechanism on the UC2 v0 cubes. I therefore needed to create a new design for use with our M4All cubes. As mentioned in section 4.3.4, the size of optic is too large to use with the 30 mm cage rod system. Therefore there were two options for designing an insert:

- To create a mechanism in the base cube that allows custom inserts to be taken in and out.
- To create a specific cube for the beamsplitter where the insert is printed monolithically inside the cube.

Both options have limitations. The first option brings in potential risks of 3D printer tolerances and printing errors causing the inserts to not fit in the cubes properly. The second option lacks flexibility in swapping optics in and out of the cube, especially if the cube is printed monolithically to other cubes. I designed and tested both options, these are shown in figure 4.17.

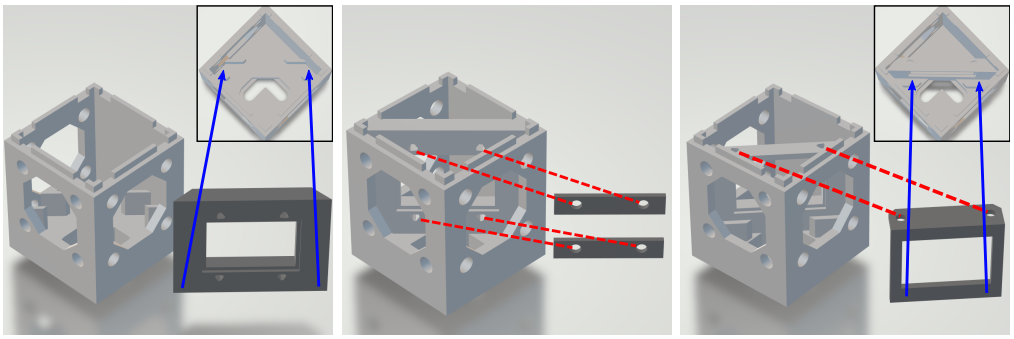

(a) (b) (c)

Figure 4.17: M4All beamsplitter cube options. **(a)** Option 1 with slot mechanism to take insert in and out of the cube. The top view and blue arrows indicate where the insert slots in. **(b)** Option 2 where the insert is printed monolithically inside the cube. The red lines highlight the mounting points for the locking plates. **(c)** Option 3 is also printed monolithically, however the locking plate holes have been moved to the top of the insert (red lines) and there is two slots for the bottom of the locking plate (blue arrows).

Figure 4.17(a) shows option one which includes two slots inside of the cube to hold

the beamsplitter insert at 45°. The insert includes two sets of self tapping holes above and below the optic for locking plates, similar to figure 4.4. Figures 4.17(b) and 4.17(c) show option two. The difference between these two is the position of the screw holes for the locking plate. In 4.17(b) the screw holes are on the same face as the beamsplitter. The screws must be screwed in through the holes in the side of the cube which can be problematic if the cube is printed joined to another cube. The design in figure 4.17(c) solves this problem by moving the top two screw holes to the top face of the insert and replacing the bottom two holes with two slots for the new locking plate. The third design is the one we chose to use for all of our microscope designs in chapter 5.

4.5.2 Microscope Stage

As discussed in section 4.3.2, we wanted to continue using the OpenFlexure stage due to our positive prior experience with it. Therefore I altered the UC2-OpenFlexure attachment in figure 4.8(c), replacing the ball magnet functionality with the jigsaw system for the M4All cubes (figure 4.18).

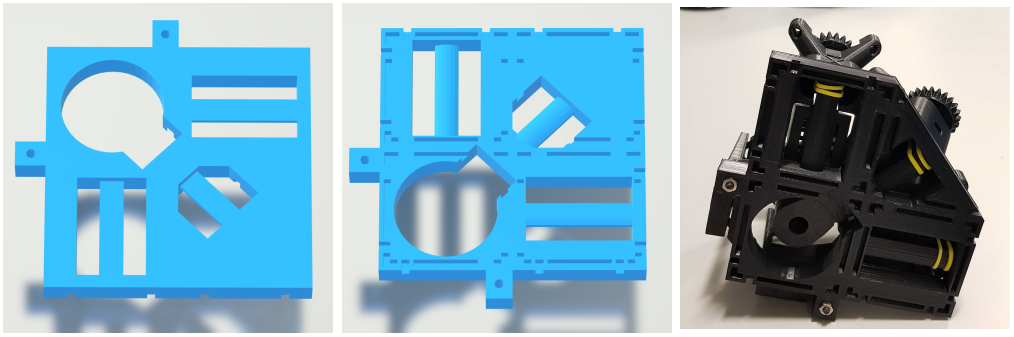

(a) (b) (c)

Figure 4.18: M4All OpenFlexure stage attachment utilising the jigsaw system. **(a)** Top view. **(b)** Bottom view. **(c)** The attachment connected to an OpenFlexure stage. The version in **(c)** has the corner removed for partial access to the cube underneath.

This included making the attachment square to sit neatly on top of the cubes and reducing the size of the holes next to the elastic band bars to make it as light tight as possible. The attachment in practice can be seen in figure 4.18(c), where this version of the attachment has the corner removed for easier access to the cube underneath. This is helpful if, for example, the position of a lens in this cube needs adjusted, as was the

case in our dual channel fluorescence microscope in section 5.3.

4.5.3 Test Parts for Printing

From our experience with open-source 3D printable hardware, we identified the need for test pieces for users to optimise their prints, addressing any issues with discrepancies between different printer tolerances. We wanted to provide test pieces for M4All that would allow either printer settings or part dimensions to be optimised before printing larger parts, thus minimising time and the print material used. The two sections of the base cube that are most sensitive to printing tolerances are the cage rod holes (also relevant for inserts) and the jigsaw system (relevant for lids and the OpenFlexure attachment).

To address the former, I designed test pieces including different sizes of cage rod holes, which can be printed and tested with a 6mm diameter metal rod to select the hole radius in the CAD files for the cubes and inserts before printing. The print orientation can also affect the size and accuracy of the print, therefore I created a vertical piece and horizontal pieces. We wanted to simulate a rod travelling through multiple cubes and check that friction adding up across the cubes also wasn't a problem, and so the vertical test piece has six different hole radii and three walls (figure 4.19(a)). I found that for printing horizontally, we needed to include a greater range of hole radii and so there are two pieces to allow 12 different radii to be tested for printing any inserts in this orientation (figure 4.19(b)).

To address the latter and optimise the jigsaw section dimensions, I created test pieces for the tab and blank jigsaw parts, corresponding to the cube and lid/attachment sections. This can be seen in figure 4.20 and means the fit can be tested and dimensions can be altered in the cube/lid/attachment CAD designs without the need to print full cubes or the full OpenFlexure stage attachment.

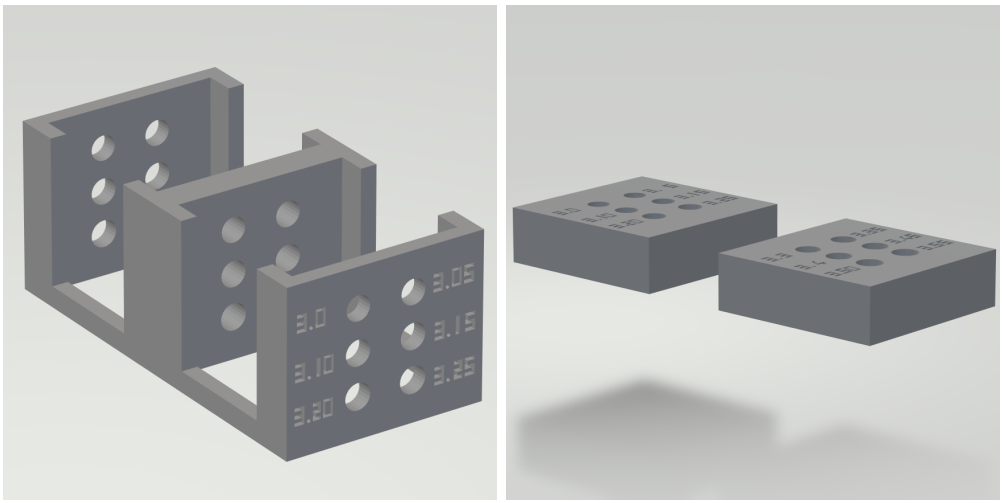

(a) (b)

Figure 4.19: M4All cage rod test pieces. **(a)** Vertical test piece with three walls to simulate rod travelling through multiple cubes, and six different hole radii ranging from 3.0 mm to 3.25 mm. **(b)** Two horizontal test pieces, each with six different hole radii. The first ranges from 3.0 mm to 3.25 mm and the second ranges from 3.3 mm to 3.55 mm.

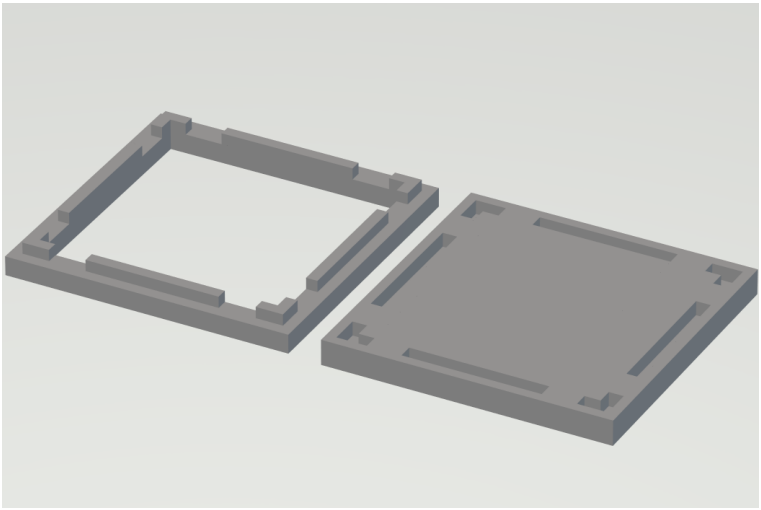

Figure 4.20: M4All jigsaw test piece including both male (left) and female (right) sections.

4.5.4 3D Printing Material Choice

All of the 3D printed parts in this research project were printed with PLA as the main material and PVA as support material when required. Stability tests carried out in chapter 5 displayed good levels of stability using parts printed in PLA, including initial tests within an incubator. The use of print materials with higher tolerances to

increased temperature environments were not tested during this project. All prints were also carried out using an Ultimaker S5 3D printer which uses the FDM method of printing.

4.6 M4All Initial Tests

Figure 4.21 shows alignment of the initial test microscope design in figure 4.2 set up using the M4All system.

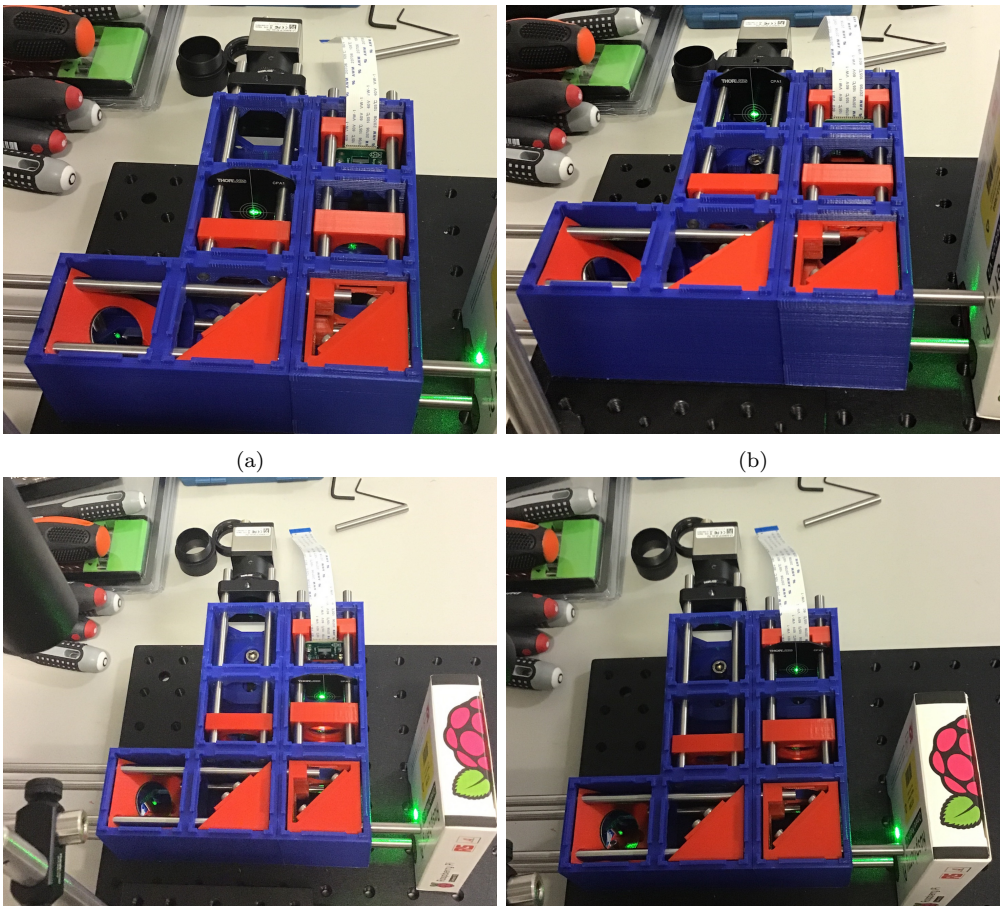

(a) (b)

(c) (d)

Figure 4.21: M4All initial test microscope. The OpenFlexure stage and objective lens were not included so the beam alignment within the cubes could be checked. **(a)** Laser aligned on centre of alignment target on channel one. **(b)** Alignment target moved further along the optical axis of channel one to show the beam was still centred. **(c)** Laser aligned on centre of alignment target on channel two. **(d)** Alignment target moved further along the optical axis of channel two to show the beam was still centred.

The turning mirror and fluorescence channel cubes were printed monolithically as one part and the brightfield channel was printed as a separate part. The cubes were fixed onto an optical breadboard and the same illumination system as in figure 4.9 was used. It can be seen that alignment of the two channels was achieved by only adjusting the laser position and angle. Figures 4.21(a) and 4.21(b) show the laser centred on the alignment target at two positions on the fluorescence channel. Figures 4.21(c) and 4.21(d) shows the expected translation due to transmission through the dichroic mirror, however the beam was still aligned straight through the channel as required. Note that the beamsplitter cube shown in this figure is a previous design iteration to those shown in figure 4.17, however the setup still shows the stability and accuracy of the M4All system.

4.7 Conclusions

This chapter has outlined the hardware development of a new open-source 3D printed modular microscopy system, M4All. We believe our approach of printing modular cubes monolithically is a novel approach to increasing stability in a modular system and adds value to the open-source microscopy community. We believe users of open-source hardware should test different open-source projects to determine which is the most suitable for their specific application. Advantages to M4All include fully open-source and easily modifiable CAD files, minimisation of printing errors by printing modular parts monolithically, test pieces to aid with print optimisation, compatibility with commercial optomechanics, light tight system and compatibility with the OpenFlexure microscope. I have shown that alignment of an optical system with M4All is made simple by a reduction in the number of degrees of freedom in the system. As cubes are printed together, they are inherently aligned to one another and the inserts for optical elements are designed to centre the optic on the optical axis. Therefore the user only needs to set up the optical elements at the correct position along the optical axis and also align the illumination source. Figure 4.21 confirms this is the case. Printing parts monolithically does however reduce flexibility to change the system post print, therefore the optical

design of the imaging system does need to be determined prior to printing. Whereas systems such as UC2 and μCube can flexibly add and remove components and cubes as required. Chapter 5 details three practical applications of M4All, showing its versatility and applicability to macrophage host defence research.

Chapter 5

M4All Practical Applications

5.1 Introduction

5.1.1 Optical Design Theory

Infinite-Conjugate System Optical Design

Microscope setups can follow either finite-conjugate or infinite-conjugate optical designs. In a finite-conjugate design the sample is positioned between f_o and $2f_o$ before the objective lens (where f_o is the effective focal length of the objective lens). The objective lens then focuses light at an intermediate image plane [149] where either an imaging sensor or relay lens, such as an eyepiece for direct observation, can be placed (figure 5.1(a)). An infinite-conjugate system on the other hand positions the sample at f_o before the objective lens and produces a collimated beam after the objective lens from a single point source in the focal plane. The collimated beam subsequently must be focused using a tube lens to form an image (figure 5.1(b)) [149].

Note that, figure 5.1 depicts the objective lenses as single lens elements, however in practice objective lenses contain multiple lens elements. Therefore, f_o is measured from an effective plane within the objective lens body, which is not normally marked. Instead, objective lens manufacturers also state a working distance for the lens, which is defined as the distance between the sample coverslip and the front element of the lens when the sample is at f_o (figure 5.2).

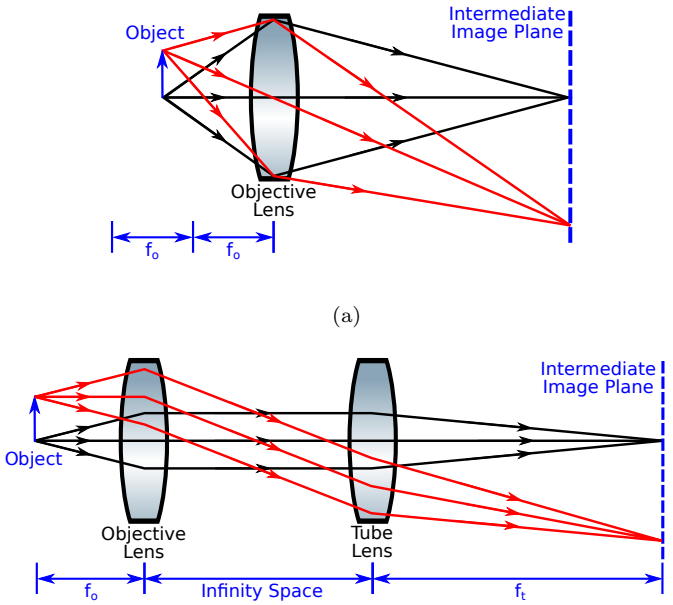

Figure 5.1: Optical schematics of **(a)** a finite-conjugate optical system where the sample is positioned between f_o and $2f_o$ and the objective lens focuses and forms an image at a finite distance, and **(b)** an infinite-conjugate optical system where the sample is positioned at f_o and objective lens does not directly form a real image of the object, therefore a tube lens with focal length f_t must be used to focus the collimated beam. The collimated path is referred to as the infinity space.

This figure partly includes illustrations of optical components from the gwoptics ComponentLibrary designed by Alexander Franzen with reuse permitted under a CC BY-NC 3.0 licence

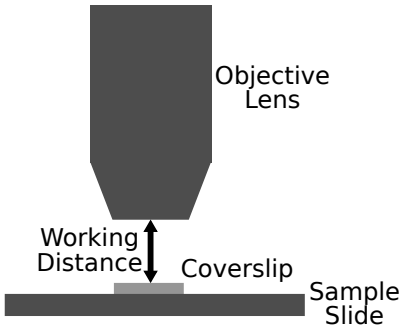

Figure 5.2: Illustration of the definition of the working distance of an objective lens with reference to the sample coverslip.

Finite-conjugate imaging systems can produce highly capable low-cost microscopes, such as the one our research group has previously published which enables computational SRRF imaging [140]. However, infinite-conjugate systems allow multichannel microscopes to be easily created. The reason for this is non-focusing optics for splitting light into different detection channels, such as dichroic mirrors and beamsplitters,

can be placed between the objective and tube lenses in the "infinity space" without introducing spherical aberration into the system and without changing the position of the image plane [150]. Therefore the M4All TIE and fluorescence, and dual channel fluorescence microscopes in the following sections were designed as infinite-conjugate systems. In microscopy infinite-conjugate systems are also commonly referred to as infinity-corrected microscopes. The following introductory sections explain the theory that was used to design the M4All microscopes.

To determine the appropriate focal length for the tube lenses in the infinity-corrected system (f_t), the required imaging field of view (FOV) must first be decided. The lateral magnification (M) needed to create the required FOV is the ratio between the dimension of the camera sensor (the smallest dimension if not square) and the FOV:

$$M = \frac{camera\ sensor\ dimension}{FOV} \tag{5.1}$$

M is also equal to the ratio between f_t and the objective lens effective focal length, f_o (equation 5.2) [151]. Therefore knowing M and f_o, means f_t can be calculated using equation 5.3.

$$M = \frac{f_t}{f_o} \tag{5.2}$$

$$f_t = M f_o \tag{5.3}$$

Nyquist Sampling Theorem

The Nyquist sampling theorem states that to adequately reconstruct a signal, the sampling frequency must be at least twice the highest frequency of the signal [152]. In microscopy, the resolution of the system can be considered in terms of the imaging spatial frequency and so the critical sampling distance is the pixel size required to adequately reconstruct the sample. Therefore according to Nyquist's theorem the effective pixel size, taking into account the optical magnification of the microscope, must be at least half the size of the smallest resolvable sample feature [153].

The smallest resolvable lateral feature of a widefield microscope can be defined by Abbe's diffraction limit where the resolution, d, is dependent upon the wavelength, λ, and the numerical aperture of the objective lens, NA [154]:

$$d = \frac{\lambda}{2NA} \tag{5.4}$$

Thus for a wide field microscope the lateral critical Nyquist sampling distance is given by:

$$\Delta_x = \frac{\lambda}{4NA} \tag{5.5}$$

To calculate whether the system is Nyquist sampled laterally, the sampling distance of the system is calculated using equation 5.6 and compared to the value obtained using equation 5.5. If the sampling distance is larger than Δ_x, the specimen will be undersampled and information will be lost. Therefore the optics must be chosen so that the sampling distance is smaller than the critical sampling distance (oversampling).

$$sampling\ distance = \frac{pixel\ size}{M} \tag{5.6}$$

Divergence Calculations

A problem that can occur when designing imaging systems is the required FOV being clipped on one of the optical elements due to beam divergence from the objective lens. To theoretically determine whether clipping will occur, calculation of beam divergence can be carried out. In this thesis I will refer to these calculations as "divergence analysis". For simplicity, the infinity-corrected objective lens will be considered as a single lens element in this analysis.

Imaging a point on the sample which lies on the centre of the optical axis will result in collimated rays which are parallel to the optical axis (depicted by the black rays in figures 5.1(b) and 5.3(a)). A point on the sample further away from the optical axis will still produce collimated rays, however they will diverge away from the optical axis (depicted by the red rays in figures 5.1(b) and 5.3(a)). The half angular field of view

($AFOV/2$) defines the angle of divergence between rays originating from a sample point on the optical axis and the diverging rays.

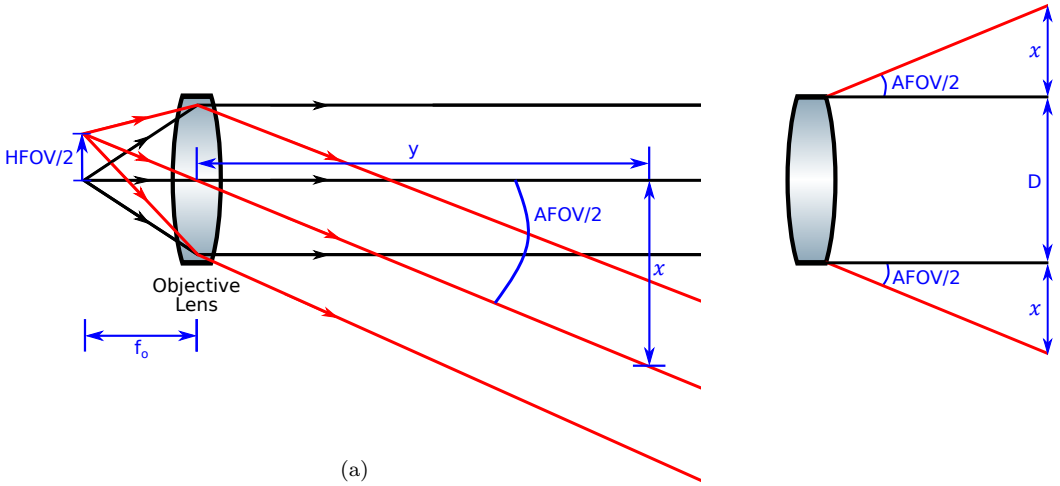

Figure 5.3: **(a)** Schematic indicating the variables needed to analyse the divergence of an objective lens, including the horizontal field of view ($HFOV$), the angular field of view ($AFOV$) and the effective focal length of the objective lens (f_o). The divergence x at a distance along the optical axis y is calculated using equation 5.8. **(b)** Schematic showing that to calculate the total beam width at a distance y then the diameter of the objective lens aperture D also needs to be added.

This figure partly includes illustrations of optical components from the gwoptics ComponentLibrary designed by Alexander Franzen with reuse permitted under a CC BY-NC 3.0 licence

The full $AFOV$ is dependent upon the horizontal field of view ($HFOV$) and f_o, and can be worked out from figure 5.3(a) using trigonometry:

$$AFOV = 2 \times tan^{-1}\left(\frac{HFOV}{2f_o}\right) \tag{5.7}$$

Also from trigonometry, the divergence on one side of the optical axis, x, at a distance y from the objective lens is therefore calculated by:

$$x = y \times tan\left(\frac{AFOV}{2}\right) \tag{5.8}$$

To calculate the full width of the beam for a particular FOV at a point along the optical axis, the aperture of the objective lens must also be taken into account. If unknown, the diameter of the aperture, D, can be calculated by [155]:

$$D = 2NAf_o \tag{5.9}$$

Therefore the beam width is calculated as in equation 5.10. If the beam width is larger than the dimensions of an optical element at distance y along the optical axis then clipping will occur.

$$beam\ width = 2x + D \tag{5.10}$$

I carried out a divergence analysis for the M4All microscopes manually using the above equations (section 5.2.2). At the time we were not aware there was a Python module available which enables ray tracing based on ray transfer matrices [156]. However, we can now highly recommend using the module for checking clipping and vignetting prior to building optical systems as it has been used successfully for other projects in our research group. Further information on ray transfer matrices is given in the next section.

5.1.2 Ray Transfer Matrix Analysis (RTMA)

RTMA Theory

Along with the calculations presented in section 5.1.1, simulation of optical systems during the design process is beneficial as it can highlight problem areas and provides a better understanding of the system and its limitations before construction. Optical engineers often have knowledge and use of specialised software for optical design, such as Zemax and CODE V [156]. There is a large learning curve involved in using these packages [156] and they also include a number of advanced features that are not directly relevant for the intended multidisciplinary use of the M4All system. Along with often expensive maintenance costs of subscriptions and licenses, these software packages are not open-source, therefore also not in keeping with the value that the M4All system aims to bring to the open-source community.

An alternative to complex optical design software is the use of ray transfer matrix analysis (RTMA), also known as ABCD matrix analysis, for mathematical ray tracing within the paraxial approximation [156]. Paraxial rays are those which make a small angle (θ) to the system's optical axis such that the small-angle approximation can be

used, where $sin(\theta) \approx \theta$ [157]. Under the paraxial approximation RTMA can be used to calculate magnifications, focal lengths and imaging planes, however is not suitable for analysing aberrations [158] as they are higher-order effects [159]. For high-NA (>0.5) systems, the RTMA approach can be helpful in a first pass assessment of the viability of the system.

Using a Cartesian coordinate system, a ray at a plane along the optical axis, z, will have a height, y, and angle, θ, with respect to z [159], which is represented as a column vector [156]:

$$\boldsymbol{r} = \begin{bmatrix} y \\ \theta \end{bmatrix} \tag{5.11}$$

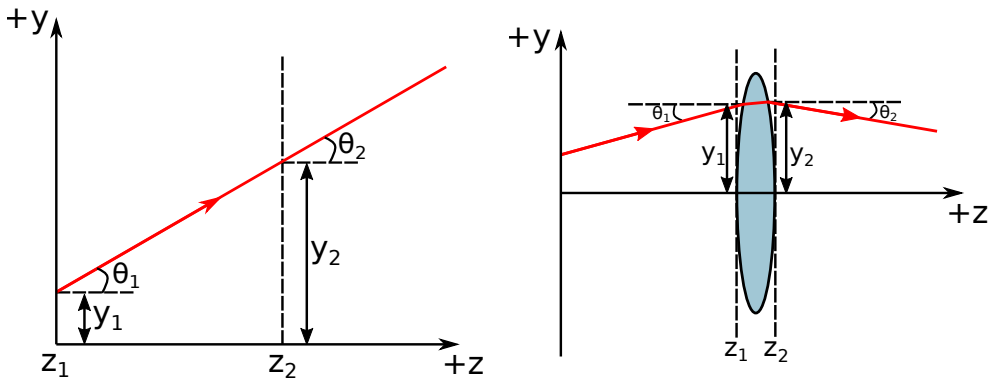

Figure 5.4: **(a)** Schematic for the propagation of a ray in free space where two reference planes, z_1 and z_2, and the corresponding height, y, and angle, θ, with respect to the optical axis z at each plane are indicated. **(b)** Schematic for the propagation of a ray through a thin lens where z_1 and z_2 correspond to the front and back surfaces of the lens.

In RTMA the ray vector is transformed through different optical elements or free space which are described by ABCD matrices [156], known as transfer matrices. The output ray vector at plane 2, z_2, is defined by left multiplication of the input ray vector at plane 1, z_1, with the transfer matrix (equation 5.12). Examples of input and output rays and planes for free space and a thin lens are illustrated in figure 5.4.

$$\begin{bmatrix} y_2 \\ \theta_2 \end{bmatrix} = \begin{bmatrix} A & B \\ C & D \end{bmatrix} \begin{bmatrix} y_1 \\ \theta_1 \end{bmatrix} = \begin{bmatrix} Ay_1 + B\theta_1 \\ Cy_1 + D\theta_1 \end{bmatrix} \tag{5.12}$$

Matrices 5.13 and 5.14 are the specific ray transfer matrices for free space and a thin lens respectively, where d is the propagation distance in free space and f is the focal length of the thin lens [156] (see [159] for matrix derivations). If the system contains multiple free space and optical elements, the ABCD matrix for the total system is the left multiplication of the matrices for each element.

$$\begin{bmatrix} 1 & d \\ 0 & 1 \end{bmatrix} \tag{5.13}$$

$$\begin{bmatrix} 1 & 0 \\ -\frac{1}{f} & 1 \end{bmatrix} \tag{5.14}$$

The total ABCD matrix can be used to derive some useful properties of the system [156, 159]:

- If $B = 0$ the system produces a real image at the output plane from an object at the input plane, where y_2 is independent of θ_1. The lateral and angular magnifications in this case are given by A and D respectively (a negative A value indicates an inverted image).
- If $C = 0$ the system is a telescopic system where parallel rays entering the system at an angle θ_1 at the input plane will remain parallel to one another at the output plane at a new angle θ_2 .
- If $A = 0$, packets of parallel input rays will focus at points on the output reference plane (the back focal plane). The opposite occurs for $D = 0$ where rays originating from points along the input reference plane (the front focal plane) will leave the system as packets of parallel rays, which is the case for an infinite-conjugate objective lens.

Application to Infinity-Corrected Systems

For an infinity-corrected multichannel system, whether it be brightfield or fluorescence microscopy, or a mix of the two, it is important for our imaging requirements that the system is set up correctly so each channel has equal lateral magnifications, especially

for colocalization studies. To ensure equal magnifications, the objective lens must be positioned at the correct working distance to the sample. If the objective lens is not positioned correctly, the path between the objective lens and the tube lenses will not be collimated. Therefore due to the different path lengths of each detection channel, the beam will diverge by differing degrees for each channel, thus resulting in different magnifications when focused onto the cameras. RTMA allows us to model to what extent the lateral magnification for multiple channels vary at different objective lens positions. This section outlines the model theory and the model is then shown in practice in section 5.2.4 for our M4All TIE and fluorescence microscope where we also use the model data as a calibration and alignment tool for multichannel microscopes.

The variables for RTMA of a single infinity-corrected imaging channel are set up as shown in figure 5.5. We define the total length of the channel from the sample to the camera sensor as *d_total*. Treating the objective lens as a single thin lens, the distance between the sample and the objective lens is *d_sample*. The distance between the objective lens and the camera sensor, and the objective lens and the tube lens is *d_intercam* and *d_interlens* respectively. Finally, we define the distance between the tube lens and the camera sensor as *d_cam*.

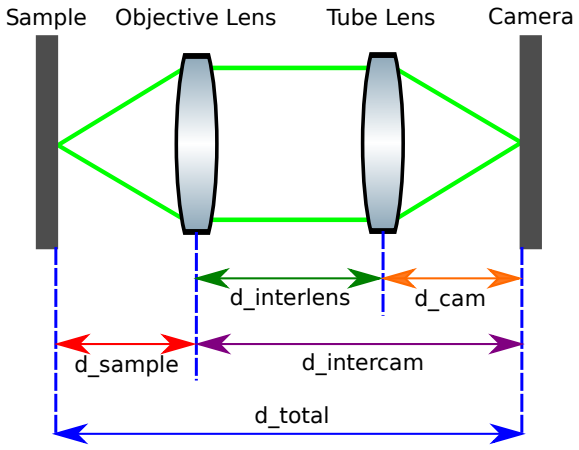

Figure 5.5: Simplified schematic of a single infinity-corrected imaging channel to define variables for ray transfer matrix analysis.

This figure partly includes illustrations of optical components from the gwoptics ComponentLibrary designed by Alexander Franzen with reuse permitted under a CC BY-NC 3.0 licence

The defined variables, along with f_o and f_t, can be substituted into the ABCD matrices 5.13 and 5.14 to build the matrix equation 5.15 for the infinity-corrected

imaging channel (where the matrices are left multiplied in the order they are positioned in the optical path).

$$\begin{bmatrix} x_2 \\ \theta_2 \end{bmatrix} = \begin{bmatrix} 1 & d_cam \\ 0 & 1 \end{bmatrix} \begin{bmatrix} 1 & 0 \\ -\frac{1}{f_t} & 1 \end{bmatrix} \begin{bmatrix} 1 & d_interlens \\ 0 & 1 \end{bmatrix} \begin{bmatrix} 1 & 0 \\ -\frac{1}{f_o} & 1 \end{bmatrix} \begin{bmatrix} 1 & d_sample \\ 0 & 1 \end{bmatrix} \begin{bmatrix} x_1 \\ \theta_1 \end{bmatrix} \tag{5.15}$$

The variable *d_total* is first set. Then, in a correctly aligned system, *d_sample* is equal to the effective focal length of the objective lens and *d_cam* is equal to f_t. The following definitions can also be made for *d_intercam* and *d_interlens*:

$$d_intercam = d_total - d_sample \tag{5.16}$$

$$d_interlens = d_intercam - d_cam \tag{5.17}$$

Upon substituting the variable values into the matrix equation for a correctly aligned system and multiplying the transfer matrices to obtain a single transfer matrix for the total channel, the lateral magnification of the image, A, will equal the value M obtained using equation 5.2.

To model the magnification of the channel when the objective lens is not at the correct working distance, we iterate the matrix equation 5.15 over a range of suitable *d_sample* values, centred around the real effective focal length of the objective lens, f_o. Iterating the objective lens position around f_o is equivalent to practically moving the objective lens the same range around the working distance value. As values for *d_total*, f_o and f_t are set for each channel and we define *d_intercam* and *d_interlens* according to equations 5.16 and 5.17, *d_cam* is the only unknown variable. Therefore for each iteration of *d_sample*, the matrix equation can be solved for *d_cam*. Substituting the solved *d_cam* value for each *d_sample* value back into the matrix equation, allows the lateral magnification A to be determined. A plot of lateral magnification vs *d_sample* shows the deviation in magnification when the objective lens is moved away from the correct working distance. Repeating the analysis for each channel in a multichannel microscope allows the difference in magnification between each channel to be assessed when the objective lens is not at the correct position.

5.2 M4All TIE and Fluorescence Microscope

5.2.1 Camera and Lens Selection

As discussed in section 4.2, one of our aims was to develop a low-cost multichannel microscope combining TIE and fluorescence microscopy. An extension of the initial test design in figure 4.2 can be seen in figure 5.6, where a second beamsplitter, 50:50, was added to create two more brightfield channels for TIE microscopy. Using three brightfield channels allows the three images required for TIE microscopy to be acquired in a single shot by adjusting the focal position of the three tube lenses to image a different focal plane on each channel.

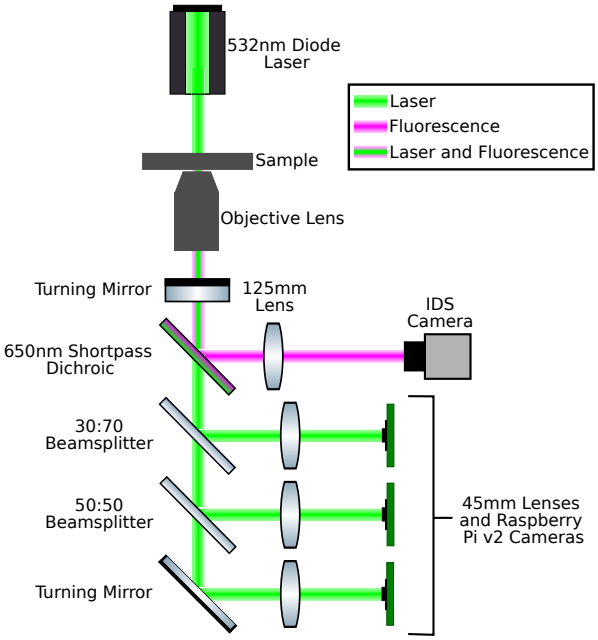

Figure 5.6: TIE and fluorescence microscope optical design schematic. This is an extension of the design in figure 4.2, including two more brightfield channels, separated by a 50:50 beamsplitter, to allow for multifocal plane microscopy. The turning mirror on the third brightfield channel is included to make the system more compact. Tube lens focal lengths determined by equations 5.1 and 5.3.

This figure partly includes illustrations of optical components from the gwoptics ComponentLibrary designed by Alexander Franzen with reuse permitted under a CC BY-NC 3.0 licence

For the brightfield channels we wanted to use as low-cost a camera as possible which still allowed suitable data to be acquired for TIE processing. It has been shown that there is no statistically significant difference between the TIE refractive index measurement results produced from data acquired by the very low-cost Raspberry Pi

v2 camera modules and the more expensive IDS CMOS camera (UI-3060CP-M-GL Rev. 2) [104]. Therefore, due to the low price of the Raspberry Pi cameras and the Raspberry Pi computers themselves (compared to traditional PC's) we chose to continue using them for the brightfield detection branches.

We however required a camera with greater quantum efficiency for the fluorescence channel. The IDS CMOS camera has a Sony IMX174 sensor which is 11.345 mm × 7.126 mm in size and has 5.86 μm square pixels, allowing for a better signal to noise ratio (SNR) and sensitivity compared to the Raspberry Pi v2 camera which has a Sony IMX219 3.68 mm × 2.76 mm sensor with 1.12 μm square pixels. The IDS camera has been shown to achieve a resolution of 115 nm from SRRF microscopy when combined with the OpenFlexure microscope and a finite oil immersion objective lens (1.25 NA, 100×) [140]. Therefore, due to the combination of the camera's technical capability and its reasonable $<$ £1k price point, we chose the IDS camera for the fluorescence channel.

Also discussed in section 4.2, was our desired imaging FOV of 250 μm x 250 μm for our application of imaging mitochondria and bacteria in macrophages. The specified FOV would allow us to image multiple cells in the same FOV whilst retaining good spatial sampling. The total system magnification required to achieve a 250 μm x 250 μm FOV, based on our camera selections, was 10x for the brightfield channels and 28x for the fluorescence channel, using equation 5.1.

For TIE and fluorescence microscopy, we required a low-cost infinity-corrected objective lens ($\leq$ £150) with a suitably high NA and for use with 0.17 mm coverslips. Therefore, we chose to use a Newport LI-40X objective lens (40x, 0.65 NA) with 4.5 mm effective focal length and 0.36 mm working distance. Thus, using equation 5.3, the tube lens focal lengths required for the brightfield and fluorescence channels were 45 mm and 126 mm respectively. Therefore we used Thorlabs 45 mm and 125 mm achromatic doublets (note: 125 mm was the closest standard focal length lens to 126 mm available). The choice of using achromatic doublets as opposed to speciality infinity-corrected tube lenses came down to cost (tens of pounds versus hundreds of pounds) and to allow for our custom FOV (speciality tube lenses typically have longer focal lengths of 160−200 mm).

To check whether the designed system produced images which were at least critically Nyquist sampled, we used the equations in section 5.1.1. The critical Nyquist sampling distance (equation 5.5) for the brightfield channels was 204 nm, using $\lambda_{em} = 532\,nm$. Using equation 5.6 the practical sampling distance of the designed brightfield channels was 112 nm per pixel and so the brightfield channels were oversampled, as desired. For the fluorescence channel, the critical Nyquist sampling distance was 250 nm, using $\lambda_{em} = 650\,nm$, and the practical sampling distance was 209 nm. So the fluorescence channel was also oversampled and thus the chosen optical components for the TIE and fluorescence microscope were deemed to adequately reconstruct the sample according to Nyquist's theorem.

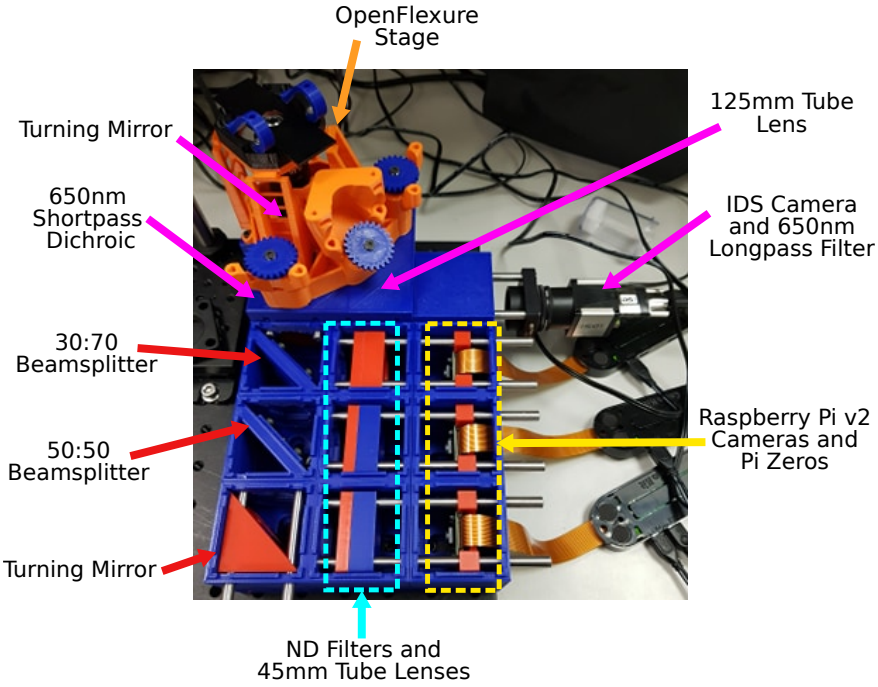

Figure 5.7: First iteration of a TIE and fluorescence microscope built using the M4All system in combination with the OpenFlexure microscope stage.

The initial setup of the M4All TIE and fluorescence microscope can be seen in figure 5.7. To avoid camera saturation on the brightfield channels, neutral density (ND) filters (Thorlabs ND20B) were added to attenuate the laser light. A 650 nm longpass filter (Thorlabs FELH0650) was also included in front of the fluorescence channel camera

to reject any remaining laser light from the channel which would reduce the signal to noise ratio.

5.2.2 Imaging Challenges

Initially we wanted to set the TIE and fluorescence microscope up with the three brightfield channels each imaging the same focal plane before adjusting the tube lenses to allow for multifocal plane imaging for TIE microscopy. The first set of images captured on the microscope from the three brightfield channels can be seen in figure 5.8.

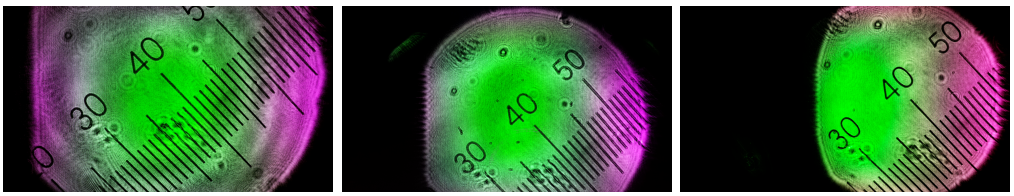

(a) (b) (c)

Figure 5.8: Initial brightfield images of a 10 μm graticule slide from the M4All TIE and fluorescence microscope: **(a)** first brightfield channel, **(b)** second brightfield channel, **(c)** third brightfield channel.

From the image data set we highlighted the following imaging challenges (note that, some of these were expected but we didn't know to what extent and others were easily explained once we saw them and arose from tolerances in hardware):

- Magnification differences between the channels.
- Image clipping on the third brightfield channel.
- Translation effects:
    * Refractive effects - expected image translation following transmission through the dichroic mirror and beamsplitters.
    * Differences in image height on the cameras due to 3D printed insert tolerances.
- Colour crosstalk on the Raspberry Pi v2 cameras.
- Lens/barrel distortion in the images.

The remainder of this section will discuss the above imaging challenges in further

detail and the solutions that we implemented to address them (note they are listed and discussed in no particular order as their importance would depend on the final imaging application).

Magnification

From figure 5.8 it can be seen that the three brightfield channels did not have equal FOV's and magnifications when the tube lenses and sample were first focused and aligned. The difference is a result of the objective lens not being positioned at the correct working distance to the sample, causing the infinity space to not be collimated, as discussed in section 5.1.2. As there is an interlink between the tube lens position and the corresponding focal plane in the sample, setting the tube lenses at the in focus position for the correct objective working distance means if the lenses were to be set up correctly the first time, the microscope would always be imaging at the correct working distance and thus correct magnification.

One potential approach to position the objective lens to the correct working distance was to use a mechanical shim, or spacer. To do this, we tried fixing two coverslips, one on top of the other, onto a microscope slide (figure 5.9). As the working distance of the Newport LI-40X objective lens was 0.36 mm and the thickness of a coverslip is 0.17 mm, the thickness of two coverslips was close to the working distance. The objective lens was carefully raised until it was just touching the top coverslip, where at this point the objective lens would be placed at roughly the correct working distance. We had also drawn a cross on the microscope slide before mounting the coverslips on top which was used to then focus the tube lenses to image the cross on the cameras after positioning the objective lens. However, it was difficult to focus on the cross and because of the risk of damaging the objective lens by touching the coverslip the method was unsuitable.



Figure 5.9: Cross drawn on microscope slide with permanent marker pen. A drop of immersion oil was placed on the cross before fixing two 0.17 mm thick coverslips on top and securing with nail varnish.

Next, I carried out a ray transfer matrix analysis to investigate theoretically how the magnifications of the three channels vary as the objective is moved further away from the working distance on either side of it (i.e. the objective is too close or too far away from the sample). I then used the analysis as a tool for calibrating the microscope which will be described fully in section 5.2.4.

Clipping

Outlined in section 5.1.1 is the problem of image clipping due to divergence. The problem can be seen in figure 5.8(c), where the image was significantly clipped compared to the first two channels in figures 5.8(a) and 5.8(b). To determine which optical element the beam was being clipped on I carried out a divergence analysis for each optical element position in the microscope. Note that again this can now easily be carried out using the ray tracing python module [156] which we recommend for future applications, however working through the method outlined in section 5.1.1 is still valid.

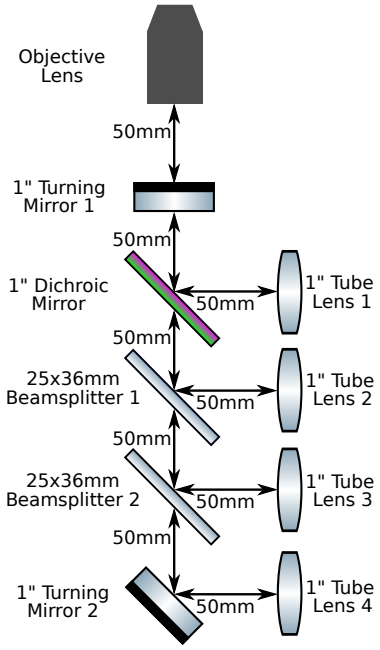

Figure 5.10: Schematic of the fluorescence and TIE microscope noting the size of the optics and the distances between them which are used for divergence calculations and analysis.

This figure partly includes illustrations of optical components from the gwoptics ComponentLibrary designed by Alexander Franzen with reuse permitted under a CC BY-NC 3.0 licence

The following variables were defined for the analysis; $HFOV$=250 μm, f_o=4.5 mm and NA=0.65. The half AFOV was 0.027 from equation 5.7 and D=5.85 mm from

equation 5.9. I also defined the optics as being positioned at the centre of each cube, therefore the distance between each element was 50 mm, as shown in figure 5.10, giving the value of y for each element. Equations 5.8 and 5.10 were then used to calculate x and the beam width respectively. It can be seen in figure 5.10 that some optical elements were orientated at 90° to the optical axis, whereas others were orientated at 45°. If the optic was at 90° then the beam width cross section was simply the calculated beam width value. If the optic was at 45° then the cross section of the beam width was calculated as:

$$beam\ width\ cross\ section = \frac{beam\ width}{\frac{1}{\sqrt{2}}} \tag{5.18}$$

The results are shown in table 5.1 where the optical elements are listed in order of their distance from the objective lens. The analysis results showed the beam was being clipped on the 1 inch turning mirror on the third brightfield channel (turning mirror 2), highlighted in red in table 5.1, where the beam width cross section was larger than the optical element size. Therefore I replaced the mirror with a 25 x 36 mm mirror (Thorlabs PFR10-P01) which is larger than the beam width cross section. Replacing the component fixed the clipping problem and thus the approach works.

Optical Element	y (mm)	x (mm)	Beam Width Cross Section (mm)	Optical Element Size (mm)
Turning Mirror 1	50	1.35	12.09	25.40
Dichroic Mirror	100	2.70	15.90	25.40
Tube Lens 1	150	4.05	13.95	25.40
Beamsplitter 1	150	4.05	19.72	36.00
Tube Lens 2	200	5.40	16.65	25.40
Beamsplitter 2	200	5.40	23.54	36.00
Tube Lens 3	250	6.75	19.35	25.40
Turning Mirror 2	250	6.75	27.37	25.40
Tube Lens 4	300	8.10	22.05	25.40

Table 5.1: Divergence analysis results for the M4All TIE and fluorescence microscope. The optical elements are listed in order of their position in the optical path. The y distances are the distance between the back face of the objective lens and the centre of the optical element. Equation 5.8 was used to calculate x. The beam width cross section is the width of the beam at the optical element for the desired FOV, calculated using equation 5.10 (if the element was at 45° then equation 5.18 was also used). The highlighted values in red indicate that clipping occurred on turning mirror 2.

Camera Height and Image Translation

Figure 5.8 shows that the camera on the second brightfield channel was at a different height to the first and third brightfield channels (the camera was higher, causing the image to be lower on the sensor). The Raspberry Pi camera insert used in the initial setup in figure 5.7 was an older version than the final design in figure 4.16(f). The older version did not include the indent for the camera to sit into and so there was a larger tolerance in camera position on the insert. The problem was solved in the final version of the microscope by using the insert in figure 4.16(f).

It can also be seen in figure 5.8 that there was an image translation from left to right as the bean transmits through the beamsplitters. The translation is a feature of refracting optics and was therefore expected. Although we have not corrected for the translation in our final version of the microscope, it is possible in future to offset the cubes to compensate for the translation.

Colour Crosstalk

Colour crosstalk due to the lenslet array on the Raspberry Pi v2 camera module can be seen in figure 5.8. The problem of colour crosstalk was not a surprise as we knew from Bowman *et al.* [143] and previous work from our research group [104] that the problem would occur, but I am including a discussion here for reference. The following discussion relies heavily on information from Bowman *et al.* [143].

The Sony IMX219 sensor on the Raspberry Pi v2 camera module has a microlens array bonded to it to improve the sensor's low light performance by focusing the light onto each pixel. The microlens array is designed for use with the very short focal length (3.04 mm) lens that is provided with the camera module. Using such a short focal length lens causes light at the edge of the sensor to not be normally incident on the sensor. Therefore Chief Ray Angle (CRA) compensation is used where the microlenses towards the edges of the sensor are spaced with an offset compared to the pixels so that the light is focused correctly on each pixel. Whereas the microlenses in the centre of the sensor, where light is normally incident, are spaced centred above each pixel.

The issue with colour crosstalk arises when the stock lens provided with the camera

module is removed and replaced by a lens with a different focal length, thus changing the angle of incidence of the rays at the edges of the sensor. As the microlens array spacing is not designed for the new angle of incidence, light incident on the microlenses may focus onto the wrong pixels and due to the Bayer filter will lead to colour crosstalk. A Bayer filter is an RGB colour filter array which is placed on top of the image sensor to create a colour image. The red, green and blue filters are arranged in a mosaic pattern where a quarter of the filters are red, half are green, and a quarter are blue. In the M4All TIE and fluorescence microscope we replaced the stock lens on each brightfield channel camera module with 1 inch 45 mm Thorlabs achromatic doublets as tube lenses for the infinity-corrected system, as discussed in section 5.2.1, which is the reason for the colour crosstalk effect in figure 5.8.

Bowman *et al.* [143] have developed a colour correction pipeline which is applied during post-processing to address the problem. Although I have not used the correction in my research, the pipeline could be used in future to correct for colour crosstalk in the TIE and fluorescence microscope. A second option could be to use a different camera module which does not include a microlens array and is compatible with different focusing lenses. Since developing the M4All TIE and fluorescence microscope, a new Raspberry Pi HQ camera module became available which has a larger sensor size, larger pixels and no microlens array, thus mitigates the problem of colour crosstalk. Therefore when we developed the M4All dual channel fluorescence microscope, which will be discussed in section 5.3, we used the new HQ camera module for the detection channels. In future the TIE and fluorescence microscope could be redesigned to also use the new cameras.

Lens Distortion

The f_t values calculated in section 5.2.1 were in theory optimum for the system requirements. However, in practice the brightfield images (figure 5.8) had lens distortion, more specifically barrel (negative) distortion. The refractive power of spherical lenses differs across the diameter of the lens due to the edges of the lens being thinner than at the centre [160]. Therefore if the full aperture of the lens is used, the edges of the lens will

have a lateral magnification which differs to that at the centre calculated from paraxial theory. Thus, straight lines will become distorted towards the edge of the image.

To preserve the desired FOV and correct the distortion, either a multi lens element designed to create a flat image could be used, or potentially swapping the tube lens for one with a larger aperture and only using the centre of the lens may reduce the distortion. However, to avoid the complexity and increased cost of setting up a multi lens element, or adjusting the optics dimensions, the FOV can be traded off by using longer focal length achromatic doublets to correct for the distortion. To practically determine which focal length lens was required for correction, I set up a test rig on an optical bench with standard optomechanics, illustrated in figure 5.11.

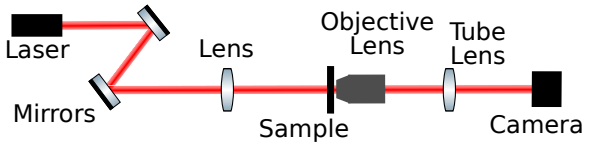

Figure 5.11: Schematic of a simple microscope rig which is sufficient to test the level of lens distortion for different focal length tube lenses, camera and objective lens combinations. Laser - Thorlabs CPS635. Mirrors - Thorlabs PF10-03-P01. Lens - Thorlabs 35 mm bi-convex lens LB1811-A. Sample - 10 μm grid sample. Objective lens - either Newport LI-40X or LI-60X. Tube lens - Thorlabs 50 mm (LB1471-A), 75 mm (LB1901-A), 100 mm (LB1676-A) and 125 mm (LB1904-A) bi-convex lenses. Camera - either Raspberry Pi v2 camera module, Raspberry Pi HQ camera module, IDS CMOS UI-3060CP-M-GL Rev. 2 or Thorlabs CMOS CS235MU.

This figure partly includes illustrations of optical components from the gwoptics ComponentLibrary designed by Alexander Franzen with reuse permitted under a CC BY-NC 3.0 licence

I used the test rig to easily swap out and compare different combinations of objective lenses, tube lenses and cameras. Figure 5.12 shows the results for the Raspberry Pi v2 camera in combination with both the Newport LI-40X (40x, 0.65 NA) and LI-60X (60x, 0.85 NA) objective lenses. Three different focal length Thorlabs bi-convex tube lenses (50 mm, 75 mm and 100 mm) were tested for each objective lens. We used bi-convex lenses as opposed to achromatic doublets because we had a range of focal lengths already available in the lab to test. Barrel distortion can clearly be seen in figures 5.12(a) and 5.12(d) for the 50 mm tube lens. The distortion was reduced in figures 5.12(b) and 5.12(e) for the 75 mm lens. The 100 mm lens in figures 5.12(c) and 5.12(f) produced images with minimal distortion for both objective lenses, though at the expense of reduced FOV. The horizontal FOV in figure 5.12(c) is $\approx$ 160 μm and is $\approx$ 110 μm in figure 5.12(f) compared to the desired FOV of 250 μm.

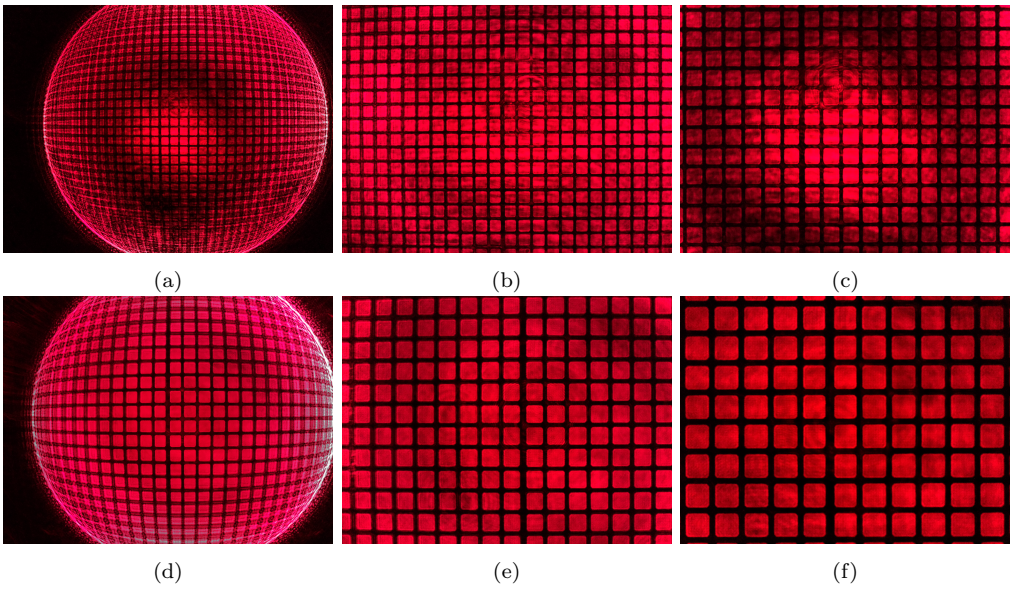

Figure 5.12: Images of a 10 μm calibration grid from the test rig in figure 5.11 showing the level of lens distortion for different combinations of objective and tube lenses for the Raspberry Pi v2 camera module. **(a)** Newport LI-40X and Thorlabs 50 mm bi-convex tube lens. **(b)** Newport LI-40X and Thorlabs 75 mm bi-convex tube lens. **(c)** Newport LI-40X and Thorlabs 100 mm bi-convex tube lens. **(d)** Newport LI-60X and Thorlabs 50 mm bi-convex tube lens. **(e)** Newport LI-60X and Thorlabs 75 mm bi-convex tube lens. **(f)** Newport LI-60X and Thorlabs 100 mm bi-convex tube lens.

I repeated the test for the Raspberry Pi HQ camera (figure 5.13) which had a larger image sensor. Therefore to correct the distortion, a longer focal length tube lens was required than for the v2 camera module - a focal length of 125 mm gave good results for both objective lenses (figures 5.13(c) and 5.13(f)). The resulting horizontal FOV for the 40x and 60x objective lenses were $\approx 230\,\mu$m and $\approx 150\,\mu$m respectively. Therefore the trade off on FOV vs correction was smaller than that with the v2 camera as the imaging sensor is larger. I also tested more expensive cameras (IDS CMOS UI-3060CP-M-GL Rev. 2 and Thorlabs CMOS CS235MU) to compare to the image quality of the Raspberry Pi camera modules. Distortion tests for both cameras can be seen in figures 5.14 and 5.15. In both cases the 125 mm lens gave an adequately flat image with an $\approx 270\,\mu$m horizontal FOV, which is a larger FOV than both of the Raspberry Pi camera modules, again due to a larger sensor size. Directly comparing figures 5.14(d) and 5.15(b) we noted that there was no considerable qualitative difference in the level of distortion or image quality between the two cameras which is important as the Thorlabs CMOS camera was the most expensive.

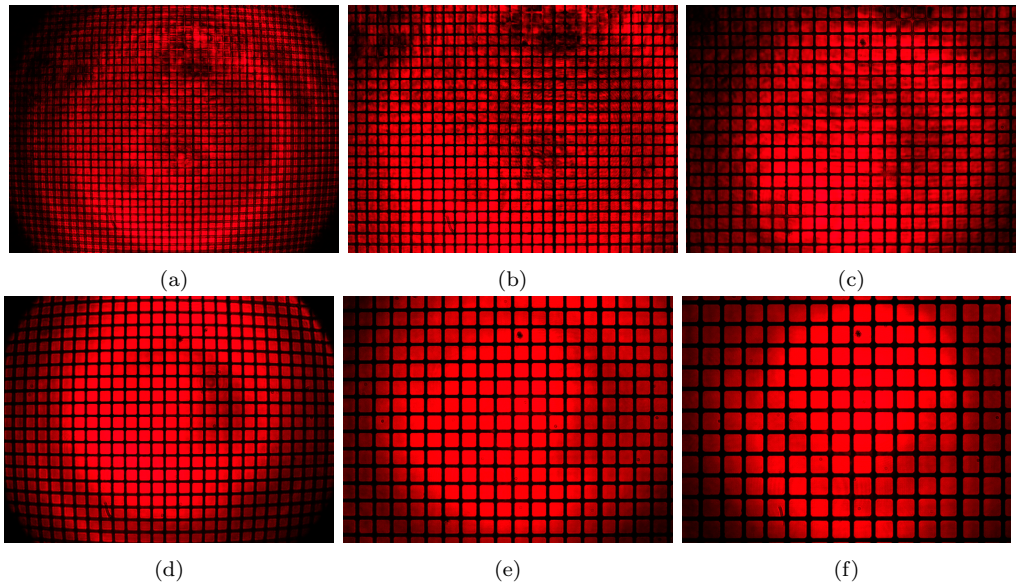

(a) (b) (c)

(d) (e) (f)

Figure 5.13: Images of a 10 μm grid from the test rig showing the level of lens distortion for different combinations of objective and tube lenses for the Raspberry Pi HQ camera module. **(a)** Newport LI-40X and Thorlabs 75 mm bi-convex tube lens. **(b)** Newport LI-40X and Thorlabs 100 mm bi-convex tube lens. **(c)** Newport LI-40X and Thorlabs 125 mm bi-convex tube lens. **(d)** Newport LI-60X and Thorlabs 75 mm bi-convex tube lens. **(e)** Newport LI-60X and Thorlabs 100 mm bi-convex tube lens. **(f)** Newport LI-60X and Thorlabs 125 mm bi-convex tube lens.

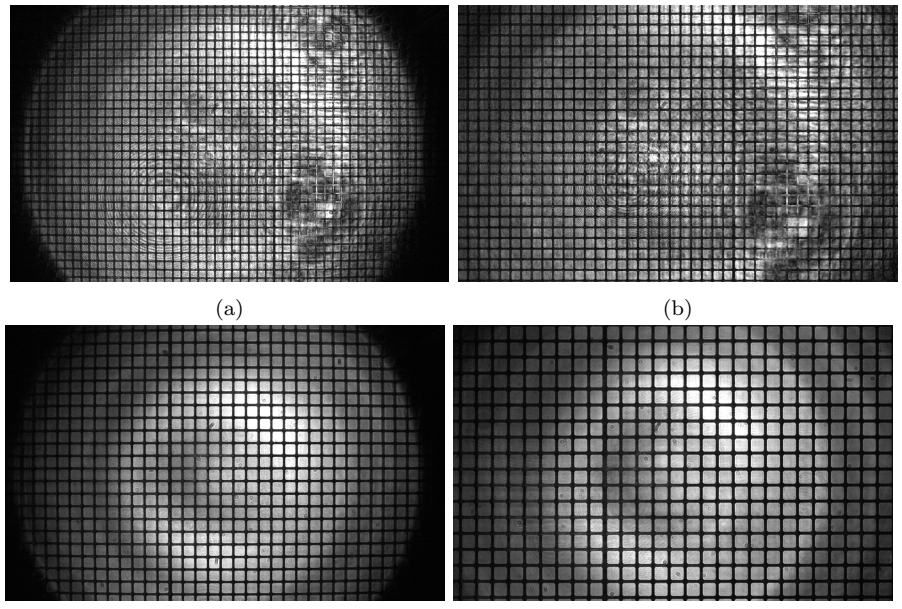

(a) (b)

(c) (d)

Figure 5.14: Images of a 10 μm grid from the test rig showing the level of lens distortion for different combinations of objective and tube lenses for the IDS CMOS camera. **(a)** Newport LI-40X and Thorlabs 100 mm bi-convex tube lens. **(b)** Newport LI-40X and Thorlabs 125 mm bi-convex tube lens. **(c)** Newport LI-60X and Thorlabs 100 mm bi-convex tube lens. **(d)** Newport LI-60X and Thorlabs 125 mm bi-convex tube lens.

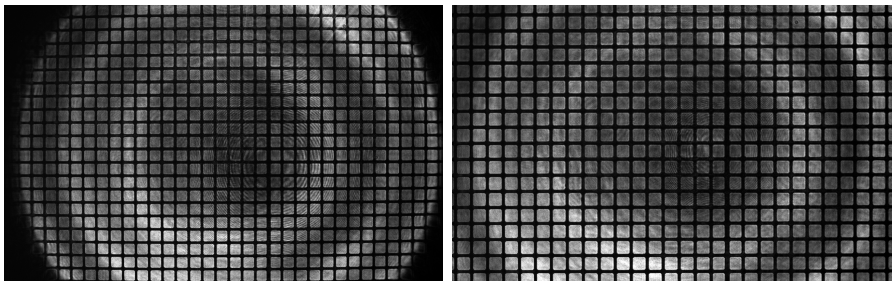

(a) (b)

Figure 5.15: Images of a 10 μm calibration grid taken on the test rig in figure 5.11 showing the level of lens distortion for different combinations of objective and tube lenses for the Thorlabs CMOS camera. **(a)** Newport LI-60X and Thorlabs 100 mm bi-convex tube lens. **(b)** Newport LI-60X and Thorlabs 125 mm bi-convex tube lens.

From the data we note that another option to retain the desired FOV whilst correcting for lens distortion other than correcting with a multi lens element is to use a camera with larger sensor dimensions at the expense of camera cost. We have not redesigned the TIE and fluorescence microscope to correct for the lens distortion due to time constraints, however the information gained from the distortion data acquired on the test rig influenced our design decisions for the dual channel fluorescence microscope in section 5.3. We chose to use the Raspberry Pi HQ cameras in combination with the Newport LI-60X objective lens and Thorlabs 125 mm achromatic doublet tube lenses as the low-cost of the HQ cameras ($\approx$ £50) was a greater priority than the $\approx 100\,\mu$m reduction in desired FOV. If we were to redesign the TIE and fluorescence microscope, we would also use this combination of camera and tube lens with either the Newport LI-40X or LI-60X objective lens.

Whilst the test rig was in place I investigated the difference in levels of chromatic aberration between using the Thorlabs achromatic doublet lenses and Thorlabs bi-convex lenses as tube lenses. Reducing chromatic aberration is important for multicolour imaging, as is the case in the M4All dual channel fluorescence microscope (section 5.3). To test the difference I swapped the laser on the test rig for a WORLD STAR TECH RGB laser to easily switch between illumination wavelengths. Using the IDS CMOS camera I first focused a 125 mm bi-convex lens with the 635 nm laser channel and captured an image. I then captured two further images using the 520 nm and 450 nm laser lines without refocusing the objective or bi-convex lenses. Figure

5.16(a) shows the three images merged together. The same procedure was followed for a 125 mm achromatic doublet lens and the result is shown in figure 5.16(b). Comparing the two images, it can be seen that qualitatively there is noticeably less chromatic aberration in figure 5.16(b), where the black grid lines are sharp compared to figure 5.16(a) where the red and blue chromatic shift of the grid can be seen. Therefore the achromatic doublets are more suitable for multicolour fluorescence imaging than the bi-convex lenses, as expected.

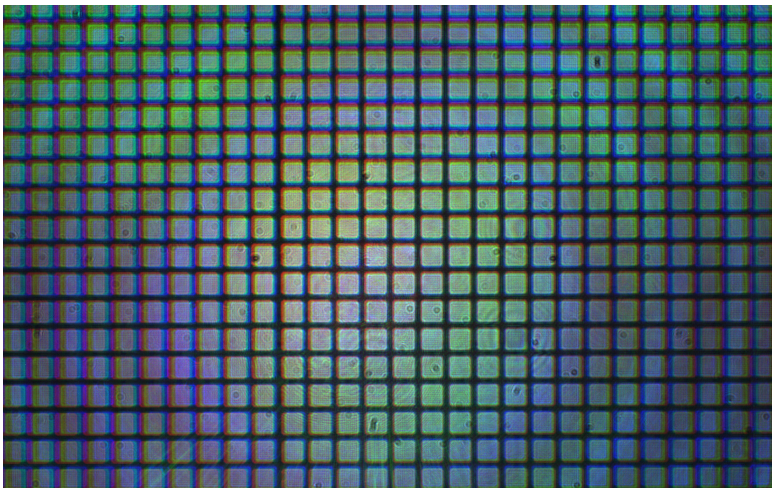

(a)

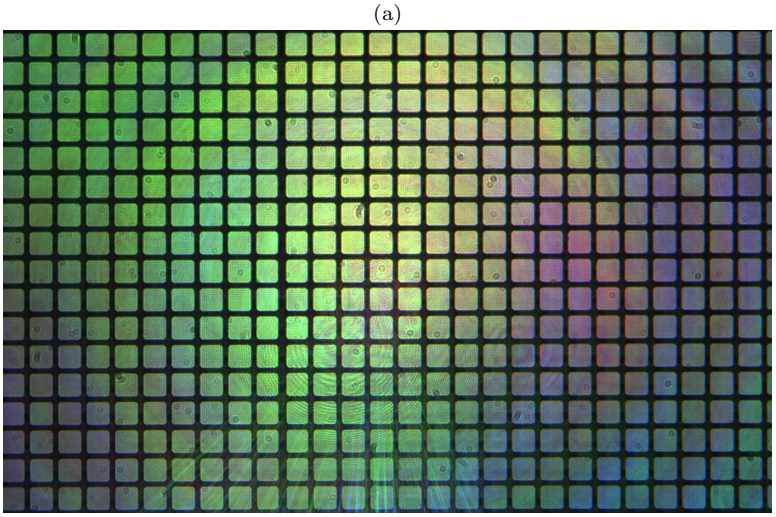

(b)

Figure 5.16: Images of a 10 μm calibration grid from the test rig in figure 5.11 showing the difference in chromatic aberration between a **(a)** Thorlabs bi-convex lens and a **(b)** Thorlabs achromatic doublet lens. There is noticeably less chromatic distortion for the latter.

5.2.3 Final Microscope

Figure 5.17 shows the final version of the M4All TIE and fluorescence microscope. The first image shows a close up of the updated optics inserts within the cube system, which were updated to address some of the problems discussed in section 5.2.2, such as the updated Raspberry Pi camera insert. The beamsplitter inserts were updated to the version in figure 4.17(c) and the 1 inch turning mirror on the third brightfield channel was replaced for a 25 x 36 mm mirror, using the same insert as for the beamsplitters. The second image is an overall view of the microscope with the cube lids on. The illumination rig shown contains the same translation and kinematic mounts as in figure 4.9(a). In this particular photo a WORLD STAR TECH RGB laser diode is coupled into the microscope via a multimode optical fibre, however as discussed, for this microscope we normally used a 532 nm diode laser (Thorlabs CPS532) which is suitable for exciting nanodiamond fluorescence. The Raspberry Pi v2 camera modules are each connected to a different Raspberry Pi Zero board which are contained within a 3D printed holder towards the right of the image. Chapter 6 contains full information on microscope control.

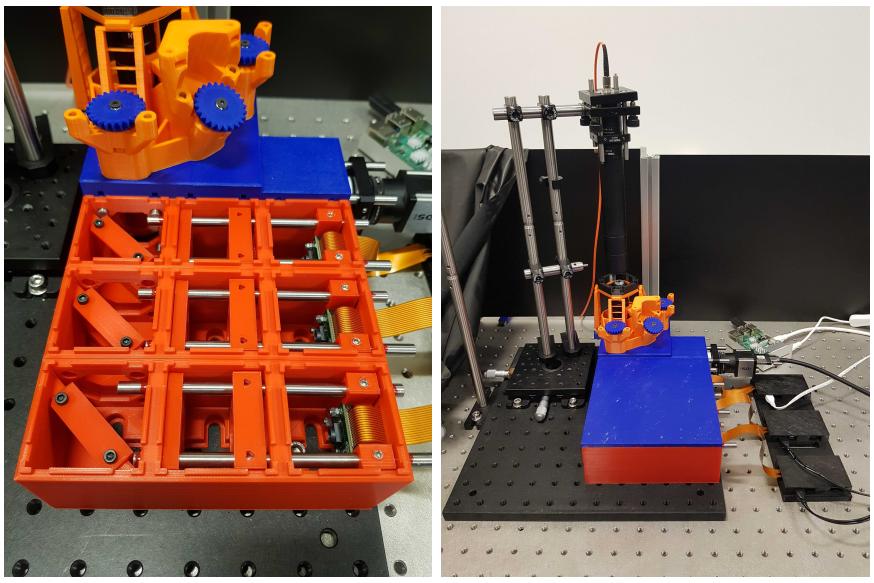

(a) (b)

Figure 5.17: Final version of the M4All TIE and fluorescence microscope. **(a)** Close up image of the optical component inserts within the cubes. **(b)** Overall view of the microscope with the lids on, also showing the illumination rig and the Raspberry Pi Zeros within 3D printed holders.

5.2.4 RTMA Magnification Analysis and Calibration

As discussed in section 5.2.2, the initial data from the M4All TIE and fluorescence microscope (figure 5.8) showed a considerable difference between the magnifications of the three brightfield channels. This section will present the results of carrying out a ray transfer matrix analysis on the system and how we used the analysis data in practice as a calibration tool for the microscope.

Lateral Magnification Analysis

I used the mathematical software package Maple to carry out the ray transfer matrix analysis where I set up the variables and equation 5.15 outlined in section 5.1.2. The variable values used were $f_o = 4.5\,\text{mm}$ and $d_total = 300$, 350 and 400 mm for the three brightfield channels. Equation 5.15 was solved for d_cam for a range of d_sample values from 4.4 mm to 4.6 mm in 0.005 mm steps, which simulates the required position of the tube lens to focus on the camera when the objective lens is moved either 0.1 mm too close or too far away from the sample. The solved d_cam values were then substituted back into the matrix equation 5.15 to determine the lateral magnification at each d_sample distance. The analysis was repeated for each of the brightfield channels by simply changing the d_total value.

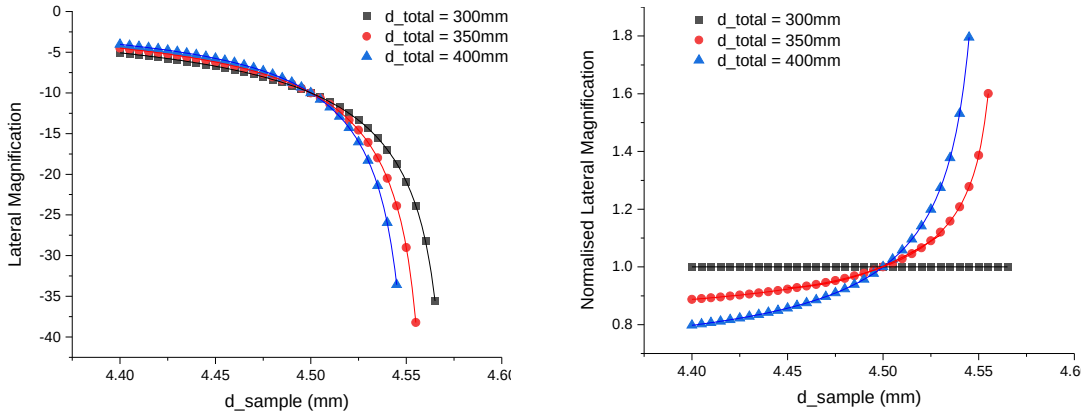

Figure 5.18: **(a)** Plot of lateral magnification (calculated by ray transfer matrix analysis) vs d_sample for the three brightfield channels in the TIE and fluorescence microscope. **(b)** The lateral magnification values in **(a)** have been normalised to the first brightfield channel.

The lateral magnification is plotted against *d_sample* in figure 5.18(a). It can be seen that at the point where $d_sample = f_o$ the three channels have equal magnifications as expected. Then, as the objective lens is moved away from the correct positions, the magnifications vary from one another. When the objective lens is too close to the sample, $d_sample < 4.5\,\text{mm}$, the third channel has the smallest magnification. Whereas the first channel has the smallest magnification when the objective lens is too far away from the sample, $d_sample > 4.5\,\text{mm}$.

Lateral Magnification Calibration

The theoretical data in figure 5.18(a) produced from the RTMA can be used to calibrate the position of the lenses in an infinity-corrected multichannel microscope. We believe this is a novel method that is not only applicable to our M4All system but can be used for aligning any infinity-corrected microscope. However, it is a particularly useful method for our M4All microscopes as they have compact designs, meaning other methods of aligning the objective lens, such as using an autocollimator, are unsuitable.

The process we used to calibrate the microscope lenses was as follows; firstly, the lateral magnification values obtained from the RTMA were normalised to the first detection channel (figure 5.18(b)). We define the normalised values as the theoretical normalised magnifications. After setting up the microscope with each channel in focus, an image of a calibration sample was captured on each channel. Then, the distance, in pixels, of the same feature on each image was measured. We used a $10\,\mu\text{m}$ calibration grid slide, however any sample where the same feature on each image can be measured accurately is suitable. A specific calibration slide allows absolute magnifications to be calibrated and measured, while a general sample will allow for alignment but not confirm the final magnification. From figure 5.19 it can be seen that after drawing a line profile across the grid image (top left), a plot of the line profile was produced (top right). Measuring the corresponding number of pixels for a certain number of grid squares on the line profile was more accurate than measuring the distance on the image.

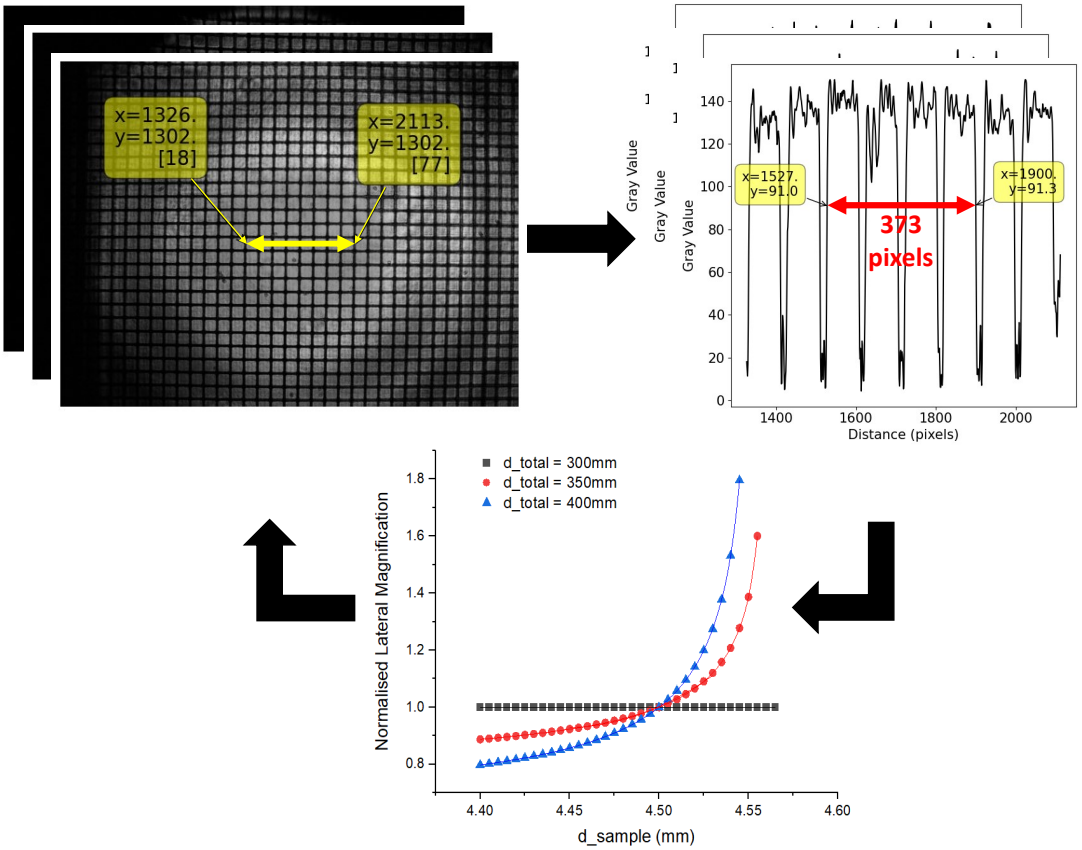

Figure 5.19: Flow chart to highlight the steps in the magnification calibration of an infinity corrected system using RTMA data. A line profile on each channel image of the calibration grid is drawn and then plotted. From the plots the distance (number of pixels) corresponding to a number of grid squares on each channel is obtained. The distances are normalised to the first channel (measured normalised magnifications) and compared to the theoretical plot of normalised lateral magnification to determine the theoretical *d_sample* value. The position of the objective lens is then corrected and the process repeated until $d_sample = f_o$ within the axial resolution of the system.

The distances (number of pixels) for the feature (in this case a certain number of grid squares) from each channel were then normalised to the distance measured for the first channel. We define the normalised distances as the measured normalised magnifications. The benefit of using normalised magnifications vs absolute magnifications is that the real feature size in the image does not need to be known, thereby allowing this method to be used with a general sample, and not just a calibration slide. To determine the predicted error in the position of the objective lens, the measured normalised magnification value for the third channel, the one with the largest *d_total* value, was plotted on the theoretical normalised magnification graph (figure 5.18(b)) and the correspond-

ing *d_sample* value was interpolated, which we define as *d_sample_interpolated*. The error in the position of the objective lens was then calculated as:

$$working\ distance\ error = d_sample_interpolated - f_o \tag{5.19}$$

If the working distance error was a positive value then the objective lens was that magnitude too far away from the sample, and if it was a negative value then it was that magnitude too close to the sample. The objective lens could then be re-positioned by the magnitude and direction determined from the calibration analysis. For our M4All microscopes where we used the OpenFlexure microscope stage, and controlled the movement of the stage with stepper motors, we determined how far the objective lens moved in z per step using the method described in section 5.2.5. After re-positioning the objective lens, the tube lenses were then refocused and the calibration routine repeated to check the new magnifications. The whole process was repeated until the three channels had equal magnifications within the tolerances of the equipment and $d_sample = f_o$ within the optical axial resolution limit. The maximum number of iterations of the calibration we needed to perform on the TIE and fluorescence M4All microscope was three to achieve sufficiently equal magnifications across the three brightfield channels.

To test the repeatability of the calibration process, the tube lenses on the TIE and fluorescence microscope were deliberately moved to the wrong position and then recalibrated. Firstly, the first channel tube lens was moved too close to the camera by an arbitrary distance. The objective lens was then refocused (causing it to be positioned too far away from the sample than the required working distance) and subsequently the other two tube lenses brought into focus at the new objective lens position. The calibration routine was then used to correct for the deliberate miscalibration. I carried out a total of three miscalibrations and recalibrations (labelled as repetition 1,2 and 3 in figure 5.20). Figure 5.20(a) shows the measured normalised magnifications for the three repetitions (only the values for cameras/channels 2 and 3 are shown as the normalised magnification of the first channel is always 1.00). Figure 5.20(b) shows the calculated working distance errors for the three repetitions.

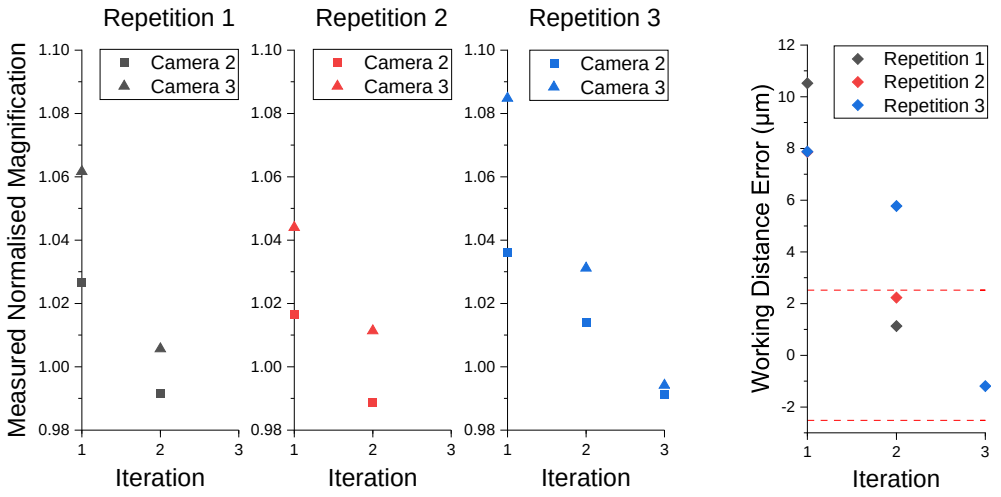

(a) (b)

Figure 5.20: Magnification calibration repeatability data for the situation where the objective lens was deliberately positioned too far away from the sample. **(a)** Three repetitions showing the measured normalised magnification values for two iterations of the calibration routine for repetitions 1 and 2, and three iterations for repetition 3. **(b)** The resulting working distance error for the calibration iterations for each repetition based on the data in **(a)**. The red dashed lines in **(b)** indicate the positive and negative axial resolution values of $\pm 2.518\,\mu$m.

It can be seen from figure 5.20 that for repetitions 1 and 2, two iterations of the calibration routine were required to correct the working distance error to within the axial resolution limit of the system, which is marked by the red dashed lines on the working distance error plot. Whereas repetition 3 required three iterations. We defined the axial resolution, d, using Abbe's axial diffraction formula (equation 5.20). As the excitation wavelength was 532 nm and the NA of the LI-40X objective lens was 0.65, the axial resolution was $2.518\,\mu$m.

$$d = \frac{2\lambda}{NA^2} \tag{5.20}$$

The process was then repeated for the opposite situation where the tube lenses were deliberately moved too far away from the cameras, resulting in the objective lens being positioned too close to the sample than the required working distance. Again for each repetition the working distance error was corrected to within the axial resolution limit of the system within three iterations of the calibration routine (figure 5.21).

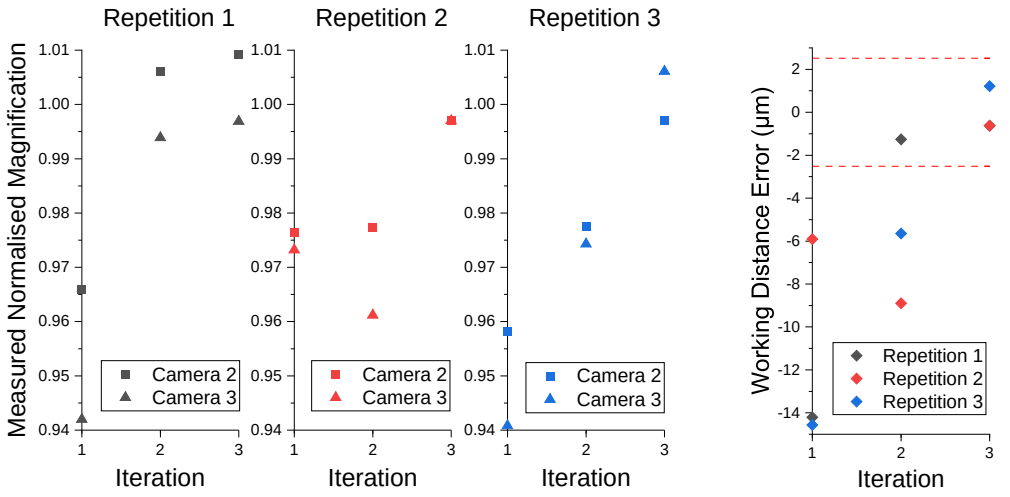

Figure 5.21: Magnification calibration repeatability data for the situation where the objective lens was deliberately positioned too close to the sample. **(a)** Three repetitions showing the measured normalised magnification values for three iterations of the calibration routine for each repetition. **(b)** The resulting working distance error for the three calibration iterations for each repetition based on the data in **(a)**. The red dashed lines in **(b)** indicate the positive and negative axial resolution values of $\pm 2.518\,\mu$m.

Once the position of the objective lens and tube lenses are calibrated, if *d_total* is increased but *d_sample* and *d_cam* remain the same, the magnifications of the three channels should remain equal. To confirm that this was the case for the TIE and fluorescence microscope and to validate the calibration, we increased *d_total* by raising the sample up in increments and refocusing the objective lens each time.

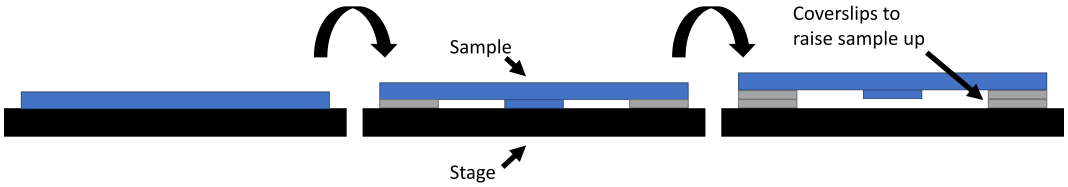

Figure 5.22: Illustration of the process of increasing *d_total* by raising the sample up with coverslips as the axial sample position on the OpenFlexure microscope stage is fixed.

Because the OpenFlexure stage has a fixed sample position, I raised the sample by placing standard 0.17 mm coverslips underneath the sample on either side (depicted in figure 5.22) up to a total of six coverslips high. At each sample height the objective lens was refocused and images were taken on the first and third channels to check their magnification values were still equal. The data is shown in figure 5.23 where the real

magnifications were measured (the expected magnification was 10x from equation 5.2). It can be seen from figure 5.23 however that as the number of coverslips added was increased, the magnifications of the two channels did not remain equal to the starting value or equal to each other, which was unexpected.

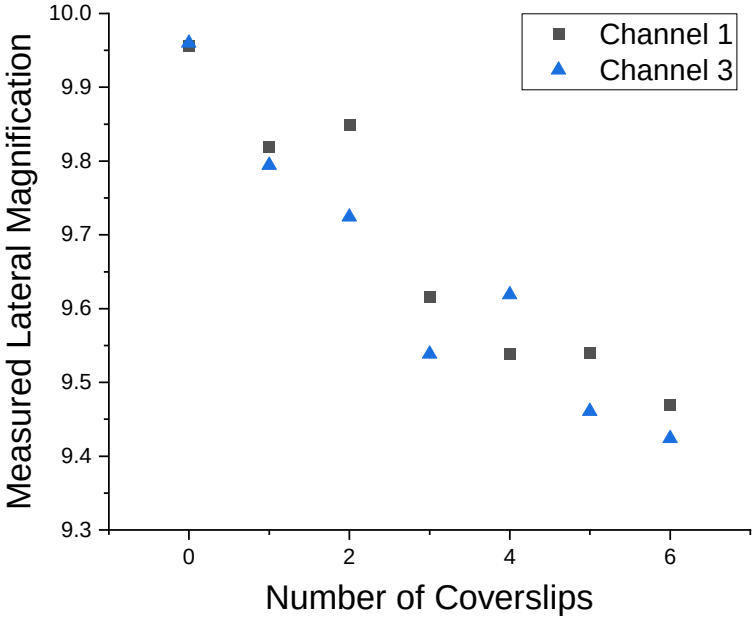

Figure 5.23: Measured real lateral magnifications of brightfield channels 1 and 3 as *d_total* was increased by raising the height of the sample with coverslips. The magnifications of the two channels did not remain equal and at their starting values which was not the expected result.

Therefore I checked that the expected result was obtained using a test rig built with standard commercial optomechanics before troubleshooting the issue on the M4All microscope. The test rig can be seen in figure 5.24 and is an extension of the test rig in figure 5.11, where a 50:50 beamsplitter was added to create a second brightfield channel. The objective lens was mounted on a Thorlabs CT1 translation stage. The sample was mounted on a Thorlabs XYF1/M translation mount. The objective and sample mounts were then mounted on a Thorlabs MT1/M translation stage, allowing the objective lens to be focused at the correct working distance and then move both the objective lens and sample together to increase *d_total* by increasing *d_interlens* whilst retaining the set *d_sample* value.

The objective used on the test rig was the Newport LI-60X (NA = 0.85) and the

tube lenses were Thorlabs $f_t = 125\,\text{mm}$ achromatic doublets, thus the expected magnification was 41.6x from equation 5.2. At the starting position the two cameras had magnifications of 41.61x and 41.17x respectively. The MT1/M translation stage was then moved to the left in increments of $200\,\mu\text{m}$. It can be seen from figure 5.25(a) that the magnifications of the two channels remained within 0.7% of their starting values, confirming that we expected the magnifications to remain the same no matter the *d_interlens* distance when the objective lens is at the correct working distance to the sample.

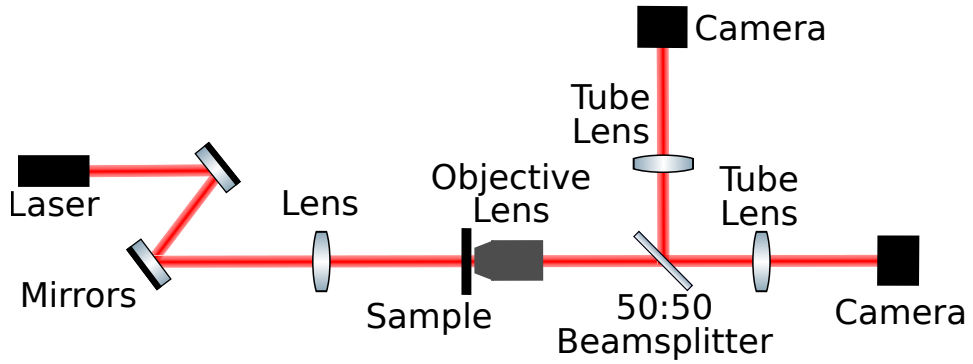

(a)

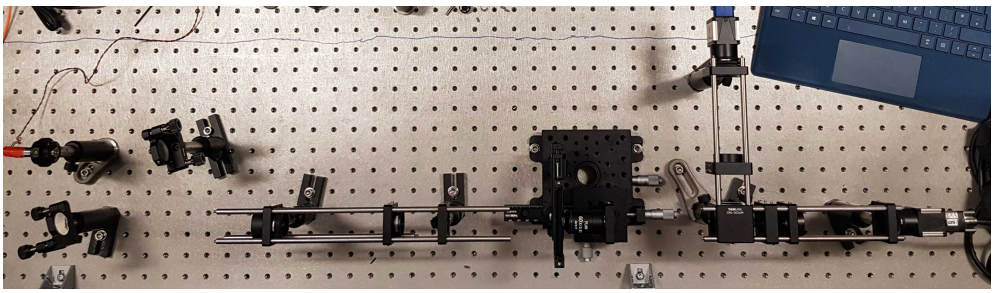

(b)

Figure 5.24: Test rig to check that the magnifications of two brightfield channels remained equal after calibration when *d_total* was increased. **(a)** Test rig schematic. **(b)** Test rig in practice. Laser - Thorlabs CPS635. Mirrors - Thorlabs PF10-03-P01. Lens - Thorlabs 35 mm bi-convex lens LB1811-A. Sample - 10 m grid sample. Objective lens - Newport LI-60X. Tube lenses - Thorlabs achromatic doublets. Camera - IDS CMOS UI-3060CP-M-GL Rev. 2.

This figure partly includes illustrations of optical components from the gwoptics ComponentLibrary designed by Alexander Franzen with reuse permitted under a CC BY-NC 3.0 licence

To confirm the calibration also worked and stayed calibrated over different *d total* values for two different focal length tube lenses (thus two different channel magnifications) I swapped one of the tube lenses on the test rig for one with $f_t = 75\,\text{mm}$. The

expected magnification with the new lens was therefore 25x. Practically the two starting magnifications were 41.31x and 24.32x and from figure 5.25(b) it can be seen the magnifications of the two channels remained within 1% of their starting values.

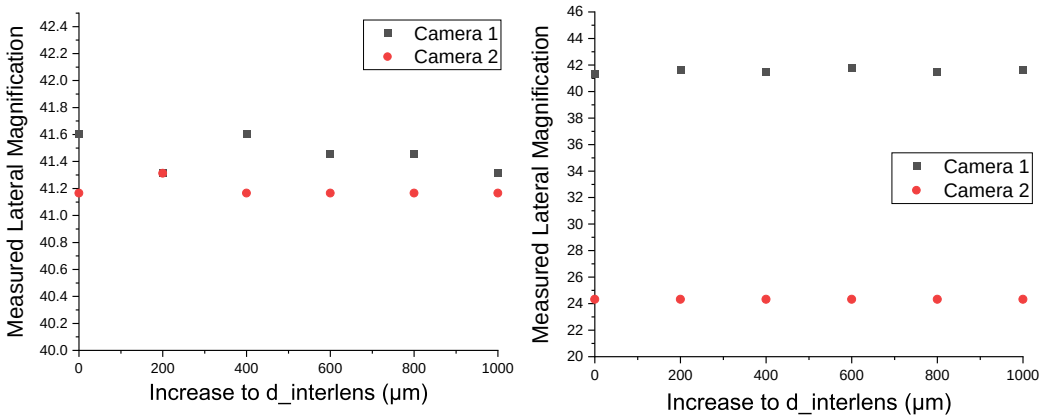

Figure 5.25: The measured real lateral magnification of the two brightfield channels on the test rig in figure 5.24 as *d_interlens* was increased. **(a)** Both channels had $f_t = 125\,\text{mm}$ thus the expected lateral magnification of both channels was 41.6x. **(b)** The result of swapping the tube lens on one of the channels for one with $f_t = 125\,\text{mm}$, changing the expected lateral magnification of the channel to 25x.

From using the test rig, I also noted that as the objective lens was moved through different focal planes, the calibration grid sample appeared to be in focus at various different planes, however was only truly in focus at one. The effect can be seen in figure 5.26 where 5.26(c) is the calibration grid correctly in focus. On either side of the correct focal plane, figures 5.26(b) and 5.26(d) are both clearly out of focus. However, as the objective lens was moved further out of focus on either side, the calibration grid appeared like it had come back into focus again (figures 5.26(a) and 5.26(e)) although not as sharply as figure 5.26(c).

The images in figure 5.26 suggested when the data set in figure 5.23 was acquired, each time the sample was raised by a coverslip, the objective lens was not focused to the correct plane, but instead one that I believed was in focus. As a result, the objective lens would be at an incorrect working distance, causing an incorrect magnification value. Therefore, I retook the data in figure 5.23, ensuring the objective lens was moved to the correct focal plane each time. The repeated data is shown in figure 5.27.

It can be seen that for each coverslip height increment, the magnifications of the two channels remained within 0.7 % of the expected magnification of 10x, thus validating the calibration on the M4All microscope.

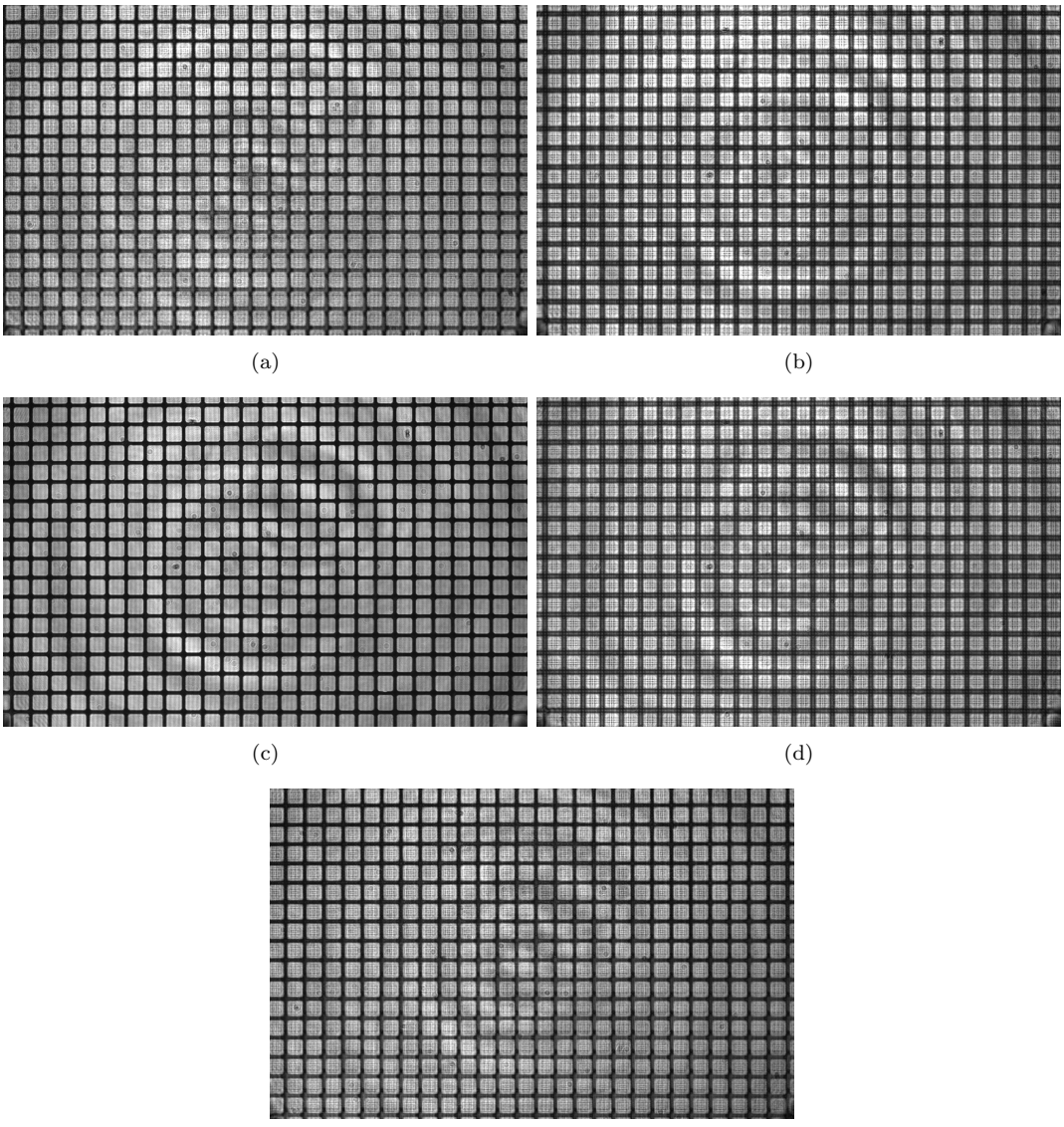

(a) (b) (c) (d) (e)

Figure 5.26: Images of a 10 μm calibration grid at different focal planes acquired on one of the channels on the test rig in figure 5.24, highlighting that there is a plane above **(a)** and below **(e)** the correct focal plane **(c)** which could be mistaken for being in focus. **(b)** and **(d)** show clearly out of focus planes above and below the correct focal plane.

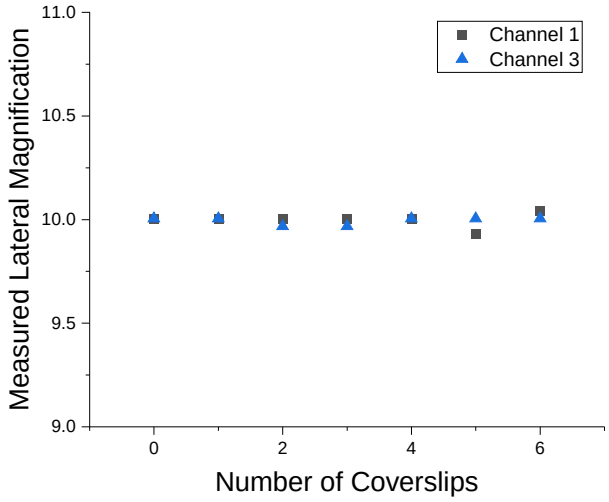

Figure 5.27: Repeated data set of measured lateral magnification of brightfield channels 1 and 3 as *d_total* was increased by raising the height of the sample with coverslips. It was made sure the objective lens was focused on the correct focal plane of the calibration grid each time the sample was raised. The magnifications of the two channels remained within 0.7 % of the expected magnification of 10x.

Axial Magnification

We have investigated how a miscalibrated system effects the lateral magnifications of detection channels in a multichannel system and also used the nearest and furthest (channels 1 and 3) tube lenses to show that the correct calibration will give the correct lateral magnification regardless of the *d_interlens* value. We also wanted to investigate the effect of a badly calibrated system on the axial magnification - how non-uniform is the z position? A bad calibration could be a large source of error and result in a feature that is thought to be say 100 μm thick actually being for example 150 μm thick.

To investigate the problem, the channel 1 and 3 tube lenses were kept at the correct calibrated position and the channel 2 tube lens was then miscalibrated by offsetting it closer to the objective lens. As *d_total* was increased, by raising the sample on the OpenFlexure stage with coverslips as before, we wanted to look at how non-linear the refocus distance of the objective lens between channels 1/3 and 2 was. Firstly, I set the problem up theoretically by altering the ray transfer matrix analysis for the TIE and fluorescence microscope. I set *d_cam* at a fixed value and the ray transfer matrix equation was solved for *d_sample* over a range of *d_total* values. As $f_t = 45$ mm for the brightfield channel tube lenses, the analysis was carried out for *d_cam* values of 46,47

and 48 mm, which is equivalent to the channel 2 tube lens being moved 1,2 and 3 mm closer to the objective lens. The objective lens refocus distance between channels 1/3 and 2 was then:

$$refocus\ distance = f_o - d_sample \tag{5.21}$$

The theoretical results from the ray transfer matrix analysis can be seen in figure 5.28. The theoretical data shows that for each value of channel 2 tube lens offset, the refocus distance remains linear over a *d_total* range of 350 to 351.02 mm, which would be equivalent to adding 6 coverslips to the height of the sample. In each case the difference in refocus distance between $d_total = 350$ and 351.02 mm was also smaller than the axial resolution of the system and thus in practice would not be a significant source of error.

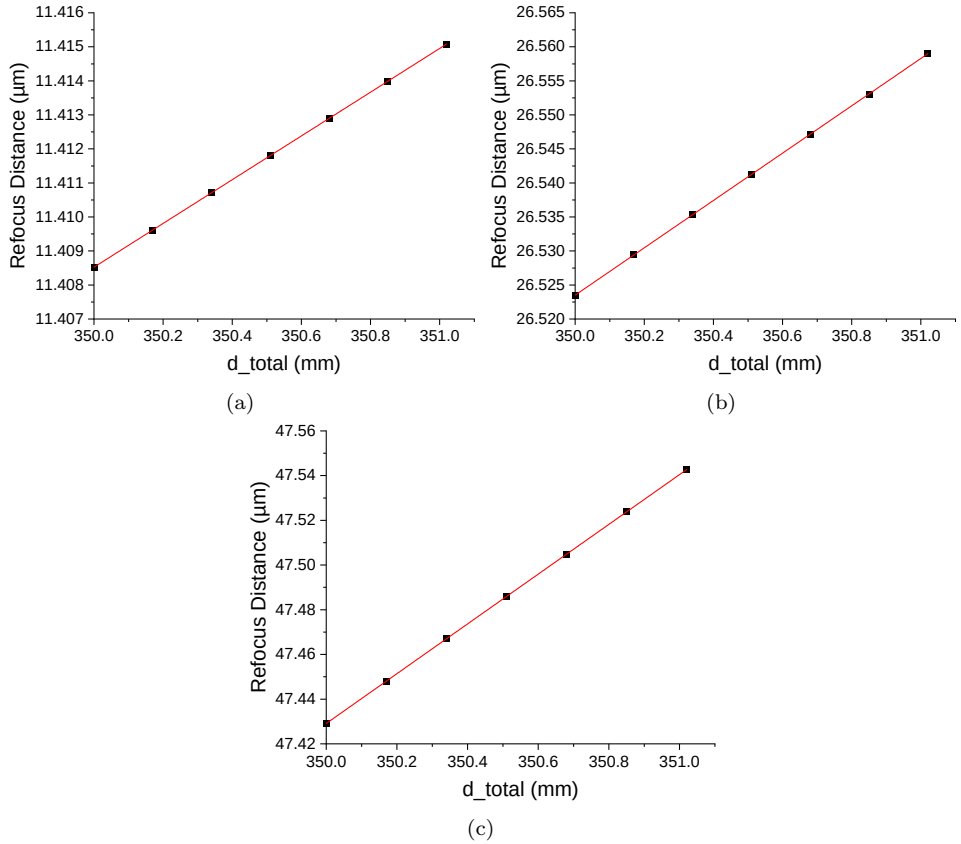

Figure 5.28: Theoretical data from RTMA to determine the refocus distance of the objective lens between channels 1/3 and 2 on the TIE and fluorescence microscope when the channel 2 tube lens is offset **(a)** 1 mm, **(b)** 2 mm and **(c)** 3 mm towards the objective lens. The theoretical refocus distance was determined for a range of *d_total* values.

I confirmed the theoretical results in practice by offsetting the channel 2 tube lens by 2mm towards the objective lens and increasing *d_total* by raising the height of the sample in increments with coverslips up to a total height of six coverslips. For each increase in *d_total* the number of steps the axial stepper motor needed to move on the OpenFlexure stage to refocus the objective lens between channels 1/3 and channel 2 was the same. Therefore confirming that the axial resolution of the system is not small enough to observe the error in axial magnification.

5.2.5 Stepper Motor Calibration

The OpenFlexure microscope stage movement was controlled by three stepper motors (two for lateral movement and one for axial movement). We needed to calibrate the motors to determine the distance moved in x,y and z per stepper motor step.

Lateral Motor Calibration

The first brightfield channel on the microscope was used to calibrate the lateral control stepper motors. Firstly, the real magnification of the channel was determined using a 10 μm calibration grid sample. 40 μm on the grid corresponded to 349 pixels on the Raspberry Pi v2 camera module. The camera had 1.12 μm square pixels and therefore the lateral magnification was 9.77x (expected magnification was 10x).

The calibration grid was then also used to calibrate the motor steps. Figure 5.29(a) shows the starting position of the calibration grid. The centre vertical and horizontal lines of the grid were thicker and therefore I used them as the reference lines. The grid was moved in increments of 10 steps in one direction up to a total of 100 steps and an image captured on the first brightfield channel at each increment. The first two increments moving the y stepper motor can be seen in figures 5.29(b) and 5.29(c). Then the motor was moved in 10 step increments back to the original starting position and subsequently moved in 10 step increments in the opposite direction and again back to the initial position again. The process was repeated for both the lateral stepper motors (figure 5.30).

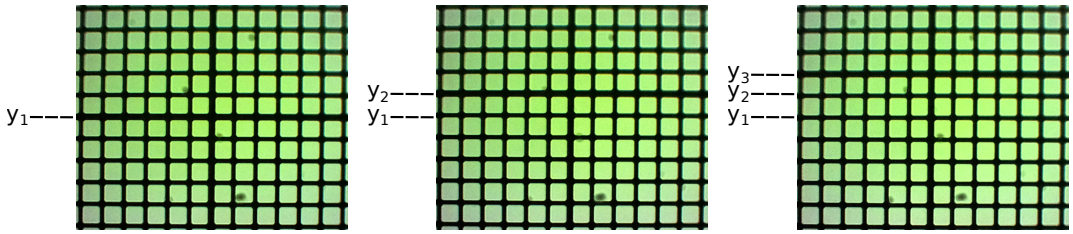

Figure 5.29: **(a)** Starting position of the 10 μm calibration grid for lateral stepper motor calibration where y_1 highlights the starting position in y of the central thick line of the calibration grid. **(b)** Position of the calibration grid after moving the y lateral stepper motor by 10 steps, highlighting the y_2 position of the thick grid line. **(c)** Position of the calibration grid after moving the y lateral stepper motor another 10 steps, highlighting the y_3 position of the thick grid line.

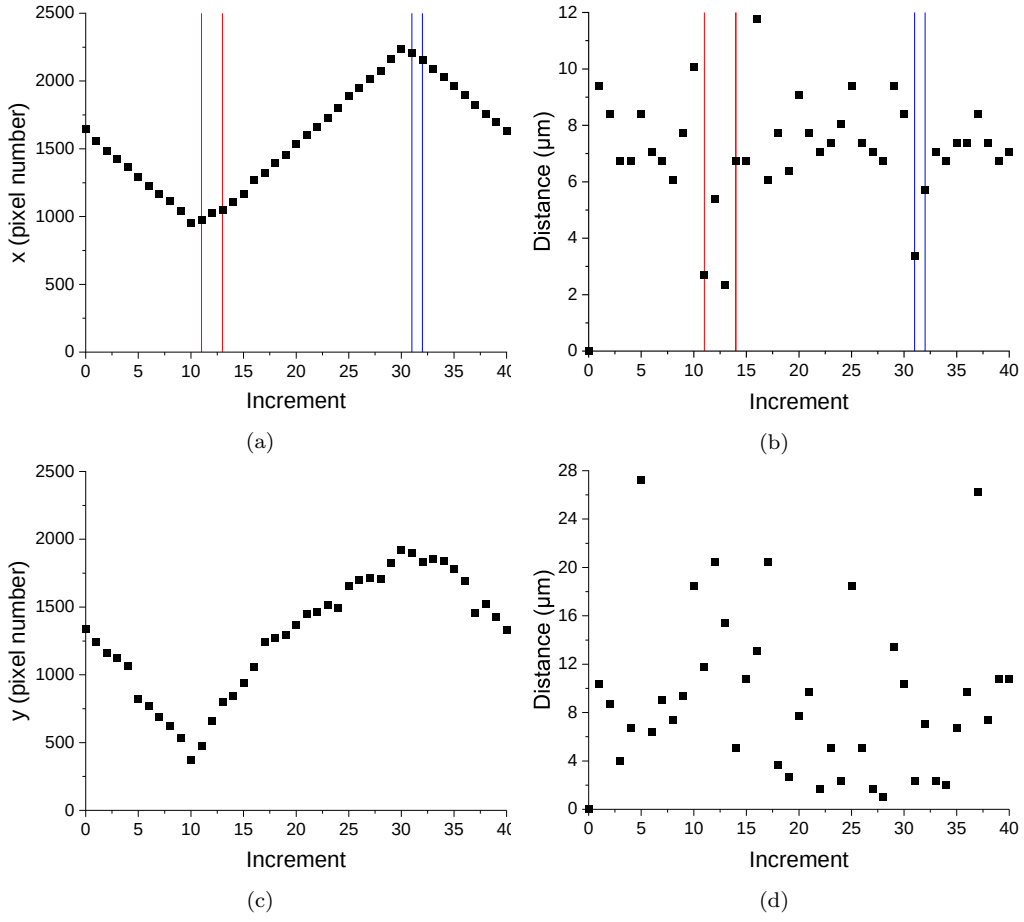

Figure 5.30: **(a)** Plot of x pixel coordinate of the thick vertical line on the calibration grid shown in figure 5.29 vs increment of movement of the x lateral stepper motor on the OpenFlexure stage. **(b)** Plot of real distance the grid moved in x per x motor increment. **(c)** Plot of y pixel coordinate of the thick horizontal line on the calibration grid shown in figure 5.29 vs increment of movement of the y lateral stepper motor. **(d)** Plot of real distance the grid moved in y per y motor increment. Each motor increment for both the x and y motors was 10 motor steps.

Figures 5.30(a) and 5.30(c) are plots of the x and y pixel positions of the thick vertical and horizontal grid lines respectively vs stepper motor increment (each increment was 10 motor steps). Figures 5.30(b) and 5.30(d) are plots of the real distance the x and y stepper motors moved each increment of 10 steps. Although the shape of the x axis stepper motor movement qualitatively looks smooth (figure 5.30(a)), it can be seen in figure 5.30(b) there is a large spread in the real distance the sample moved per increment of 10 motor steps. The mean value was 7.12 μm with a standard deviation of 1.78 μm.

The data was acquired on an OpenFlexure stage which had been used consistently for 1-2 years therefore the flexures will have weakened over time. The error can be seen to a greater extent in figures 5.30(c) and 5.30(d) for the y axis stepper motor where the flexure had degraded further. We did not require an accurate lateral motor calibration for the work carried out on the stage prior to obtaining the data in figure 5.30, however in future the OpenFlexure stage would need to be replaced with a new one if an accurate motor calibration were to be required.

The x axis stepper motor data does however show a feature of the motor system. When changing direction of movement there is a period of mechanical backlash causing an error in the distance the sample moves [142]. The backlash points are highlighted between the red and blue lines on figures 5.30(a) and 5.30(b). Omitting the backlash points, the mean distance moved per x axis motor step was $0.879 \pm 0.142\,\mu$m. Knapper *et al.* [142] have calibrated the backlash on the OpenFlexure stage to be $12.1 \pm 1.9\,\mu$m in x and y. The two backlash regions on figures 5.30(a) and 5.30(b) are 30 steps (26.37 μm) and 20 steps (17.58 μm). The greater region of backlash that we see may be due to degradation of the flexures.

Axial Motor Calibration

To calibrate the axial control stepper motor, an approach similar to the method carried out in Grant *et al.* [104] was used. In Grant *et al.*, three 1.5H coverslips (thickness $170 \pm 5\,\mu$m) were mounted one on top of each other with a permanent marker spot on each (similar to figure 5.31(a) where there are four coverslips). The number of axial

motor steps needed to focus between each one was recorded and averaged. As the average corresponds to 170 μm, the distance moved for one step can be determined.

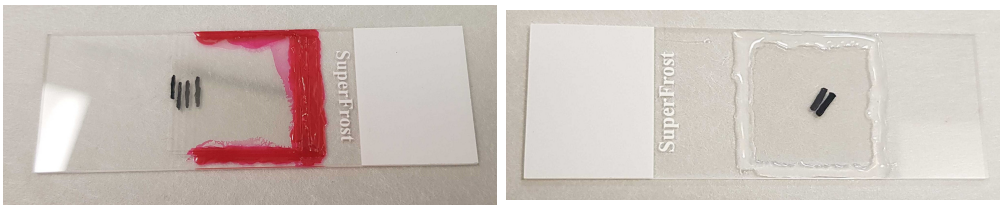

(a) (b)

Figure 5.31: **(a)** Custom axial stepper motor calibration sample where four 1.5H coverslips are mounted one on top of the other with a permanent marker line drawn on each. **(b)** Second custom axial stepper motor calibration sample with two 1.5H coverslips.

However, as the Newport LI-40X objective lens on the TIE and fluorescence microscope had a working distance of 0.36 mm the maximum number of coverslips that could be used for the calibration process was two (figure 5.31(b)). Therefore, I carried out 5 iterations of measuring the number of steps to focus between the top to bottom coverslip and repeated for moving in the opposite direction from the bottom to the top coverslip. The average number of steps for each direction were 324 steps and 320 steps respectively (table 5.2). The distance moved per step in each direction was therefore 0.524 μm and 0.531 μm, which I rounded to 0.5 μm per axial motor step.

Iteration	No. of steps moving from the top to the bottom coverslip	No. of steps moving from the bottom to the top coverslip
1	340	330
2	300	300
3	320	320
4	330	320
5	330	330
Average	324	320

Table 5.2: Number of axial motor steps recorded for focusing between the two coverslips on the calibration sample in figure 5.31(b). Five iterations were recorded for moving between the top and bottom coverslip and repeated for the opposite direction. The average of each was calculated.

5.2.6 Stability Tests

We wanted to determine the stability of the M4All system independent of any drift from the OpenFlexure microscope stage. Therefore to test the stability, I used the lateral magnification calibration of the three brightfield channels on the TIE and fluorescence microscope. If the magnifications remained calibrated we knew the position of the tube lenses and cameras would not have drifted by a significant distance.

Short Term Stability

To test the short term stability of the microscope system, we tested whether any vibrations from the stepper motors on the attached OpenFlexure stage would cause component drift in the M4All system. Firstly, after calibrating the TIE and fluorescence microscope I measured the size of the same feature on all three brightfield channels - I used a 10 μm calibration grid and measured the number of pixels across four grid lines, which was 349 pixels for all three channels. I then programmed the three stepper motors to run on a loop for two hours before remeasuring the distance on each channel and comparing to before (stepper motor control is discussed in chapter 6).

The two lateral control stepper motors were looped back and forth over a range of 800 steps ($\approx 700\,\mu$m based on the calibration in section 5.2.5), which would cover panning across around 25-30 macrophages. The axial control stepper motor was looped back and forth over a range of 20 steps ($\approx 10\,\mu$m again based on the calibration in section 5.2.5) which covers greater than the axial height of fixed macrophages.

The process of looping the stepper motors and measuring the distance on each channel was repeated three times and the results are in figure 5.32, showing the distance measured on each channel for before looping the motors (iteration 0) and after looping the motors for two hours at a time (iterations 1, 2 and 3). It can be seen that the feature distance remained equal on the three channels within 2 pixels (224 nm) after each iteration, which is within the lateral resolution of the microscope (409 nm as calculated from equation 5.4). Therefore imaging over the course of 6 hours with the stepper motors consistently running did not lead to a significant drift in the position of the tube lenses and cameras in the M4All microscope.

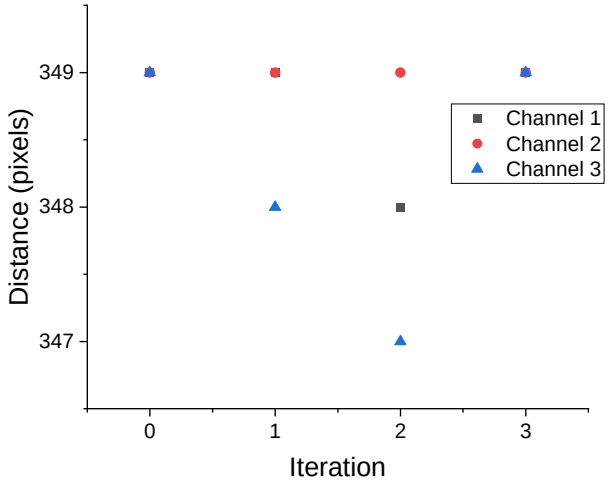

Figure 5.32: Distance in pixels measured across four grid lines of a 10 μm grid sample on the three brightfield channels of the M4All TIE and fluorescence microscope before looping the stepper motors (iteration 0) and after looping the stepper motors for two hours at a time (iterations 1, 2 and 3) to test short term stability of the microscope.

Long Term Stability

I determined the longer term stability of the M4All microscope by calibrating the lateral magnifications of the first and third brightfield channels, using a 10 μm calibration grid sample, on the TIE and fluorescence microscope and repeating the lateral magnification measurements after a period of two months. In the initial data set the number of pixels corresponding to 30 μm on the calibration grid was 268 pixels on both channels, corresponding to a real magnification of 10.005x, where the expected magnification was 10x. Two months later, the repeated data gave results of 266 pixels and 267 pixels corresponding to 30 μm on the calibration grid for the first and third channels respectively, which is magnifications of 9.931x and 9.968x. Therefore the magnifications remained within 0.74% of their initial values and after two months the magnifications of the two channels were equal to within 0.37% of each other.

I would like to highlight that the tube lenses and cameras on the microscope were not fixed completely in place on the cage rods over the two month period other than a small amount of friction from the grub screws on the top of the mounts. Also during the 2 month period, other work was carried out on the optical bench which the microscope was positioned on and on the day the magnifications were measured

after the 2 month period, the microscope was also moved across the optical bench before acquiring the data. Therefore the M4All system displays very good long term stability and would not require re-calibration often, which was one of our aims as in future the microscope system could be used in remote settings by non-experts in optical engineering for macrophage research or testing patient samples.

5.2.7 TIE Microscopy

Tube Lens Positioning

After calibrating the TIE and fluorescence microscope as in section 5.2.4, the brightfield channels were then set up to acquire data for TIE microscopy. As described in section 3.1.3, TIE microscopy requires three brightfield images; one at a reference focal plane and another two spaced equally above and below that focal plane. Therefore the tube lenses on channels two and three needed to be offset to focus on planes above and below the reference focal plane on channel one.

I chose the spacing between the focal planes to be 5 μm for initial testing. To focus the channel two and three tube lenses on planes 5 μm above and below channel one required offsetting the tube lenses by less than 1 mm. Therefore I decided that rather than repositioning the tube lenses with calipers, a more accurate method would be to adjust the position of the objective lens using the axial stepper motor on the OpenFlexure stage to 5 μm above and below the calibration position and subsequently refocusing the channel two and three tube lenses to each position.

As the tube lenses on channels two and three were no longer positioned at the calibrated position for the correct working distance/magnification, not only did the focal planes of each channel differ, but their magnifications differed as well. Therefore I captured an image of the 10 μm calibration grid on each channel when the objective lens was in focus on that channel to calculate the magnification of the channels for image registration prior to TIE processing. The normalised magnifications of the three channels, measured from the calibration grid images in figure 5.33, were 1.000, 0.942 and 1.046 respectively. Therefore, images from channel two needed to be magnification scaled by x1.062 and images from channel three needed to be scaled by x0.956.

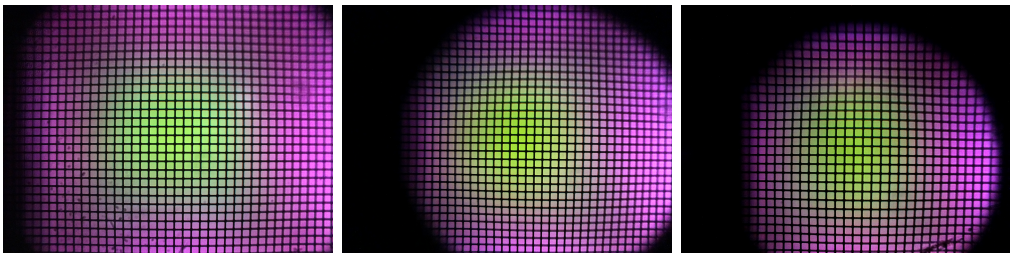

(a) (b) (c)

Figure 5.33: In focus images from brightfield **(a)** channel 1, **(b)** channel 2 and **(c)** channel 3 after offsetting the tube lenses of channels 2 and 3 for TIE microscopy.

Initial Data and Processing

This section follows the processing steps used to produce a TIE image of a diatom sample before showing final results from various different samples. The pre-processing steps for a data set are illustrated in figure 5.34. After acquiring images of three focal planes from the three brightfield channels on the TIE and fluorescence microscope (where channel 1 was the reference focal plane, channel 2 was set 5 μm below the focal plane of channel 1, and channel 3 was set 5 μm above the focal plane of channel 1), step 1 was to scale the magnifications of channels 2 and 3 as calculated in the previous section. Step 2 was to then convert the images from RGB to 32-bit and crop each image to an area of the same width and height containing the feature of interest. Image registration was then performed in step 3, we used the NanoJ-Core Drift Correction plugin [84] on ImageJ/Fiji. Once drift corrected, the images were all cropped to the same FOV to remove empty space in the registered images.

Due to the availability of standard plate beamsplitters, the three brightfield channels in the TIE and fluorescence microscope did not all have equal intensities. The light was split 30:35:35. Therefore it was necessary to scale the intensities of the three channels. We expected to need to scale the intensity of the first channel to channels two and three. However it can be seen in step 3 in figure 5.34 that each channel had a different background intensity, and, in fact, channel one appeared to have the brightest background. We believe there are automatic gain settings applied by the Raspberry Pi camera module, which will be discussed further in section 6.4. Therefore step 4 was to normalise the image intensities to channel one. This was achieved using the mean gray

value of the same region of interest of the background on each image (yellow box in step 3), which in the case of the data set in figure 5.34 was 110.538, 88.316 and 73.898. Meaning the pixel values of channel two needed to be multiplied by 1.252 and channel three by 1.496 to normalise to channel one (figure 5.34 step 4).

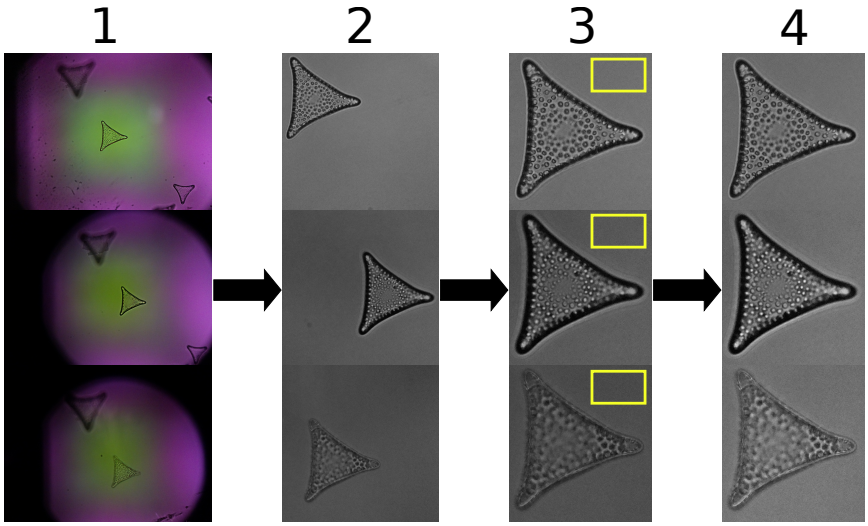

Figure 5.34: TIE pre-processing steps. Step 1: Import images to ImageJ/Fiji and scale magnifications, normalising to camera 1. Step 2: Convert images to 32-bit and crop each image to an area of the same width and height containing the feature of interest. Step 3: Image registration using NanoJ-Core Drift Correction plugin, then crop images to same FOV. Step 4: Scale intensities using the yellow ROIs shown in step 3, normalising to the background of camera 1.

Figure 5.35 shows different TIE microscopy data sets acquired on the M4All microscope, including the diatom sample in figure 5.34, a second diatom sample, a nanodiamond sample, and a human MDM sample. The pre-processing steps in figure 5.34 were applied to each of the brightfield image sets and the processed brightfield images are shown along with the TIE image for each set, obtained using the TIE method in section 3.1.3. Quantitative phase information has not been measured from these data sets, however the data shows proof of principle that the M4All microscope is capable of acquiring the images required for TIE microscopy of different samples in a single shot. Figure 5.35(n) shows the case where the macrophage sample appears almost transparent at the focal plane position and figure 5.35(p) shows the increase in contrast from TIE microscopy. Although, like figures 3.21 and 3.22, specific sub cellular structures are not immediately identifiable, further modelling of multiple scattering may increase the amount of obtainable quantitative information as discussed in section 3.5

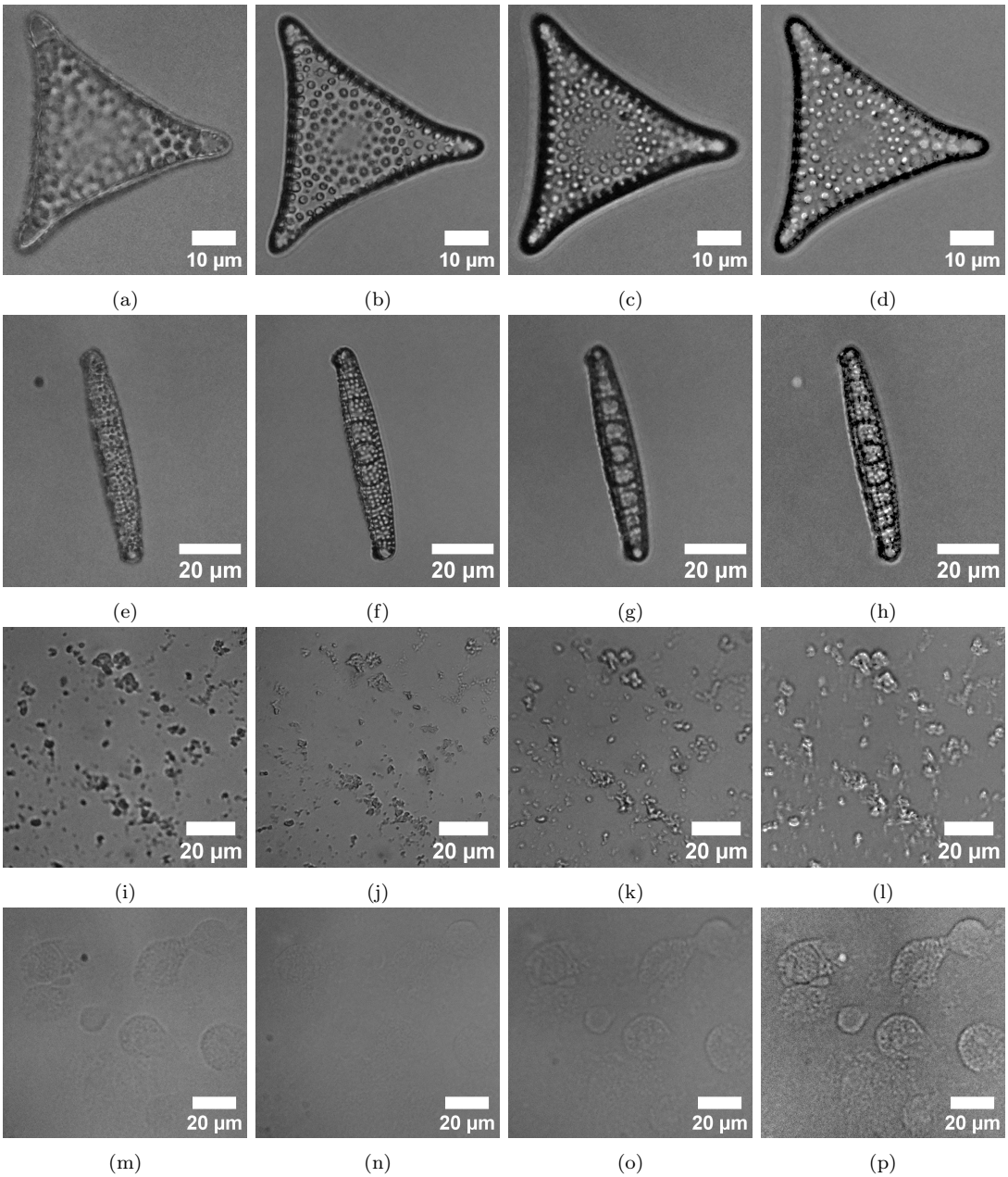

Figure 5.35: Row 1 is a TIE data set of a Diatom sample where **(a)** is the brightfield image above the focal plane, **(b)** is the brightfield image at the focal plane, **(c)** is the brightfield image below the focal plane, and **(d)** is the TIE image. Row 2 is a TIE data set of a second Diatom sample where **(a)** is the brightfield image above the focal plane, **(b)** is the brightfield image at the focal plane, **(c)** is the brightfield image below the focal plane, and **(d)** is the TIE image. Row 3 is a TIE data set of a nanodiamond sample where **(a)** is the brightfield image above the focal plane, **(b)** is the brightfield image at the focal plane, **(c)** is the brightfield image below the focal plane, and **(d)** is the TIE image. Row 4 is a TIE data set of a human MDM sample where **(a)** is the brightfield image above the focal plane, **(b)** is the brightfield image at the focal plane, **(c)** is the brightfield image below the focal plane, and **(d)** is the TIE image. Brightfield images acquired on the M4All TIE and Fluorescence microscope and pre-processed with the steps in figure 5.34.

Discussion

I wanted to check how accurately the z spacing between the three channels had been set up using the method of moving the objective lens a certain distance with the stepper motor on the OpenFlexure stage and then refocusing the tube lens to that focal position. Measuring the normalised magnifications of the three channels after repositioning the lenses gave 1.0, 0.942 and 1.046 respectively. Using the RTMA theoretical normalised magnification data in figure 5.18, the channel two focal plane was theoretically 32.8 μm below the channel one focal plane, and the channel three focal plane was theoretically 8.2 μm above the channel one focal plane. The expected z spacing between each plane from moving the objective lens was 5 μm. Therefore there was a discrepancy between the expected and measured results according to the theoretical plot. In future, the RTMA magnification calibration data could be used to optimise the z spacing based on measuring the normalised magnifications of the three channels and adjusting until the normalised magnifications match the desired theoretical *d_sample* value, which directly relates to the z spacing.

Another change that we would make to the system would be to swap the Raspberry Pi v2 camera modules for USB monochrome cameras, with greater control over image acquisition settings, to mitigate problems with auto gain settings on the camera and allow simpler/more accurate intensity scaling correction between the three brightfield channels.

Finally, multifocal plane imaging allows the data for TIE microscopy to be acquired in a single shot without needing to move the sample position, which has advantages for live samples and for minimising drift while acquiring data. Using an infinite-conjugate optical system and splitting the light into different detection paths using beamsplitters is an optically simple method to achieve multifocal plane imaging, albeit care must be taken to scale magnifications and intensities of the channels and to register images to one another. Other options for multifocal plane imaging require more complex optical elements. For example methods based on using diffractive elements such as quadratically distorted diffraction gratings [161] (which has been combined recently with optical tweezers [162] and adaptive optics [163]), an SLM [164], or a multifocus

grating (corrected for spherical aberration and combined with a chromatic correction grating) [165]. Implementing these methods was outwith the scope of this research project as we had a key focus on developing a low-cost system with wide ranging accessibility, however I believe the M4All system would be capable of realising the highlighted multifocal plane methods in future if desired.

5.2.8 Fluorescence Microscopy

The fluorescence channel on the TIE and fluorescence microscope was designed to be capable of capturing data suitable for SRRF reconstructions. For proof of concept, I prepared a 90 nm nanodiamond sample by pipetting a drop of diluted 90 nm ND solution onto a coverslip, which was placed onto a heated bed to evaporate the water, leaving only the NDs on the coverslip. The coverslip was then mounted onto a microscope slide using ProLong Diamond and allowed to cure then sealed around the edges with nail polish. I then acquired 100 image frames of the sample on the fluorescence channel for processing with the SRRF algorithm in ImageJ. The IDS camera settings were gain = 0 and exposure = 300 ms. Figure 5.36(a) shows a cropped region from one of the image frames and figure 5.36(b) is the processed SRRF image. Figures 5.36(c) and 5.36(d) are zoomed in figures of the highlighted (yellow box) regions of interest in 5.36(a) and 5.36(b) respectively.

The NanoJ-SRRF plugin settings used were: Ring Radius - 0.5, Radiality Magnification - 10, axes in ring - 8 and Temporal Analysis - TRPPM. Note that the scale bars in figure 5.36 are an estimate based on the expected magnification of the fluorescence channel and that the magnification of the fluorescence channel was not fully calibrated before acquiring the data set.

In future, the fluorescence channel would need to be calibrated using the RTMA calibration method. This would allow images of samples to be acquired in both bright-field and fluorescence modes, where fluorescence images could be overlaid with TIE images to potentially correlate structural information from the fluorescence image with quantitative refractive index measurements from the TIE image.

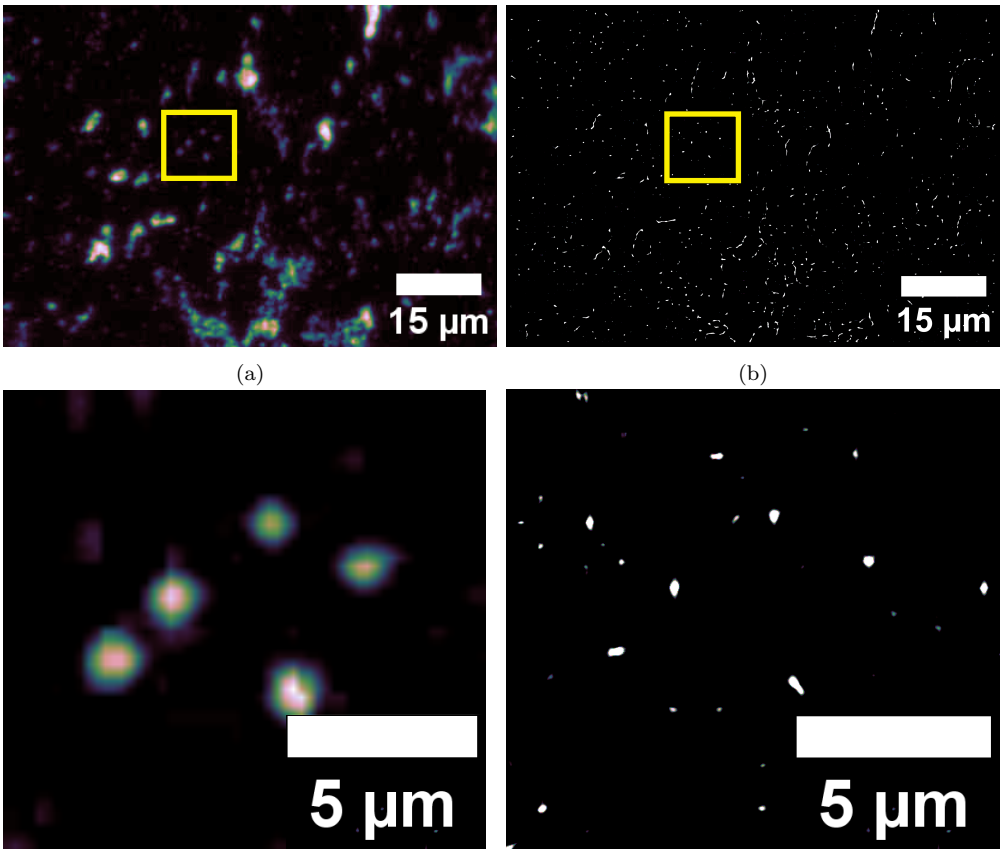

Figure 5.36: **(a)** One image frame from the set of 100 images of a 90 nm nanodiamond sample captured on the fluorescence channel of the M4All TIE and fluorescence microscope. **(b)** SRRF processed image of the data set in **(a)**. **(c)** and **(d)** are zoomed in images of the highlighted region of interest shown in **(a)** and **(b)** respectively.

5.3 M4All Dual Channel Fluorescence Microscope

5.3.1 Design Parameters

To enable low-cost and widely accessible colocalization studies in human monocyte derived macrophages, the second microscope I developed with the M4All system facilitates dual colour fluorescence microscopy with two spectrally separated fluorescence detection channels. An optical schematic of the microscope design can be seen in figure 5.37.

For the first detection channel, we chose to use the same design parameters as for the fluorescence channel on the M4All TIE and fluorescence microscope as we knew,

from section 5.2.8, imaging nanodiamond on the channel gave good results. Therefore either nanodiamond or another far red fluorescence marker could be used to label a structure of interest within macrophages. We however substituted the IDS CMOS camera for the much lower cost Raspberry Pi HQ camera module as it was also able to sufficiently detect fluorescent nanodiamond, which I tested on the test rig in figure 5.11. It is important to note that there is an infrared filter (Hoya CM500) on the HQ camera module [166] which must be removed if imaging in the far red.

The second detection channel was designed to have a detection range of $490 - 650\,\text{nm}$, which was spectrally separated using a 490 nm shortpass dichroic mirror (Thorlabs DMSP490). The upper limit of 650 nm was chosen as it matches the lower limit of the first detection channel. The lower limit of 490 nm was chosen for compatibility with the chosen excitation source, which was a WORLD STAR TECH compact-multiwave laser, with three excitation lines of 450 nm, 520 nm and 635 nm (figure 5.38), and for compatibility with common fluorophores such as Alexa Fluor 488.

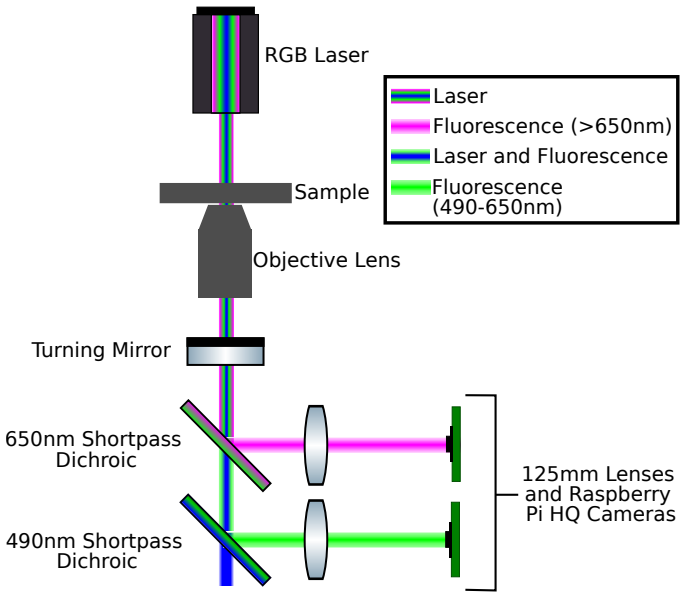

Figure 5.37: Optical schematic of the M4All dual channel fluorescence microscope design. The microscope is an infinity-corrected design including a far red (> 650 nm) fluorescence imaging channel (magenta) separated by a 650 nm shortpass dichroic mirror (Thorlabs DMSP650). The second fluorescence channel detects between 490 − 650 nm (green) and is separated by a 490 nm shortpass dichroic mirror (Thorlabs DMSP490). The RGB laser provides illumination at 450 nm, 520 nm and 635 nm. Raspberry Pi HQ camera modules are used to capture the fluorescence signal.

This figure partly includes illustrations of optical components from the gwoptics ComponentLibrary designed by Alexander Franzen with reuse permitted under a CC BY-NC 3.0 licence

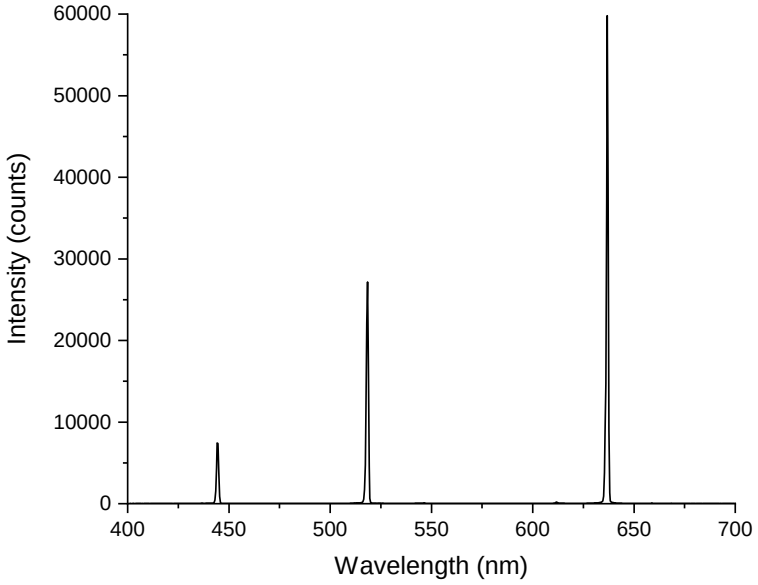

Figure 5.38: WORLD STAR TECH compact-multiwave laser spectrum. Data was acquired on an Ocean Optics QE65000 Scientific-grade Spectrometer.

The objective lens chosen for the microscope was a Newport LI-60X (effective focal length 3 mm, 0.85NA, 60x). Based on the images in figure 5.13 we chose the tube lens focal length to be 125 mm (Thorlabs AC254-125-A) for both channels to minimise barrel distortion. Thus the resulting theoretical lateral magnification of both channels was 41.6x. Using the equations in section 5.1.1, the critical Nyquist sampling distance, using $\lambda = 520\,\text{nm}$, was 153 nm. The Raspberry Pi HQ cameras had a pixel size of 1.55 μm and so the practical sampling distance was 37 nm per pixel, which was therefore oversampled, as desired.

Figure 5.39 shows the final printed and set up microscope. The first image is a close up showing the two fluorescence channels and the Raspberry Pi HQ cameras connected to two Raspberry Pi 4 8GB boards. The stepper motors on the OpenFlexure stage were connected to a PiStep2 Quad Stepper Motor Control Board connected to the GPIO (General Purpose Input/Output) pins on a Raspberry Pi Zero board. A 650 nm longpass filter (Thorlabs FELH0650) and a 500 nm longpass filter (Thorlabs FELH0500) were also included before the HQ cameras on the first and second channels respectively to clean up the fluorescence signal. The longpass filters were mounted in the drop in filter insert shown in figure 4.16(e). The second figure is a zoomed out

photo including the illumination rig.

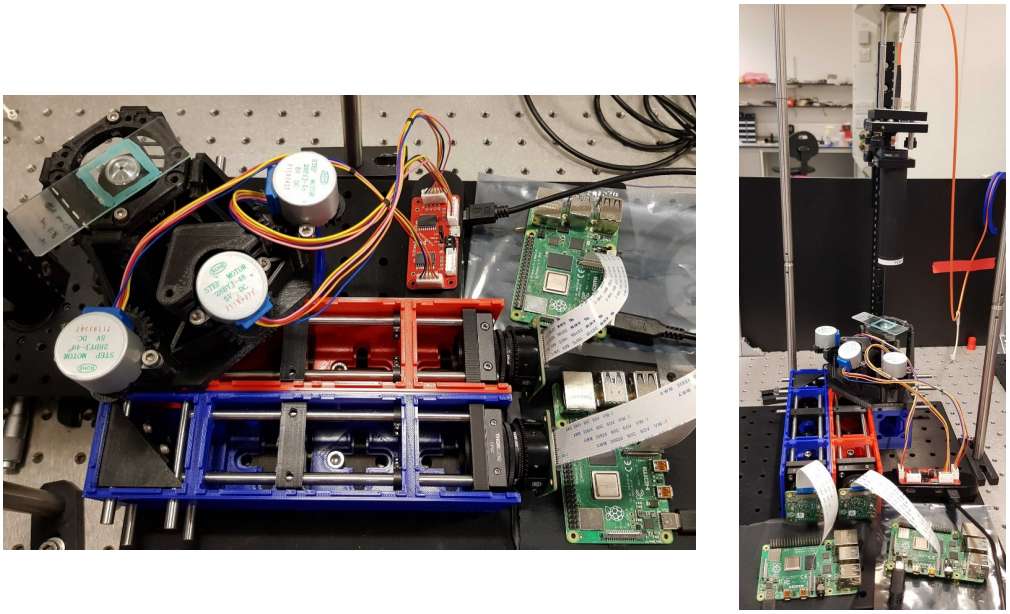

(a) (b)

Figure 5.39: Final version of the M4All dual channel fluorescence microscope. **(a)** Close up image of the optical component inserts within the cubes, the OpenFlexure stage with stepper motors connected to a Raspberry Pi Zero and PiStep2, and Raspberry Pi HQ cameras connected to two Raspberry Pi 4 8GB boards. **(b)** Overall view of the microscope also showing the illumination rig.

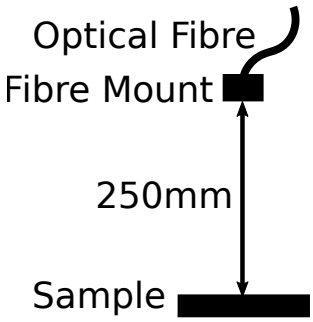

Figure 5.40: Illustration of the illumination rig. The WORLD STAR TECH compact-multiwave RGB laser is coupled into the system via a Thorlabs M42L02 patch cable containing a FG050LGA multimode fiber (50 μm core diameter). The fibre mount consists of a Thorlabs SM1FC fibre adapter attached to a Thorlabs KC1-T/M SM1 threaded kinematic mount.

The illumination rig coupled the RGB laser into the microscope. Figure 5.40 illustrates the illumination rig. The laser was coupled in via a multimode optical fibre (Thorlabs M42L02 patch cable) with a core diameter of 50 μm. The fibre mount consisted of a Thorlabs SM1FC fibre adapter attached to a Thorlabs KC1-T/M SM1

threaded kinematic mount for tip/tilt control of the fibre. As in figure 4.9(a) the kinematic mount was attached via posts to a Thorlabs XYT1/M linear translation stage to provide linear positioning of the optical fibre output. To focus the output of the optical fibre onto the sample, we needed to calculate the focal length of a lens to be placed between the fibre and the sample.

As the core diameter of the optical fibre was 50 μm and our desired FOV diameter was 250 μm, we needed to magnify the output by x5. The following equations were used to calculate the focal length of the lens:

$$v = Mu = 5u \tag{5.22}$$

$$u + v = 250\,mm \tag{5.23}$$

$$f = \frac{1}{u} + \frac{1}{v} \tag{5.24}$$

where M is the magnification (x5), v is the image distance, u is the object distance and f is the focal length of the required lens. The total distance between the fibre mount and the sample, $u + v$, was arbitrarily chosen to be 250 mm. Equation 5.22 was substituted into equation 5.23 to calculate a value for u, which was then subsequently substituted back into equation 5.22 to calculate v. The values for u and v were then substituted into equation 5.24 to calculate f, which in this case was 35 mm. The lens was positioned $u = 41$ mm below the fibre output.

The laser power was controlled by setting the current. Figures 5.41(a), 5.41(b) and 5.41(c) shows the measured power at the sample versus the current for each laser wavelength (a Thorlabs PM16-130 was set up at the sample position to measure the power). Figures 5.41(d), 5.41(e) and 5.41(f) are images of the beam profile, obtained by mounting a Raspberry Pi HQ camera at the sample plane. The focal spot area on each image was measured, which can be used to calculate the power density from the measured power data.

The expected focal spot area was 0.05 mm^2 based on the desired FOV diameter of

250 μm and the calculations for the focal length of the lens above. The area of the focal spots shown in figure 5.41 are however larger and differ in size for each excitation wavelength. Therefore there may be an error in the practical position of the lens. Also the lens used was a Thorlabs bi-convex lens which, as shown in figure 5.16(a), has no chromatic aberration correction and so each of the wavelengths will be focused to a different position, explaining the difference between the focal spot sizes. Thus it would be favourable to use a lens such as a Thorlabs achromatic doublet which is corrected for chromatic aberration. However, in this case, each wavelength overfilled the desired FOV and so was suitable for initial imaging studies.

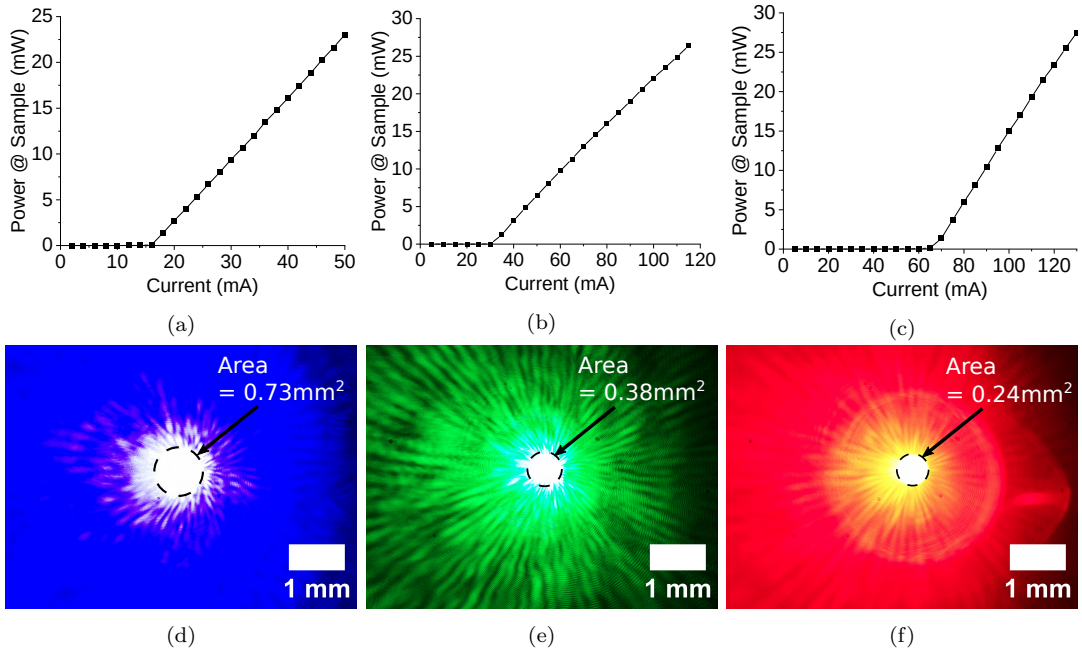

Figure 5.41: Power at the sample vs current for the **(a)** 450 nm, **(b)** 520 nm, and **(c)** 635 nm laser lines (WORLD STAR TECH compact-multiwave laser). Beam profile at the sample for the **(c)** 450 nm, **(d)** 520 nm, and **(e)** 635 nm laser lines. The area of the focal spot is highlighted on each image which can be used to calculate the power density.

5.3.2 RTMA Magnification Analysis and Calibration

The RTMA lateral magnification calibration was also used to set up and align the M4All dual channel fluorescence microscope. A new theoretical plot of normalised lateral magnification versus *d_sample*, specific to the dual channel fluorescence microscope was

produced for the calibration using the same method as for the TIE and fluorescence microscope. The variable values used were f_o =3 mm and *d_total* = 275 and 325 mm for the two fluorescence channels. Equation 5.15 was solved for *d_cam* for a range of *d_sample* values from 2.966 mm to 3.028 mm in 0.001 mm steps. As before, the solved *d_cam* values were substituted back into the matrix equation 5.15 to determine the lateral magnification at each *d_sample* distance. The analysis was repeated for both of the fluorescence channels by changing the *d_total* value. Figure 5.42 shows the plot of normalised lateral magnification versus *d_sample*.

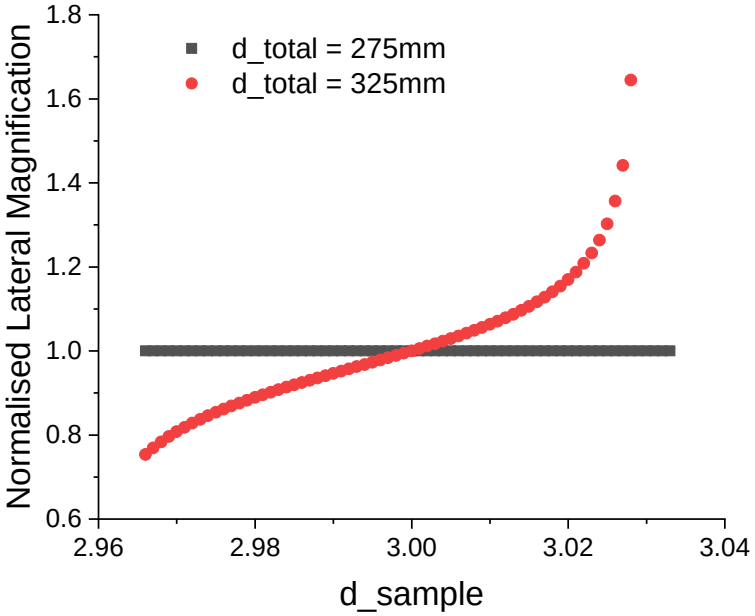

Figure 5.42: Plot of normalised lateral magnification (calculated by ray transfer matrix analysis and normalised to the first brightfield channel) vs *d_sample* for the two fluorescence channels in the dual fluorescence channel microscope.

I then used the plot to calibrate the channels. Removing the 650 nm longpass filter from the first channel allowed the 520 nm laser line on the RGB laser to break through. Removing the 500 nm longpass filter also allowed the 520 nm laser line to break through to the second channel camera. The 10 μm calibration grid used for the TIE and fluorescence microscope calibration was mounted onto the microscope and used to measure the normalised magnifications on each channel. The calibration process outlined in figure 5.19 was repeated until the magnifications of the two channels were

equal so the working distance position was correct to within the axial resolution.

5.3.3 Single and Dual Channel Fluorescence Microscopy

Once I calibrated the microscope I added the longpass filters back into the detection channels and acquired image data sets to test the microscope. The first sample imaged on the second channel of the microscope was a mock infected human MDM sample with labelled mitochondria (Alexa Fluor 488). One of the images can be seen in figure 5.43, where figure 5.43(b) is a cropped and enlarged image of the central cell in figure 5.43(a) to show the microscope is capable of imaging the branched mitochondrial network of a healthy human MDM. The brightness/contrast of the images were adjusted in ImageJ/Fiji for representation.

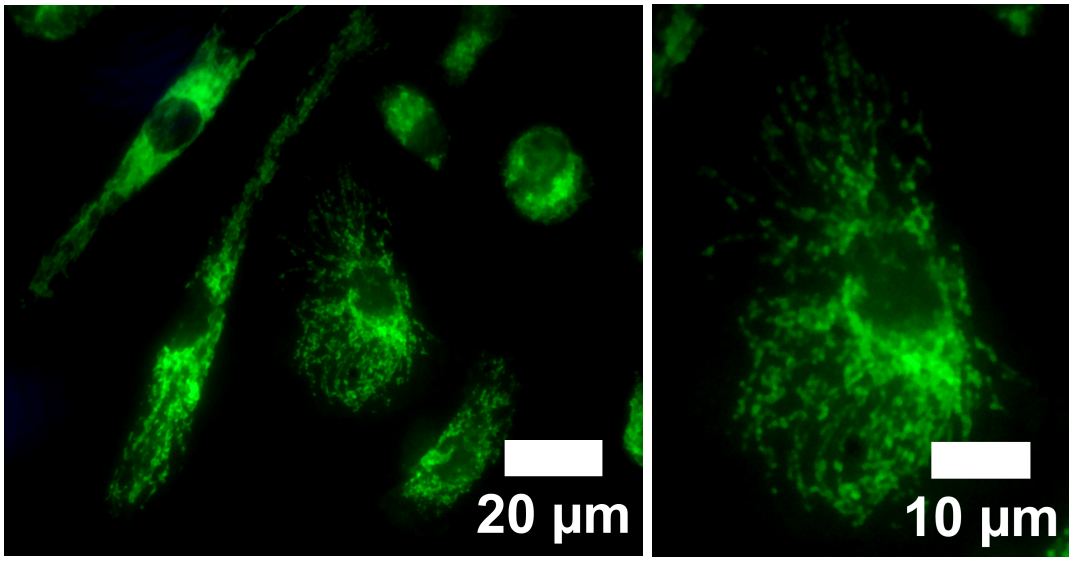

(a) (b)

Figure 5.43: **(a)** Mock infected human MDM sample with labelled mitochondria (Alexa Fluor 488). Image acquired on the M4All dual channel fluorescence microscope. **(b)** Cropped and enlarged view of the central cell in **(a).** Brightness/contrast adjusted in ImageJ/Fiji for representation.

The second sample imaged was a human MDM sample challenged with *Staphylococcus aureus* (4 hour time point). The sample was prepared by Katharin Balbirnie-Cumming at the University of Edinburgh - Centre for Inflammation Research. *S. aureus* is a Gram-positive bacterium also found in the upper respiratory tract [167] like *S. pneumoniae*. Katharin and I decided to challenge human MDMs with *S. aureus* for

initial imaging studies on the M4All system, as opposed to *S. pneumoniae*, as *S. aureus* is more abundant within the cells at earlier time points. Therefore the sample would be more suitable for proof of principle dual channel fluorescence images of mitochondria and bacteria.

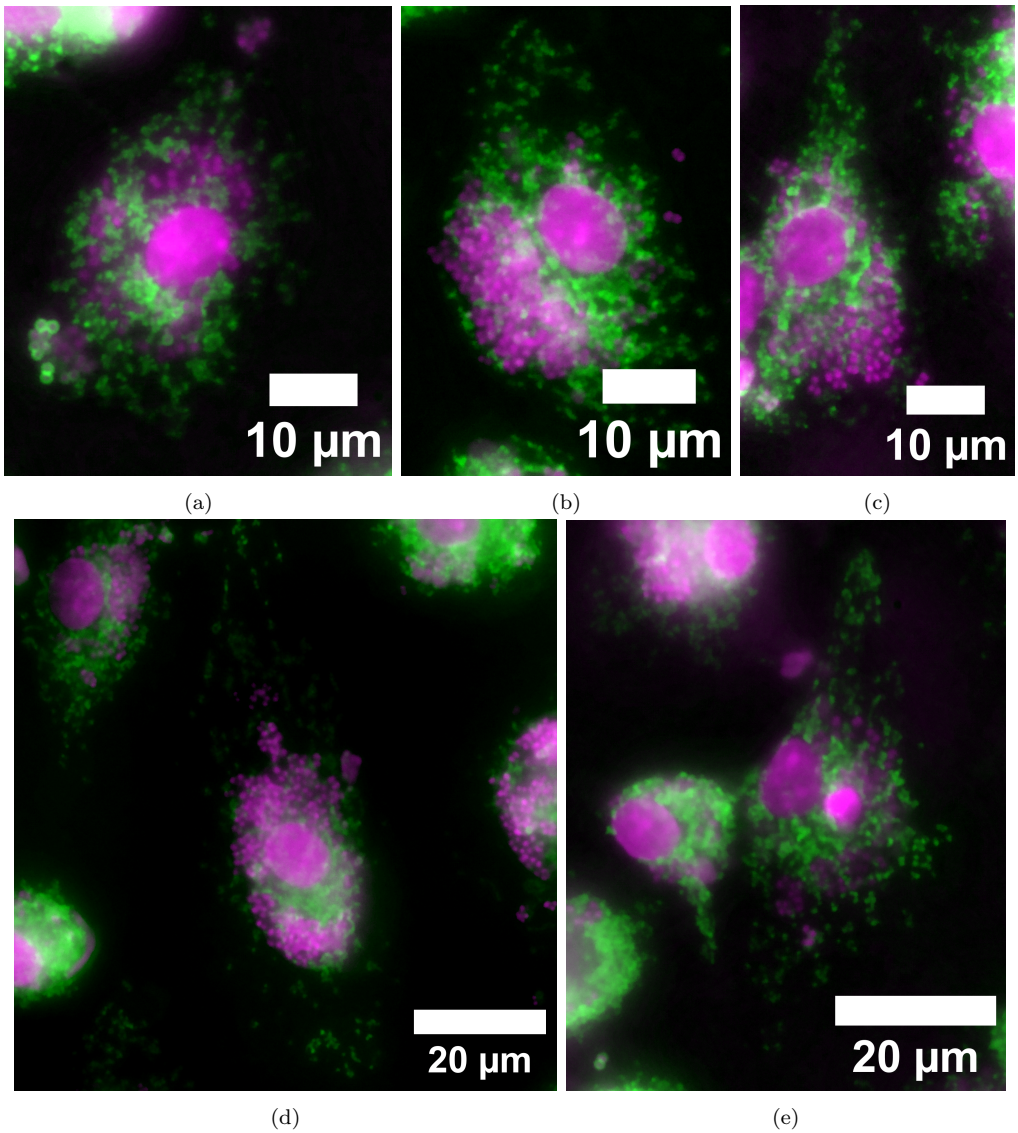

Figure 5.44: Images of a human MDM sample challenged with *S. aureus* (4 hour time point). Mitochondria labelled with Alexa Fluor 488. Nuclei and *S. aureus* labelled with DRAQ5. **(a)-(e)** are images of different areas of the same sample. Images were processed using the process outlined in figure 5.45. The 450 nm RGB laser emission line was set to 50 mA and the 635 nm emission line was set to 85 mA for image acquisition.

Figure 5.44 shows dual channel fluorescence images of multiple areas of the sample.

The mitochondria were labelled with Alexa Fluor 488 and therefore imaged on channel two. The nuclei and bacteria were labelled with DRAQ5 and imaged on channel one. The images show the M4All dual channel fluorescence microscope is capable of imaging bacteria and resolving individual bacteria when their PSFs do not overlap. Qualitatively the mitochondrial network of the cells in figure 3.13 appears to be more fragmented than the mitochondrial network of the mock infected cell in figure 5.43(b). Therefore, I believe the M4All microscope would be suitable for mitochondrial network studies in future.

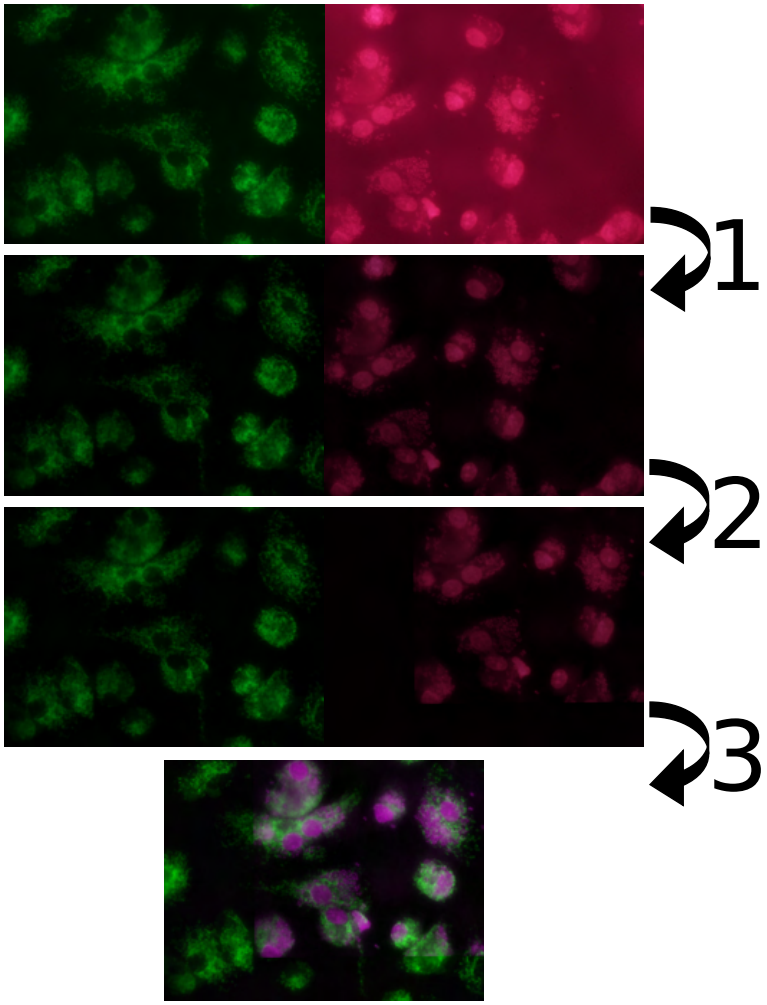

Figure 5.45: Image processing steps (ImageJ/Fiji) used to produce the representative images in figure 3.13. Step 1: Rolling ball background subtraction. Step 2: Manual image registration using Fijiyama [168]. Step 3: Create composite image.

As the images in figure 5.44 were acquired using two different spectrally separated

detection channels, the images required processing to achieve the representative images shown in the figure. The processing steps, which were carried out in ImageJ/Fiji, are outlined in figure 5.45. Step 1 was to carry out a rolling ball background subtraction. In the first row of images in figure 5.45 it can be seen that the raw image of the nuclei and bacteria had a very high background signal. I believe the background signal is due to background labelling as the concentration of DRAQ5 used was not optimised. I checked by also imaging a commercial sample with labelled actin filaments on the same detection channel (figure 5.46) and the background signal was ≈70% lower.

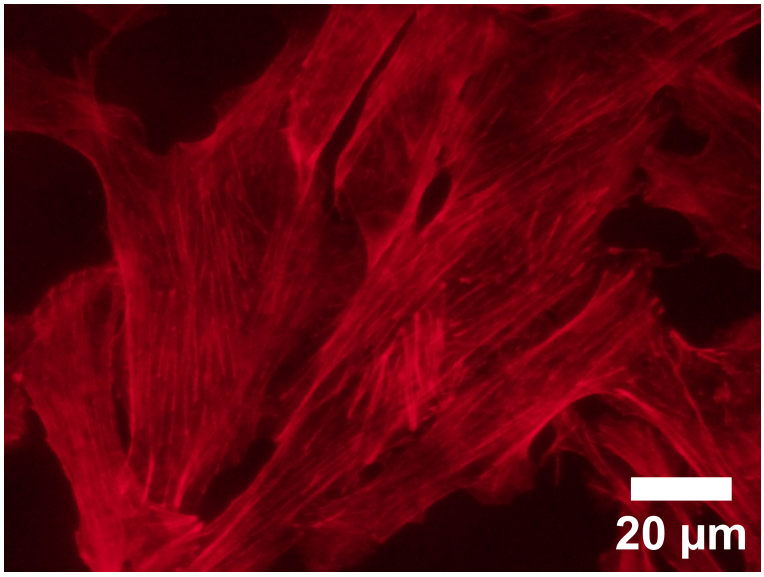

Figure 5.46: Raw image from detection channel two of the M4All dual channel fluorescence microscope of a commercial sample with labelled actin filament.

Processing step 2 was to carry out image registration between the two detection channels. For proof of principle I manually registered the images to one another using Fijiyama [168], an ImageJ/Fiji plugin, using the nuclei in the nuclei and bacteria image and corresponding nuclei shaped gaps in the mitochondria image. In future however, a more accurate method would be to capture an image of the same structure in both detection channels, such as a fluorescent bead sample which emits fluorescence in both channels. Then, for example, use the NanoJ-Core Drift Correction plugin [84] to generate a drift correction table which could be applied to register all data sets acquired on the microscope. The third processing step was to create a composite image and crop

images to regions of interest, then adjust brightness/contrast for representation.

5.3.4 SRRF Reconstruction

I also acquired imaging data on the M4All dual channel fluorescence microscope to test whether the system is capable of acquiring data sets suitable for SRRF reconstructions. Figure 5.47(a) is the first raw image frame from the set of 100 frames acquired of the same cell as in figure 5.43(b). Figure 5.47(b) is the SRRF reconstruction using SRRF settings: Ring Radius - 0.5, Radiality Magnification - 10, Axes in Ring - 8, and Temporal Analysis - Temporal Radiality Pairwise Product Mean (TRPPM). The raw data set was drift corrected using the NanoJ-Core Drift Correction [84] ImageJ/Fiji plugin before SRRF reconstruction.

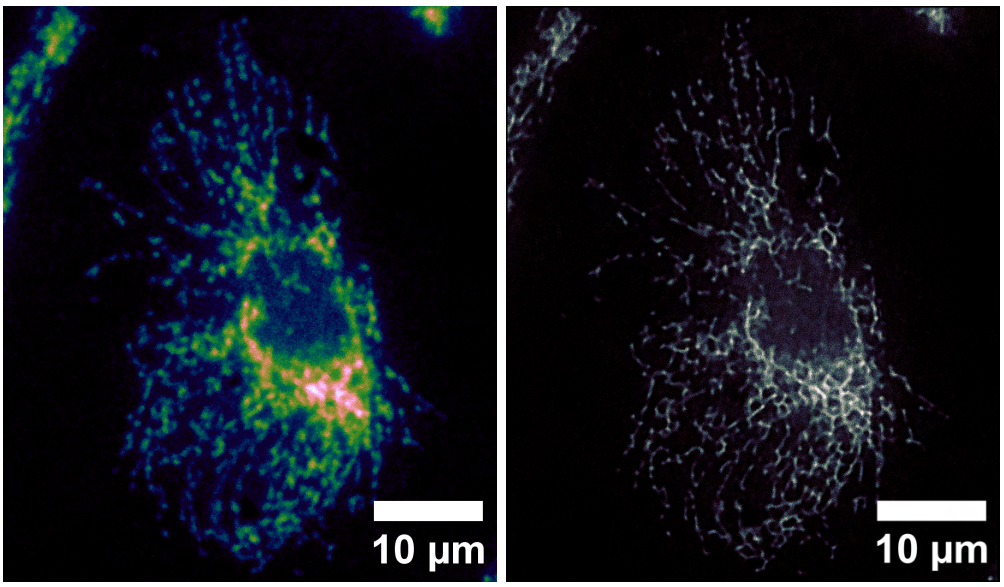

(a) (b)

Figure 5.47: **(a)** First raw image frame from the 100 image frames acquired on the second channel of the M4All dual channel fluorescence microscope. Mock infected human MDM sample with labelled mitochondria. **(b)** SRRF reconstruction using settings Ring Radius - 0.5, Radiality Magnification - 10, Axes in Ring - 8, Temporal Analysis - Temporal Radiality Pairwise Product Mean (TRPPM).

I have shown the M4All dual channel fluorescence microscope is stable enough to acquire data sets suitable for carrying out SRRF reconstructions. Further studies need to be carried out to assess methods of improving SRRF reconstructions on the system. For example, using higher quality imaging optics or changing the focal length of the tube

lenses or the objective lens to image a smaller but higher resolution FOV. As discussed in section 5.3.1, the critical Nyquist sampling distance for the system was 153 nm and the practical sampling distance was 37 nm, which is oversampled. Oversampling will also oversample any noise in the image, therefore the camera or optics could be changed to increase the practical sampling distance so it is closer to the critical Nyquist value to avoid oversampling noise. Improvements in sample labelling to reduce background labelling may also improve results. Once image acquisition is optimised, it would be interesting to carry out SRRF reconstructions on images from both detection channels to investigate colocalization of bacteria and mitochondria. Furthermore, if a third detection channel were to be added to the microscope to allow spectrally separated imaging of bacteria, mitochondria and mROS, SRRF reconstructions could be extended to investigate colocalization of all three structures within macrophages.

5.4 M4All Incubator Microscope

5.4.1 Design Parameters

The ability to use low-cost 3D printed microscopes within a cell culture incubator has the potential to increase accessibility to live cell microscopy to image macrophage host-pathogen responses to *S. pneumoniae*. Therefore I set up a single brightfield channel microscope with the M4All system to carry out initial incubator studies. An illustration of the microscope can be seen in figure 5.48(a) and the practical microscope set up within an incubator can be seen in figure 5.48(b). The microscope is a finite-conjugate optical design for simplicity. The Raspberry Pi v2 camera module was placed at the primary imaging plane of the finite-conjugate objective lens (Newport M-60X). The sample was illuminated with a low-cost LED which sits in the OpenFlexure stage illumination dovetail and condenser 3D printed attachment. The LED was powered and controlled via the GPIO pins on a Raspberry Pi 4 8GB board.

We decided to position the Raspberry Pi board outside the incubator to minimise heating within the incubator from electrical components and to minimise any effects of heat on the board itself. Therefore extension cables for the stepper motors and the

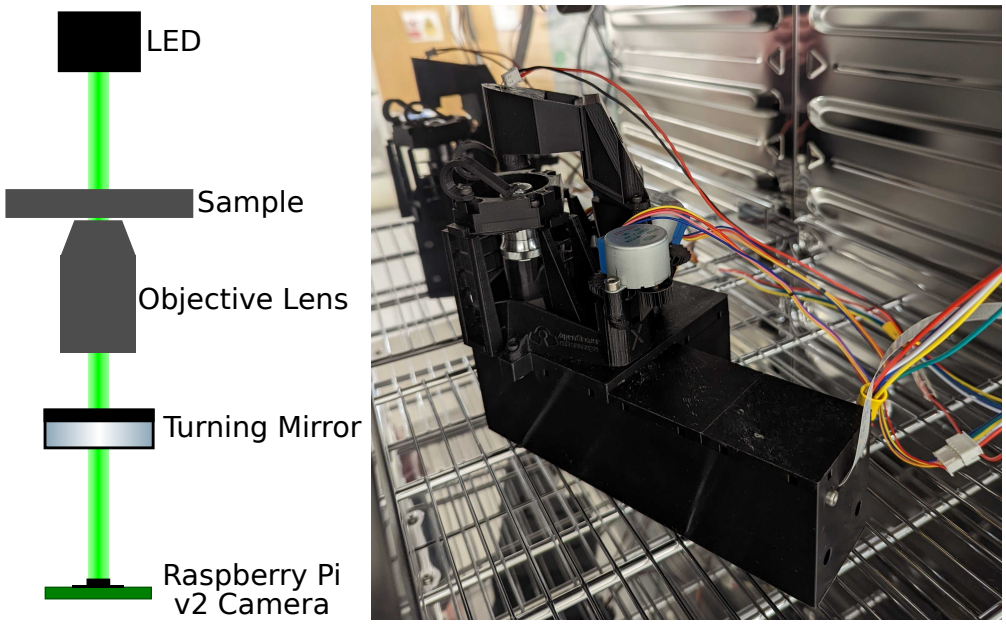

(a) (b)

Figure 5.48: **(a)** M4All incubator microscope optical design schematic. The microscope is a finite conjugate optical design where the camera is placed at the primary image plane of the finite conjugate objective lens (Newport M-60X). **(b)** Practical M4All incubator microscope set up within an incubator.

This figure partly includes illustrations of optical components from the gwoptics ComponentLibrary designed by Alexander Franzen with reuse permitted under a CC BY-NC 3.0 licence

LED were made using insulated wire, crimp pins and JST connectors to allow the wires to be fed out of the incubator and a 2 meter Raspberry Pi camera cable was used. The cables were thin enough to allow them to be fed out of the main incubator door and the door subsequently shut on them without damaging the cables or the incubator (this also did not affect the performance of the incubator). The incubator used was a Binder BD 115 natural convection incubator with no CO_2 connection/control.

5.4.2 Initial Incubator Microscope Drift Measurements

I wanted to carry out initial measurements of the extent to which the microscope drifts within the incubator when it is set at 37°C (the temperature used to culture human MDMs). Before placing the microscope within the incubator the objective lens and camera were aligned to achieve the expected magnification of 60x (the magnification of the objective lens). A 0.01 mm graticule sample was placed on the microscope and the position of the camera was iterated, acquiring an image each time and measuring the magnification until the magnification was close to 60x. Then, once the microscope was

positioned within the incubator, the incubator was allowed to stabilise to the correct temperature and the objective lens refocused and re-positioned on the sample using the stepper motors.

Three 6 hour time lapse data sets were acquired of the graticule sample on three consecutive days, capturing one image frame every minute. To assess the sample drift, each data set was first cropped to a region of interest which included the sample feature highlighted in the yellow box in figure 5.49(a). The cropped data sets were converted to 8-bit images from RGB images to reduce file sizes and conserve processing time (figure 5.49(b)). Sample drift, using the cropped data sets, was calculated using the NanoJ-Core Drift Correction ImageJ/Fiji plugin. The resulting drift plots for drift in the x and y axes can be seen in figure 5.50. Each data set within each plot appears to follow roughly the same shape of movement, suggesting the largest source of drift is the flexures on the OpenFlexure stage.

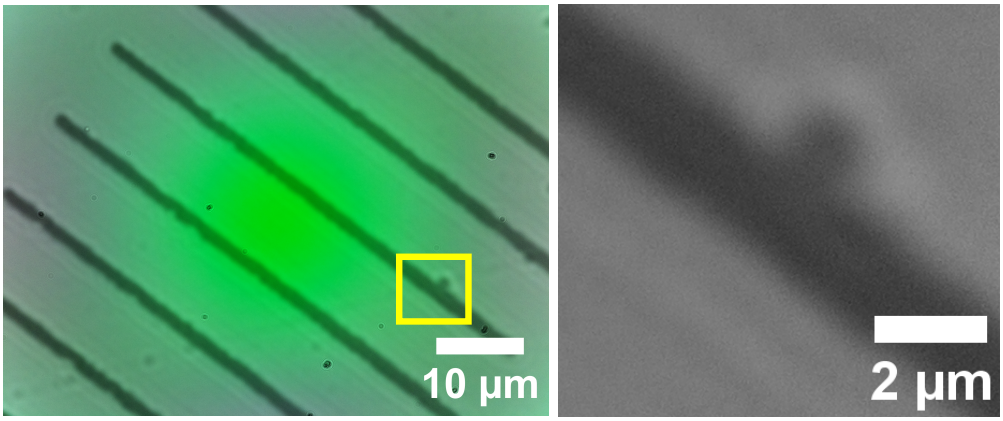

(a) (b)

Figure 5.49: **(a)** Single time point image from time lapse of a 0.01 mm graticule acquired on the M4All incubator microscope. **(b)** Cropped region of interest highlighted by the yellow region of interest in **(a)**. Cropped image was converted to an 8-bit image from an RGB image.

Data set 1 drifted the greatest distance in x, where the greatest difference from the starting pixel position was 36 pixels (0.684 μm). Both data sets 1 and 3 drifted the greatest distance in y, where the greatest difference from the starting pixel position was 71 pixels (1.349 μm). Therefore over a period of 6 hours, the microscope within the incubator was very stable and a region of interest in a fixed sample would be able to be kept within the FOV. If a live sample were to be imaged, the stability of the microscope

means tracking algorithms could be implemented to control the stepper motors to track a cell of interest. The NanoJ-Core Drift Correction plugin is unable to assess drift in the z axis, however in future drift in z could also be corrected for during image acquisition using autofocus methods, such as the sharpness based method implemented in the OpenFlexure Connect software [139, 141].

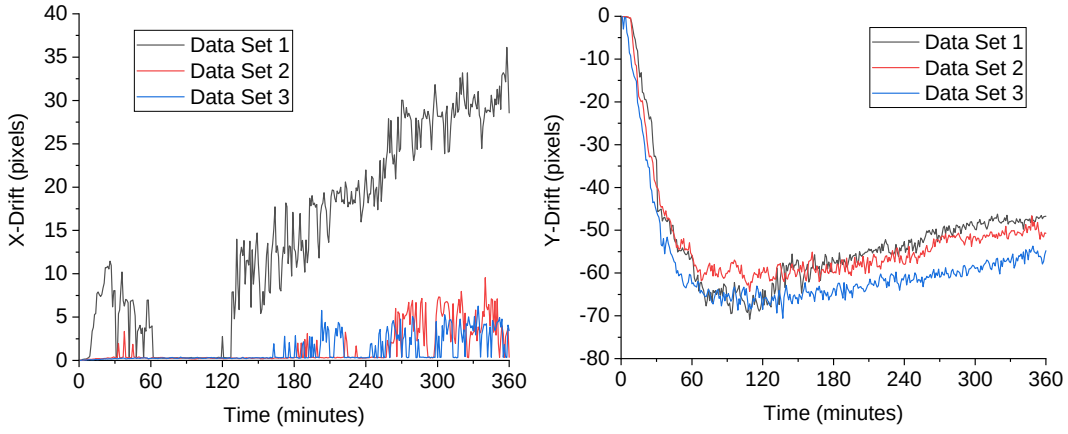

(a) (b)

Figure 5.50: **(a)** X-drift plot of three 6 hour time lapse data sets of a 0.01 mm graticule sample acquired on the M4All incubator microscope. **(b)** Y-drift plot of three 6 hour time lapse data sets of a 0.01 mm graticule sample acquired on the M4All incubator microscope. Drift plots obtained using the NanoJ-Core Drift Correction ImageJ/Fiji plugin.

5.5 Conclusions

This chapter has presented three practical applications of the M4All system and shown their applicability to future macrophage host-defence research. The first microscope, the M4All TIE and fluorescence microscope has not only produced data showing its capability of implementing both TIE microscopy and fluorescence microscopy, including SRRF reconstructions, but has been used as a tool for developing calibration methods and for stability testing. We have shown how ray transfer matrix analysis is a useful tool for modelling an optical system within the paraxial approximation, especially for analysing theoretical magnifications of multiple detection channels in infinite-conjugate systems for different lens positions. We believe we have also provided a novel method using the results of RTMA to calibrate/align the position of lenses within an infinite-

conjugate microscope in situations where other methods, such as using an autocollimator, are unsuitable. Short and long term stability tests showed the M4All microscope system is highly stable and would not require re-calibration of lens positions often.

The second microscope, the M4All dual channel fluorescence microscope, has been shown to be capable of dual colour fluorescence imaging of mitochondria and bacteria within human MDMs using low-cost components. Initial images have shown the potential for the microscope to carry out mitochondrial network studies. In future, a third fluorescence detection channel added to the microscope, suitable for imaging mROS fluorescent labels, could allow colocalization studies between mitochondria, bacteria and mROS within macrophages to investigate interactions between them after bacterial challenge with *S. pneumoniae*. This offers the potential to widen accessibility of imaging studies of macrophages to resource limited areas, such as some developing countries in Africa and Asia where prevalence of invasive pneumococcal disease is high. We have implemented computational super-resolution microscopy reconstructions using SRRF on images from the M4All microscopes. In future there is also the potential to implement super-resolution techniques, such as STORM, on the M4All system to enable wider accessibility to conventional super-resolution methods, which are often limited by costs and complexity.

Furthermore, low-cost live cell imaging would also increase functionality. Initial tests of a simple brightfield M4All incubator microscope has shown high stability of the microscope within a natural convection incubator. Over a period of six hours at 37°C the feature we tracked did not leave the FOV. Drift in z was also small enough that in future autofocus methods would be able to be implemented. Due to time constraints I was unable to test the dual channel fluorescence microscope within the incubator or test within a cell culture incubator with live cells, however the initial tests with the brightfield microscope are promising and offer great potential for a low-cost, live cell, dual channel fluorescence microscope for macrophage host-pathogen response studies.

Chapter 6

M4All Microscope Control

6.1 Introduction

This chapter will include the details of the hardware and software used to control the M4All microscopes in this research project. We wanted to use low-cost hardware and free open-source software to stay within the theme of developing a system which reduces barriers to accessing advanced microscopy techniques. As our research group did not have specialist knowledge of software engineering, I investigated what open-source software options were already available in the community and thus this chapter will include a review of what I tried and implemented. I also present a graphical user interface (GUI), which I developed in Python, to control the M4All incubator microscope.

6.2 Control Hardware

As we wanted to use low-cost microscope control hardware which was compatible with Raspberry Pi camera modules, we controlled the M4All microscopes using Raspberry Pi computer boards. Already shown in figures 5.6, 5.37 and 5.48 are the optical schematics for the M4All TIE and fluorescence microscope, dual channel fluorescence microscope and incubator microscope respectively, including the Raspberry Pi cameras used in each microscope. Figure 6.1 shows the control hardware implemented for the M4All

TIE and fluorescence microscope. Each stepper motor on the OpenFlexure microscope stage was connected to a PiStep2 quad stepper motor control board, which was connected to a Raspberry Pi 4 8Gb board via the GPIO (General Purpose Input/Output) pins. This allowed a Python GUI to be developed which could control stepper motor movement using the GPIO pins. All Raspberry Pi computer boards only include one camera module port, therefore each Raspberry Pi v2 camera module was connected to a separate Raspberry Pi Zero W board. The Raspberry Pi 4 computer board was connected to a computer monitor, keyboard and mouse. The Raspberry Pi Zero W boards were set up headless. Not shown in the figure is the IDS camera for the fluorescence channel, which was connected to and controlled separately with a Microsoft Surface tablet computer. Information on control software will be included in the next section.

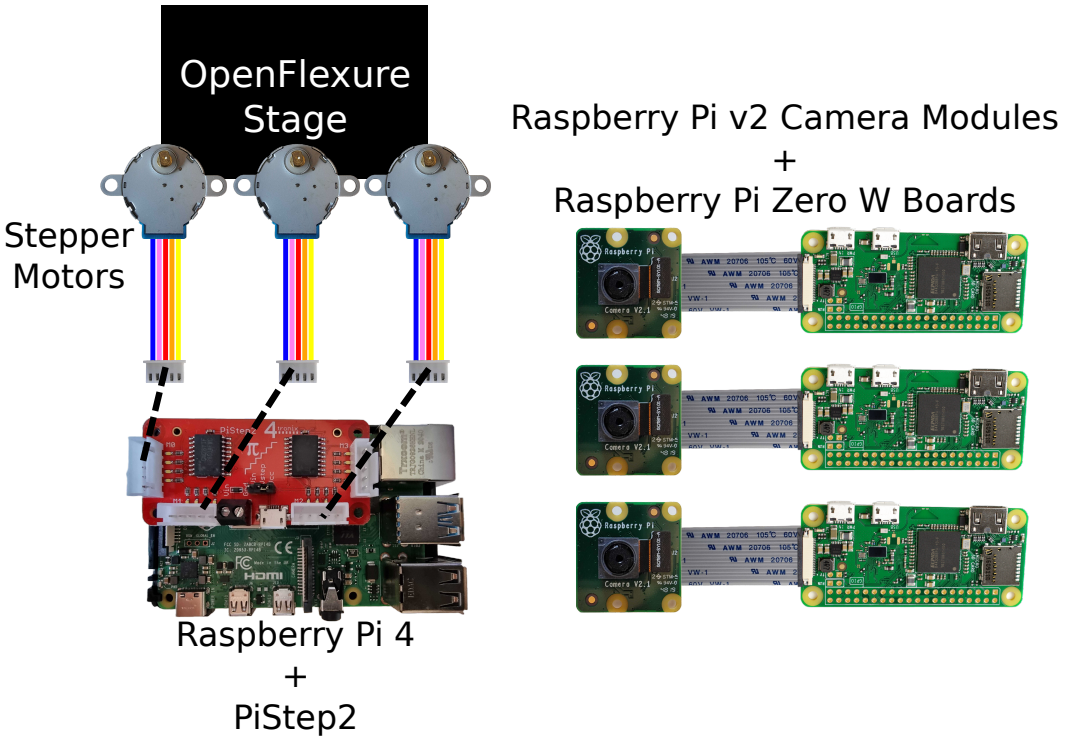

Figure 6.1: M4All TIE and fluorescence microscope control hardware. Each 28BYJ-48 stepper motor on the OpenFlexure microscope stage was connected to a PiStep2 Quad Stepper Motor Control Board, which was connected to the GPIO pins on a Raspberry Pi 4 8Gb board. Each Raspberry Pi v2 camera module was connected to a separate Raspberry Pi Zero W board.

The same hardware setup as in figure 6.1 was used for the M4All dual channel fluorescence microscope, however the Raspberry Pi v2 camera modules were replaced

with two Raspberry Pi HQ camera modules. The Raspberry Pi Zero W boards were also replaced with two Raspberry Pi 4 8Gb boards to provide greater processing speed and RAM (random access memory) for the higher quality cameras as they had larger imaging sensors.

For the M4All incubator microscope (figure 6.2), a single Raspberry Pi v2 camera module was connected to the camera port on the Raspberry Pi 4 computer board which the stepper motors were connected to. An LED was also connected to the PiStep2 board on the spare motor connector. The cathode was connected to the ground pin and the anode was connected to the pin next to it via a 330Ω resistor.

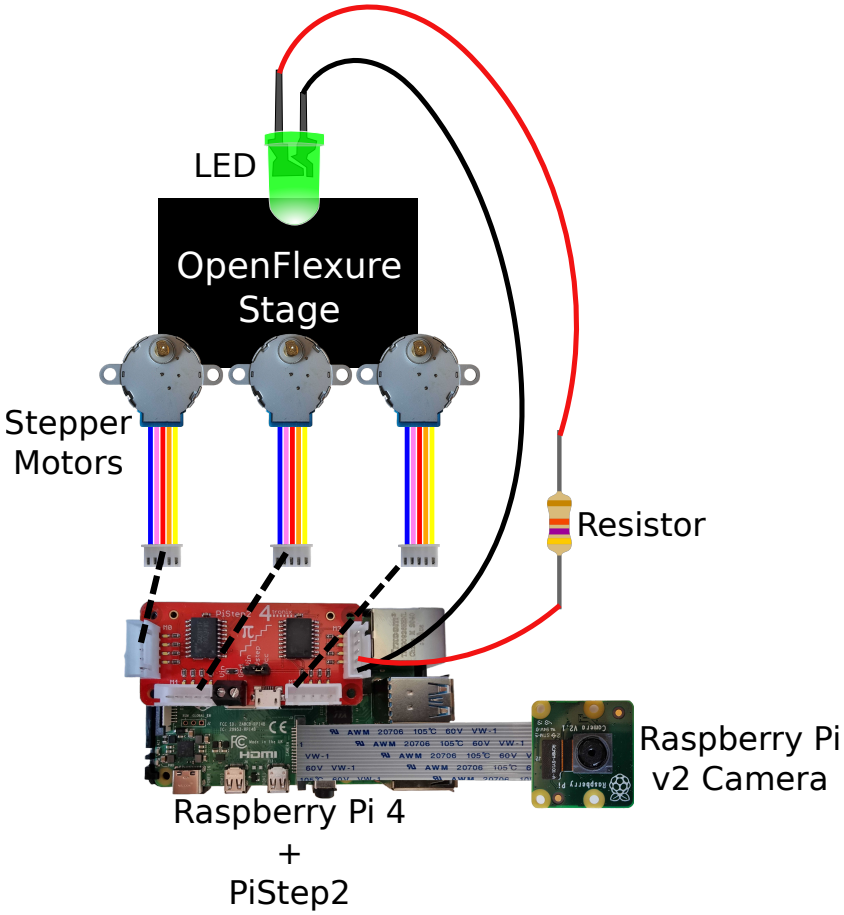

Figure 6.2: M4All incubator microscope control hardware. Each 28BYJ-48 stepper motor on the OpenFlexure microscope stage was connected to a PiStep2 Quad Stepper Motor Control Board, which was connected to the GPIO pins on a Raspberry Pi 4 8Gb board. An LED was also connected to the PiStep2 board, connecting the cathode to the ground pin on the spare motor controller connector, and the anode to the pin next to it via a resistor. A Raspberry Pi v2 camera module was connected to the camera port on the Raspberry Pi 4 8Gb board.

6.3 Control Software

6.3.1 M4All TIE and Fluorescence, and Dual Channel Fluorescence Microscopes

As highlighted in figure 6.1, each of the Raspberry Pi camera modules in the M4All TIE and fluorescence, and dual channel fluorescence microscopes were connected to separate Raspberry Pi computer boards as each board only had one camera connector. As we wanted to be able to acquire images simultaneously from the Raspberry Pi cameras, we required a method of controlling the camera Raspberry Pi boards via a single Raspberry Pi board (the one which the stepper motors were connected to). In computing this is called setting up a client and servers, which all need to be synchronized to the same computer clock time. As Raspberry Pi computer boards do not include RTC (Real-Time Clock) chips, a NTP (Network Time Protocol) needed to be set up.

NTP synchronizes network devices to a clock source [169]. We created a local network using a TP-LINK TL-WR802N wireless network router with which the client and server Raspberry Pi boards were connected to. We wanted to use NTP to synchronize the server Raspberry Pi boards to a relative clock on the client Raspberry Pi (which was not synchronized to a UTC (Coordinated Universal Time) source [169]). A signal from the client Raspberry Pi board could then be sent to the server Raspberry Pi boards telling them to acquire an image. As experience with software engineering within our research group was limited, I investigated options already available within the open-source community which implemented this logic to control multiple Raspberry Pi boards.

motionEyeOS

The first option I tried was motionEyeOS [170], which is a Linux distribution to create a video surveillance system from multiple single-board computers. The Linux image containing motionEyeOS (obtained from the GitHub repository in [170]) was written to a separate microSD card for each of the server Raspberry Pi boards. Files for pre-configuring a wireless network connection and static IP address were also added. Once

configured, the microSD cards were inserted into the server Raspberry Pi boards and booted. On the client Raspberry Pi board a web browser was opened and directed to the web page for the IP address of one of the servers (e.g. http://192.168.0.101). The web page then brings up the motionEyeOS with a live stream from the camera on that server. Within motionEyeOS further IP addresses could be added to include the camera streams from the other servers. Screenshots of the motionEyeOS software can be found on the GitHub repository for the project [171].

Advantages to the software were the simple setup procedure and the ability to view a live stream from each of the cameras on the same screen of a single client Raspberry Pi board. There were however also a few disadvantages. The first was images from each of the cameras could not be captured/saved simultaneously - a separate button on each of the live streams needed to be clicked to either capture a frame or begin recording a video. Therefore the software would not be suitable for live cell imaging using the M4All TIE and fluorescence microscope, or dual channel fluorescence microscope where simultaneously recorded images from the different channels would be required. The software was a useful tool however for initial setup of the microscopes using a fixed sample. The second disadvantage was the number of camera settings which could be controlled was limited. For example, you could change brightness, contrast, saturation and hue, but not exposure time or gain. The software also did not allow the full resolution of the Raspberry Pi camera to be used, the maximum resolution available was 1920x1080, whereas the Raspberry Pi v2 camera has 3280x2464 pixels and the Raspberry Pi HQ camera has 4056x3040 pixels. The limit in resolution comes from motionEyeOS using the Raspberry Pi cameras in video mode. The third disadvantage was image captures were only able to be saved in a JPEG file format, which involves lossy image compression, and so not optimal for microscopy data acquisition.

Compound Pi

The second software option I tried was Compound Pi [172], a Python package for controlling multiple Raspberry Pi cameras connected to different Raspberry Pi computer boards. A microSD card was set up for each of the servers. Firstly, using a PC, a

Raspberry Pi OS image was flashed onto each of the microSD cards and files added for pre-configuring wireless network connection to the local network and setting up a static IP address. Then the microSD card was booted in a Raspberry Pi board connected to a monitor, keyboard and mouse, and the Compound Pi server package and NTP daemon were installed. This was repeated for the number of servers required. A similar process was carried out for the client microSD card, installing the Compound Pi client package and NTP daemon. The microSD cards were then all booted in the correct Raspberry Pi boards in the system. On the client Raspberry Pi, the Compound Pi package was run from a terminal (figure 6.3).

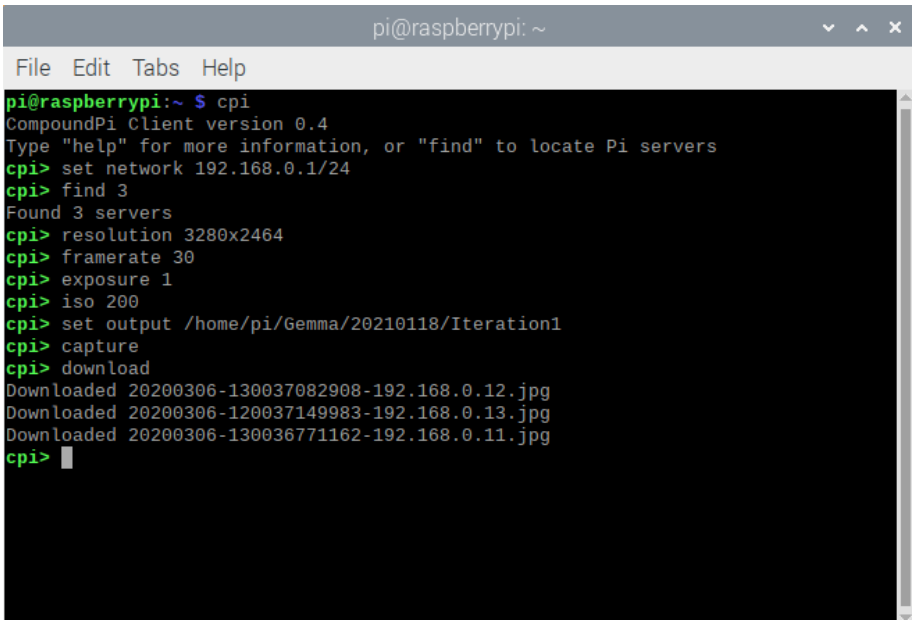

Figure 6.3: Running Compound Pi from a client Raspberry Pi terminal where camera settings can be set and images can be captured from servers and then downloaded onto the client.

As can be seen in figure 6.3, image acquisition settings could be set, such as resolution, framerate, exposure and ISO. Compound Pi uses the picamera Python interface [173] to control Raspberry Pi camera settings. Images could then be captured simultaneously (within 0.01s determined by acquiring an image of a stopclock from two cameras - precision limited by stopclock precision) from each of the Raspberry Pi cameras connected to server Raspberry Pi boards, and then downloaded over the network onto the client Raspberry Pi board.

Advantages of CompoundPi were the ability to fully control Raspberry Pi camera settings, acquire images simultaneously, simple setup including NTP setup and the ability to download images over the server onto the client Raspberry Pi board. However, a major disadvantage of Compound Pi was there was no functionality to view a live stream from the cameras. Therefore there was no ability to use the package for calibration and alignment of the microscope, or for determining a region of interest within the sample and focusing before image acquisition.

Remote Desktop

A third option was to remotely access the desktop of the server Raspberry Pi boards from the client Raspberry Pi board using RealVNC, which is included in Raspberry Pi OS. This would allow a live stream of each of the Raspberry Pi cameras to be viewed on separate remote desktops. However, as remote desktops alone would not allow simultaneous image capture, I combined remote desktops with Compound Pi.

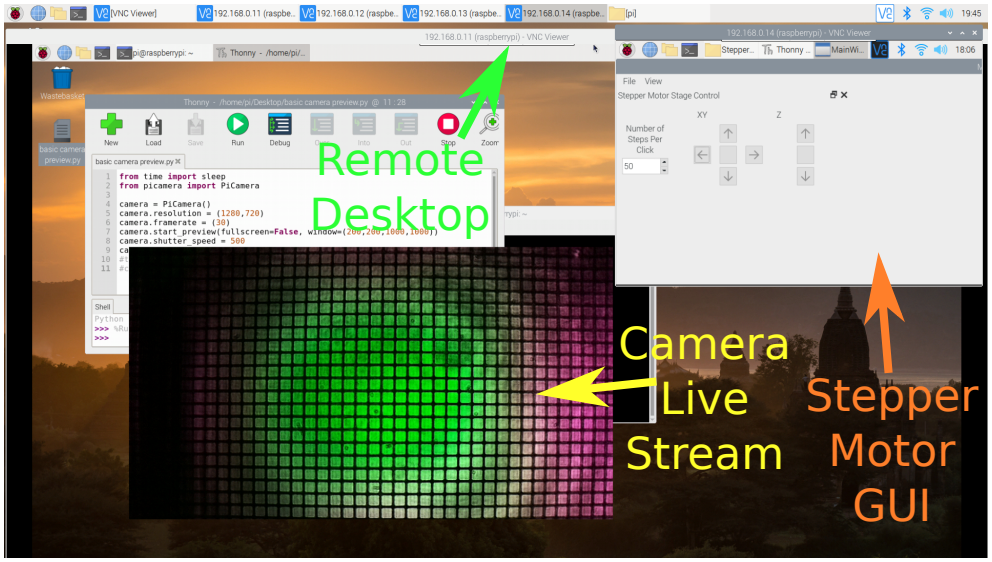

Figure 6.4: Client Raspberry Pi desktop showing one of the server remote desktops with a live stream from the Raspberry Pi camera. The stepper motor Python GUI for controlling the motors on the OpenFlexure stage is also shown.

The client Raspberry Pi board was used to view live streams of the three brightfield cameras in the TIE and fluorescence microscope, or two cameras in the dual channel fluorescence microscope on separate remote desktops. Positioning and focusing the

sample was carried out using a GUI programmed to control the stepper motors connected to the client Raspberry Pi board (discussed in the next section). The camera streams were then stopped and Compound Pi was used to acquire images from the cameras and download them onto the client. Figure 6.4 shows the client Raspberry Pi desktop with one of the server Raspberry Pi remote desktops with a camera live stream running. The stepper motor Python GUI I developed for controlling the motors attached to the OpenFlexure stage is also shown. Note that typically the stepper motors were connected to the client Raspberry Pi board itself, however in the case of figure 6.4 the motors and PiStep2 hat were connected to a separate Raspberry Pi Zero W board which acted as another server and so the stepper motor GUI was also controlled from a remote desktop.

Combining Compound Pi with remote desktops had the advantage of allowing live streams of the cameras to be accessed for sample positioning and focusing, whilst using Compound Pi also enabled simultaneous image acquisition from the cameras. However, this method was not streamlined or elegant and required complex setup. Also only either Compound Pi or the live streams could be running at any one time and so the live streams needed to be stopped before carrying out image acquisition. The method allowed images to be acquired for initial testing of the microscopes, however in future a bespoke software package combining simultaneous image acquisition from multiple Raspberry Pi boards/cameras, camera setting control and stepper motor control would be advantageous. Another option would be to swap the Raspberry Pi cameras for USB cameras which could all connect to a single Raspberry Pi board and be easily controlled from a single Python GUI.

6.3.2 Stepper Motor GUI

As mentioned, I programmed a Python GUI for controlling the stepper motors on the OpenFlexure stage. I used PyQt5 which is a set of Python bindings for the Qt GUI toolkit. A screenshot of the GUI interface can be seen in figure 6.5, which includes buttons to control the x,y and z stepper motors and a box to change how many steps the motors rotate per button click.

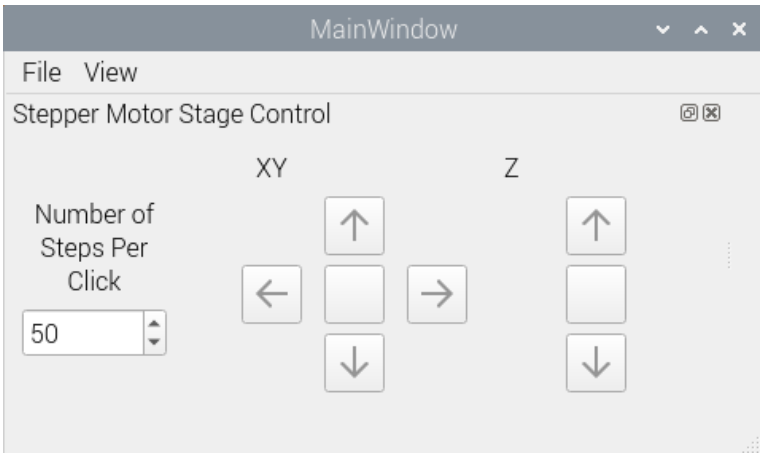

Figure 6.5: Stepper motor Python GUI interface including buttons for controlling the x,y and z stepper motors and a box to change how many steps the motors rotate per button click.

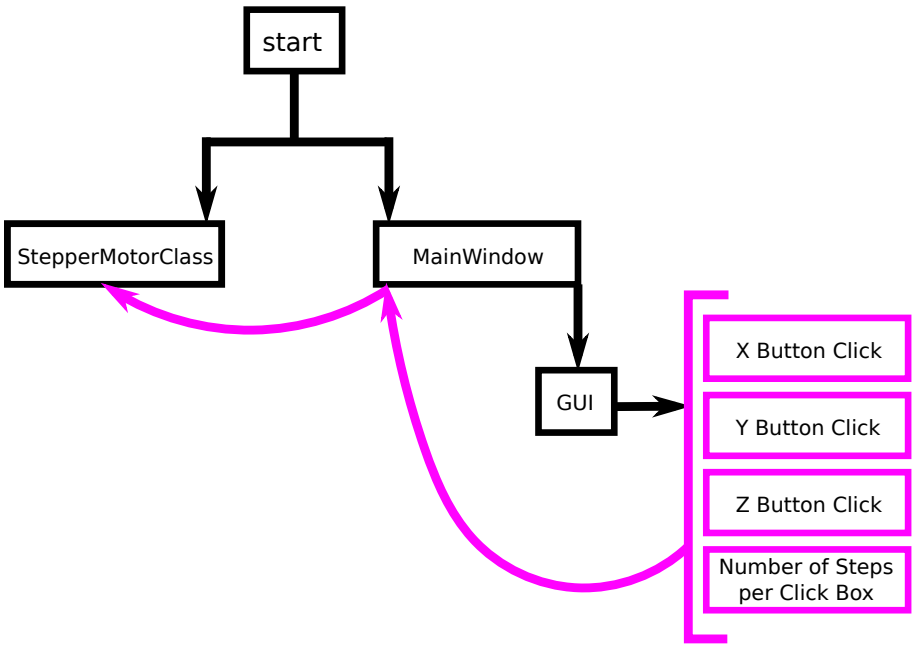

Figure 6.6: Stepper motor Python GUI process diagram.

Figure 6.6 is a process diagram for the stepper motor GUI. Running the "start" Python script initiates a "StepperMotorClass" Python class script containing the methods to control the motors, and also initiates a "MainWindow" script which opens the GUI. When the buttons on the GUI are clicked, or the number of steps per click changed, the "Main Window" script sends a signal to the "StepperMotorClass" script to run a certain method within the class to control the motor movement.

6.3.3 M4All Incubator Microscope GUI

As the M4All incubator microscope only included one Raspberry Pi camera and a single Raspberry Pi computer board, I developed a GUI to control the stepper motors, LED and camera, including setting up and acquiring a timelapse data set. A screenshot of the GUI interface can be seen in figure 6.7. There are two buttons for switching the LED on and off. The same controls for the stepper motor as in the stepper motor GUI above are included. There are also buttons to start and stop a live camera preview stream to position and focus the sample before acquiring a timelapse with the start timelapse button. Three parameters can be set before acquiring a timelapse: the camera resolution, the total number of frames to acquire, and the time interval between each frame. A save directory for the timelapse files can also be set.

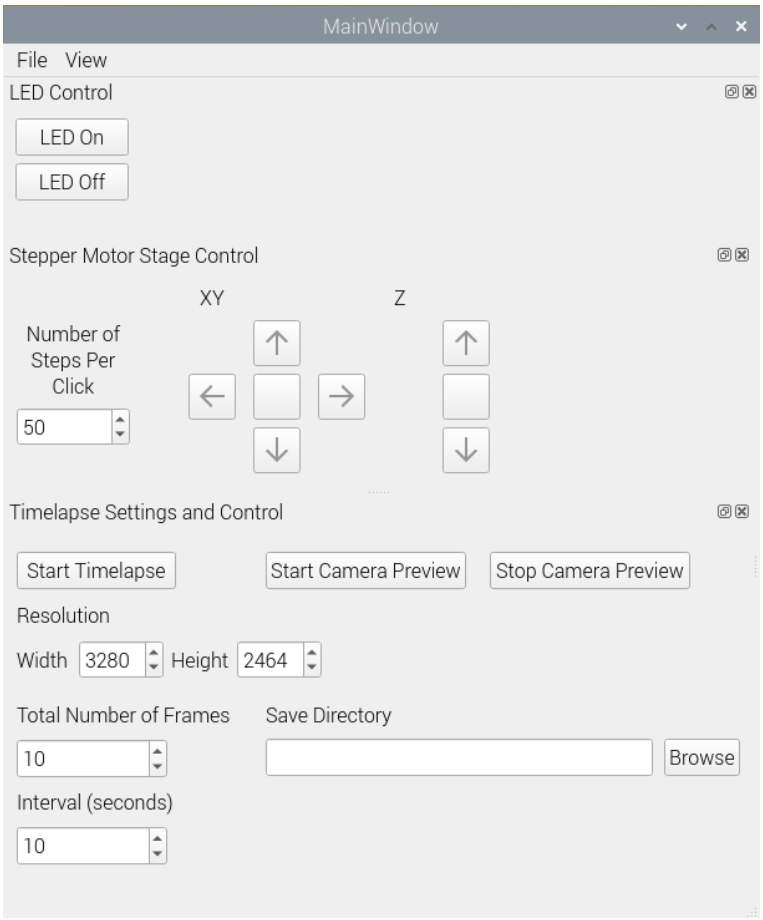

Figure 6.7: M4All incubator microscope Python GUI interface.

Figure 6.8 is a process diagram for the M4All incubator microscope GUI. Like the stepper motor GUI in the previous section, running the "start" Python script initiates the "StepperMotorClass" and "MainWindow" scripts. In this case, two more Python class scripts are also initiated for the LED ("LEDClass") and camera/timelapse ("TimelapseClass"). As for the stepper motor GUI, when the stepper motor control buttons are clicked (pink in the process diagram), the "MainWindow" script sends signals to the "StepperMotorClass" script to run certain methods within the class. Similarly when the LED on and off buttons (green in the process diagram) are clicked, the "MainWindow" script sends signals to the "LEDClass" script to run the methods to switch the LED on and off. Lastly, when the start timelapse button, camera preview buttons, resolution values, total number of frames value, interval value, or save directory are clicked or changed (blue in the process diagram), the "MainWindow" script sends signals to the "TimelapseClass" script to run the specific methods within the class.

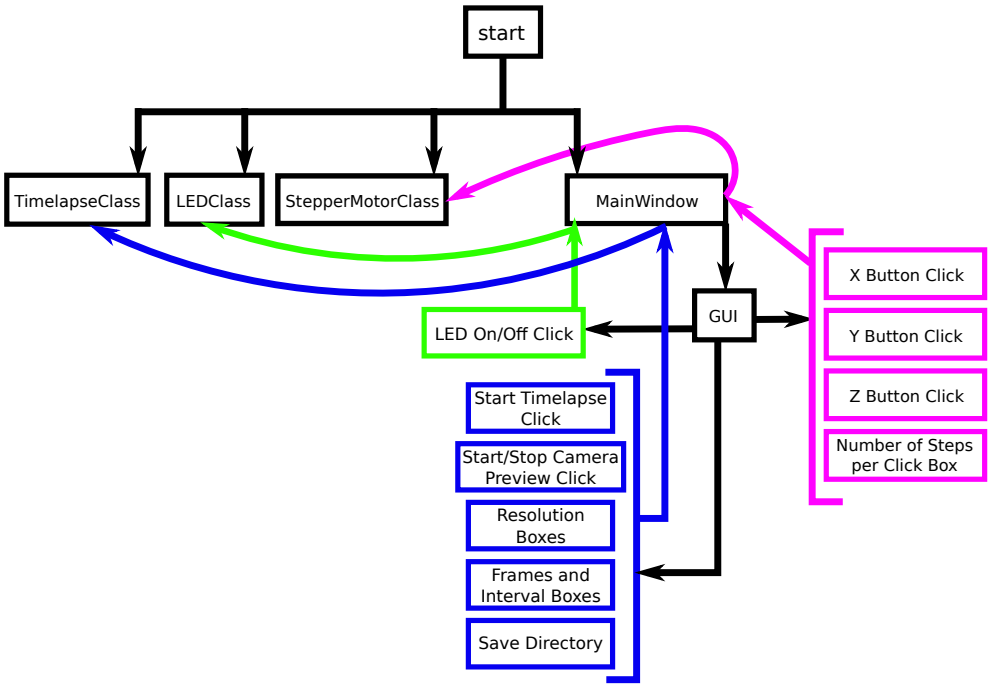

Figure 6.8: M4All incubator microscope Python GUI process diagram.

The source code for both the stepper motor GUI and the M4All incubator microscope GUI can be found on the M4All GitHub repository [9].

6.4 Note on Raspberry Pi Camera Settings

As discussed in section 5.2.7, for the M4All TIE and fluorescence microscope we expected the intensity of the three brightfield channels to be split 30:35:35. However, each channel had a different background intensity, where the first channel had the brightest background, which we believe is due to different automatic gain settings on each of the cameras. Using the Picamera Python interface for the Raspberry Pi camera modules, the exposure time, framerate and ISO can all be set. However, direct control of the analog gain is not possible [174]. The analog and digital gains can be locked so that all frames acquired from the same camera have the same gain settings, however the gain of different cameras cannot be set to the same value. Therefore for applications where it is necessary to set all of the cameras in a multichannel microscope to have the same acquisition settings, the Raspberry Pi camera modules may not be suitable and could be swapped for USB CMOS cameras with greater control over settings.

6.5 Conclusions

This chapter has outlined the control hardware and software used to control the M4All microscopes in this research project. I have highlighted a limitation of Raspberry Pi computer boards in that they only have one Raspberry Pi camera port per board. This causes problems when using multiple Raspberry Pi camera modules for multichannel microscopes. Each camera must be connected to a different Raspberry Pi board which increases the complexity of software required to perform simultaneous image acquisition and view live streams from the cameras. A review of control software for controlling multiple Raspberry Pi boards/cameras highlighted advantages and disadvantages of motionEyeOS, Compound Pi and remote desktops. Further software development is required to overcome the limitations of the reviewed methods for the M4All microscopes. For example extending the Python GUI developed for the M4All incubator microscope to include functionality for multiple Raspberry Pi cameras would provide an all inclusive software package for the M4All multichannel microscopes.

Chapter 7

Conclusions

The primary aim of this research project was to develop microscopy hardware and imaging techniques for macrophage host defence research to, in future, allow macrophage microbicidal responses to the pneumococcus to be fully characterised. This in turn would provide a basis for the development of alternative therapies to conventional antimicrobials, by pharmacologically enhancing the responses of macrophages, to not only improve treatment for those who are more susceptible to invasive pneumococcal diseases, such as infants, the elderly and those with underlying health conditions like COPD and HIV, but to also tackle the continuing issue of antimicrobial resistance. We focused on addressing spatial and temporal resolution imaging challenges when carrying out colocalization imaging studies of mitochondria, mROS and bacteria within macrophages, especially the need to correlate location with dynamics. We also addressed the issue of widening accessibility to advanced microscopy techniques for imaging macrophage host-pathogen responses in resource limited areas, such as some developing countries in Africa and Asia where prevalence of invasive pneumococcal disease is high. The main outputs from this research project were:

1. Initial imaging studies of fluorescently labelled mitochondria within human monocyte derived macrophages, using adaptive optics enhanced confocal microscopy, have suggested a targeted approach to aberration correction of smaller regions of interest of the sample is more optimal than a global aberration correction across

the sample, due to the variation in type and amplitude of aberration modes we saw across different sample regions.

2. We have shown the applicability of SRRF to image data sets of human MDMs to provide computational super-resolution reconstructions of the mitochondrial network without the barriers of complex and expensive hardware often required for conventional super-resolution microscopy techniques. We also showed how aberrations can have a negative effect on SRRF reconstructions, however the improvement in reconstructions gained from correcting aberrations does not appear to be quantifiable by SQUIRREL.
3. Early computational quantitative phase imaging studies using the Transport of Intensity equation have shown further data interpretation and modelling, such as modelling multiple scattering, is required to obtain useful quantitative phase information from TIE images of human MDM samples.
4. We have developed a new open-source, 3D printable, and modular microscopy system (M4All). We focused on stability for macrophage host defence research by 3D printing modular cube CAD files as monolithic parts, which we believe is a new approach in the field of open-hardware for microscopy. Three microscopes were built using M4All which display high levels of stability and the ability to produce research quality data, most notably dual channel fluorescence images of mitochondria and bacteria within human MDMs, offering the potential to widen access to imaging hardware for macrophage research in resource limited areas.
5. We also believe we have developed a novel method of aligning and calibrating multichannel infinite-conjugate microscopes based on ray transfer matrix analysis data.

Microscopy colocalization studies require accurate localization of structures within cells with respect to one another. As we were interested in investigating interactions between mitochondria, mROS and bacteria within macrophages, it was important to investigate to what extent aberrations were present within confocal images of macrophages and how they could affect colocalization results. As we witnessed spherical aberration in the orthogonal planes of a confocal z-stack of a human MDM sample with

labelled mitochondria, and also saw variation in the types and magnitudes of aberration modes across different regions of a MDM sample, it will be important in future to take into account and correct for any aberrations when accurate localization of structures is required. Further investigation into the most optimal method of correcting aberrations when imaging macrophages using adaptive optics is required.

Accurate localization for colocalization studies also requires high spatial resolution. We have shown that computational super-resolution reconstructions using SRRF offers improvement in resolution from diffraction limited image data sets of mitochondria labelled within human MDMs, without the requirement for complex and expensive hardware used in conventional super-resolution techniques. Also, as SRRF reconstructions can be carried out using diffraction limited microscopy image sets, issues with photobleaching and phototoxicity caused by the high laser powers required for conventional super-resolution techniques are reduced. This is advantageous for imaging studies of macrophages as not only are we interested in fast dynamic processes, such as mROS production and mitochondrial fission and fusion, but as host defence responses of macrophages occur over a time period of 16+ hours, long live cell imaging scans would particularly suffer from phototoxic effects. Originally, we also aimed to combine STED microscopy with adaptive optics to improve spatial resolution by breaking the diffraction limit for colocalization studies between mitochondria, mROS and bacteria within macrophages. However, due to time constraints and extenuating circumstances this was not possible. In future, it would be interesting to compare results using STED with SRRF reconstructions. Note that I mentioned the higher the spatial resolution of the microscope is, the more accurate colocalization studies will be when aberrations are low. Improving resolution and correcting for aberrations may however not be the only method of improving colocalization studies in macrophages. For example, in future, a technique such as FRET (Förster Resonance Energy Transfer) microscopy, where energy is transferred between donor and acceptor fluorophores when interactions occur, could be a particularly useful technique.

Not only has the development of a stable, low-cost and 3D printable microscopy system, with specific design parameters for macrophage research, opened up the poten-

tial for widening access to advanced microscopy techniques in resource limited areas for macrophage host defence research, but the system is also in a good position to address challenges with temporal resolution. As discussed, there can be limitations with access to live cell microscopy, where microscopes are normally limited to research institute facilities or research groups with the means to purchase commercial microscopes or build custom systems. A 3D printable incubator microscope could allow for low-cost live cell imaging within the lab, giving flexibility to optimise labelling protocols and determine time points of interest to image before booking facility systems.

The three M4All microscopes built in this project all have diffraction limited spatial resolution and were tested with a range of low-cost cameras with frame rates ranging from 30 fps to 166 fps. These design choices for spatial and temporal resolution were made as starting points for developing the microscopes as we wanted to first test and validate the M4All 3D printed designs using basic optical systems (developing a super-resolution microscope would involve more complex optical designs). The choice of cameras was to test what quantitative information is achievable from the very low-cost Raspberry Pi cameras (£30 - £50) and a more expensive, but still relatively low-cost, USB CMOS camera ($\leq$ £1000). All cameras used in this project were able to resolve the mitochondrial network and individual bacteria when included in a diffraction limited optical design. I have also shown the M4All dual channel fluorescence microscope is compatible with the computational super-resolution technique SRRF, although the improvement in resolution still needs to be quantified in future. I was unable to test the temporal quantitative information achievable with the different camera frame rates as I was only able to work with fixed macrophage samples and not live samples due to project time constraints. In future it needs to be tested whether these cameras can temporally resolve mitochondria fission and fusion events and also the production of mROS before it is neutralized, or whether more expensive cameras with higher frame rates would need to be used.

To test and optimise the temporal resolution an incubator microscope could be set up to firstly image over longer time scales with lower temporal resolution (to reduce phototoxic effects) to firstly determine interesting time points for macrophage

responses. Then, the microscope could be used to image over short time scales with increased temporal resolution to image dynamic processes like mROS production or mitochondrial dynamics. We have shown from initial drift measurements within an incubator that the M4All system provides excellent stability. In future the M4All dual channel fluorescence microscope has the potential to be be adapted to image within a cell culture incubator for low-cost, live cell multichannel fluorescence microscopy of macrophages for colocalization studies. For increased spatial resolution, M4All could potentially also in future be combined with, for example, STORM imaging for low-cost super-resolution microscopy.

From this research project, we have highlighted and begun to implement a number of microscopy techniques and new microscopy hardware which could aid in discovering specific microbicidal methods of macrophages in response to *S. pneumoniae*, and we hope that in future the presented methods will help to overcome some of the imaging challenges and barriers faced in this field of immunology.

Bibliography

1. Bewley, M. A. *et al.* Impaired Mitochondrial Microbicidal Responses in Chronic Obstructive Pulmonary Disease Macrophages. *American Journal of Respiratory and Critical Care Medicine* **196,** 845–855. (2020) (2017).
2. Randle, E., Ninis, N. & Inwald, D. Invasive pneumococcal disease. *Archives of Disease in Childhood - Education and Practice* **96,** 183–190 (2011).
3. Brooks, L. R. K. & Mias, G. I. Streptococcus pneumoniae's Virulence and Host Immunity: Aging, Diagnostics, and Prevention. *Frontiers in Immunology* **9** (2018).
4. Appelbaum, P. C. Antimicrobial Resistance in Streptococcus pneumoniae: An Overview. *Clinical Infectious Diseases* **15,** 77–83 (1992).
5. Masomian, M., Ahmad, Z., Ti Gew, L. & Poh, C. L. Development of Next Generation Streptococcus pneumoniae Vaccines Conferring Broad Protection. *Vaccines* **8** (2020).
6. Daniels, C. C., Rogers, P. D. & Shelton, C. M. A Review of Pneumococcal Vaccines: Current Polysaccharide Vaccine Recommendations and Future Protein Antigens. *The Journal of Pediatric Pharmacology and Therapeutics* **21,** 27–35 (2016).
7. Wahl, B. *et al.* Burden of Streptococcus pneumoniae and Haemophilus influenzae type b disease in children in the era of conjugate vaccines: global, regional, and national estimates for 2000–15. *The Lancet Global Health* **6,** e744–e757 (2018).

8. Tam, P. Y. I. *et al.* Childhood pneumococcal disease in Africa – A systematic review and meta-analysis of incidence, serotype distribution, and antimicrobial susceptibility. *Vaccine* **35,** 1817–1827 (2017).

9. Cairns, G. S. *NanoBioPhotonics-Strathclyde/M4All* version 1.0.0. 2021. `https://doi.org/10.5281/zenodo.5569711`.

10. Gustafsson, N. *et al.* Fast live-cell conventional fluorophore nanoscopy with ImageJ through super-resolution radial fluctuations. *Nature Communications* **7,** 12471 (2016).

11. Davis, Q. T. Transport of Intensity Equation Microscopy for Dynamic Microtubules. *arXiv* (2017).

12. Duarte, F. G. *et al.* Incidence, aetiology and serotype coverage for pneumococcal vaccines of community-acquired pneumonia in adults: a population-based prospective active surveillance study in Brazil. *BMJ Open* **12,** e059824 (2022).

13. Bogaert, D., de Groot, R. & Hermans, P. W. M. Streptococcus pneumoniae colonisation: the key to pneumococcal disease. *The Lancet Infectious Diseases* **4,** 144–154 (2004).

14. Braeken, D. C. *et al.* Risk of community-acquired pneumonia in chronic obstructive pulmonary disease stratified by smoking status: a population-based cohort study in the United Kingdom. *International journal of chronic obstructive pulmonary disease* **12,** 2425–2432 (2017).

15. Sadlier, C., O'Connell, S., Kelleher, M. & Bergin, C. Incidence and risk factors for invasive pneumococcal disease in HIV-positive individuals in the era of highly active antiretroviral therapy. *International Journal of STD & AIDS* **30,** 472–478 (2019).

16. Garcia Garrido, H. M. *et al.* Incidence and Risk Factors for Invasive Pneumococcal Disease and Community-acquired Pneumonia in Human Immunodeficiency Virus–Infected Individuals in a High-income Setting. *Clinical Infectious Diseases* **71,** 41–50 (2019).

17. Loughran, A. J. *et al. Streptococcus pneumoniae*: Invasion and Inflammation. *Microbiology Spectrum* **7,** 7.2.15 (2019).

18. Kadioglu, A., Weiser, J. N., Paton, J. C. & Andrew, P. W. The role of Streptococcus pneumoniae virulence factors in host respiratory colonization and disease. *Nature Reviews Microbiology* **6,** 288–301 (2008).

19. De Roux, A. *et al.* Comparison of Pneumococcal Conjugate Polysaccharide and Free Polysaccharide Vaccines in Elderly Adults: Conjugate Vaccine Elicits Improved Antibacterial Immune Responses and Immunological Memory. *Clinical Infectious Diseases* **46,** 1015–1023 (2008).

20. McGee, L., Pletz, M. W., Fobiwe, J. P. & Klugman, K. P. in *Streptococcus Pneumoniae* (eds Brown, J., Hammerschmidt, S. & Orihuela, C.) 21–40 (Academic Press, Amsterdam, 2015).

21. Coico, R. & Sunshine, G. in *Immunology : A Short Course* 1–10 (John Wiley & Sons, Incorporated, United Kingdom, 2015).

22. McDonald, D. R. & Levy, O. in *Clinical Immunology (Fourth Edition)* (eds Rich, R. R. *et al.*) Fourth Edition, 35–46 (Elsevier, London, 2013).

23. in. *Primer to the Immune Response (Second Edition)* (eds Mak, T. W., Saunders, M. E. & Jett, B. D.) Second Edition, 55–83 (Academic Cell, Boston, 2014).

24. Netea, M. G. *et al.* Trained immunity: A program of innate immune memory in health and disease. *Science* **352** (2016).

25. Ernst, J. D. in *Strain Variation in the Mycobacterium tuberculosis Complex: Its Role in Biology, Epidemiology and Control* (ed Gagneux, S.) 171–190 (Springer International Publishing, Cham, 2017).

26. Actor, J. K. in *Introductory Immunology* (ed Actor, J. K.) 1–15 (Academic Press, Amsterdam, 2014).

27. Murphy, K., Weaver, C. & Janeway, C. in *Janeway's immunobiology.* Ninth edition, 37–76 (Garland Science/Taylor & Francis Group, LLC, New York, 2017).

28. Murphy, K., Weaver, C. & Janeway, C. in *Janeway's immunobiology.* Ninth edition, 77–138 (Garland Science/Taylor & Francis Group, LLC, New York, 2017).

29. Flannagan, R. S., Cosío, G. & Grinstein, S. Antimicrobial mechanisms of phagocytes and bacterial evasion strategies. *Nature Reviews Microbiology* **7,** 355–366 (2009).

30. Elgert, K. D. *Immunology: Understanding The Immune System* (John Wiley & Sons, Inc., New Jersey, 2009).

31. Kumar, A. *Textbook of Immunology* (The Energy and Resources Institute, New Delhi, 2013).

32. Epelman, S., Lavine, K. J. & Randolph, G. J. Origin and Functions of Tissue Macrophages. *Immunity* **41,** 21–35 (2014).

33. Gallego, C., Golenbock, D., Gomez, M. A. & Saravia, N. G. Toll-like receptors participate in macrophage activation and intracellular control of Leishmania (Viannia) panamensis. *Infection and immunity* **79,** 2871–2879 (2011).

34. Grassin-Delyle, S. *et al.* The Role of Toll-Like Receptors in the Production of Cytokines by Human Lung Macrophages. *Journal of Innate Immunity* **12,** 63–73 (2020).

35. Aberdein, J. D., Cole, J., Bewley, M. A., Marriott, H. M. & Dockrell, D. H. Alveolar macrophages in pulmonary host defence – the unrecognized role of apoptosis as a mechanism of intracellular bacterial killing. *Clinical & Experimental Immunology* **174,** 193–202 (2013).

36. Preston, J. A. *et al.* Alveolar Macrophage Apoptosis–associated Bacterial Killing Helps Prevent Murine Pneumonia. *American Journal of Respiratory and Critical Care Medicine* **200,** 84–97 (2019).

37. Houghton, A. M., Hartzell, W. O., Robbins, C. S., Gomis-Rüth, F. X. & Shapiro, S. D. Macrophage elastase kills bacteria within murine macrophages. *Nature* **460,** 637–641 (2009).

38. Marriott, H. M. *et al.* Dynamic changes in Mcl-1 expression regulate macrophage viability or commitment to apoptosis during bacterial clearance. *The Journal of Clinical Investigation* **115,** 359–368 (2005).

39. Liu, H., Perlman, H., Pagliari, L. J. & Pope, R. M. Constitutively Activated Akt-1 Is Vital for the Survival of Human Monocyte-Differentiated Macrophages Role of Mcl-1, Independent of Nuclear Factor (Nf)-kb, Bad, or Caspase Activation. *Journal of Experimental Medicine* **194,** 113–126 (2001).

40. Bewley, M. A. *et al.* Pneumolysin Activates Macrophage Lysosomal Membrane Permeabilization and Executes Apoptosis by Distinct Mechanisms without Membrane Pore Formation. *mBio* **5** (2014).

41. Alberts, B. *Essential cell biology.* Fifth edition (W.W. Norton & Company, New York, 2019).

42. Sancho, D., Enamorado, M. & Garaude, J. Innate Immune Function of Mitochondrial Metabolism. *Frontiers in Immunology* **8** (2017).

43. West, A. P., Shadel, G. S. & Ghosh, S. Mitochondria in innate immune responses. *Nature Reviews Immunology* **11,** 389–402 (2011).

44. Mohasin, M. *et al.* Mitochondrial fission is increased in macrophages during mROS production in response to S. pneumoniae. *bioRxiv* (2021).

45. Yu, T., Robotham, J. L. & Yoon, Y. Increased production of reactive oxygen species in hyperglycemic conditions requires dynamic change of mitochondrial morphology. *Proceedings of the National Academy of Sciences* **103,** 2653–2658 (2006).

46. Kelly, B. & O'Neill, L. A. Metabolic reprogramming in macrophages and dendritic cells in innate immunity. *Cell Research* **25,** 771–784 (2015).

47. Li, X. *et al.* Targeting mitochondrial reactive oxygen species as novel therapy for inflammatory diseases and cancers. *Journal of Hematology & Oncology* **6,** 19 (2013).

48. Fukai, T. & Ushio-Fukai, M. Superoxide Dismutases: Role in Redox Signaling, Vascular Function, and Diseases. *Antioxidants & Redox Signaling* **15,** 1583–1606 (2011).

49. Sena, L. A. & Chandel, N. S. Physiological Roles of Mitochondrial Reactive Oxygen Species. *Molecular Cell* **48,** 158–167 (2012).

50. Chandel, N. S. Mitochondria as signaling organelles. *BMC Biology* **12,** 34 (2014).

51. Murphy, M. P. & Siegel, R. M. Mitochondrial ROS Fire Up T Cell Activation. *Immunity* **38,** 201–202 (2013).

52. Sena, L. A. *et al.* Mitochondria Are Required for Antigen-Specific T Cell Activation through Reactive Oxygen Species Signaling. *Immunity* **38,** 225–236 (2013).

53. Indo, H. P. *et al.* in *Pharmacology of Mitochondria* (eds Singh, H. & Sheu, S.-S.) 439–456 (Springer International Publishing, Cham, 2017).

54. Youle, R. J. & Bliek, A. M. v. d. Mitochondrial Fission, Fusion, and Stress. *Science* **337,** 1062–1065 (2012).

55. Adebayo, M., Singh, S., Singh, A. P. & Dasgupta, S. Mitochondrial fusion and fission: The fine-tune balance for cellular homeostasis. *The FASEB Journal* **35,** e21620 (2021).

56. Chazotte, B. Labeling mitochondria with MitoTracker dyes. *Cold Spring Harbor protocols* **2011,** 990–992 (2011).

57. Alberts, B. *et al. Molecular Biology of the Cell* Fourth edition (Garland Science, New York, 2002).

58. SIES, H. Strategies of antioxidant defense. *European Journal of Biochemistry* **215,** 213–219 (1993).

59. Polster, B. M., Nicholls, D. G., Ge, S. X. & Roelofs, B. A. in *Methods in Enzymology* (eds Murphy, A. N. & Chan, D. C.) 225–250 (Academic Press, 2014).

60. Choi, S. *et al.* Development of a high speed laser scanning confocal microscope with an acquisition rate up to 200 frames per second. *Opt. Express* **21,** 23611–23618 (2013).

61. Zhang, X. & Gao, F. Imaging mitochondrial reactive oxygen species with fluorescent probes: Current applications and challenges. *Free Radical Research* **49,** 374–382 (2015).

62. Zhao, H. *et al.* Superoxide reacts with hydroethidine but forms a fluorescent product that is distinctly different from ethidium: potential implications in intracellular fluorescence detection of superoxide. *Free Radical Biology and Medicine* **34,** 1359–1368 (2003).

63. Dikalov, S. I. & Harrison, D. G. Methods for Detection of Mitochondrial and Cellular Reactive Oxygen Species. *Antioxidants & Redox Signaling* **20,** 372–382 (2012).

64. Murphy, M. P. Selective targeting of bioactive compounds to mitochondria. *Trends in Biotechnology* **15,** 326–330 (1997).

65. Murphy, M. P. Targeting lipophilic cations to mitochondria. *Biochimica et Biophysica Acta (BBA) - Bioenergetics* **1777,** 1028–1031 (2008).

66. Dickinson, B. C. & Chang, C. J. A Targetable Fluorescent Probe for Imaging Hydrogen Peroxide in the Mitochondria of Living Cells. *Journal of the American Chemical Society* **130,** 9638–9639 (2008).

67. Diederich, B. *et al.* A versatile and customizable low-cost 3D-printed open standard for microscopic imaging. *Nature Communications* **11,** 5979 (2020).

68. *The OpenFlexure project* `https://openflexure.org/` (2022).

69. Abbas, A. K., Lichtman, A. H. & Pillai, S. in *Basic Immunology: Functions and Disorders of the Immune System* (Elsevier - Health Sciences Division, Saint Louis, 2012).

70. Bolte, S. & Cordelières, F. P. A guided tour into subcellular colocalization analysis in light microscopy. *Journal of Microscopy* **224,** 213–232 (2006).

71. Hell, S. W. & Wichmann, J. Breaking the diffraction resolution limit by stimulated emission: stimulated-emission-depletion fluorescence microscopy. *Optics Letters* **19,** 780–782 (1994).

72. Gustafsson, M. G. L. Surpassing the lateral resolution limit by a factor of two using structured illumination microscopy. *Journal of Microscopy* **198,** 82–87 (2000).

73. Betzig, E. *et al.* Imaging Intracellular Fluorescent Proteins at Nanometer Resolution. *Science* **313,** 1642–1645 (2006).

74. Rust, M. J., Bates, M. & Zhuang, X. Sub-diffraction-limit imaging by stochastic optical reconstruction microscopy (STORM). *Nature Methods* **3,** 793–796 (2006).

75. Culley, S., Tosheva, K. L., Pereira, P. M. & Henriques, R. SRRF: Universal live-cell super-resolution microscopy. *The International Journal of Biochemistry & Cell Biology* **101,** 74–79 (2018).

76. Hell, S. W. *et al.* in *Handbook Of Biological Confocal Microscopy* (ed Pawley, J. B.) 571–579 (Springer US, Boston, MA, 2006).

77. Vicidomini, G., Bianchini, P. & Diaspro, A. STED super-resolved microscopy. *Nature Methods* **15,** 173–182 (2018).

78. Henriques, R., Griffiths, C., Hesper Rego, E. & Mhlanga, M. M. PALM and STORM: Unlocking live-cell super-resolution. *Biopolymers* **95,** 322–331 (2011).

79. Leung, B. O. & Chou, K. C. Review of Super-Resolution Fluorescence Microscopy for Biology. *Applied Spectroscopy* **65,** 967–980 (2011).

80. Schneider, C. A., Rasband, W. S. & Eliceiri, K. W. NIH Image to ImageJ: 25 years of image analysis. *Nature Methods* **9,** 671–675 (2012).

81. Schindelin, J. *et al.* Fiji: an open-source platform for biological-image analysis. *Nature Methods* **9,** 676–682 (2012).

82. Culley, S. *et al.* Quantitative mapping and minimization of super-resolution optical imaging artifacts. *Nature Methods* **15,** 263–266 (2018).

83. Nieuwenhuizen, R. P. J. *et al.* Measuring image resolution in optical nanoscopy. *Nature Methods* **10,** 557–562 (2013).

84. Laine, R. F. *et al.* NanoJ: a high-performance open-source super-resolution microscopy toolbox. *Journal of Physics D: Applied Physics* **52,** 163001 (2019).

85. Johnstone, G. E., Cairns, G. S. & Patton, B. R. Nanodiamonds enable adaptive-optics enhanced, super-resolution, two-photon excitation microscopy. *Royal Society Open Science* **6,** 190589 (2019).

86. Booth, M. J. in *Optical and Digital Image Processing* (eds Cristobal, G., Schelkens, P. & Thienpont, H.) 295–322 (John Wiley & Sons, Ltd, 2011).

87. Tyson, R. *Adaptive Optics Engineering Handbook* (Taylor & Francis, 1999).

88. Booth, M. J. Adaptive optics in microscopy. *Philosophical Transactions of the Royal Society A: Mathematical, Physical and Engineering Sciences* **365,** 2829–2843 (2007).

89. Booth, M., Andrade, D., Burke, D., Patton, B. & Zurauskas, M. Aberrations and adaptive optics in super-resolution microscopy. *Microscopy* **64,** 251–261 (2015).

90. Tyson, R. K. *Principles of Adaptive Optics* (CRC Press, 2015).

91. Ji, N. Adaptive optical fluorescence microscopy. *Nature Methods* **14,** 374–380 (2017).

92. Burke, D., Patton, B., Huang, F., Bewersdorf, J. & Booth, M. J. Adaptive optics correction of specimen-induced aberrations in single-molecule switching microscopy. *Optica* **2,** 177–185 (2015).

93. Birk, U. J. *Super-Resolution Microscopy: A Practical Guide* (John Wiley & Sons, Incorporated, Germany, 2017).

94. Wojciechowski, A. M. *et al.* Optical Magnetometry Based on Nanodiamonds with Nitrogen-Vacancy Color Centers. *Materials* **12** (2019).

95. Patton, B. R., Burke, D., Vrees, R. & Booth, M. J. Is phase-mask alignment aberrating your STED microscope? *Methods and Applications in Fluorescence* **3,** 024002 (2015).

96. Booth, M., Wilson, T., Sun, H.-B., Ota, T. & Kawata, S. Methods for the characterization of deformable membrane mirrors. *Applied Optics* **44,** 5131–5139 (2005).

97. Thayil, A. & Booth, M. J. Self calibration of sensorless adaptive optical microscopes. *Journal of the European Optical Society - Rapid publications* **6** (2011).

98. Antonello, J., Wang, J., He, C., Phillips, M. & Booth, M. *Interferometric calibration of a deformable mirror* `https://doi.org/10.5281/zenodo.3714951` (2022).

99. Zuo, C. *et al.* High-resolution transport-of-intensity quantitative phase microscopy with annular illumination. *Scientific Reports* **7,** 7654 (2017).

100. Park, Y., Depeursinge, C. & Popescu, G. Quantitative phase imaging in biomedicine. *Nature Photonics* **12,** 578–589 (2018).

101. Zuo, C. *et al.* Transport of intensity equation: a tutorial. *Optics and Lasers in Engineering* **135,** 106187 (2020).

102. Teague, M. R. Deterministic phase retrieval: a Green's function solution. *Journal of the Optical Society of America* **73,** 1434–1441 (1983).

103. Zuo, C., Chen, Q., Qu, W. & Asundi, A. Noninterferometric single-shot quantitative phase microscopy. *Opt. Lett.* **38,** 3538–3541 (2013).

104. Grant, S. D., Richford, K., Burdett, H. L., McKee, D. & Patton, B. R. Low-cost, open-access quantitative phase imaging of algal cells using the transport of intensity equation. *Royal Society Open Science* **7,** 191921 (2020).

105. North, A. J. Seeing is believing? A beginners' guide to practical pitfalls in image acquisition. *Journal of Cell Biology* **172,** 9–18 (2006).

106. Yoo, H. W. *et al.* Automated spherical aberration correction in scanning confocal microscopy. *Review of Scientific Instruments* **85,** 123706 (2014).

107. Patton, B. R. *et al.* Three-dimensional STED microscopy of aberrating tissue using dual adaptive optics. *Opt. Express* **24,** 8862–8876 (2016).

108. Ekpenyong, A. E. *et al.* Bacterial infection of macrophages induces decrease in refractive index. *Journal of Biophotonics* **6,** 393–397 (2013).

109. Neto, J. C., Agero, U., Gazzinelli, R. T. & Mesquita, O. N. Measuring Optical and Mechanical Properties of a Living Cell with Defocusing Microscopy. *Biophysical Journal* **91,** 1108–1115 (2006).

110. Booth, M., Neil, M. & Wilson, T. Aberration correction for confocal imaging in refractive-index-mismatched media. *Journal of Microscopy* **192,** 90–98 (1998).

111. Mercado, R. R. d. *et al.* Characterization of cell-induced astigmatism in high-resolution imaging. *Biomed. Opt. Express* **13,** 464–473 (2022).

112. Dertinger, T., Colyer, R., Iyer, G., Weiss, S. & Enderlein, J. Fast, background-free, 3D super-resolution optical fluctuation imaging (SOFI). *Proceedings of the National Academy of Sciences* **106,** 22287–22292 (2009).

113. Paganin, D., Barty, A., McMahon, P. J. & Nugent, K. A. Quantitative phase-amplitude microscopy. III. The effects of noise. *Journal of Microscopy* **214,** 51–61 (2004).

114. Soto, M. & Acosta, E. Improved phase imaging from intensity measurements in multiple planes. *Applied Optics* **46,** 7978–7981 (2007).

115. Waller, L., Tian, L. & Barbastathis, G. Transport of Intensity phase-amplitude imaging with higher order intensity derivatives. *Optics Express* **18,** 12552–12561 (2010).

116. Jingshan, Z., Claus, R. A., Dauwels, J., Tian, L. & Waller, L. Transport of Intensity phase imaging by intensity spectrum fitting of exponentially spaced defocus planes. *Opt. Express* **22,** 10661–10674 (2014).

117. Gunjala, G. & Waller, L. *Open Source PhaseGUI* 2014.

118. Kou, S. S., Waller, L., Barbastathis, G. & Sheppard, C. J. R. Transport-of-intensity approach to differential interference contrast (TI-DIC) microscopy for quantitative phase imaging. *Optics Letters* **35,** 447–449 (2010).

119. Chen, M., Ren, D., Liu, H.-Y., Chowdhury, S. & Waller, L. Multi-layer Born multiple-scattering model for 3D phase microscopy. *Optica* **7,** 394–403 (2020).

120. Kafle, A. *et al.* 3D/4D Printing of Polymers: Fused Deposition Modelling (FDM), Selective Laser Sintering (SLS), and Stereolithography (SLA). *Polymers* **13** (2021).

121. *HohlbeinLab/OpenMicroscopy/OM_Hardware* `https://github.com/HohlbeinLab/OpenMicroscopy/blob/main/src/OM_Hardware.md` (2022).

122. Kwakwa, K. *et al.* easySTORM: a robust, lower-cost approach to localisation and TIRF microscopy. *Journal of Biophotonics* **9,** 948–957 (2016).

123. Cybulski, J. S., Clements, J. & Prakash, M. Foldscope: Origami-Based Paper Microscope. *PLOS ONE* **9,** 1–11 (2014).

124. Gürkan, G. & Gürkan, K. Incu-Stream 1.0: An Open-Hardware Live-Cell Imaging System Based on Inverted Bright-Field Microscopy and Automated Mechanical Scanning for Real-Time and Long-Term Imaging of Microplates in Incubator. *IEEE Access* **7,** 58764–58779 (2019).

125. Voigt, F. F. *et al.* The mesoSPIM initiative: open-source light-sheet microscopes for imaging cleared tissue. *Nature Methods* **16,** 1105–1108 (2019).

126. Martens, K. J. A. *et al.* Visualisation of dCas9 target search in vivo using an open-microscopy framework. *Nature Communications* **10,** 3552 (2019).

127. *LifeHack Microscope: Home* `https://holdenlab.github.io/LifeHackWebsite/home.html` (2022).

128. Delmans, M. & Haseloff, J. Cube: A Framework for 3D Printable Optomechanics. *Journal of Open Hardware* **2** (2018).

129. *miCube* `https://hohlbeinlab.github.io/miCube/index.html` (2022).

130. *LifeHack Microscope: Excitation Module* `https://holdenlab.github.io/LifeHackWebsite/Excitation.html` (2022).

131. *LifeHack Microscope: Beam Expansion Module* `https://holdenlab.github.io/LifeHackWebsite/BeamExpansion.html` (2022).

132. *LifeHack Microscope: Main Body* `https://holdenlab.github.io/LifeHackWebsite/MainBody.html` (2022).

133. *openUC2/UC2-GIT/MDK* `https://github.com/openUC2/UC2-GIT/tree/master/MDK` (2022).

134. *openUC2/UC2-GIT/UC2_v2* `https://github.com/openUC2/UC2-GIT/tree/UC2_v2` (2022).

135. *openUC2/UC2-GIT/CAD/ASSEMBLY_CUBE_Z-STAGE_v3* `https://github.com/openUC2/UC2-GIT/tree/UC2_v2/CAD/ASSEMBLY_CUBE_Z-STAGE_v3` (2022).

136. *openUC2/UC2-GIT/CAD/ASSEMBLY_XYZ-STAGE* `https://github.com/openUC2/UC2-GIT/tree/UC2_v2/CAD/ASSEMBLY_XYZ-STAGE` (2022).

137. Sharkey, J. P., Foo, D. C. W., Kabla, A., Baumberg, J. J. & Bowman, R. W. A one-piece 3D printed flexure translation stage for open-source microscopy. *Review of Scientific Instruments* **87,** 025104 (2016).

138. Liu, M., Zhang, X. & Fatikow, S. Design and analysis of a high-accuracy flexure hinge. *Review of Scientific Instruments* **87,** 055106 (2016).

139. Collins, J. T. *et al.* Robotic microscopy for everyone: the OpenFlexure microscope. *Biomedical Optics Express* **11,** 2447–2460 (2020).

140. Grant, S. D., Cairns, G. S., Wistuba, J. & Patton, B. R. Adapting the 3D-printed Openflexure microscope enables computational super-resolution imaging. *F1000Research* **8** (2019).

141. Collins, J. T. *et al.* Simplifying the OpenFlexure microscope software with the web of things. *Royal Society Open Science* **8,** 211158 (2021).

142. Knapper, J. *et al.* Fast, high-precision autofocus on a motorised microscope: Automating blood sample imaging on the OpenFlexure Microscope. *Journal of Microscopy* **285,** 29–39 (2022).

143. Bowman, R. W., Vodenicharski, B., Collins, J. T. & Stirling, J. Flat-Field and Colour Correction for the Raspberry Pi Camera Module. *Journal of Open Hardware* **4,** 1 (2020).

144. Merces, G. O. *et al.* The incubot: A 3D printer-based microscope for long-term live cell imaging within a tissue culture incubator. *HardwareX* **9** (2021).

145. Krombach, F. *et al.* Cell size of alveolar macrophages: an interspecies comparison. *Environmental Health Perspectives* **105,** 1261–1263 (1997).

146. *A test object for "self-tapping" triangular holes in printed parts.* `https://gist.github.com/rwb27/9c3ac259831a2d4316a7ae65a9f460fc` (2022).

147. *WIP: Support for UC2 modular optics* `https://gitlab.com/openflexure/openflexure-microscope/-/merge_requests/127` (2022).

148. *FreeCAD* version 0.18.4. `https://github.com/FreeCAD/FreeCAD/releases/tag/0.18.4`.

149. Sanderson, J. in *Understanding Light Microscopy* 55–74 (John Wiley & Sons, Ltd, 2019).

150. Sanderson, J. in *Understanding Light Microscopy* 127–160 (John Wiley & Sons, Ltd, 2019).

151. Kubitscheck, U. in *Fluorescence Microscopy : From Principles to Biological Applications* (John Wiley & Sons, Incorporated, Germany, 2013).

152. Jerome, W. G. J. in *Basic Confocal Microscopy* (eds Price, R. L. & Jerome, W. G. J.) 133–155 (Springer, New York, 2011).

153. Sanderson, J. in *Understanding Light Microscopy* 733–768 (John Wiley & Sons, Ltd, 2019).

154. Masters, B. R. in *Superresolution Optical Microscopy: The Quest for Enhanced Resolution and Contrast* 13–32 (Springer International Publishing, Cham, 2020).

155. Hecht, E. in *Optics* 148–246 (Addison Wesley Longman, 1998).

156. Valérie Pineau Noël *et al.* Tools and tutorial on practical ray tracing for microscopy. *Neurophotonics* **8,** 1–19 (2021).

157. Verma, R. in *Ray Optics* 43–91 (Discovery Publishing House Pvt. Limited, New Delhi, 2006).

158. Allen Nussbaum. *Modernizing the teaching of advanced geometric optics* in. Proc.SPIE. **1603** (1992).

159. Gerrard, A. & Burch, J. M. *Introduction to matrix methods in optics* (Dover, New York, 1994).

160. Schulz, J. in *Subsea Optics and Imaging* (eds Watson, J. & Zielinski, O.) 243–276 (Woodhead Publishing, 2013).

161. Dalgarno, P. A. *et al.* Multiplane imaging and three dimensional nanoscale particle tracking in biological microscopy. *Opt. Express* **18,** 877–884 (2010).

162. Matheson, A. B. *et al.* Optical Tweezers with Integrated Multiplane Microscopy (OpTIMuM): a new tool for 3D microrheology. *Scientific Reports* **11,** 5614 (2021).

163. Gore, B., Schwartz, N. & Dalgarno, P. A. Adaptive optics for multifocal plane microscopy. *arXiv: Optics* (2020).

164. Amin, M. J., Petry, S., Yang, H. & Shaevitz, J. W. Uniform intensity in multifocal microscopy using a spatial light modulator. *PLOS ONE* **15,** 1–8 (2020).

165. Abrahamsson, S. *et al.* Fast multicolor 3D imaging using aberration-corrected multifocus microscopy. *Nature Methods* **10,** 60–63 (2013).

166. *Raspberry Pi Documentation - Camera* `https://www.raspberrypi.com/documentation/accessories/camera.html` (2022).

167. Cole, J., Aberdein, J., Jubrail, J. & Dockrell, D. H. in *Advances in Microbial Physiology* (ed Poole, R. K.) 125–202 (Academic Press, 2014).

168. Fernandez, R. & Moisy, C. *Fijiyama: a registration tool for 3D multimodal time-lapse imaging.* 2020.

169. Rybaczyk, P. *Expert Network Time Protocol an experience in time with NTP* (Apress, Berkeley, 2005).

170. *motionEyeOS* `https://github.com/motioneye-project/motioneyeos` (2022).

171. *motionEyeOS Screenshots* `https://github.com/motioneye-project/motioneyeos/wiki/Screenshots` (2022).

172. *Compound Pi* `https://github.com/waveform-computing/compoundpi` (2022).

173. *picamera* https://github.com/waveform80/picamera (2022).

174. Jones, D. *Picamera: Camera Hardware* https://picamera.readthedocs.io/en/release-1.13/fov.html (2022).